



**HAL**  
open science

# Observing at-surface irradiance and albedo from space : the Tibet experiment

Laure Roupioz

► **To cite this version:**

Laure Roupioz. Observing at-surface irradiance and albedo from space : the Tibet experiment. Optics / Photonic. Université de Strasbourg; Technische universiteit (Delft, Pays-Bas), 2015. English. ⟨NNT : 2015STRAD022⟩. ⟨tel-01316949⟩

**HAL Id: tel-01316949**

**<https://theses.hal.science/tel-01316949v1>**

Submitted on 17 May 2016

**HAL** is a multi-disciplinary open access archive for the deposit and dissemination of scientific research documents, whether they are published or not. The documents may come from teaching and research institutions in France or abroad, or from public or private research centers.

L'archive ouverte pluridisciplinaire **HAL**, est destinée au dépôt et à la diffusion de documents scientifiques de niveau recherche, publiés ou non, émanant des établissements d'enseignement et de recherche français ou étrangers, des laboratoires publics ou privés.



HAL Authorization



**UNIVERSITÉ DE STRASBOURG**

**ÉCOLE DOCTORALE MSII**

**ICube, équipe TRIO**

**THÈSE** présentée par :

**Laure ROUPIOZ**

soutenue le : **10 juillet 2015**

pour obtenir le grade de : **Docteur de l'université de Strasbourg**

Discipline/ Spécialité : **Téledétection**

**Modélisation et suivi de l'éclairement et de  
l'albédo de surface à partir de données  
satellitaires: le cas du Tibet**

**THÈSE dirigée par :**

**Mme NERRY Françoise**  
**M. MENENTI Massimo**

Dr., université de Strasbourg  
Prof., université de Delft

**RAPPORTEURS :**

**M. LOPEZ-BAEZA Ernesto**  
**M. YANG Kun**

Prof., université de Valence  
Prof., académie chinoise des sciences

---

**AUTRES MEMBRES DU JURY :**

**Mme LI Jia**  
**M. TAKAKURA Yoshitane**  
**M. HANSSEN Ramon**

Prof., académie chinoise des sciences  
Dr., université de Strasbourg  
Prof., université de Delft



**Observing at-surface irradiance and albedo  
from space: the Tibet experiment**

PhD thesis

**Laure Roupioz**



# **Observing at-surface irradiance and albedo from space: the Tibet experiment**

## **Proefschrift**

ter verkrijging van de graad van doctor  
aan de Technische Universiteit Delft,  
op gezag van de Rector Magnificus prof. ir. K. C. A. M. Luyben;  
voorzitter van het College voor Promoties,  
in het openbaar te verdedigen op vrijdag 10 juli 2015 om 12:30 uur

Door

**Laure ROUPIOZ**

Master of Science in Geo-Information Science  
Wageningen University, The Netherlands

geboren te Lyon, France.

Dit proefschrift is goedgekeurd door de promotoren:

Prof. dr. Massimo Menenti  
Dr. Françoise Nerry  
Prof. dr. Li Jia

Samenstelling promotiecommissie:

Rector Magnificus, Prof. dr. M. Menenti Dr. F. Nerry, Prof. dr. L. Jia	voorzitter CiTG, Technische Universiteit Delft, promotor CNRS (France), promotor Chinese Academy of Science (China), promotor
---	--

Onafhankelijke leden:

Dr. hab. Y. Takakura	Université de Strasbourg (France)
Prof. dr. E. Lopez Baeza	Universidad of Valencia (Spain)
Prof. dr. K. Yang	Chinese Academy of Science (China)
Prof. dr. ir. R.F. Hanssen	CiTG, Technische Universiteit Delft
Prof. Dr.-Ing. R. Klees	CiTG, Technische Universiteit Delft, reservelid

Copyright © 2015 by L. Roupioz

All rights reserved. No part of the material protected by this copyright notice may be reproduced or utilized in any form or by any means, electronic, mechanical, including photocopying, recording or by any information storage and retrieval system, without the prior permission of the author.

ISBN 978-94-6186-502-1

An electronic version of this dissertation is available at  
<http://repository.tudelft.nl/>.

---

# Abstract

Monitoring the solar radiation budget on a daily basis is a prerequisite to study land surface processes, especially in climatology and hydrology, and in derived applications like drought early warning. Current space-born radiometers can provide daily observations to derive surface radiative fluxes at a spatial resolution of one square kilometer at best, which is not enough to properly take into account surface heterogeneity in many regions of the globe. As part of a major scientific initiative to study the hydrology of the Tibetan Plateau -especially known for its rough topography- this thesis focuses on developing a method to adequately estimate at-surface daily solar radiation budget over this particular area. Following a first effort to produce a time series of the radiative budget from existing satellite data products, it appeared that it is necessary to consider terrain and clouds spatial variability at the sub-pixel level when working over heterogeneous areas such as the Tibetan Plateau. Thus, the impact of spatial and temporal variability of clouds on solar radiation was investigated through a case study conducted on the field whose results demonstrate that the surface irradiance estimation would benefit from using cloud distribution instead of cloud fraction to account for the cloud cover. Furthermore, a high temporal resolution cloud cover leads to a better temporal average of the radiative fluxes. Regarding the effects of the terrain, a new sub-pixel topographic correction method is proposed and applied. It demonstrates that the integration of the sub-pixel topographic effects using high resolution DEM improves the irradiance as well as the albedo retrieval. The temporal resolution of the latter is also to consider and the use of geostationary satellite allows to increase the retrieval frequency.

Based on multi-source and multi-resolution remote sensing data, the developed method provides a usable solar radiation budget dataset. Combined with the outcomes of the in-depth researches on clouds and topography, it paves the way for a new operational methodology which adequately accounts for sub-pixel heterogeneity when producing large area time series of solar radiation budget at the surface.



---

# Preface

A PhD is an important step in the life of a young scientist. Get to grips with your very own research topic, go through ups and downs, alternating from enthusiasm to weariness, all this not only teaches you how to become a researcher, but also teaches you a lot about who you are and what you actually want to do. Fortunately, you don't do that alone, you grow surrounded by many persons who contribute to this achievement and allow you to learn, improve and outdo yourself. I would like to dedicate the following lines to thank all those people who supported me scientifically or personally, regularly or punctually, during this rich and intense part of my life.

First of all, I would like to express my gratitude to my three promotors without whom I would not have been able to complete successfully this PhD. Thank you Li Jia, you trusted my scientific abilities and offered me this PhD opportunity. Many thanks also for inviting me to your institute in China and for helping me with setting up my fieldwork in Tibet. I enjoyed every trip and I'm missing the China already. Thank you Massimo Menenti, you guided me through the whole scientific process, leading me in the good direction, and always made time for answering my questions despite your very busy schedule. Thank you Françoise Nerry, you supported me on a daily basis, cheered me up in the hard times, patiently dealt with my comings and goings in your office and allowed me to stay on track to submit my PhD. I am really grateful to have had you three as promotors, I learned and grew a lot thanks to you during those four years and also shared really nice moments with you. I wish this will continue in the future.

This PhD started in the Netherlands, where I spent the two first years, and I would like to thank my colleagues from Alterra (Wageningen), especially Marta Perez-Soba and Sander Mûcher, who helped me building up myself as a researcher and offered me many enriching opportunities in large scale projects. Without you, I wouldn't have reached this point. You supported my decision to start a PhD and were on my side when needed. To stop working with you was a hard choice to make, and I hope will have occasions to collaborate again.

This research was initiated in the framework of the CEOP-AEGIS project and I would like to thank its members for the interesting discussions and collaborations. I'm very thankful to Yaoming Ma who welcomed me in his institute. Then, the research was continued within the Dragon 3 young scientist program (ESA and MOST) during which I

appreciated to benefit from the good advices and nice company of Hervé Yesou. Many thanks also to Haolu Shang, without you I wouldn't have found my way in China, and to Zhang Guoshuai, it was very pleasant to travel with both of you.

Many thanks to all the very nice PhD students I had the chance to meet. You broadly contributed to the fact that I enjoyed my PhD time, you always had good advices, cheering words or good beers. The list is a bit too long to name you all, but I guess you will recognize yourself.

I integrated the TRIO team (Icube, Illkirch) half way my PhD and I would like to thank my colleagues for their support, the nice atmosphere, the cookies and the coffee breaks which turned the workspace into a nice place. I'm also thankful to the team from INSA (Strasbourg) and especially to Tania Landes who gave me the opportunity and the necessary support to experiment teaching.

I would like to thank my family, and especially my mum for her unfailing support. Thank you to my family in law as well, always very kind with me. Thank you to my Dutch, French and international friends for bringing me mental support and distraction. Thank you Amandine, Elise and Lucie for the sushi's, the falafels and the vodka limes. Thank you Mirianna, without you I would probably have drove crazy before the end. For more than 10 years we support each other, we took the "bac" together now the PhD. Thank you also Sébastien for the perfect organization of the trips that opened and concluded my PhD. Finally, I would like to thank Jérôme, my future husband. I met you thanks to this PhD, you have always been there, patient and bearing my good and bad moods, listening me evenings long turning a problem upside down until I found the solution. You did so much, and probably more than I realized, which allowed me to enjoy this time and finish successfully this PhD.

To all of you and to all the people I did not mentioned here but who still played a role in this achievement, thank you! Merci!

# Contents

<b>Abstract</b>	<b>i</b>
<b>Preface</b>	<b>iii</b>
<b>Contents</b>	<b>v</b>
<b>List of Figures</b>	<b>vii</b>
<b>List of Tables</b>	<b>xiii</b>
<b>List of Symbols</b>	<b>xv</b>
<b>List of Acronyms</b>	<b>xix</b>
<b>1 Introduction</b>	
1.1 Context .....	1
1.2 Research objectives .....	6
1.3 Thesis outline .....	10
<b>2 The Tibetan Plateau: field and remote data sources</b>	
2.1 Introduction .....	11
2.2 The Tibet Plateau .....	12
2.3 Topographic data .....	15
2.4 Satellite data .....	16
2.5 Validation data .....	20
2.6 Conclusion .....	27
<b>3 Solar radiation budget from existing satellite data products</b>	
3.1 Introduction .....	29
3.2 Surface irradiance .....	30
3.3 Surface albedo .....	36
3.4 Daily integration of solar radiation .....	38
3.5 Challenge in mountainous area .....	39
3.6 Solar radiation from MODIS data .....	40
3.7 Results and validation .....	46
3.8 Conclusion .....	55

---

<b>4</b>	<b>Impact of spatial and temporal variability of clouds on solar radiation: a case study</b>	
4.1	Introduction .....	57
4.2	Fieldwork set up and data calibration.....	59
4.3	Results and validation .....	70
4.4	Conclusion .....	83
<b>5</b>	<b>Sub-pixel topography effects on solar irradiance estimated using remote sensing</b>	
5.1	Introduction .....	85
5.2	Impact of topography: Sub-pixel topographic correction.....	87
5.3	Impact of the atmosphere: Fraction of diffuse skylight estimation .....	103
5.4	Conclusion .....	111
<b>6</b>	<b>Land surface albedo in rugged terrain</b>	
6.1	Introduction .....	113
6.2	Albedo estimation using sub-pixel topography correction.....	114
6.3	Sub-pixel topographically corrected reflectance .....	121
6.4	Sub-pixel topographically corrected albedo.....	126
6.5	Conclusion .....	139
<b>7</b>	<b>Conclusions and perspectives</b>	
7.1	Achievements.....	142
7.2	Perspectives.....	144
	<b>References</b>	<b>147</b>
	<b>Summary</b>	<b>163</b>
	<b>Samenvatting</b>	<b>167</b>
	<b>Résumé</b>	<b>171</b>
	<b>Résumé étendu</b>	<b>177</b>
	<b>Curriculum Vitae</b>	<b>197</b>
	<b>List of Publications</b>	<b>199</b>

## List of Figures

<b>1.1</b>	Sub-pixel and pixel level concept	6
<b>2.1</b>	The Tibetan Plateau and surroundings with the CEOP-AEGIS project extent delimitation	13
<b>2.2</b>	Study area subset	14
<b>2.3</b>	Location of the meteorological station of NamCo, on the South bank of the NamCo Lake	14
<b>2.4</b>	Slope values distribution over the Tibetan Plateau	15
<b>2.5</b>	ASTER-GDEM2 for the entire study area	16
<b>2.6</b>	MODIS daily products gap filling procedure	18
<b>2.7</b>	Location of the ground stations within the study area	21
<b>2.8</b>	Picture of the BJ site and land cover map of the surroundings	22
<b>2.9</b>	Picture of the Linzhi site and land cover map of the surroundings	23
<b>2.10</b>	Picture of the NamCo site and land cover map of the surroundings	24
<b>2.11</b>	Picture of the Qomolangma site and land cover map of the surroundings	25
<b>3.1</b>	Interactions between the extraterrestrial irradiance and the Earth's atmosphere	33
<b>3.2</b>	Solar position for a given location on the Earth's surface	35
<b>3.3</b>	General steps for albedo retrieval from remote sensing imagery	38
<b>3.4</b>	Estimation of TOA irradiance using MODIS Terra overpass time and terrain slope and azimuth	41
<b>3.5</b>	Computation of surface irradiance for clear sky conditions integrating atmospheric transmissivity derived from MODIS products	44
<b>3.6</b>	Computation of the solar radiation budget for all skies using MODIS products	46
<b>3.7</b>	Surface irradiance computed using a constant atmospheric transmission factor or the proposed methodology	47
<b>3.8</b>	Computation of the solar zenith angle or the sun incident angle	47
<b>3.9</b>	Time series of instantaneous solar downwelling and upwelling radiations	48

---

<b>3.10</b>	Time series of surface albedo derived from MODIS	49
<b>3.11</b>	Solar radiation validation for downwelling and upwelling fluxes, for all skies or clear sky conditions, at BJ station for the entire time series	50
<b>3.12</b>	Solar radiation validation for downwelling and upwelling fluxes, for all skies or clear sky conditions, at Qomo station for the entire time series	50
<b>3.13</b>	Solar radiation validation for downwelling and upwelling fluxes, for all skies or clear sky conditions, at Linzhi station for the entire time series	51
<b>3.14</b>	Solar radiation validation for downwelling and upwelling fluxes, for all skies or clear sky conditions, at NamCo station for the entire time series	51
<b>3.15</b>	The four ground stations location on the Tibetan Plateau and the footprint of the pixel used for the validation	53
<b>3.16</b>	Comparison between TOA upwelling radiance estimated using MODIS surface reflectance and TOA upwelling radiance measured by MODIS sensor	54
<b>4.1</b>	Instrument set up to record the hemispherical images and net radiation instrument to record the radiative fluxes at the NamCo station	59
<b>4.2</b>	An example of raw hemispherical image	60
<b>4.3</b>	Can-Eye calibration module output	61
<b>4.4</b>	Hemispherical processing steps for a pixel p	63
<b>4.5</b>	Comparison of different band pre-processing (normalized) for cloud classification	66
<b>4.6</b>	Comparison of classifications using split value based on local min or median	67
<b>4.7</b>	Comparison of classifications obtained using split value identified based on local min and median for three different cloud cover conditions	67
<b>4.8</b>	Decision tree to define the split value between clear sky and clouds	68
<b>4.9</b>	Left: pixel distribution plots with classification threshold to cluster pixels into open sky and clouds. Middle: classification mask with the sky in blue and the clouds in green obtained using the red band, the red/blue ratio, the normalized red/ blue index and the saturation band. Right: the original image	70
<b>4.10</b>	Left: pixel distribution plots with classification threshold to cluster pixels into open sky and clouds. Middle: classification mask with the sky in blue and the clouds in green obtained using the red band and the saturation band. Right: the original image	71
<b>4.11</b>	Example of the different classification difficulties encountered during the cloud detection	73
<b>4.12</b>	Segmentation grid and example of cloud distribution maps	75

<b>4.13</b>	Correlation between downward ground fluxes measurement for shortwave and longwave and the different cloud fractions	75
<b>4.14</b>	Time series of solar irradiance measured at the ground and cloud fraction estimates	76
<b>4.15</b>	Illustration corresponding to the first (a) and second (b) anomalies	77
<b>4.16</b>	Time series of downward longwave measured at the ground and cloud fraction estimates	78
<b>4.17</b>	Regression analysis between estimated $C_{fS}$ and (a) difference between clear sky modelled and measured shortwave irradiance, (b) downward longwave fluxes	79
<b>4.18</b>	Comparisons between hourly $C_{fS}$ (a) and sunshine duration (b) computed with different time steps	81
<b>4.19</b>	Comparisons between daily $C_{fS}$ (a) and sunshine duration (b) computed with different time steps	82
<b>4.20</b>	Comparison between (a) the three sunshine duration estimates over 2 hours periods and (b) the 2-hourly solar radiation budget averages computed using the three sunshine duration estimates and plotted against the solar radiation budget measured at the ground	83
<b>5.1</b>	Slope and azimuth sub-pixel normality distribution maps (a) and statistics (b) within each square kilometer pixel over the Tibet Plateau and the surroundings	91
<b>5.2</b>	Irradiance sub-pixel topographic correction steps	92
<b>5.3</b>	Correlation between anisotropic and isotropic radiance values for 5 solar illumination angle classes and 5 different BRDF	93
<b>5.4</b>	Shadow Binary Factor computation: decision tree	95
<b>5.5</b>	SBF computation steps	95
<b>5.6</b>	Shadow Binary Factor evolution over day time	96
<b>5.7</b>	Sky-view factor parameter tests	98
<b>5.8</b>	Difference between irradiance ( $W.m^{-2}$ ) computed without and with sub-pixel topographic correction over the day	100
<b>5.9</b>	Hourly and daily variation of differences between sub-pixel and pixel level corrections for: (a) Shadow binary factor; (b) ratio between incidence and zenith solar angle; (c) and (d) Total irradiance values	102
<b>5.10</b>	Comparison of topographic correction at pixel and sub-pixel levels	103
<b>5.11</b>	Comparison between MODTRAN and MODIS-based: (a) Direct irradiance, (b) Diffuse irradiance and (c) Fraction of diffuse skylight every 5 days over the whole year 2010	105

<b>5.12</b>	Daily $E$ mean and standard deviation from MODTRAN and MODIS over the entire Plateau every 5 days for the year 2010	105
<b>5.13</b>	Daily irradiance mean and standard deviation from MODTRAN and MODIS over the study site every 5 days for 2010	108
<b>5.14</b>	Ratio between $E_{csp}$ mean and standard deviation and $E_{ini}$ by topography types and sun zenith angle for different direct-diffuse ratios ( $F_{DD}$ )	110
<b>6.1</b>	Sub-pixel topographically corrected surface reflectance computation steps	115
<b>6.2</b>	Principle of angular sampling data accumulation from geostationary satellite	118
<b>6.3</b>	Main steps of land surface albedo retrieval using sub-pixel topographic correction	119
<b>6.4</b>	Regression between broadband and narrowband albedo	121
<b>6.5</b>	Difference between reference reflectance and pixel or sub-pixel topographically corrected reflectance for the band 8 of Landsat-7	122
<b>6.6</b>	Comparison of pixel and sub-pixel topographically corrected reflectance for bands number 1, 2, 3, 4 and 8 of Landsat 7	124
<b>6.7</b>	Maps of the differences between reflectance values estimated from Landsat-7 band 8 with sub-pixel topographic reflectance as compared to the uncorrected reflectance value	125
<b>6.8</b>	Comparison of the topographic correction at different levels	126
<b>6.9</b>	Land cover classes distribution for the three synthetic land cover maps used as input with an increasing degree of heterogeneity: (a) low, (b) medium and (c) high	127
<b>6.10</b>	Topographic maps used as input with an increasing degree of roughness (a) relatively flat, (b) medium and (c) rough topography	128
<b>6.11</b>	Processing steps for the simulated datasets representing the radiance data measured from a satellite, without atmospheric effects	128
<b>6.12</b>	Processing steps for the computation of the uncorrected albedo, the sub-pixel topographically corrected albedo, the sub-pixel LC heterogeneity corrected albedo and sub-pixel topographically and LC corrected albedo	130
<b>6.13</b>	Comparison of the RMSE, the IQ range difference, the positive and negative median difference between the four computed albedos and the reference albedo	131
<b>6.14</b>	Comparison between MSA, MODIS and FY-2E uncorrected black-sky and white-sky albedos and corrected black-sky and white-sky albedos over the Gobi desert area	133

---

<b>6.15</b>	Minimum, maximum and mean illumination zenith angles used for the BRDF reconstruction over the Gobi	134
<b>6.16</b>	Difference between ground measured and estimated albedo according to the RPV input dataset mean zenith angle	134
<b>6.17</b>	Comparison of the different albedo products with measurements at two ground stations NamCo and Qomolangma	135
<b>6.18</b>	Unfiltered TOA reflectance comparison between MODIS and FY-2E over Qomolangma for the year 2010	136
<b>6.19</b>	Illumination zenith angular sampling used for the BRDF reconstruction over Gobi, NamCo and Qomolangma	137
<b>6.20</b>	Number of reflectance measurements used to reconstruct the BRDF every 3 days over Gobi, NamCo and Qomolangma	137
<b>6.21</b>	Difference between broadband albedo measured at the ground and derived from corrected FY-2E data	138



## List of Tables

2.1	MODIS data products level 2 used for the estimation of solar radiative fluxes	17
2.2	MODIS data products level 3 used for the daily product gap filling	19
2.3	FY-2E sensor characteristics	19
2.4	Landsat-7 sensor characteristics	20
2.5	Instruments set up for each stations	26
3.1	Percentage of missing data for some randomly chosen day of the year for each of the atmospheric products used in the atmospheric transmissivity factor calculation	52
4.1	RMSE between cloud fractions retrieved from images classified automatically and the same cloud fractions retrieved from images classified manually	73
5.1	MODTRAN parameters and options set for the estimation of $E_d$ , $E_f$ and $k$ used in the topographic correction method	90
5.2	Normalized RMSE between anisotropic and isotropic radiance values for 5 solar illumination angle classes and 5 different BRDF	94
6.1	Difference mean and standard deviation between the reference reflectance and pixel or sub-pixel topographically corrected reflectance for Landat-7 band 1, 2, 3, 4 and 8	123
6.2	Land cover classes BRDF parameters for RPV	127



## List of Symbols

<b><i>a</i></b>	Surface albedo (blue-sky albedo)	-
<b><i>a<sub>BS</sub></i></b>	Black-sky albedo	-
<b><i>a<sub>WS</sub></i></b>	White-sky albedo	-
<b><i>Bi</i></b>	Cloud brokenness index	-
<b><i>bet</i></b>	Stephen's coefficient	-
<b><i>C<sub>fD</sub></i></b>	Cloud fraction weight according to the distance to the sunspot	-
<b><i>C<sub>fC</sub></i></b>	Cloud fraction in a buffer around the sunspot	-
<b><i>C<sub>fN</sub></i></b>	Cloud fraction weight according to the distance to the nadir	-
<b><i>C<sub>fS</sub></i></b>	Total cloud fraction excluding sunspot	-
<b><i>C<sub>fT</sub></i></b>	Total cloud fraction	-
<b><i>d</i></b>	day of the year	-
<b><i>D<sub>N</sub></i></b>	Distance of the clouds from the nadir	Pixel
<b><i>D<sub>S</sub></i></b>	Distance of the clouds from the sunspot	Pixel
<b><i>Diff<sub>E</sub></i></b>	Normalized difference between the irradiance estimated using MODIS or MODTRAN	%
<b><i>Diff<sub>n</sub></i></b>	Normalized difference between the irradiance corrected at sub-pixel and at pixel level	%
<b><i>E</i></b>	BOA solar irradiance	W.m <sup>-2</sup>
<b><i>E<sub>0</sub></i></b>	TOA solar irradiance	W.m <sup>-2</sup>
<b><i>E<sub>c</sub></i></b>	Solar irradiance for a tilted surface corrected at pixel level	W.m <sup>-2</sup>
<b><i>E<sub>ctr</sub></i></b>	Circumsolar (anisotropic) diffuse irradiance	W.m <sup>-2</sup>
<b><i>E<sub>csp</sub></i></b>	Solar irradiance for a tilted surface corrected at sub-pixel level	W.m <sup>-2</sup>
<b><i>E<sub>d</sub></i></b>	Direct solar irradiance	W.m <sup>-2</sup>
<b><i>E<sub>dc</sub></i></b>	Direct irradiance for a tilted surface	W.m <sup>-2</sup>
<b><i>E<sub>f</sub></i></b>	Diffuse solar irradiance	W.m <sup>-2</sup>
<b><i>E<sub>fc</sub></i></b>	Diffuse irradiance for a tilted surface	W.m <sup>-2</sup>
<b><i>E<sub>ini</sub></i></b>	Predefined value for the total irradiance on a horizontal surface	W.m <sup>-2</sup>
<b><i>E<sub>iso</sub></i></b>	Isotropic diffuse irradiance	W.m <sup>-2</sup>
<b><i>E<sub>MODIS</sub></i></b>	BOA solar irradiance estimated using MODIS data	W.m <sup>-2</sup>
<b><i>E<sub>MODTRAN</sub></i></b>	BOA solar irradiance estimated using MODTRAN	W.m <sup>-2</sup>
<b><i>E<sub>t</sub></i></b>	BOA terrain solar irradiance	W.m <sup>-2</sup>

---

$f$	Satellite response function	-
$F_{DD}$	Direct-diffuse ratio (fraction of skylight)	-
$h$	Local time	Hour
$k$	Anisotropy index	-
$k'$	BRDF bowl-bell shaped anisotropy	-
$k_g$	Absorption coefficients of uniformly-mixed gases	$\text{Km}^{-1}$
$k_o$	Absorption coefficients of ozone	$\text{Cm}^{-1}$
$k_w$	Absorption coefficients of water vapor	$\text{Cm}^2\text{g}^{-1}$
$l$	Thickness of ozone layer	Cm
$L_s$	Reflected surface radiance	$\text{W}\cdot\text{sr}^{-1}\cdot\text{m}^{-2}$
$lat$	Latitude	Rad
$lon$	Longitude	Rad
$m$	Air mass	-
$mc$	Pressure-corrected air mass for cloudy conditions	-
$ms$	Pressure-corrected air mass	-
$otc$	Cloud optical thickness	-
$P$	Surface pressure	Pa
$P_0$	Standard atmospheric pressure	Pa
$P_c$	Cloud top pressure	Pa
$R_D$	Distance to the optical center	Degree
$R_{L\downarrow}$	Instantaneous downwelling longwave radiation	$\text{W}\cdot\text{m}^{-2}$
$R_{L\uparrow}$	Instantaneous upwelling longwave radiation	$\text{W}\cdot\text{m}^{-2}$
$R_n$	Instantaneous surface radiation budget	$\text{W}\cdot\text{m}^{-2}$
$R_{ns}$	Instantaneous solar radiation budget	$\text{W}\cdot\text{m}^{-2}$
$R_{ns_d}$	Daily solar radiation budget	$\text{W}\cdot\text{m}^{-2}$
$R_p$	Distance to the optical center	Pixel
$R_{S\downarrow}$	Instantaneous downwelling shortwave radiation	$\text{W}\cdot\text{m}^{-2}$
$R_{S\uparrow}$	Instantaneous upwelling shortwave radiation	$\text{W}\cdot\text{m}^{-2}$
$S$	Given time interval	Hour
$s$	Sunshine duration	Hour
$S_0$	TOA solar constant	$\text{W}\cdot\text{m}^{-2}$
$S_f$	Sunshine fraction	-
$SE_d$	Sun-Earth distance	AU
$T_B$	Beam atmospheric transmittance	-
$T_D$	Diffuse atmospheric transmittance	-
$r_{Em}$	Sub-pixel corrected irradiance mean - initial irradiance ratio	-

---

$r_{Esd}$	Sub-pixel corrected irradiance standard deviation - initial irradiance ratio	-
$t_{sat}$	Local satellite overpass time	Hour
$t_{sr}$	Local sunrise time	Hour
$t_{ss}$	Local sunset time	Hour
$V_d$	Sky-view factor	-
$V_t$	Terrain view factor	-
$w$	Precipitable water	Cm
$W_S$	Weight factor according to the distance of the clouds from the sunspot	-
$W_N$	Weight factor according to the distance of the clouds from the nadir	-
$\alpha_s$	Sun elevation angle	Rad
$\alpha_t$	Terrain elevation angle (Slope)	Rad
$\beta$	Ångström's turbidity coefficient	-
$\Gamma$	day angle	Rad
$\delta$	Sun declination	Rad
$H$	Horizon angle	Rad
$\theta$	Shadow binary factor	-
$\theta$	Zenith angle	Rad
$\theta_i$	Sun incidence angle	Rad
$\theta_s$	Sun zenith angle	Rad
$\theta_v$	View zenith angle	Rad
$\lambda$	Wavelength of solar spectrum	$\mu\text{m}$
$\lambda_{max}$	Solar spectrum upper bound	$\mu\text{m}$
$\lambda_{min}$	Solar spectrum lower bound	$\mu\text{m}$
$\Xi$	BRDF degree of forward or backward scattering	-
$\rho$	Surface reflectance (also called bidirectional reflectance factor BRF)	-
$\rho_0$	BRDF overall brightness	-
$\rho_{adj}$	Average reflectance of adjacent objects	-
$\rho_{csp}$	Sub-pixel corrected surface reflectance	-
$\rho_h$	BRDF hotspot	-
$\rho_{nc}$	Uncorrected surface reflectance	-
$\tau$	Atmospheric shortwave transmittance	-
$\tau_a$	Aerosol extinction transmittance factor	-

---

$\overline{\tau_a}$	Energy-weighted average aerosol extinction transmittance factor	-
$\tau_c$	Cloud transmittance factor	-
$\tau_g$	Permanent gas absorption transmittance factor	-
$\overline{\tau_g}$	Energy-weighted average permanent gas absorption transmittance factor	-
$\tau_{oz}$	Ozone absorption transmittance factor	-
$\overline{\tau_{oz}}$	Energy-weighted average ozone absorption transmittance factor	-
$\tau_r$	Rayleigh scattering transmittance factor	-
$\overline{\tau_r}$	Energy-weighted average Rayleigh transmittance factor	-
$\tau_w$	Water vapor absorption transmittance factor	-
$\overline{\tau_w}$	Energy-weighted average water vapor absorption transmittance factor	-
$\overline{\tau_x}$	Energy-weighted average transmittance factor	-
$\phi$	Azimuth angle	Rad
$\phi_r$	Relative azimuth angle	Rad
$\phi_s$	Sun azimuth angle	Rad
$\phi_t$	Terrain azimuth angle (Aspect)	Rad
$\phi_v$	View azimuth angle	Rad
$\Omega$	Solid angle	Rad
$\omega$	Hour angle	Rad

---

## List of Acronyms

<b>AOD</b>	Atmospheric Optical Depth
<b>ASTER</b>	Advanced Spaceborne Thermal Emission and Reflection Radiometer
<b>ASTER-GDEM2</b>	ASTER Global Digital Elevation Model version 2
<b>AU</b>	Astronomical Unit
<b>AVHRR</b>	Advanced Very High Resolution Radiometer
<b>BOA</b>	Bottom Of Atmosphere
<b>BRDF</b>	Bidirectional Reflectance Distribution Function
<b>BSRN</b>	Baseline Surface Radiation Network
<b>CAS</b>	Chinese Academy of Sciences
<b>CAREERI</b>	Cold and Arid Regions Environmental and Engineering Research Institute
<b>CCD</b>	Charged Coupled Device
<b>CEOP-AEGIS</b>	Coordinated Asia-European long-term Observing system of Qinghai-Tibet Plateau hydro-meteorological processes and the Asian-monsoon system with Ground satellite Image data and numerical Simulations
<b>CERES</b>	Cloud and the Earth's Radiant Energy System
<b>CMA</b>	China Meteorological Administration
<b>CM SAF</b>	Satellite Application Facility on Climate Monitoring
<b>DEM</b>	Digital Elevation Model
<b>DOY</b>	Day Of the Year
<b>DSSF</b>	Downward Surface Shortwave Flux
<b>ECMWF</b>	European Centre for Medium-Range Weather Forecasts
<b>EOS</b>	Earth Observing System
<b>ERB</b>	Earth Radiation Budget
<b>ERBE</b>	Earth Radiation Budget Experiment
<b>ESA</b>	European Space Agency
<b>ETM+</b>	Enhanced Thematic Mapper Plus
<b>EUMETSAT</b>	European Organisation for the Exploitation of Meteorological Satellites
<b>EXIF</b>	Exchangeable Image File format
<b>FOV</b>	Field Of View

---

<b>FY-2</b>	Feng-Yun 2 series
<b>GAME</b>	GEWEX Asian Monsoon Experiment
<b>GCOS</b>	Global Climate Observing System
<b>GEBA</b>	Global Energy Balance Archive
<b>GOES</b>	Geostationary Operational Environmental Satellites
<b>GEWEX</b>	Global Energy and Water cycle EXperiment
<b>GLASS</b>	Global LAnd Surface Satellite
<b>HadGEM1</b>	Hadley Centre Global Environmental Model version 1
<b>HSV</b>	Hue Saturation Value
<b>IPCC</b>	Intergovernmental Panel on Climate Change
<b>IQ</b>	Inter-Quartile
<b>IR</b>	InfraRed
<b>IRGA</b>	Infrared Gas Analyzer
<b>ISCCP</b>	International Satellite Cloud Climatology Project
<b>ITP</b>	Institute of Tibetan Plateau Research
<b>JEPG</b>	Joint Photographic Experts Group
<b>kNN</b>	k-Nearest-Neighbor
<b>LC</b>	Land Cover
<b>LP DAAC</b>	Land Processes Distributed Active Archive Center
<b>LSA SAF</b>	Land Surface Analysis Satellite Applications Facility
<b>MFG</b>	METEOSAT First Generation
<b>MIR</b>	Middle InfraRed
<b>MISR</b>	Multiangle Imaging Spectro Radiometer
<b>MODIS</b>	Moderate-Resolution Imaging Spectroradiometer
<b>MODTRAN</b>	MODerate resolution atmospheric TRANsmittance and radiance
<b>MSA</b>	Meteosat Surface Albedo
<b>MSG</b>	METEOSAT Second Generation
<b>NCEP</b>	National Centers for Environmental Prediction
<b>NIR</b>	Near InfraRed
<b>NSMC</b>	Chinese National Satellite Meteorological Center
<b>NTAM</b>	Nonlinear Temporal Angular Model
<b>RMSE</b>	Root Mean Square Error
<b>RPV</b>	Rahman-Pinty-Verstraete
<b>S-VISSR</b>	Stretched Visible and Infrared Spin Scan Radiometer
<b>SBF</b>	Shadow Binary Factor
<b>SRB</b>	Surface Radiation Budget
<b>SURFRAD</b>	SURFace RADiation budget network

---

<b>RGB</b>	Red Green Blue
<b>TIR</b>	Thermal InfraRed
<b>TOA</b>	Top Of Atmosphere
<b>UTC</b>	Coordinated Universal Time
<b>USGS</b>	United States Geological Survey
<b>WCRP</b>	World Climate Research Program
<b>WMO</b>	World Meteorological Organization
<b>WRF</b>	Weather Research and Forecasting
<b>WWRP</b>	World Weather Research programme



# Chapter 1

## Introduction

### 1.1 Context

The sun is the primary source of energy of the Earth's climate system (Pekarek 2001). The radiative energy exchanges between the Earth's surface and the atmosphere are one of the driving mechanisms of this system. Most of those exchanges take place at the surface (Ohmura et al. 2005), where part of the incident solar radiation is absorbed while the rest is reflected back into space. The solar radiation budget ( $R_{ns}$ ) is defined as the difference between the incident ( $R_{S\downarrow}$ ) and reflected ( $R_{S\uparrow}$ ) solar radiative fluxes at the surface at a certain time (Equation 1.1):

$$R_{ns} = R_{S\downarrow} - R_{S\uparrow} \tag{1.1}$$

A radiative flux is usually expressed as a flux density in  $\text{W}/\text{m}^2$ , *i.e.* the amount of energy per unit time per unit area. While the energy budget at the Earth's surface also integrates longwave radiations, this thesis focuses on the solar radiation as it is, as such, a complex issue. An exception is made in Chapter 4 where longwave radiations are mentioned in the context of surface fluxes measurements analysis. The net radiation flux at

the surface, including the solar and longwave radiations, is redistributed within heat flux down the soil layers and turbulent fluxes, namely the sensible heat and latent heat fluxes (Monteith et al. 1990). The latter two affect in turn the atmospheric boundary layer, and by extent the global circulation and Earth's climate as a whole. In this scheme, the solar radiation budget is the main driver of processes like evaporation and heating of soil and air (Bisht et al. 2010) and its monitoring is crucial for many applications such as climate change study, water resources management, vegetation dynamic, food production or drought early warning (Jia et al. 2006; Jia et al. 2011b). As stated in the GCOS report (2007), it is a fundamental component of the surface energy budget that is crucial to nearly all aspects of climate and needs to be monitored systematically at regional or global scale.

The estimation of the solar radiation budget requires an accurate quantification of the solar incident radiative flux reaching the Earth's surface, commonly named irradiance and noted  $E$  hereafter, and the determination of the fraction of irradiance reflected by the surface. The amount of radiation reflected by the surface is directly linked to the reflective property of the surface usually described by the surface reflectance  $\rho$  and the surface albedo  $a$ . The surface reflectance is defined as the fraction of the irradiance reflected by the surface for a single incident angle while the surface albedo is a directional integration of reflectance over all sun-view geometries (Schaepman-Strub et al. 2006). This directional integration is commonly expressed as the bidirectional reflectance distribution function (BRDF), which describes how reflectance depends on view and solar angles.  $R_{ns}$  can therefore be expressed as function of the surface albedo ( $a$ ) and irradiance ( $E$ ,  $\text{W}\cdot\text{m}^{-2}$ ) as follow:

$$R_{ns} = (1 - a) E \quad 1.2$$

The solar radiation covers the total shortwave spectral domain, spreading approximately from 0.4 to 2.5  $\mu\text{m}$ , and is named broadband solar radiation. Unlike the broadband, the narrowband solar radiation covers only part of the solar spectrum. In this research, the term radiation refers to broadband radiation, unless stated otherwise.

### 1.1.1 Solar radiation budget data

The estimation of at-surface solar radiative fluxes is a field of ongoing climate research. Estimates can be retrieved from ground-based measurements, satellite observations or model simulations, with some uncertainty associated to each method. The irradiance is commonly measured at meteorological stations using a sensor called pyranometer, which captures radiation over a spectral range nearly equivalent to the solar spectrum with an angle of view close to a hemisphere (*e.g.* the CMP 11 from Kipp & Zonen). Some stations also include a second pyranometer oriented downward, which captures the surface outgoing radiation, allowing for the computation of the albedo and the solar radiation budget. There are several radiation observations networks all over the globe.

Among others, one can mention the FLUXNET network<sup>1</sup>, a "network of regional networks" coordinating regional and global analysis of observations from micrometeorological tower sites, the Global Energy Balance Archive (GEBA) database providing flux monthly means measured at 1500 stations across the globe (Gilgen et al. 1999) and the Baseline Surface Radiation Network (BSRN)<sup>2</sup>, a project of the Data Assimilation Panel from the Global Energy and Water Cycle Experiment (GEWEX) within the World Climate Research Programme (WCRP). There are also some regional networks such as the GEWEX Asian Monsoon Experiment (GAME)<sup>3</sup>, implemented in several locations in Asia, which ended in 2005. Worth also mentioning is the Surface Radiation Budget Network (SURFRAD) providing long-term measurements of the surface radiation budget over the United States (Augustine et al. 2005). The radiative fluxes measured at a ground station are considered as accurate data ( $< 20 \text{ W/m}^2$  according to (Liang et al. 2010)), as long as the sensors are correctly set up, well calibrated and maintained. The major uncertainty is due to sensor deviation over time, requiring regular re-calibration. The temporal resolution of those datasets can be very high (up to a few minutes), but are only representative of the close neighborhood of the station. These data are often used for validating satellite products and numerical simulations, although the spatial resolutions of both often mismatch with the footprint of ground measurements (Liang et al. 2010).

With the advent of space-borne imaging radiometers, a number of algorithms have been developed to estimate the solar radiation budget at the Earth's surface from broadband or multispectral sensors data on both polar-orbiting and geostationary satellites at regional or global scale. One of the earliest shortwave radiation budget product were obtained from the Earth Radiation Budget (ERB) and the Earth Radiation Budget Experiment (ERBE) sensors between 1978 and 1990 (Jacobowitz et al. 1984; Barkstrom 1984; Kyle 1990). This mission was followed by the Clouds and the Earth's Radiant Energy System (CERES)<sup>4</sup> project providing solar radiation products such as CERES-SSF and CERES-EBAF. The International Satellite Cloud Climatology Project (ISCCP)<sup>5</sup> made available a global radiative flux dataset called ISCCP FD (Zhang 2004). In the framework of WCRP, the NASA GEWEX SRB (Global Energy and Water Exchanges - Surface Radiation Budget)<sup>6</sup> project produced a global gridded datasets for radiative fluxes at the surface (Zhang et al. 2013). Over Europe, the Satellite Application Facility on Climate Monitoring (CM SAF) proposes a suite of products including radiation budget parameters (Hollmann et al. 2006). Concerning the irradiance only, the DSSF (downward surface shortwave flux) product from LANDSAF (Brisson et al. 1999) and the GLASS surface shortwave radiation product

---

<sup>1</sup> <http://fluxnet.ornl.gov/introduction>

<sup>2</sup> <http://www.bsrn.awi.de>

<sup>3</sup> <http://www.gewex.org/game.html>

<sup>4</sup> <http://ceres.larc.nasa.gov>

<sup>5</sup> <http://isccp.giss.nasa.gov/projects/flux.html>

<sup>6</sup> <http://gewex-srb.larc.nasa.gov>

(Liang et al. 2012) can be mentioned. Several algorithms were also developed for local applications. Space-borne observations, allowing for global spatial coverage, lead to more advance research about the Earth radiation budget. However, even though results are promising, surface radiative fluxes estimation from space remains a challenge especially under cloudy conditions (Wang et al. 2009a). Sensors calibration can also be an issue, especially if there is no on-board calibration system. Finally, it is important to mention that whereas the temporal resolution can be up to hourly, the spatial resolution of the products is often coarse (from 1 to hundred kilometers), with the spatial resolution usually decreasing when the temporal resolution is increasing.

The radiative fluxes products from general circulation models and numerical weather prediction models usually have much coarser spatial resolutions and finer temporal resolutions than remote sensing products. However, most models tend to overestimate surface insolation (Liang et al. 2010). Among the most commonly used climate models there is the Hadley Centre Global Environmental Model version 1 (HadGEM1) (Martin et al. 2006; Ringer et al. 2006) used in the IPCC Fourth Assessment Report on climate change, the European Center for Medium range Weather Forecasting (ECMWF) (Molteni et al. 1996), the National Center for Environment Prediction (NCEP) (Kalnay et al. 1996) and the Weather Research and Forecasting (WRF). Each model has different degrees of complexity in its parameterization scheme to physically characterize the dynamics of land surfaces. Numerous studies have found serious discrepancies when these models were compared to satellite products (Liang et al. 2010).

### **1.1.2 Solar radiation budget from remote sensing**

The solar radiation budget depends on many factors such as the atmospheric composition and the cloud cover, as well as the land surface properties such as the land cover and its related albedo, but also its slope and orientation (Baede et al. 2001). The irradiance itself varies according to the Sun-Earth geometry according to the time of the day, the time of the year and the geographic location under consideration (Boes 1981). Therefore, the solar radiation budget varies significantly in space and time and accurate estimates are essential to take into account this spatial heterogeneity and temporal variability. For regional to global monitoring of this budget, ground observations remain too sparse while remote sensing perfectly fits the need for large coverage and regular observation over time.

As stated in Equation 1.2, the two main components required to estimate the solar radiation budget are the surface irradiance and albedo. There are roughly two approaches to estimate the surface irradiance using satellite radiometric measurements. The first approach is to establish the relationship between the top of atmosphere (TOA) radiance and the surface irradiance based on radiative transfer simulations whereas the second is to use estimated atmospheric transmittance to convert TOA irradiance into surface irradiance. In

this thesis, the surface irradiance is not directly retrieved from satellite data but the latter are used to retrieve the atmospheric transmittance required to estimate the surface irradiance. The albedo is usually retrieved from an accumulation of satellite observations over time and multiple view and/or illumination angles used to reconstruct the surface BRDF based on physical methods. Accurate estimates of surface irradiance and albedo can be retrieved, provided that the combined effects of the atmosphere and topography are well taken into account. Several algorithms allow for an accurate description of atmospheric effects (Turner et al. 1972; Kaufman 1984; Rahman et al. 1994; Song et al. 2003; Van Laake et al. 2004; Jiménez-Muñoz et al. 2010). However, the effects of clouds remain hard to parameterize (Wang et al. 2009a) while their impact on irradiance is strong, since they can reflect about 70-80% of the incoming solar radiation (Saha 2008). Regarding the impact of the topography, even if many studies and algorithms were developed to correct for the terrain induced effects (Rochon et al. 1979; Kawata et al. 1988; Proy et al. 1989; Meyer et al. 1993; Richter 1998; Richter et al. 2009; Szantoi et al. 2013), this aspect is often neglected, resulting in significant errors in many data products, especially in mountainous areas (Yang et al. 2008; Wang et al. 2014).

One of the main advantages of remote sensing is its capability for large spatial coverage. However, the radiative fluxes estimations are constrained to the satellite overpass times, *i.e.* the frequency of the estimates is directly linked to the satellite temporal resolution. Geostationary satellites record data up to every 15 min at medium or low spatial resolution whereas polar orbiting satellites can provide higher spatial resolution but with daily revisit periods at best. The temporal frequency required by solar radiation budget monitoring imposes the use of high temporal resolution satellites, whose spatial resolution is of a square kilometer at best. At this scale, the problem of the pixel spatial heterogeneity arises, especially concerning clouds and topography which strongly impact the solar radiation budget. Some studies explored the effects of within pixel spatial heterogeneity on the retrieved surface properties (Kustas 2000; Liu et al. 2008; Wen et al. 2009b; Román et al. 2011). So far, most of these studies focused on pixel land cover heterogeneity and few started to look into sub-pixel topography variability. From the latter, it appeared that in rugged terrain when neglecting the sub-pixel terrain variability, the surface properties derived at different spatial resolutions can be considerably different even though using the same model (Liu et al. 2008), highlighting the necessity to take into account these sub-pixel effects. However, most of the current retrieval algorithms consider that the aggregation of terrain and clouds heterogeneity within kilometric pixels avoids considering the local spatial variability, which leads to large estimation errors. In this thesis, this intra-pixel variability is considered and expressed through the concept of sub-pixel, as illustrated in Figure 1.1. The sub-pixel topography, mostly through shadowing effects has an impact on irradiance and albedo estimates. Likewise, the sub-pixel spatial distribution of clouds directly influences the partitioning between direct and diffuse irradiance. The sub-pixel

spatial distribution of clouds is commonly summarized as cloud fraction removing all spatial information about the cloud cover.

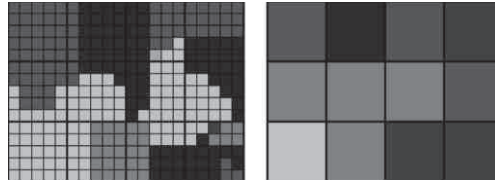


Figure 1.1: Sub-pixel and pixel level concept (the greyscale represents theoretical radiance values)

Remote sensing observations provide instantaneous values of radiation fluxes, which are of limited interest for climate or hydrological applications since they commonly need daily to monthly products. Moreover, several problems can complicate the use of instantaneous observation, since the overpass time of a given satellite may differ from one day to another. Furthermore, considering the seasonal variation of the Sun-Earth geometry, the use of daily average solar radiative fluxes is more suitable for monitoring purposes than different instantaneous value for each day through the year. There are several methods to average instantaneous to daily solar radiation budget, mainly based on the sunshine duration, also called sunshine hours. The sunshine duration expresses the cumulative length of direct sun exposure periods from sunrise to sunset for a given location on Earth. While astronomical considerations allow for an empirical estimate of this parameter for cloud free sky, very few studies try to account for the actual cloud cover variability, leading to large errors in many regions of the globe (Bisht et al. 2010).

A last point to consider when using satellite measurement is the fact that the data are collected in one or several narrow bands over the entire solar spectrum. Numerous methods for converting narrowband to broadband estimates have been developed. They usually use conversion coefficients derived from interpolations or simulations and are based on physical assumptions. Defining those coefficients is complex as they are very specific to the atmospheric conditions and surface properties for which they have been derived. This conversion is a common issue when retrieving radiative fluxes from remote sensing and is often a source of error in albedo estimates.

## 1.2 Research objectives

As underlined by the World Meteorological Organization (WMO), there is a crucial need for regional to global monitoring of solar radiation budget. Currently, very few datasets are available at that scale. Furthermore, their spatial and/or temporal resolutions are often not appropriate to properly capture the variations in space and time of the solar

radiative fluxes and, despite the efforts to integrate the effects of the topography and the cloud cover, improvements are still needed to meet climate studies requirements. Therefore, the objective of this thesis can be expressed as follow:

*To develop an operational method based on remote sensing for all-sky solar radiation budget daily monitoring over large heterogeneous areas and to propose improvements for the estimation of irradiance and albedo considering sub-pixel spatial variability of topography and clouds.*

As explained earlier, a fine grained temporal monitoring of the surface radiative fluxes leads to limitations in spatial resolution. The objective to operationally monitor these fluxes on a daily basis using Earth Observation satellites constraints the estimation to a square kilometer pixel resolution. Some satellite data products characterizing atmospheric and land surface properties are available at these spatial and temporal scales. At first, an algorithm combining those products to estimate the solar radiation budget is proposed. However, the latter does not take into account sub-pixel variability. Therefore, further research is carried out to improve the solar radiation budget estimates addressing the sub-pixel heterogeneity in terms of spatial variability of the topography and distribution of the clouds. The temporal variability of the cloud cover and its relation to temporal aggregation of radiative flux estimates is also investigated. Based on multi-source and multi-resolution remote sensing data, the proposed approach provides a usable solar radiation budget dataset and paves the way for a new operational methodology which adequately takes into account sub-pixel heterogeneity when producing large scale time series of solar radiation.

### **1.2.1 Research approach**

From the objective described above, three research questions are raised and led to the research presented in this thesis:

*1<sup>st</sup>: Do the current satellite data products allow to accurately monitor solar radiation budget at large scale daily and at a square kilometer resolution over heterogeneous areas?*

Several satellite data products currently provide daily estimates of the atmospheric parameters required to estimate surface irradiance as well as weekly estimates of albedo, all at the square kilometer. The idea is to provide an operational method to produce daily solar radiative fluxes time series at the square kilometer, based on existing retrieval algorithms and the latest developments in the field. The time series can then be assessed to check if the estimates provided by the satellite data products allow to accurately monitor the solar radiation budget over large heterogeneous areas. Then two methods are proposed to improve the currently operational methods by considering the sub-pixel variability inherent to the kilometric footprint.

*2<sup>nd</sup>: Does the spatial and temporal characterization of the cloud cover improve the estimation of irradiance and of the daily average solar radiation budget?*

The current integration of clouds in the solar radiation budget has two main issues. First, in most cases, the spatial distribution of clouds within each pixel is summarized using a cloud fraction index with no information on spatial patterns. Second, the characterization of the cloud cover over the day to compute the daily average of solar radiation budget is made using very few measurements. Then, this research question aims at investigating in detail the relation between cloud cover and irradiance at the surface as well as the impact of the temporal variability of cloud cover on daily aggregation of the solar radiation budget. To this end, a fieldwork experiment was designed to collect hemispherical images of the sky at very high temporal resolution simultaneously to solar radiative fluxes measured at the ground level. The idea is to use the cloud cover spatial information derived from the hemispherical images to correlate with the ground radiative fluxes and to identify potential relationships. Then, impact of the temporal variability of cloud cover on daily solar radiation budget can be quantified. Finally, three methods to estimate sunshine duration are compared and used to temporally average the solar radiation budget.

*3<sup>rd</sup>: Can the irradiance and albedo estimated from space be improved by integrating topographic variability at a finer spatial resolution, i.e. at sub-pixel level?*

In order to monitor solar radiation budget, fine temporal resolution is required with the counterpart being a kilometric spatial resolution which leads to topographic variability inside the pixels. Thus, the assumption is made that instead of using digital elevation model (DEM) at the same spatial resolution as the satellite radiometric data, it could be beneficial to take advantage of the finer resolution DEM currently available to take into account sub-pixel topography. This third research question is addressed in two steps. First, some tests are performed to quantify the impact of topography on solar irradiance retrieved from satellite data. Second, the sub-pixel corrected irradiance is used to retrieve the surface reflectance which in turn allows to derive the albedo to check if it leads to an improvement of those two parameters.

### **1.2.2 A case study over the Tibetan Plateau**

The Tibetan Plateau has a strong influence on the hydrology and the climate scheme of the whole South East Asia. Recent studies documented the role of the Plateau in atmospheric processes at continental scale and particularly in determining the dynamics of the Asian Monsoon and extreme precipitation events in China and India (Liu et al. 2013; Bothe et al. 2011; Wu et al. 2007; Zhang et al. 2007; Wu et al. 2006). Considering that more than 40% of the Earth's population and the entire ecosystem of South East Asia depend upon the monsoon climate and its predictability, and regularly suffer from extreme droughts and floods events, the monitoring of radiative fluxes over the Plateau is a critical

prerequisite to better understand and model this peculiar hydro-system. This is why the Tibetan Plateau is an area of interest for meteorological and hydrological studies for several decades now. It started in 1996 with the GAME-Tibet project conducted under the framework of the World Climate Research Programme (WCRP) / Global Energy and Water Cycle Experiment (GEWEX) Asian Monsoon Experiment (GAME) and aiming at a better understanding of land-atmosphere interactions over the Plateau. Following 10 years of experimental and modeling research, the CEOP-AEGIS (Coordinated Asia-European long-term Observing system of Qinghai–Tibet Plateau hydro-meteorological processes and the Asian-monsoon system with Ground satellite Image data and numerical Simulations) project was initiated with the goal of improving knowledge on the hydrology and meteorology of the Tibetan Plateau and its role in climate, monsoon and extreme meteorological events. The research work was constructed out of existing ground measurements and current/future satellites observing system to determine and monitor the water yield of the Plateau as well as monitoring the evolution of snow, vegetation cover, surface wetness and surface fluxes and analyze their linkage with convective activity, precipitation events and the Asian Monsoon. In this context and because of its particular geomorphologic characteristics along with the interesting seasonal cloud coverage patterns, the Tibetan Plateau is an excellent candidate area for the study presented in this thesis.

This research falls within the scope of the CEOP-AEGIS project, aiming at supporting water resources management in South-East Asia. As quoted previously, one of the major current issues when monitoring land surface solar radiative fluxes over large area is the lack of fundamental knowledge on the spatial and temporal variability of the fluxes and this is especially true for the Tibetan Plateau. Because of its elevation, the Plateau surface absorbs a large amount of solar radiation energy, and undergoes important seasonal changes of surface heat and water fluxes. In this context, spatialized estimates of surface solar radiative fluxes at fine spatial and temporal resolutions are essential not only as key input for hydrological modelling but also as a proxy for flood and drought early warning systems. Furthermore, knowing that the meteorological stations are concentrated in the South-Eastern portion of the Plateau at altitudes ranging from 1500 m to 4700 m, while the Plateau reaches up to the Everest at 8844 m, radiative fluxes cannot be accurately estimated from ground based measurements (Yang et al. 2006a), justifying the necessity to use remote sensing. Among the existing radiation budget products covering that area, most have a too coarse spatial resolution (from 30 to 280 km resolution) and are not adapted to characterize the Tibetan plateau specificities. Yang et al. (2008) compared both ISCCP-FD and GEWEX SRB data sets over the Tibetan Plateau and found large discrepancies among them in highly variable terrain (such as in the Himalayas region). Then, estimates of solar radiation budget produced daily and at the square kilometer, with improved integration of the topography and the cloud coverage, would be very beneficial for monitoring purposes in an area like the Tibetan Plateau, which affects the climate of South East Asia as a whole.

### 1.3 Thesis outline

Chapter 2 presents the Tibetan Plateau and a detailed characterization of its topography. The different data sources selected to address the research questions are also described.

Chapter 3 is dedicated to the first research question and proposes an operational method to estimate all-sky instantaneous and daily solar radiative fluxes over the Tibetan Plateau from existing Earth observation products. This method takes into account the terrain slope and azimuth in the estimation of the incident radiation and uses actual atmospheric and land surface characteristics derived from remote sensing data products.

Chapter 4 addresses the second research question by investigating the impact of cloud cover spatial and temporal variability on solar radiative fluxes at the surface and the computation of their daily average respectively. It presents the hardware and algorithms developed to collect hemispherical images from the sky at very high temporal resolution and to automatically retrieve the cloud spatial characteristics from the images. Those characteristics are then correlated with the radiative fluxes measured simultaneously at the ground. The impact of cloud cover temporal resolution on daily irradiance estimation is explored and different methods to estimate sunshine duration are compared.

Chapter 5 and 6 answer the third research question. Chapter 5 addresses the problem raised concerning the terrain sub-pixel heterogeneity by quantifying the impact of sub-pixel topography on irradiance retrieved from space and exploring the improvements brought by applying a topographic correction using a DEM at higher spatial resolution. To do so, a new topographic correction method which integrates the topographic effects at the sub-pixel level is presented. This correction method being related to the atmosphere characterization, two ways of modeling the atmosphere are compared.

Chapter 6 is a direct follow up of Chapter 5 as it explores the improvement brought by integrating sub-pixel topographic variability to estimate reflectance and albedo from geostationary satellite data. The estimated albedo is compared to ground data and already existing satellite data products.

Finally, Chapter 7 summarizes the main findings, and draws conclusions and perspectives for further development.

## **Chapter 2**

# **The Tibetan Plateau: field and remote data sources**

### **2.1 Introduction**

The Tibetan Plateau with its high altitude, unique geographical features and rich wildlife, water and mineral resources, has been called the ‘Roof of the World’ and the ‘Third Pole of the Earth’ (Bisht 2008). It is an area of interest for meteorological and hydrological studies for several decades now. The studies started in 1996 with the GAME-Tibet project conducted under the framework of the World Climate Research Programme (WCRP) / Global Energy and Water Cycle Experiment (GEWEX) Asian Monsoon Experiment (GAME) and aiming at a better understanding of land-atmosphere interactions over the Plateau. Following 10 years of experimental and modelling research, the CEOP-AEGIS project was initiated with the goal of improving knowledge on the hydrology and meteorology of the Tibetan Plateau and its role in climate, monsoon and extreme meteorological events. The research work was constructed out of existing ground measurements and current/future satellites observing system to determine and monitor the water yield of the Plateau as well as monitoring the evolution of snow, vegetation cover,

surface wetness and surface fluxes and analyze their linkage with convective activity, precipitation events and the Asian Monsoon. Concerning the solar radiative fluxes more specifically, the objective was to establish a monitoring system built upon the improvement of spatial density and temporal frequency of observations over the Plateau using satellite data. In that framework, the research conducted in this thesis led to the development of a method allowing for solar radiative fluxes monitoring over the Plateau and some further in-depth research to improve the retrieval algorithm. To do so, several satellite data sources along with a DEM and ground measurement have been used.

This chapter starts with a presentation of the Tibetan Plateau and its specificities regarding radiative fluxes. Then, the different data used in this thesis are described: starting with the topographic data, followed by the different satellite datasets used to derive the estimates and finally the ground measurements and satellite data products used for validation. Then some explanations are provided about the data pre-processing for their homogenization to finish with some conclusions.

## 2.2 The Tibet Plateau

The Tibetan Plateau is a geological structure lying between the Himalayan range to the south and the Taklimakan desert to the north (Figure 2.1). It is the largest and highest plateau area in the world spreading over 2.5 million km<sup>2</sup> and presenting an average elevation of over 4,000 m. The Plateau is the headwater of rivers that provides water to 47 % of the Earth's population which live under the influence of the monsoon system. Among the rivers originating in Tibet, the major ones are the Yellow River and the Yangtze flowing across China, the Mekong traversing down China, Laos, Burma, Thailand, Cambodia and Vietnam, the Brahmaputra running through India and Bangladesh and the Indus flowing into Pakistan. Additionally, most of the major rivers in Nepal originate in the Tibetan plateau and flow down to the Ganga. Another important characteristic of the Plateau is its very high spatial heterogeneity due to the presence of mountainous areas in the South affecting radiance measurements over space and time. In the objective of monitoring energy fluxes, the estimation of the surface radiative fluxes from space in that area cannot be accurately performed without taking into consideration those specificities.

The area delimited on Figure 2.1 corresponds to the CEOP-AEGIS project extent. Defined according to the research objectives, it covers the Qinghai-Tibet area and the surroundings of the Plateau. The output produced in the framework of the project should then fit this extent and the solar radiative fluxes retrieval is performed over this area (Chapter 3). However, this area being very large, over 7.7 million km<sup>2</sup>, the in-depth analyses carried out to improve the model are conducted over a smaller test site (Figure 2.2) because of time and computation capacity constraints. This subset was chosen because it presents an increasing effect of topography, starting from relatively flat (top left), then hilly

landscape, and finally complex relief (bottom) as identified from the DEM. It also corresponds to the Landsat scene used in some validation steps (Chapter 6).



Figure 2.1: The Tibetan Plateau and surroundings with the CEOP-AEGIS project extent delimitation (red line)

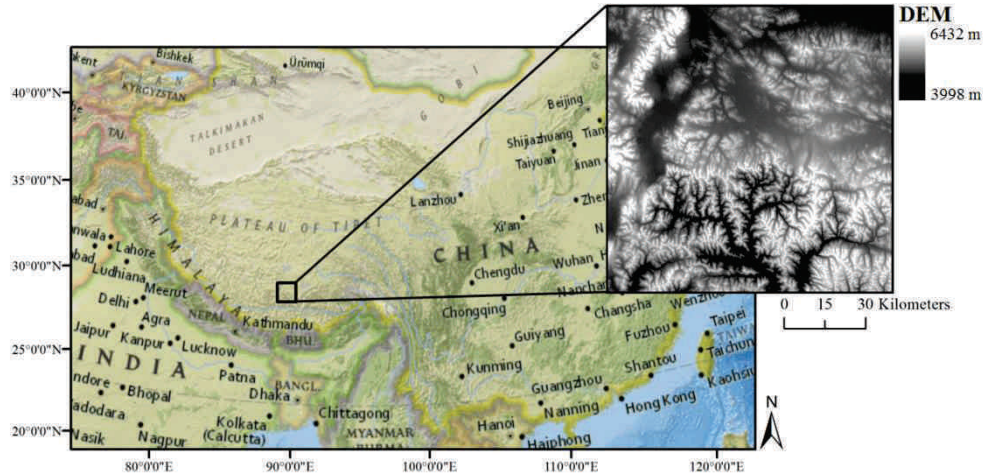


Figure 2.2: Study area subset

Additionally, the fieldwork conducted to collect data for cloud characterization (Chapter 4), was performed at the meteorological station of NamCo ( $30.46^{\circ}\text{N}$  /  $90.57^{\circ}\text{E}$ , 4730 m), located on the South bank of the Namco Lake, 200 km North from Lhasa (Figure 2.3).

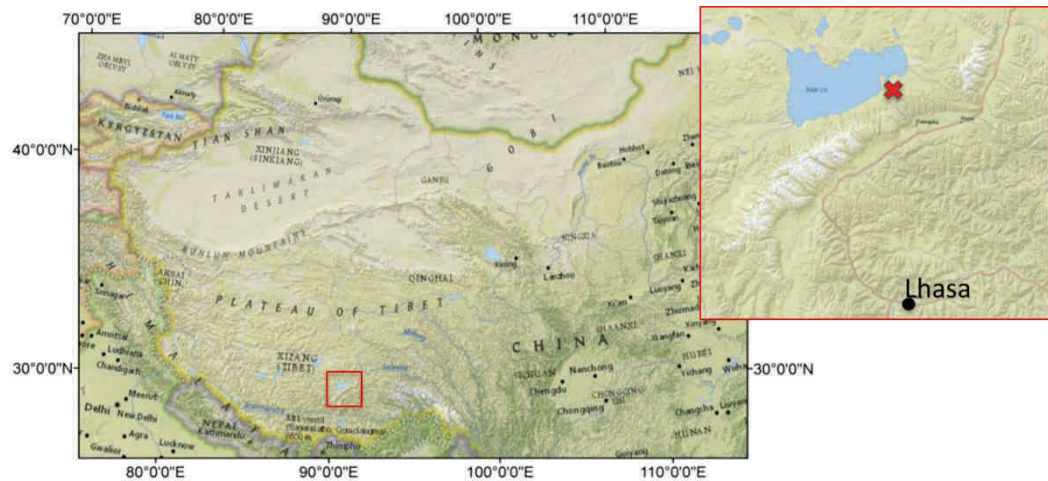


Figure 2.3: Location of the meteorological station of NamCo (red cross), on the South bank of the NamCo Lake

As explained previously, the extreme topography is one of the most important features of the Plateau regarding our research. It is then essential to characterize this

topography prior to quantifying its effects on solar radiative fluxes estimation from space. To this end, the slope and azimuth, two key topographic parameters, are derived from the DEM (presented in section 2.3) at a resolution of 30 m. By summarizing the distribution of the slope values over the entire plateau in a frequency plot, Figure 2.4(a) shows that more than 25% of the plateau is covered by terrain with a slope value over of 20°. Focusing on the subset area, Figure 2.4(b) shows a rougher terrain with an important density of slope between 5 to 35°. In that area, about 40% of the terrain presents a slope steeper than 20°.

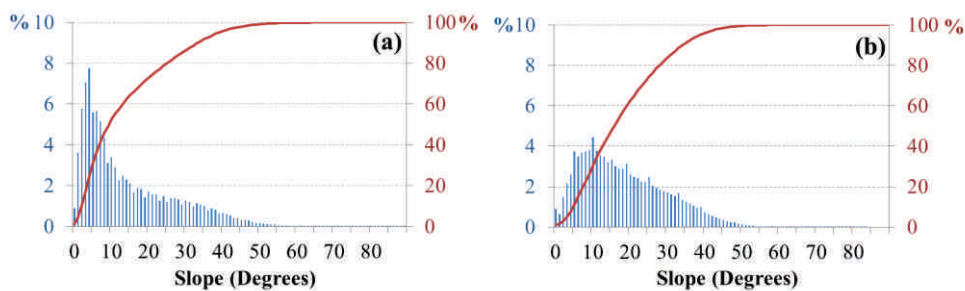


Figure 2.4: Slope values distribution over the Tibetan Plateau (a) and the study area subset (b), expressed as percentage per slope gradient (histogram) and cumulated percentage (red line)

## 2.3 Topographic data

The characteristics of the topography are retrieved at 30 m resolution from the DEM provided by the Advanced Spaceborne Thermal Emission and Reflection Radiometer (ASTER), *i.e.* the Global Digital Elevation Model (GDEM) version 2 (Figure 2.5). ASTER-GDEM2 is one of the most complete high-resolution digital topographic dataset in the world to date. The ASTER-GDEM2 covers land surfaces between 83° N and 83° S at a spatial resolution of 1 arc-second. Even if some geolocalisation errors and elevation aberrations have been identified at the global scale, this dataset remains the best alternative in accessibility to high-quality elevation data for the selected study site (Li et al. 2013).

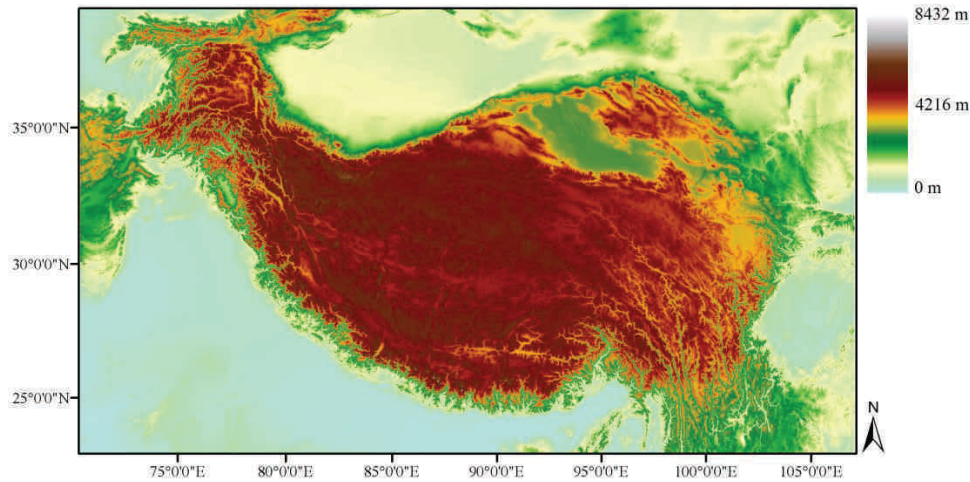


Figure 2.5: ASTER-GDEM2 for the entire study area

## 2.4 Satellite data

### 2.4.1 MODIS

MODIS (Moderate-Resolution Imaging Spectroradiometer)<sup>7</sup> is a series of scientific observation instruments coupled to an embedded satellite system launched aboard the Terra (1999) and Aqua (2002) satellites, both belonging to the EOS (Earth Observing System) NASA program for long-term observation of soil, biosphere, atmosphere and oceans. The instruments record data in 36 spectral bands ranging from 0.4 microns to 14.4 microns with a spatial resolution of 250 m to 1 km. Together, the various spectrometers take a complete picture of the Earth every 1 or 2 days.

A major advantage of the MODIS imagery is the availability of a suite of products ranging from raw images to highly processed products such as atmospheric optical depth (AOD). The products are made on varying temporal resolutions, some are made as often as daily and every 8 days. 16-day and monthly products are also available. The products are all archived and available, usually at no charge. MODIS products are organized into different processing levels. Level 0 products are raw digital number images. The level 1 products include uncalibrated and calibrated radiance values. The level 2 and 3 products have more processing and are derived from lower level products. These level 2 and 3

<sup>7</sup> <http://modis.gsfc.nasa.gov>

products are separated into four science discipline groups: (1) land<sup>8</sup>, (2) atmosphere<sup>9</sup>, (3) ocean<sup>10</sup> and (4) cryosphere<sup>11</sup>.

Table 2.1: MODIS data products level 2 used for the estimation of solar radiative fluxes

<i>Product short name</i>	<i>Product group</i>	<i>Product name</i>	<i>Spatial resolution</i>	<i>Temporal resolution</i>	<i>Data layer used</i>
<i>MOD04_L2</i>	<i>Atmosphere</i>	<i>Aerosol</i>	<i>10 km</i>	<i>Daily</i>	<i>Corrected optical depth land</i>
<i>MOD05_L2</i>	<i>Atmosphere</i>	<i>Water vapor</i>	<i>5 km</i>	<i>Daily</i>	<i>Water vapor NIR retrieval</i>
<i>MOD06</i>	<i>Atmosphere</i>	<i>Cloud</i>	<i>1 km or 5 km</i>	<i>Daily</i>	<i>Surface pressure Cloud top pressure Cloud fraction day Cloud optical thickness</i>
<i>MOD07</i>	<i>Atmosphere</i>	<i>Atmosphere profile</i>	<i>5 km</i>	<i>Daily</i>	<i>Total ozone</i>
<i>MOD11A1</i>	<i>Land</i>	<i>Land Surface Temperature &amp; Emissivity</i>	<i>1 km</i>	<i>Daily</i>	<i>Day view time</i>
<i>MCD43B3</i>	<i>Land</i>	<i>Albedo</i>	<i>1 km</i>	<i>8-day</i>	<i>Black-sky White sky albedo</i>

The methodology to estimate solar radiative fluxes over the Tibetan Plateau (Chapter 3) was implemented using Terra-MODIS atmospheric and land products level 2 and 3. All the atmospheric products are not related to the spectral wavelength and the albedo is a broadband product. The surface pressure, AOD, the precipitable water, ozone thickness and clouds properties are extracted from the level 2 atmospheric products. To compute the solar zenith angle (Equation 3.10), the local satellite overpass time is necessary and is taken from MOD11A1 day view time. The black-sky and white-sky albedo are obtained from MCD43B3. Then, the blue-sky albedo is derived according to the method given in Román et al. (2009) (Albedos definition provided in Chapter 6). All the MODIS products are presented in Table 2.1.

All the data products used during the solar radiative fluxes computation, except for the albedo product, are daily products and include missing data. Thus, a data filling plan was implemented in order to fill the gaps before using the data in the computation. The methodology applied is based on spatial and temporal gap filling. When there is less than

<sup>8</sup> <https://lpdaac.usgs.gov>

<sup>9</sup> <http://modis-atmos.gsfc.nasa.gov>

<sup>10</sup> <http://oceancolor.gsfc.nasa.gov>

<sup>11</sup> <http://nsidc.org/daac/modis/index.html>

10% of missing data in a scene, local spatial averaged are used to fill the gaps. When there is more than 10% of missing data and if the corresponding 8-day or monthly MODIS level 3 products are available, the latter are used to fill the gaps. If missing pixels remain after this operation or if no 8-day or monthly MODIS products are available, the average value of the surrounding pixels is used. If there are still some pixels without value, the last option is to fill the pixel with the average value of the whole image (Figure 2.6). In parallel, a quality flag dataset is produced to provide information about the reliability of the estimates retrieved using those filled datasets.

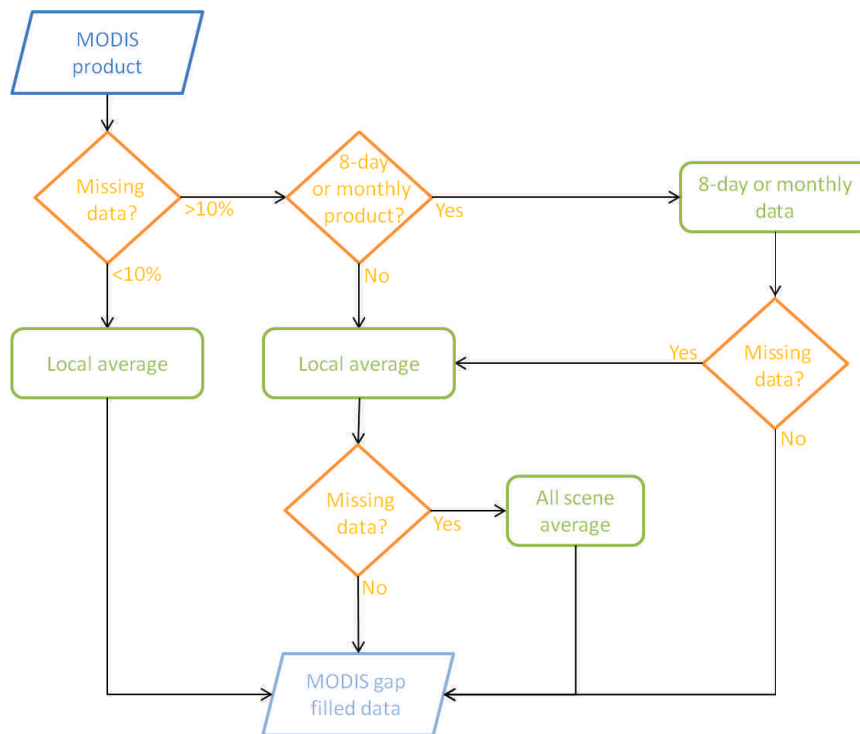


Figure 2.6: MODIS daily products gap filling procedure

8-day and monthly MODIS datasets are available for AOD, precipitable water and ozone thickness. There is no such product available for the surface pressure data but this daily product is relatively complete, then the use of the data filling procedure based on the local average is sufficient. The filling plan used the data presented in Table 2.2.

Table 2.2: MODIS data products level 3 used for the daily product gap filling

<i>Product short name</i>	<i>Product group</i>	<i>Product name</i>	<i>Spatial resolution</i>	<i>Temporal resolution</i>	<i>Data layer used</i>
<i>MOD08_E3</i>	<i>Atmosphere</i>	<i>Eight-Day Global Joint product</i>	<i>1 degree</i>	<i>8-day</i>	<i>Corrected optical depth land Water vapor NIR retrieval Total ozone</i>
<i>MOD08_M3</i>	<i>Atmosphere</i>	<i>Monthly Global Joint product</i>	<i>1 degree</i>	<i>1 month</i>	<i>Corrected optical depth land Water vapor NIR retrieval Total ozone</i>

### 2.4.2 FY-2

FengYun<sup>12</sup>, noted as FY, refers to the whole of the Chinese meteorological polar and geostationary satellites. The FengYun-2 series (FY-2) corresponds to the geostationary meteorological satellites, organized and operated by NSMC (National Satellite Meteorological Center) of CMA (China Meteorological Administration). FY-2 satellites are used to collect data in the visible and thermal domains about land and atmosphere characteristics. In this thesis data from FY-2E are used. This geostationary satellite is located at the 105°E and carries the S-VISSR (Stretched Visible and Infrared Spin Scan Radiometer) featuring 5 spectral bands, one visible and four thermal bands (Table 2.3).

Table 2.3: FY-2E sensor characteristics

<i>Band</i>	<i>Visible</i>	<i>IR1</i>	<i>IR2</i>	<i>IR3</i>	<i>IR4</i>
<i>Spectral range (μm)</i>	<i>0.55-0.99</i>	<i>10.3-11.3</i>	<i>11.5-12.5</i>	<i>6.3-7.6</i>	<i>3.5-4.0</i>
<i>Spatial resolution (km)</i>	<i>1.25</i>	<i>5</i>	<i>5</i>	<i>5</i>	<i>5</i>
<i>Temporal resolution</i>	<i>One full disk every 30 minutes</i>				

A 3-year time series of hourly daytime FY-2E full scene images from 01/01/2008 to 31/12/2010 is used in this research to derive a new land surface albedo product (Chapter 6). Only the visible band is used and the data corresponding to the subset study area (Figure 2.2) is extracted from the full scene. The visible band of FY-2E data spreads from 0.55 to 0.9 μm and is available at 1.25 km resolution. For this study, the visible band of FY-2E is resampled to 1 km using a cubic convolution interpolation.

<sup>12</sup> [http://www.nsmc.cma.gov.cn/NewSite/NSMC\\_EN/Channels/100187.html](http://www.nsmc.cma.gov.cn/NewSite/NSMC_EN/Channels/100187.html)

### 2.4.3 Landsat

Landsat-7 is the seventh satellite of the Landsat program which is managed and operated by the USGS (United States Geological Survey)<sup>13</sup>. Landsat 7 is in a polar, sun-synchronous orbit with an altitude of about 705 km and a revisit period of 16 days. The main instrument on board Landsat 7 is the Enhanced Thematic Mapper Plus (ETM+) measuring in 7 narrow and 1 panchromatic bands. The characteristics of the sensor are summarized in Table 2.4.

Table 2.4: Landsat-7 sensor characteristics

<b>Band</b>	<b>Pan</b>	<b>Blue</b>	<b>Green</b>	<b>Red</b>	<b>NIR</b>	<b>MIR1</b>	<b>MIR2</b>	<b>TIR</b>
<b>Band number</b>	8	1	2	3	4	5	7	6
<b>Spectral range (<math>\mu\text{m}</math>)</b>	0.52 - 0.9	0.45 - 0.515	0.525 - 0.605	0.63 - 0.69	0.75 - 0.9	1.55 - 1.75	2.09 - 2.35	10.4 - 12.5
<b>Spatial resolution (m)</b>	15	30	30	30	30	30	30	60
<b>Temporal resolution</b>	<i>The repeat coverage interval is 16 days</i>							

A cloud free Landsat-7 scene from the 27 October 2007 taken over the Tibetan Plateau is used for validation purposes (Chapter 6). The validation is performed in the solar domain of the spectrum so only the four first bands (bands 1-4) as well as the panchromatic band (band 8) of the Landsat image are used.

## 2.5 Validation data

### 2.5.1 Ground data

Ground measurements, coming from four radiative balance stations located on the Tibetan Plateau (Figure 2.7): BJ (now Nagqu), Linzhi, NamCo and Qomolangma, are used to evaluate the modelled net solar radiation estimates (Chapter 3), the surface albedo estimates (Chapter 6) and to correlate with the retrieved cloud indices (Chapter 4).

The information concerning the stations sites and instruments is taken from Babel et al. (2011a). The pictures and maps presented in Figure 2.8 to 2.11 are borrowed from Babel et al. (2011b) and from Yaoming Ma (ITP, CAS) presentations in the framework of the CEOP-AEGIS project.

<sup>13</sup> <http://landsat.usgs.gov>

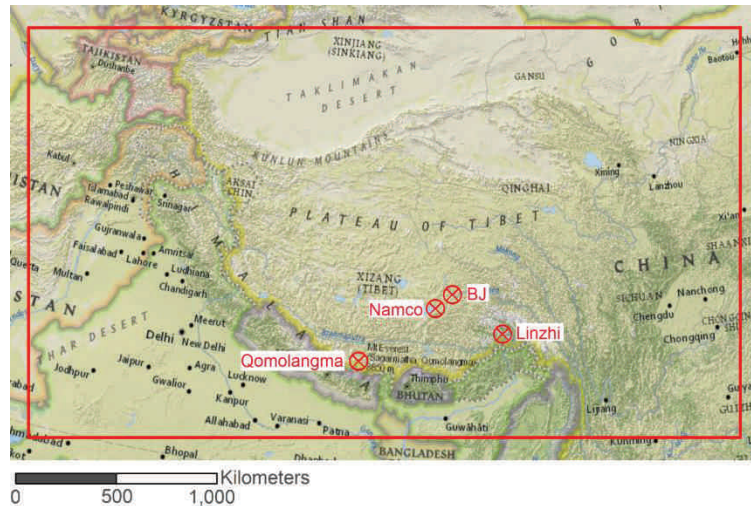


Figure 2.7: Location of the ground stations (circled red cross) within the study area

The BJ site ( $31^{\circ}22'N$ ,  $91^{\circ}53'E$ ) is set over relatively flat terrain in a large valley at 4502m. This station is managed by CAREERI, CAS (Cold and Arid Regions Environmental and Engineering Research Institute, Chinese Academy of Sciences). The vegetation is very low, sometimes interspersed with bare soil, but quite homogeneous on the landscape scale (Figure 2.8). The nearest hill slopes are located at about 1 km away.

The Linzhi station ( $29^{\circ}45'N$ ,  $94^{\circ}44'E$ ), lying at 3327 m, is located at the start of a small valley and is also managed by CAREERI, CAS. The station is located in an area covered by an alpine meadow with tall grasses and herbs during the summer period, while the meadows outside of the site are grazed and thus very short. The landscape is very heterogeneous with steep slopes, covered by mixed forest. The pastures outside the fence alternate with a small creek and bushes and single trees, respectively (Figure 2.9).

The NamCo station ( $30^{\circ}46'N$ ,  $90^{\circ}59'E$ ), at 4730 m, is located on the southeast shore of the NamCo Lake, which is the second largest saline lake in the Tibetan Plateau. This station was established by the Institute of Tibetan Plateau Research (ITP) from the Chinese Academy of Sciences (CAS) (Ma et al. 2008). The station is surrounded by several mountain ranges, especially the Nyenchentanglha mountain range in the South. The measurement site itself is settled over a flat terrain, and the typical vegetation around the station is an alpine steppe (Figure 2.10).

The Qomolangma Atmospheric and Environmental Observation and Research Station ( $28.21^{\circ}N$ ,  $86.56^{\circ}E$ ) lies at 4276 m above sea level and is also managed by ITP, CAS. Located at 30 km from the Mount Everest, it acts as an observation base for the study

of the atmospheric and the environmental processes in the Himalayas. The station is set in a valley enclosed by steep slopes at a distance of 750m east and 500m north-west and south-west of the tower with a height of about 600-800 m above ground level. A side valley comes in from west. The site land cover is dominated by riverbed gravel, with very sparse vegetation, but also small patches of short alpine meadows (Figure 2.11).

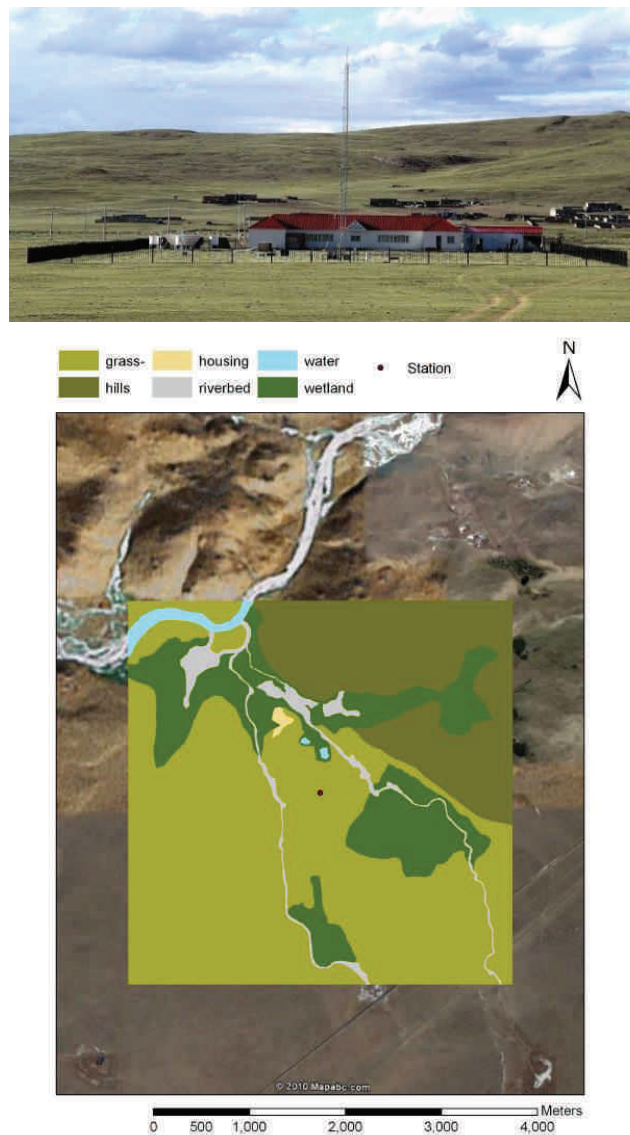


Figure 2.8: Picture of the BJ site (top) and land cover map of the surroundings (bottom) from Babel et al. (2011)

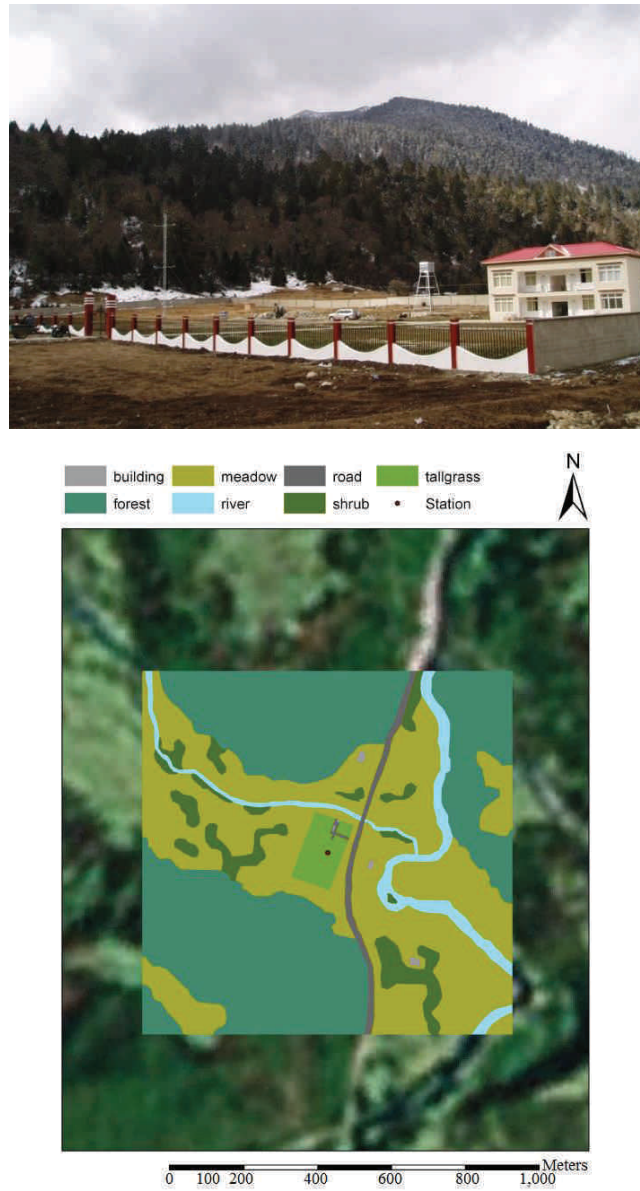


Figure 2.9: Picture of the Linzhi site (top) and land cover map of the surroundings (bottom) from Babel et al. (2011)

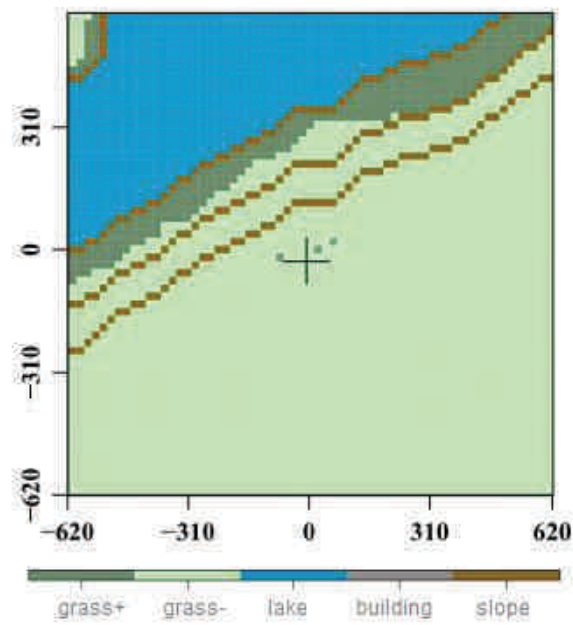


Figure 2.10: Picture of the NamCo site (top) and land cover map of the surroundings (bottom) from Babel et al. (2011)



Figure 2.11: Picture of the Qomolangma site (top) and land cover map of the surroundings (bottom) from Babel et al. (2011)

The ground based turbulent fluxes measured at the stations are provided at three levels of processing state (Babel et al. 2011). The data used in this research are the level 2 data, which correspond to the energy balance closed turbulent fluxes, for the period 2008 – 2010. The data consists of variables as time series vectors, or scalar. The time step is 30 minutes, missing values are indicated by  $-9e^{33}$ . The instruments used are listed in Table 2.5. Those data can be accessed via the CEOP AEGIS data portal<sup>14</sup>.

Table 2.5: Instruments set up for each stations (<sup>a</sup> Kaijo-Denki DAT 600 TR61A probe, after 2010 June 25; <sup>b</sup> CSAT3; <sup>c</sup> Campbell Scientific Ltd.; <sup>e</sup> LI-COR Biosciences; <sup>d</sup> Vaisala; <sup>e</sup> Kipp & Zonen; <sup>f</sup> calculated from upward longwave radiation; <sup>g</sup> unknown manufacturer)

<i>Component</i>	<i>BJ</i>	<i>Linzhi</i>	<i>NamCo</i>	<i>Qomolangma</i>
<i>Sonic anemometer</i>	<i>DAT 600<sup>a</sup></i>	<i>CSAT3<sup>b</sup></i>	<i>CSAT3<sup>b</sup></i>	<i>CSAT3<sup>b</sup></i>
<i>IRGA</i>	<i>LI-7500<sup>c</sup></i>	<i>LI-7500<sup>c</sup></i>	<i>LI-7500<sup>c</sup></i>	<i>LI-7500<sup>c</sup></i>
<i>Air temp/hum</i>	<i>HMP45<sup>d</sup></i>	<i>HMP45<sup>d</sup></i>	<i>HMP45<sup>d</sup></i>	<i>HMP45<sup>d</sup></i>
<i>Radiation</i>	<i>CM3/CG3<sup>e</sup></i>	<i>CNR1<sup>e</sup></i>	<i>CM3/CG3<sup>e</sup></i>	<i>CNR1<sup>e</sup></i>
<i>Surface temp.</i>	<i>calculated<sup>f</sup></i>	<i>IRTS-P<sup>b</sup></i>	<i>calculated<sup>f</sup></i>	<i>calculated<sup>f</sup></i>
<i>Soil temp.</i>	<i>Okazaki TS-301</i>	<i>107<sup>b</sup></i>	<i>Pt100<sup>g</sup></i>	<i>Pt100<sup>g</sup></i>
<i>Soil moisture</i>	<i>IMKO, Trime EZ</i>	<i>CS 616<sup>b</sup></i>	<i>ML2X<sup>d</sup></i>	<i>ML2X<sup>d</sup></i>

### 2.5.2 Satellite data products

As the comparison between estimates derived from remote sensing and ground measurements can be difficult, this thesis takes also advantage of available satellite data products for validation purposes. The MODIS TOA radiance (MOD021KM) and surface reflectance (MOD09) products are used for the validation of the solar radiation budget time series in Chapter 3. The estimated solar radiative fluxes are broadband estimates while the radiance and reflectance provided by MODIS are spectral. Then, prior being used for validation, they need to be converted to broadband values. To do so, the seven first spectral bands of the MODIS sensor have been used to reconstruct the spectral signature of radiance and reflectance respectively and then integrated over the solar domain.

In Chapter 6, three satellite data products are used to evaluate the retrieved surface albedo estimates. Those products are well-known broadband satellite data products, existing for several years, which have been widely used and tested by the scientific community.

<sup>14</sup> <http://ceop-aegis.itpcas.ac.cn/FinalRepository/>

The albedo products used as reference are:

- GlobAlbedo<sup>15</sup> 8-day product (Data obtained from the ESA GlobAlbedo project)
- MSA 10-day products (Meteosat Surface Albedo Product, EUMETSAT)
- MODIS albedo 16-day product collection 5.1 (NASA Land Processes Distributed Active Archive Center (LP DAAC)), already presented in section 2.4.1.

## 2.6 Conclusion

The Tibetan Plateau is a unique place on Earth, with its own particularities linked to the high altitude and the strong relief in its Southern part. Thus, to monitor solar radiative fluxes over this area, those specificities need to be taken into account and some improvements to adapt the existing retrieval methods are required, especially considering the sub-pixel heterogeneity. To do so, several data sources are used in this research. Most of the datasets are coming from satellite sensors as remote sensing is the most coherent and efficient way to retrieve data for radiative fluxes monitoring over a large area with high spatial and temporal variability. A key dataset is the high resolution DEM, essential to characterize and integrate the effects of topography on the radiative fluxes at the surface at sub-pixel level. Ground data are only used for the validation of the results.

All those data sources have their own characteristics and footprints which can make them difficult sometime to combine or compare. This is especially the case with the different satellite datasets presented in this section. Each one has its own spatial and temporal resolution as well as its own georeferencing system. To be able to combine or compare those data, some standardization steps were required. All the satellite data have been reprojected, resampled and snapped to fit the 1 km pixel resolution template grid, defined to cover the study area and presented in section 2.2. Furthermore, the validation datasets - reference albedo and field measurements - are broadband products. The MODIS TOA radiance and surface reflectance products have been previously converted to broadband values as well. In this thesis, while MODIS based estimates are produced broadband (section 3.6), FY-2 based ones are not. Therefore, the later have been converted to broadband prior to any comparison with the validation datasets (section 6.2.4)

---

<sup>15</sup> <http://www.GlobAlbedo.org>



## Chapter 3

# Solar radiation budget from existing satellite data products

### 3.1 Introduction

The solar radiation budget, also called net solar radiation, is defined as the difference between downwelling and upwelling shortwave radiative fluxes at the Earth's surface (Bisht et al. 2005). Even if there are different techniques to estimate the surface solar radiative fluxes for a given place (section 1.2), space-borne observations are the most suitable for large area monitoring. Numerous algorithms have been developed to estimate solar radiative fluxes using satellite radiometric measurements and some led to the production of regional or global datasets. To date, most of the available datasets have high temporal resolution but too coarse spatial resolution (30–280 km scale) to investigate local-scale radiation balances (Ryu et al. 2008). Moreover, they are often not suitable to characterize heterogeneous areas such as the Tibetan Plateau (Yang et al. 2008).

In order to estimate the surface radiative fluxes daily using remote sensing, the spatial resolution is limited to the square kilometer. Some satellite data products have been developed and regularly improved to characterize the atmospheric and land surface properties at these spatial and temporal scales. The objective of this chapter is then to propose an operational method based on those existing products allowing daily solar radiative fluxes monitoring at the square kilometer over heterogeneous areas and to assess the accuracy that can be achieved only by using those existing satellite data products. The solar radiative fluxes retrieval method was developed building upon existing algorithms and the latest developments in the field. MODIS data products were selected as input because they are freely, widely and -for most of the products- daily available. One of the main influencing features when modelling solar radiative fluxes over the Tibetan Plateau is the presence of very rough terrain, especially in the South part of the Plateau. The proposed method uses the mean terrain slope and azimuth of each pixel to calculate the irradiance according to the local illumination angle and integrates the atmospheric variability over a square kilometer pixel. The instantaneous fluxes computed for all skies conditions are then aggregated into daily averages.

According to Equation 1.2, the two main components to estimate when modelling the solar radiation budget ( $R_{ns}$ ) are: (1) the surface irradiance ( $E$ ) and (2) the surface albedo ( $a$ ). This chapter starts with a short introduction to the concept and estimation of surface irradiance and albedo using remote sensing. Next, the daily integration of the fluxes and the challenges when dealing with mountainous areas are described. After the presentation of the method developed to retrieve solar radiative fluxes from MODIS data, some results and conclusions are provided.

## 3.2 Surface irradiance

### 3.2.1 Extraterrestrial irradiance

The TOA solar radiation reaching the Earth is not yet affected by the atmosphere and is called extraterrestrial radiation. On average the extraterrestrial solar constant ( $S_0$ ) integrated over the entire solar spectrum is  $1367 \text{ W/m}^2$  (Equation 3.1).

$$S_0 = \int_{\lambda_{min}}^{\lambda_{max}} S_0(\lambda) d\lambda = 1367 \text{ W} \cdot \text{m}^{-2} \quad 3.1$$

where  $S_0(\lambda)$  ( $\text{W} \cdot \text{m}^{-2} \cdot \mu\text{m}^{-1}$ ) is the TOA solar constant at a given wavelength of the solar spectrum  $\lambda$  ( $\mu\text{m}$ ) and  $\lambda_{min}$  and  $\lambda_{max}$  ( $\mu\text{m}$ ) are its lower bound and upper bound, respectively. This value fluctuates by about 6.9 % during a year due to the Earth's varying distance from the Sun (Paulescu et al. 2013). The Earth revolves around the sun in an

elliptical orbit and the amount of solar radiation reaching the Earth is inversely proportional to the square of its distance from the Sun (Equation 3.2). The Sun-Earth distance ( $SE_d$ ) is expressed in astronomical unit (AU) with one AU being the mean Sun-Earth distance ( $\approx 1.496 \times 10^8$  km). This distance can be known with a very high accuracy but it is often more suitable to express it in a simple mathematical form. There are several expressions to estimate the Sun-Earth distance, and the one used in this work is as follows (Iqbal 1983):

$$SE_d = \frac{1}{\sqrt{1.00011 + 0.034221 \cos \Gamma + 0.00128 \sin \Gamma + 0.000719 \cos 2\Gamma + 0.000077 \sin 2\Gamma}} \quad 3.2$$

In this equation,  $\Gamma$  is the day angle, expressed according to the day of the year ( $d$ ):

$$\Gamma = 2\pi d/365 \quad 3.3$$

Then, for a given day of the year, the broadband extraterrestrial solar irradiance ( $E_0$ ) is expressed as:

$$E_0 = \int_{\lambda_{min}}^{\lambda_{max}} E_0(\lambda) d\lambda = S_0 \times SE_d \quad 3.4$$

### 3.2.2 Radiative transfer in the atmosphere and surface irradiance

The shortwave irradiance travelling toward the Earth's surface interacts with the atmospheric components (gases, aerosols, cloud droplets). Radiative transfer describes these interactions taking into account three key processes:

- **Reflection:** the atmosphere turns back a portion of the solar irradiance into space. It is an important process to consider as a third of the energy from the Sun is reflected.

- **Absorption:** a portion of the solar irradiance is absorbed by some of the atmospheric components, leading to a decrease of the direct irradiance reaching the surface. The atmosphere, containing many different gases and particles, absorbs and transmits incident radiation depending on the wavelength. Absorption is mainly caused by three different atmospheric gases: (1) water vapor which causes the most absorption, (2) carbon dioxide and (3) ozone.

- **Scattering:** it corresponds to a diffusion of a portion of the irradiance in all directions by the small particles and molecules, suspended in the atmosphere, at wavelengths when no quantum state transition is possible. The scattering effect diffuses the light, in other words spreads it out in all directions, generating the diffuse portion of the

irradiance. There are three different types of scattering: Rayleigh scattering, Mie scattering, and wavelength non-selective scattering. Rayleigh scattering mainly consists of scattering by atmospheric gases. As the wavelength decreases, the amount of scattering increases. Mie scattering is caused by pollen, dust, smoke, water droplets, and other particles in the lower portion of the atmosphere. It occurs when the size of the particles is larger than the wavelength of the radiation and is the primary cause of haze. Both Rayleigh and Mie scattering effects are wavelength dependent. The last type of scattering is non-selective scattering. The sum of absorption and scattering processes is called irradiance attenuation.

When the solar radiative flux passes through the Earth's atmosphere, its spectral distribution is also modified by absorption and scattering processes. The interaction between the extraterrestrial irradiance and the Earth's atmosphere is illustrated in Figure 3.1.

As a result of its passage through the atmosphere, the extraterrestrial irradiance is divided into: (1) a direct (or beam), (2) a diffuse and (3) a backscattered component. The direct irradiance is the portion of the radiation which directly reaches the Earth's surface while the diffuse irradiance comes from the scattering of the radiation in the atmosphere. The backscattered irradiance is the portion of radiation that is sent back to space. In case of significant topography, a part of the solar radiation that is reflected by the surrounding terrain may also be present in the total solar irradiance at a specific location. Those quantities are usually defined as (Paulescu et al. 2013):

- Direct irradiance ( $E_d$ ), which is the energy flux density ( $\text{W.m}^{-2}$ ) of the solar radiation incoming from Sun on a unitary surface perpendicular to the beam. According to the Lambert's cosine law, the energy flux density on a surface is directly proportional to the cosine of the incidence angle. When assuming the surface as flat, the incidence angle of the solar beam is equal to the sun zenith angle  $\theta_s$ , then:

$$E_d = E_0 \times \cos \theta_s \quad 3.5$$

- Diffuse irradiance ( $E_f$ ), which is the energy flux density of the solar radiation incoming from the entire sky dome on a horizontal surface, excluding the direct beam coming from the Sun.
- Global irradiance ( $E$ ) on a horizontal surface is the sum of the direct horizontal and diffuse components, given as:

$$E = E_d + E_f \quad 3.6$$

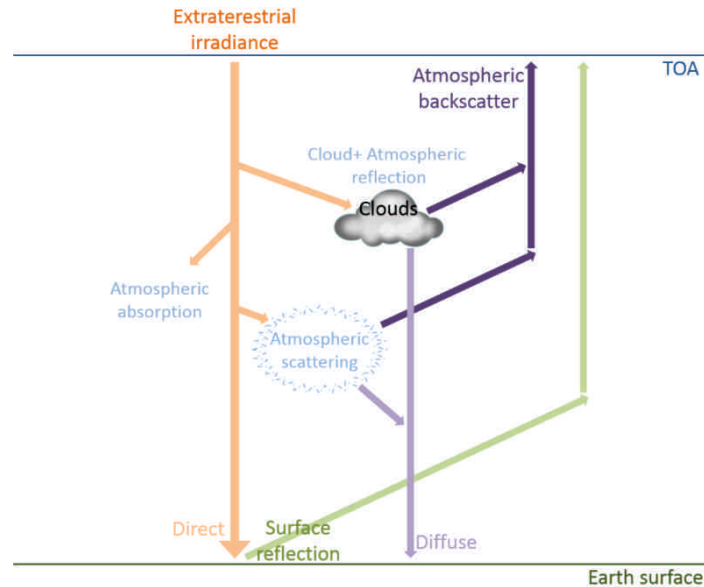


Figure 3.1: Interactions between the extraterrestrial irradiance and the Earth's atmosphere

### 1.3.1 Surface irradiance using remote sensing

During the last decades, many approaches were proposed to estimate surface irradiance using satellite measurements, at both regional and global scales, for a wide range of satellite data type, geostationary (Gautier et al. 1980; Masuda et al. 1995; Perez et al. 2002; Hammer et al. 2003; Deneke et al. 2008; Blanc et al. 2011; Geraldi et al. 2012) or polar orbiting satellite (Tang et al. 2006; Wang et al. 2009b; Perez et al. 2013). However, most of the methods make use of geostationary satellite images (Polo et al. 2008). Raphael et al. (1984), Pinker et al. (1995) and Niemela et al. (2001) provide a review for some of those methods which present different degree of complexity. The simplest methods are based on a purely statistical relation between the TOA radiance and the surface irradiance measured at the ground (Tarpley 1979; Noia et al. 1993a). Physical models are more sophisticated by including physical representations of the interaction taking place in the atmosphere using radiative transfer models (Pinker et al. 1985; Dedieu et al. 1987; Zhanqing et al. 1993; Masuda et al. 1995) or retrieved cloud and atmosphere parameters from other sources (Liang et al. 2010), such as remote sensing. A review of some existing physical models is presented in Noia et al. (1993b). Because they rely on a simple regression between satellite data and solar ground measurements and not on the composition of the atmosphere, statistical models are simpler. On the contrary, the physical models require information about atmospheric properties to take into account the irradiance

attenuation. However, since the statistical approach needs ground data, it is difficult to generalize it. Thus, in this thesis, the surface irradiance is estimated based on the physical approach using the atmospheric transmittance derived from satellite data in such a way that it also takes into account atmospheric backscattering.

Whatever the complexity of the model, the irradiance at the surface can be basically expressed as (Niemelä et al. 2001):

$$E = E_0 \times \cos \theta_s \times \int_{\lambda_{min}}^{\lambda_{max}} \tau(\lambda) d\lambda \quad 3.7$$

The solar zenith angle ( $\theta_s$ ) multiplied by  $E_0$  provides the extraterrestrial irradiance for a given time of the day. The last term of the equation,  $\tau$ , the atmospheric shortwave transmittance, allows to integrate the atmospheric effects and estimates surface irradiance from extraterrestrial irradiance. The computation of  $E_0$  is performed according to Equation 3.4, depending only on the day of the year even if more complex estimation can be found. The solar geometry depends on the day of the year as well as on the geographic coordinates of the location considered.  $\tau$  is the variable derived from satellite data.

To describe the position of the Sun in the sky for a given location on Earth, several angles relative to the surface are used. For now, the surface is represented by a tangent plane. The main angles to characterize the Sun position are the Sun zenith ( $\theta_s$ ) and elevation ( $\alpha_s$ ) angles which are the angles of the Sun relative to a line perpendicular to the surface (named surface normal) and the Sun azimuth angle ( $\phi_s$ ) which characterizes the Sun position relative to the north-south axis, as shown on Figure 3.2.

There are several parameters to take into account when computing the solar angles. First, the Earth axis is tilted approximately  $23.45^\circ$  with respect to the Earth orbit around the Sun. As viewed from space, this axis is fixed during the entire revolution period of the Earth around the Sun. Then, the orientation of the Earth toward the Sun varies during the year, leading to a Sun with a higher position in the sky during summer and lower during winter. The two seasons being inverted in the Northern and Southern hemispheres. This is taken into account by calculating the declination of the sun ( $\delta$ ) which is the angle between a plane perpendicular to a line between the Earth and the Sun and the Earth's rotation axis. Iqbal (1983) provides a formula to estimate the declination of the sun based on the day angle ( $\Gamma$ , Equation 3.3). This equation is derived from Spencer (1972) and expressed as:

$$\begin{aligned} \delta = & 0.006918 - 0.399912 \cos \Gamma - 0.006758 \cos(2\Gamma) - 0.002697 \cos(3\Gamma) \\ & + 0.070257 \sin \Gamma + 0.000907 \cos(2\Gamma) + 0.001480 \sin(3\Gamma) \end{aligned} \quad 3.8$$

Another required parameter is the hour angle ( $\omega$ ) (Equation 3.9). It is measured in the plane of the apparent orbit of the Sun as it moves across the sky. Since the Earth rotates approximately once every 24 hours, the hour angle changes by  $15^\circ$  per hour and moves through  $360^\circ$  over the day. Typically, the hour angle is defined to be zero at local solar noon, when the Sun is the highest in the sky, and depends on the local time ( $h$ ).

$$\omega = (15 \times (12 - h)) * \pi/180 \quad 3.9$$

Using the sun declination ( $\delta$ ), the hour angle ( $\omega$ ) and the latitude ( $lat$ ) of the considered location, all expressed in radians, the solar zenith ( $\theta_s$ ) and elevation ( $\alpha_s$ ) angles are computed as:

$$\cos \theta_s = \sin(lat) \times \sin \delta + \cos(lat) \times \cos \delta \times \cos \omega \quad 3.10$$

$$\alpha_s = \pi/2 - \theta_s \quad 3.11$$

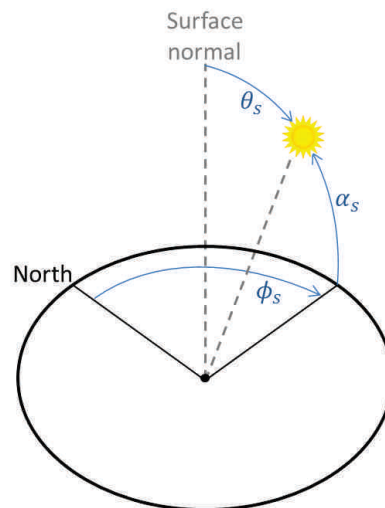


Figure 3.2: Solar position for a given location on the Earth's surface,  $\theta_s$  being the sun zenith angle,  $\alpha_s$  the sun elevation and  $\phi_s$  the sun azimuth angle

### 3.3 Surface albedo

#### 3.3.1 Albedo definition

Only a portion of the solar irradiance is absorbed by the Earth whereas the rest is immediately reflected back into space. The surface reflectance is defined as the fraction of irradiance reflected by the surface for a specific combination of illumination and view angles, while the directional integration of reflectance over all sun-view geometries is called albedo (Schaepman-Strub et al. 2006). The latter is a critical parameter for the calculation of the solar radiation budget. Both reflectance and albedo are highly variable depending on the surface type which is characterized by its bidirectional reflectance distribution function (BRDF).

Different concepts can be covered by the term “albedo”. For the sake of clarity, the ones used in this research are described below according to Geiger et al. (2008).

(1) *The directional albedo or directional-hemispherical reflectance*

Also called black-sky albedo, is the integration of the bi-directional reflectance over the viewing hemisphere. It assumes all energy is coming as direct radiation from the sun and is computed at a specific time. It is expressed as:

$$a_{BS}(\lambda, \theta_i, \phi_i) = \frac{1}{\pi} \int_{2\pi} \rho(\lambda, \theta_i, \theta_v, \phi_i, \phi_v) \cos \theta_v d\Omega_v \quad 3.12$$

with the solid angle  $\Omega_v$  :  $d\Omega_v = \sin \theta_v d\theta_v d\phi_v$

(2) *The hemispherical albedo or bi-hemispherical reflectance*

Also called white-sky albedo, is the integration of the directional albedo over the illumination hemisphere, assuming a complete diffuse illumination.

$$a_{WS}(\lambda) = \frac{1}{\pi} \int_{2\pi} a_{BS}(\lambda, \theta_i, \phi_i) \cos \theta_i d\Omega_i \quad 3.13$$

with the solid angle  $\Omega_i$  :  $d\Omega_i = \sin \theta_i d\theta_i d\phi_i$

(3) *The albedo, under actual atmospheric conditions*

Also called blue-sky albedo, can be modelled as an interpolation between black-sky and white-sky albedo as a fraction of diffuse skylight,  $F(\lambda, \theta_i, \phi_i)$  which is in turn a function of AOD (Schaaf et al. 2002; Román et al. 2010):

$$a(\lambda, \theta_i, \phi_i) = (1 - F(\lambda, \theta_i, \phi_i)) a_{BS}(\lambda, \theta_i, \phi_i) + F(\lambda, \theta_i, \phi_i) a_{WS}(\lambda) \quad 3.14$$

### 3.3.2 Albedo from remote sensing

Due to its repetitive global coverage, remote sensing is a data source of primary interest to provide regional and global albedo estimates. Sensors on-board satellites do not directly measure surface albedo, they measure the spectral radiance reflected by the surface in a given direction toward the sensor, from which the albedo needs to be derived. The spectral radiance can be defined as the radiant flux in a beam per unit wavelength and per unit area and solid angle of that beam, and is expressed in the SI units ( $\text{W}\cdot\text{sr}^{-1}\cdot\text{m}^{-2}\cdot\text{nm}^{-1}$ ) (Schaepman-Strub et al. 2006). The retrieval process starts with a cloud screening to exclude cloudy pixels. For the clear pixels, the TOA measured upwelling radiance is corrected for the atmospheric effects to obtain the reflected radiance value at the surface.

Next, the surface reflected radiance is divided by the surface irradiance to derive the surface reflectance (Equation 6.1). As the albedo is an integration of reflectance over all view angles, the difficulty is to have enough satellite data measured at different viewing or illumination angles to estimate albedo from the measured reflectance. With a sufficient angular sampling or a priori knowledge on the surface BRDF the albedo can be estimated. Knowledge about the surface BRDF is a prerequisite to derive the albedo. Since the BRDF of the surface cannot be measured directly by most of the satellites, physical or parametric models have been developed to predict it based on satellite data. There are several BRDF models based on different reconstruction principles, empirical or semi-empirical, according to the data availability. Each model requires different types of inputs. Among those, some kernel-based models such as the Ross Thick-Li Sparse (Ross-Li) model (Lucht et al. 2000b), some nonlinear models such as the parametric Rahman-Pinty-Verstraete (RPV) (Rahman et al. 1993) and the Nonlinear Temporal Angular Model (NTAM) (Latifovic et al. 2003) should be mentioned. Some of the sensors provide a good angular sampling to accurately model the surface BRDF, e.g. the Multiangle Imaging Spectro Radiometer (MISR) on Terra. With the development of geostationary satellites, methods have been proposed to retrieve the surface albedo and/or BRDF parameters using the high temporal frequency of the measurement and the variation of illumination angle (Pinty et al. 2000; Govaerts et al. 2006).

The last step of the process is the conversion from narrow to broadband albedo. The objective is to extrapolate the albedo estimated from satellites measurements usually made of one or several separate narrowband channels, called narrowband albedo, to the real broadband albedo which represents the total broadband region of solar radiation. Those processing steps are summarized in Figure 3.3.

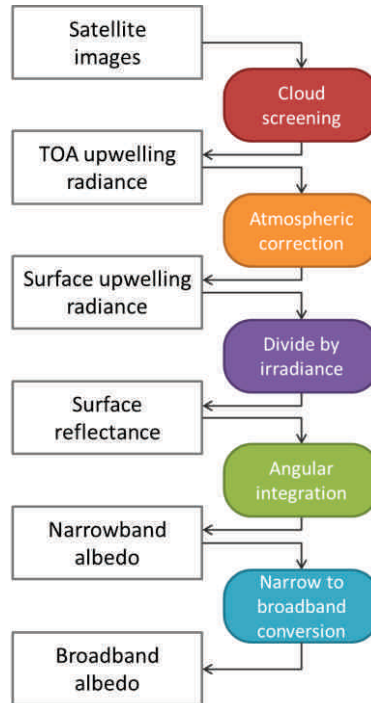


Figure 3.3: General steps for albedo retrieval from remote sensing imagery

Several operational albedo products are currently available at regional or global scale and at different spatial and temporal resolutions. Among those, the daily 3 km resolution albedo from the Advanced Very High Resolution Radiometer (AVHRR) (Strugnell et al. 2001), the MODIS 8-day 0.5 km resolution albedo (Schaaf et al. 2002) and the 10-day 3 km resolution albedo from the geostationary satellite METEOSAT first and second generation (MFG and MSG) (Carrer et al. 2009). As no large area daily albedo data products were available, the 8-day MODIS products were selected as input for the operational method.

### 3.4 Daily integration of solar radiation

While the surface properties can be relatively constant over a day, assuming that there are no important changes of the surface conditions, the surface irradiance is varying over the day because it strongly depends on the sun geometry and atmosphere conditions, especially the presence of clouds. The surface irradiance is an instantaneous value computed at satellite overpass time which needs to be extrapolated to get the daily mean

solar irradiance. There are several ways to proceed according to the data availability. For the sake of simplicity, the estimated albedo value is assumed as valid for the entire day. So, in order to characterize the solar irradiance at the surface, the variation in the Sun geometry and the state of the sky should also be taken into account. Regarding the Sun-target geometry, the solar zenith angle can be easily computed for each desired local time using Equation 3.10. To describe the state of the sky, one of the commonly used indicators is the total cloud cover which represents the fraction of the sky covered by clouds, usually measured at regular time intervals and averaged to a daily value. Another variable describing indirectly the state of the sky is the relative sunshine, or sunshine fraction ( $S_f$ ), which is the portion of bright sunshine duration ( $s$ ) during a given time interval ( $S$ ) (Equation 3.15), usually the interval between sunrise and sunset (Badescu 2008).

$$S_f = s/S \quad 3.15$$

For both quantities, regular measurements over the day are required for their accurate estimation. When no information is available, the daily solar irradiance can be approximated using a sinusoidal function proposed by Bisht et al. (2010) estimating the diurnal cycle of net solar radiation. In this function, the daily averaged net solar radiation ( $R_{ns,d}$ ), in terms of the instantaneous all skies shortwave radiation ( $R_{ns}$ ) can be obtained using the local satellite overpass time ( $t_{sat}$ ) as well as local sunrise ( $t_{sr}$ ) and sunset time ( $t_{ss}$ ) (Equation 3.16).

$$R_{ns,d} = \frac{2 \times R_{ns}}{[\pi \times \sin(\pi((t_{sat} - t_{sr})/(t_{ss} - t_{sr})))]} \quad 3.16$$

### 3.5 Challenge in mountainous area

In remote sensing, the transformation of space-borne imagery into information was and still remains a challenge, in particular in rugged terrain (Meyer et al. 1993). Retrieving the solar irradiance and the albedo at the surface from remote sensing is a complicated process. However, despite the difficulties, most of the current algorithms are beginning to meet the accuracy requirements of global climate models (Randall et al. 2007). Even if satisfying results are reached, there are still some issues to be addressed in some part of the globe such as mountainous areas. Indeed, one of the main sources of error when estimating surface irradiance and albedo is the effects induced by the underlying topography. As pointed out in section 5.2, neglecting the impact of topography by assuming a flat surface during the calculation of the solar radiation budget can lead to a very large error especially in area with such a complex terrain as the Tibetan Plateau. For global surface albedo data

products, *e.g.* MODIS or AVHRR, the effect of topography is quoted as an important source of error if retrieval assumes a horizontal surface (Riihelä et al. 2011).

The previous section briefly described the concept of solar irradiance and albedo retrieval using remote sensing, often applied considering flat terrain. Some methods were adapted or new ones developed to take into account the effects of topography on satellite measured data (Proy et al. 1989; Meyer et al. 1993; Richter 1997). Those topographic corrections have been successful in improving the quality of the retrieved surface variables (Riano et al. 2003; Richter et al. 2009). A common procedure applied in many algorithms to take into account topography is to use the average terrain slope and azimuth in the computation of the local illumination angle. This is the method used in section 3.6. However, this method does not fully consider the topographic effects, it just takes into account terrain orientation in the computation of the illumination angle while shadow and surrounding terrain effects are neglected. An improvement is necessary to integrate the shadow and surrounding terrain effects, especially considering the sub-pixel variability, for which an approach is proposed in Chapter 5.

### 3.6 Solar radiation from MODIS data

The objective of this chapter was to develop a method that actually provides daily solar radiation budget estimates time series at the kilometric resolution over the Tibetan Plateau based on existing satellite data products. With this purpose in mind, MODIS data were selected because they are freely, widely and for most of the products at the kilometric resolution and, except for albedo, daily available. Additionally, they are reliable and more than 10 years of archives are available allowing for the computation of historical averages and anomaly detection (Jia et al. 2011a). All the MODIS data used as inputs in the proposed method are level 2 or 3 products (Chapter 2). The atmospheric products provide atmosphere composition information which is not related to the spectral wavelength and the albedo is a broadband product. Then, no narrow-to-broadband conversion is needed in this case as the produced solar radiative fluxes are directly broadband estimates.

#### 3.6.1 *Instantaneous solar radiation clear sky*

The main guidelines of the proposed model come from Iqbal (1983). As shown in Equations 1.1 and 1.2, the solar radiation budget ( $R_{ns}$ ) is the difference between the downwelling and upwelling shortwave fluxes, and can also be expressed as function of the land surface albedo ( $a$ ). This section describes how the surface irradiance and albedo are retrieved using the MODIS data.

To compute the instantaneous irradiance at the surface ( $E$ ),  $E_0$  is estimated according to Equation 3.4 and  $\theta_s$  is replaced by the solar incident angle ( $\theta_i$ ).  $\theta_i$  is computed

at the satellite overpass time and accounting for the terrain slope and azimuth derived from the DEM, as expressed in Equation 3.17 (Allen et al. 2006) where  $\alpha_t$  and  $\phi_t$  are the terrain elevation and azimuth angles respectively.

$$\begin{aligned}
 \cos \theta_i = & \sin lat \times \sin \delta \times \cos \alpha_t \\
 & - \sin \delta \times \cos lat \times \sin \alpha_t \times \cos \phi_t \\
 & + \cos lat \times \cos \delta \times \cos \omega \times \cos \alpha_t \\
 & + \cos \delta \times \sin lat \times \sin \alpha_t \times \cos \phi_t \times \cos \omega \\
 & + \cos \delta \times \sin \alpha_t \times \sin \phi_t \times \sin \omega
 \end{aligned} \tag{3.17}$$

Combining Equations 3.7 and 3.17, E is expressed as:

$$E = E_0 \times \cos \theta_i \times \int_{\lambda_{min}}^{\lambda_{max}} \tau(\lambda) d\lambda \tag{3.18}$$

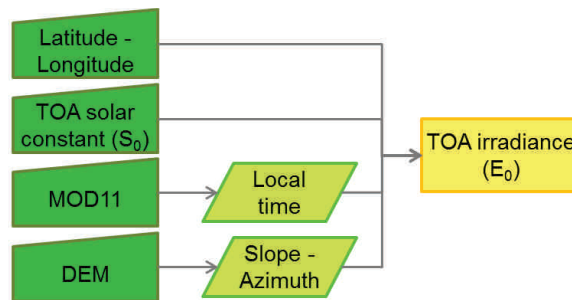


Figure 3.4: Estimation of TOA irradiance ( $E_0$ ) using MODIS Terra overpass time and terrain slope and azimuth

As described in section 3.2.2, as well as in several publications (Carroll 1985; Muneer et al. 2000; Yang et al. 2001; Van Laake et al. 2004; Chen et al. 2007),  $\tau$  is influenced by five radiation-damping processes: (1) Rayleigh scattering, (2) aerosol extinction, (3) ozone absorption, (4) water vapor absorption and (5) permanent gas absorption, leading to the partitioning of the extraterrestrial irradiance into direct, diffuse and backscattered radiations. The atmospheric transmittance estimated and used in this thesis takes into account each of those processes, which can be respectively translated in the

following spectral radiative transmittance factors:  $\tau_r, \tau_a, \tau_{oz}, \tau_w, \tau_g$ . The latter are then used to compute the spectral transmittance function of the atmosphere, defined by two elements: (1) the beam transmittance ( $T_B$ ) and (2) the diffuse transmittance ( $T_D$ ) (Equations 3.19 and 3.20). Equations 3.21 to 3.25, used to compute the spectral radiative transmittance factors, come from Yang et al. (2007) based on the Leckner's spectral model (Leckner 1978). The performance of this model was tested and verified in several studies (Gueymard 2003a; Gueymard 2003b; Paulescu et al. 2003; Madkour et al. 2006).

$$T_B = E_0^{-1} \int_{\lambda_{min}}^{\lambda_{max}} E_{0i}(\lambda) \tau_{oz}(\lambda) \times \tau_w(\lambda) \times \tau_g(\lambda) \times \tau_r(\lambda) \times \tau_a(\lambda) d\lambda \quad 3.19$$

$$T_D = 0.5 E_0^{-1} \int_{\lambda_{min}}^{\lambda_{max}} E_{0i}(\lambda) \tau_{oz}(\lambda) \times \tau_w(\lambda) \times \tau_g(\lambda) \times (1 - \tau_a(\lambda) \times \tau_r(\lambda)) d\lambda \quad 3.20$$

with the spectral transmittance factors expressed as:

$$\tau_r = \exp(-0.008735 \lambda^{-4.08} ms) \quad 3.21$$

$$\tau_a = \exp(-\beta \lambda^{-1.3} m) \quad 3.22$$

$$\tau_{oz} = \exp(-k_o(\lambda) m l) \quad 3.23$$

$$\tau_w = \exp([-0.2385 k_w(\lambda) w m]/[1 + 20.07 k_w(\lambda) w m]^{0.45}) \quad 3.24$$

$$\tau_g = \exp\left(\frac{[1.41 k_g(\lambda) ms]}{[1 + 2118.3 k_g(\lambda) ms]^{0.45}}\right) \quad 3.25$$

$k_o$  ( $\text{cm}^{-1}$ ),  $k_w$  ( $\text{cm}^2\text{g}^{-1}$ ) and  $k_g$  ( $\text{km}^{-1}$ ) are the absorption coefficients of ozone, water vapor and mixed gases respectively. Those coefficients are wavelength-dependent.  $l$  is the thickness of the ozone layer,  $w$  the precipitable water and  $\beta$  the Angstrom turbidity coefficient ( $0.406 \times AOD$ ). The air mass ( $m$ ) and pressure corrected air mass ( $ms$ ) are computed as:

$$m = 1/(\sin \alpha_s + 0.15 (57.296 \alpha_s + 3.885)^{-1.253}) \quad 3.26$$

$$ms = m (P/P_0) \quad 3.27$$

with  $P_0 = 1.013 \times 10^5$  (Pa),  $P$  representing the surface pressure and  $\alpha_s$  the solar elevation angle.

Each of the spectral radiative transmittance factors is dependent on the wavelength. Then, they can be described by an energy-weighted average transmittance factor in the form of Equation 3.28 with  $x$  being a radiation-damping process:

$$\bar{\tau}_x = E_0^{-1} \int_{\lambda_{min}}^{\lambda_{max}} E_0(\lambda) \tau_x(\lambda) d\lambda \quad 3.28$$

Yang et al. (2001), corrected in Yang et al. (2006b), proposed a simplification of the Leckner's spectral model based on the numerical integration of the Equations 3.21 to 3.25 using the absorption coefficient values provided in Leckner (1978) from which they derived approximate transmittance factor equations (Equations 3.29-3.33). The latter have been verified and validated (Yang et al. 2007).

$$\bar{\tau}_r \approx \exp(-0.008735 \text{ ms} \times (0.547 + 0.014 \text{ ms} - 0.00038 \text{ ms}^2 + 4.6 \times 10^{-6} \text{ ms}^3)^{-4.08}) \quad 3.29$$

$$\bar{\tau}_a \approx \exp\left((-m) \times \beta \times \left(0.6777 + 0.1464(m b) - (0.00626 ((m b)^2))\right)^{-1.3}\right) \quad 3.30$$

$$\bar{\tau}_{oz} \approx \exp(-0.0365 ((m l)^{0.7136})) \quad 3.31$$

$$\bar{\tau}_w \approx \exp(-0.05 (m w)^{0.3097} - 0.0138 \times \ln(m w) - 0.0581) \quad 3.32$$

$$\bar{\tau}_g \approx \exp(-0.0117 \text{ ms}^{0.3139}) \quad 3.33$$

Then, the spectral transmittance functions defined in Equations 3.19 and 3.20 are also approximated as broadband transmittance functions according to the simplified individual broadband radiative transmittances from Equations 3.29 to 3.33, as follow:

$$T_B \approx \bar{\tau}_{oz} \times \bar{\tau}_w \times \bar{\tau}_g \times \bar{\tau}_r \times \bar{\tau}_a \quad 3.34$$

$$T_D \approx 0.5 \bar{\tau}_{oz} \times \bar{\tau}_w \times \bar{\tau}_g \times (1 - \bar{\tau}_a \times \bar{\tau}_r) \quad 3.35$$

All the data required to characterize the composition of the atmosphere, such as  $l$ ,  $w$  and  $\beta$ , as well as the surface pressure,  $P$ , can be derived from the MODIS daily atmospheric products (section 2.4.1) (Figure 3.5). Once the broadband transmittance factors are computed, the beam and the diffuse transmittances can be calculated (Equations 3.34

and 3.35). Finally, as the atmospheric transmissivity is estimated using two elements,  $T_B$  and  $T_D$ , Equation 3.7 is adapted and the surface irradiance is computed as follow:

$$E = E_0 \times \cos \theta_i \times T_B + E_0 \times \cos \theta_i \times T_D \quad 3.36$$

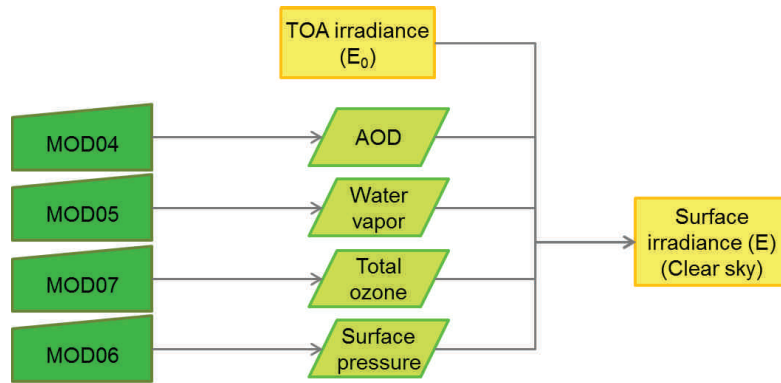


Figure 3.5: Computation of surface irradiance for clear sky conditions integrating atmospheric transmissivity derived from MODIS products

The surface albedo is derived from the 8-day composite albedo product from MODIS (Section 2.3.1), even if it is proven as having limited accuracy in areas as rugged as the Tibetan Plateau (Wen et al. 2014).

### 3.6.2 Instantaneous solar radiation all skies

The equations to compute the solar radiation budget at the surface presented in the previous section allow for estimations under clear sky condition. When the cloud cover fraction provided by MODIS (MOD06) is higher than 50%, the influence of clouds is taken into account by adapting the equations according to the parameterization described in Stephens et al. (1984), also applied and validated in Van Laake et al. (2004). To do so, the direct beam and diffuse irradiance are first computed for the atmosphere above the clouds. In that case, the pressure corrected air mass is calculated to the level of cloud top pressure ( $P_c$ ) - not surface pressure anymore - and the atmospheric water vapor content is assumed to be contained entirely below the cloud top. Those assumptions lead to modify the equations to estimate  $\bar{\tau}_r$ ,  $\bar{\tau}_g$  and  $\bar{\tau}_w$  while the ones for  $\bar{\tau}_a$  and  $\bar{\tau}_{oz}$  remain (Equations 3.37-3.39).

$$\bar{\tau}_r \approx \exp(-0.008735 mc (0.547 + 0.014 mc - 0.00038 mc^2 + 4.6 \times 10^{-6} mc^3)^{-4.08}) \quad 3.37$$

$$\bar{\tau}_w \approx 1 \quad 3.38$$

$$\bar{\tau}_g \approx \exp(-0.0117 mc^{0.3139}) \quad 3.39$$

with the pressure corrected air mass:

$$mc = m (P_c/P_0) \quad 3.40$$

A broadband cloud transmittance factor ( $\tau_c$ ) is added to integrate the effect of the cloud on the shortwave radiation transmissivity. It uses the optical thickness of the clouds ( $otc$ ) and a coefficient ( $bet$ ) linearly interpolated from the values given in Stephens et al. (1984) (Equation 3.41). For the sake of simplicity when considering the dependency of cloud absorption to wavelength, Stephens et al. (1984) provided values for two broad intervals of the solar spectrum. The first spreads from 0.3 to 0.75  $\mu\text{m}$ , where the absorption of the solar radiation by the clouds is extremely small and the second which extends from 0.75 to 4  $\mu\text{m}$  and integrates the absorption by the clouds.

$$\tau_c = 1 - \left[ \frac{(bet \times otc) / \cos \theta_s}{1 + (bet \times otc) / \cos \theta_s} \right] \quad 3.41$$

Finally  $\tau_c$  is integrated to the direct beam transmittance factor by adapting Equation 3.19 as shown in Equation 3.42 and the surface solar irradiance is still estimated with Equation 3.36.

$$T_B = \bar{\tau}_{oz} \times \bar{\tau}_w \times \bar{\tau}_g \times \bar{\tau}_r \times \bar{\tau}_a \times \tau_c \quad 3.42$$

All the cloud parameters required for the estimation of surface solar irradiance under cloudy condition, namely  $P_c$ ,  $otc$  and cloud fraction, are derived from the daily atmospheric products of MODIS (Chapter 2).

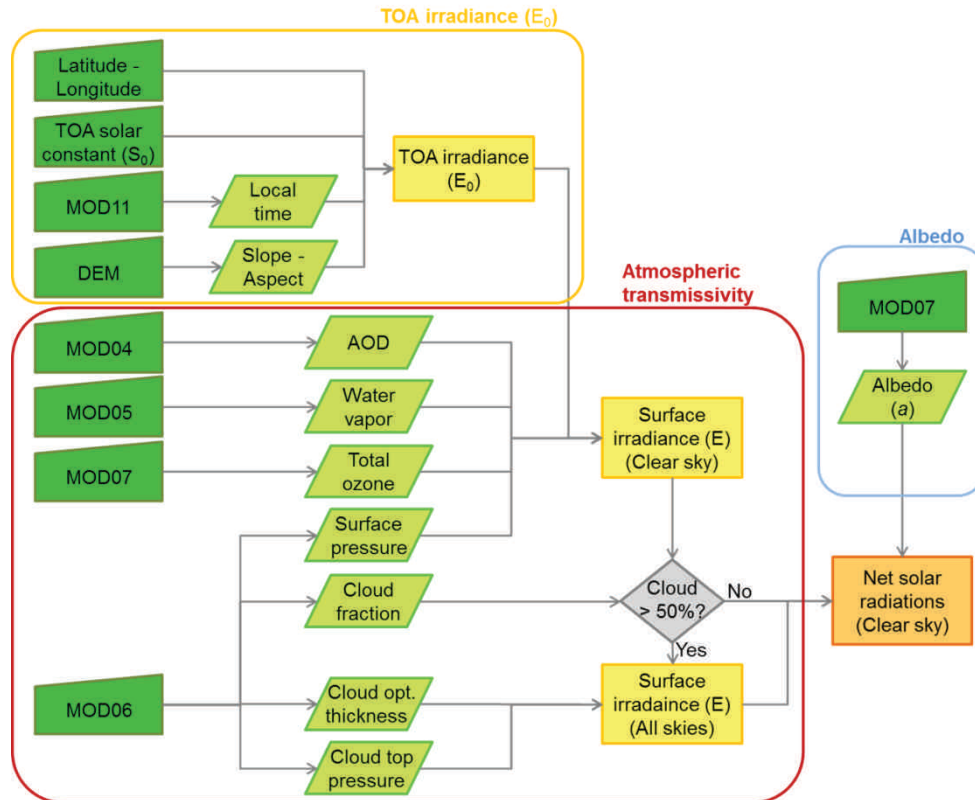


Figure 3.6: Computation of the solar radiation budget for all skies using MODIS products

### 3.6.3 Daily solar radiation

In order to reach the objective of daily monitoring, the instantaneous solar radiation budget ( $R_{ns}$ ) has to be converted into daily average ( $R_{ns,d}$ ). As the method to retrieve the instantaneous solar radiative fluxes is only based on MODIS data, there are too few measurements over the day to characterize the evolution of the state of the sky or of the sunshine duration. Thus, the conversion from instantaneous to daily radiation is performed using the sinusoidal model to estimate the diurnal cycle of net radiation proposed by Bisht et al. (2010) (Equation 3.16).

## 3.7 Results and validation

During the development of the method to estimate the solar radiation budget, some efforts have been done to represent the spatial and temporal heterogeneity of the Tibetan

Plateau affecting the solar radiative fluxes over space and time. The computation of surface irradiance using an atmospheric transmission factor (Figure 3.7) and considering terrain mean slope and azimuth to estimate the sun incident angle (Figure 3.8), both at the kilometeric resolution, highlights the importance of accounting for the spatial heterogeneity in that area.

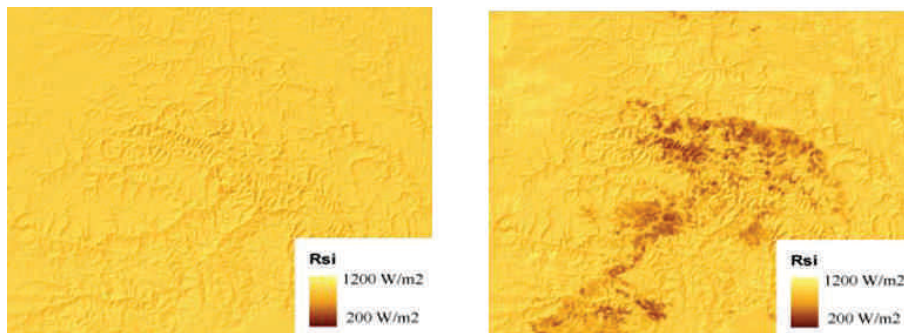


Figure 3.7: Surface irradiance computed using a constant atmospheric transmission factor (left) or the proposed methodology (right)

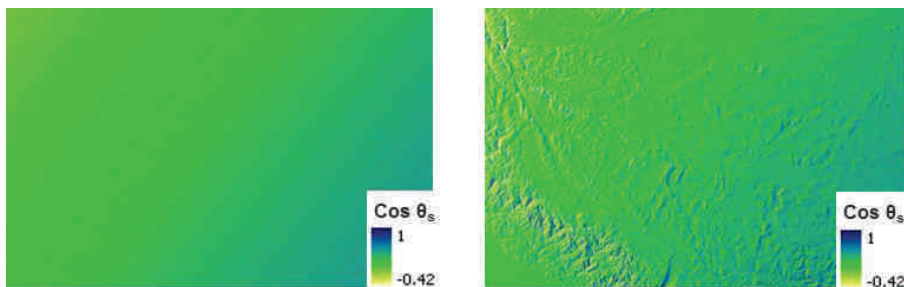


Figure 3.8: Computation of the solar zenith angle (left) or the sun incident angle (right)

The model principles presented in section 3.6 are applied in an operational tool providing radiative fluxes data at high spatial resolution and high temporal frequency to allow a daily monitoring of solar radiation budget over the Tibetan Plateau (Figure 2.1). Using the database built with the required gap filled MODIS products (section 2.4.1), a time series of daily at-surface solar radiative fluxes from 2008 to 2010 was produced at the square kilometer. Figure 3.9 shows the 3-year time series of instantaneous solar downwelling and upwelling radiative fluxes estimated for the 4 pixels corresponding to the 4 ground stations, namely BJ, Linzhi, NamCo and Qomolangma (noted as Qomo), which

data were used further on for validation (Chapter 2). The instantaneous values are estimated at satellite overpass time which is between 10.30 and 11 am local time depending on the day.

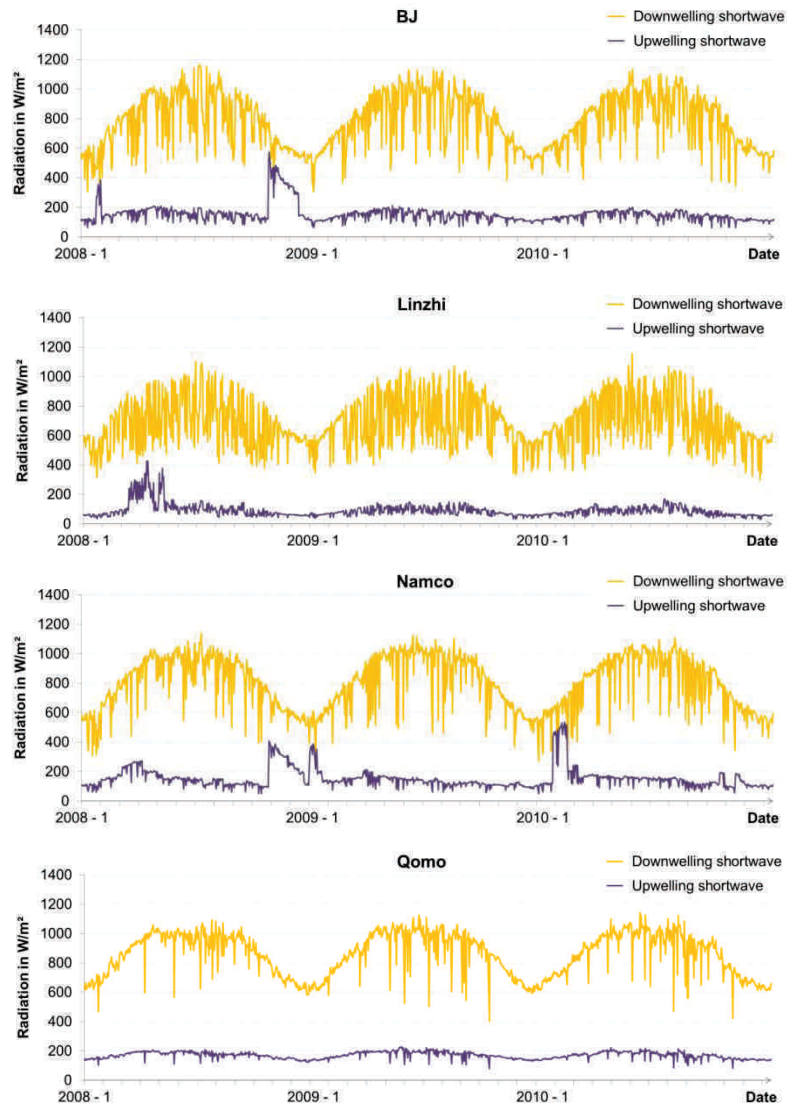


Figure 3.9: Time series of instantaneous solar downwelling (yellow) and upwelling (purple) radiations for the pixels in which the ground stations used for the validation are located: BJ, Linzhi, NamCo and Qomolangma

The radiative flux estimated at BJ, Linzhi and NamCo fluctuates more than the one obtained over Qomolangma. One of the reasons could be the lower yearly cloud fraction recorded over Qomolangma, according to the MODIS cloud products. For Qomolangma, the averaged cloud fraction over the three years is about 29%, while it is around 42%, 80% and 46% for BJ, Linzhi and NamCo respectively. Some sudden increases in upwelling radiation are also observed for BJ, Linzhi and NamCo stations. As the upwelling fluxes are derived using the MODIS albedo product (Figure 3.6), those increases are directly linked to increases of the retrieved albedo values. Figure 3.10 provides the time series of MODIS albedo values (MOD43B3) for the same period and locations. From this figure, the same jumps are identified in the time lines. Those high values of surface albedo may be caused by the presence of snow on the ground. Surprisingly, no jump is observed for Qomolangma where snow events usually occur between mid-October and mid-May. This may be due to the fact that it rapidly melts after snowing and seldom last more than one day (Wang Zhongyan, personal communication, March 31, 2015). Thus, the MODIS albedo product, which is a 8-day product, seems to miss those snow events as at least 8 individual days of snow were recorded at the station between mid-2008 to the end of 2010.

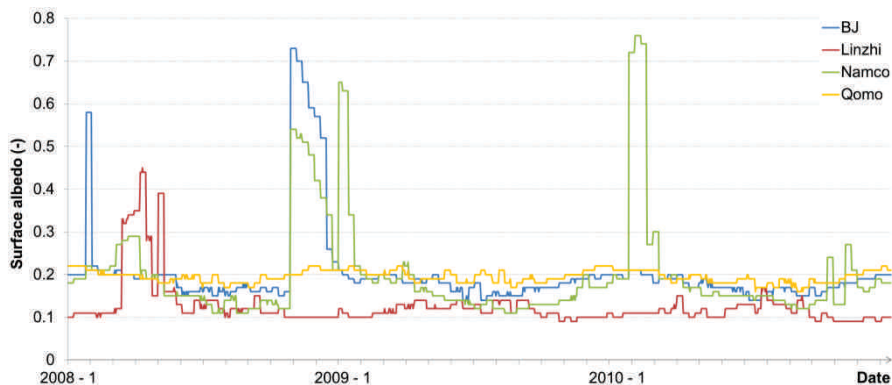


Figure 3.10: Time series of surface albedo derived from MODIS (MOD43B3) over the four ground stations used for the validation: BJ (blue), Linzhi (red), NamCo (green) and Qomolangma (yellow)

The radiative fluxes estimates are validated using the ground measurements recorded at the four stations from 2008 to 2010, considering all skies and clear sky days separately. The distinction between clear sky and cloudy conditions is made on the basis of the cloud fraction provided by MODIS. Some incoherent values were observed in the ground measured upwelling fluxes, then the data have been filtered which also masked out some possible snow events. The validation results are presented in the scatter plot in Figure 3.11 to 3.14.

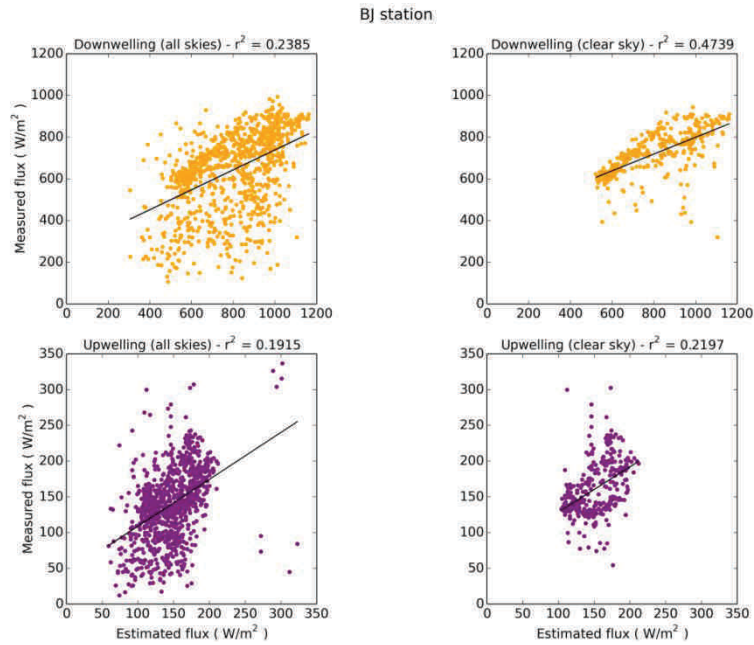


Figure 3.11: Solar radiation validation for downwelling (orange) and upwelling (purple) fluxes, for all skies (left) or clear sky (right) conditions, at BJ station for the entire time series

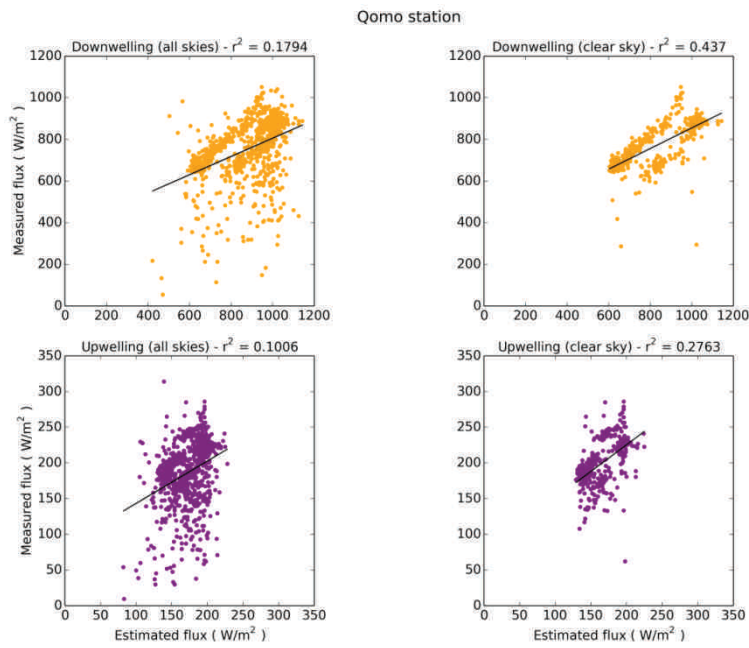


Figure 3.12: Solar radiation validation for downwelling (orange) and upwelling (purple) fluxes, for all skies (left) or clear sky (right) conditions, at Qomo station for the entire time series

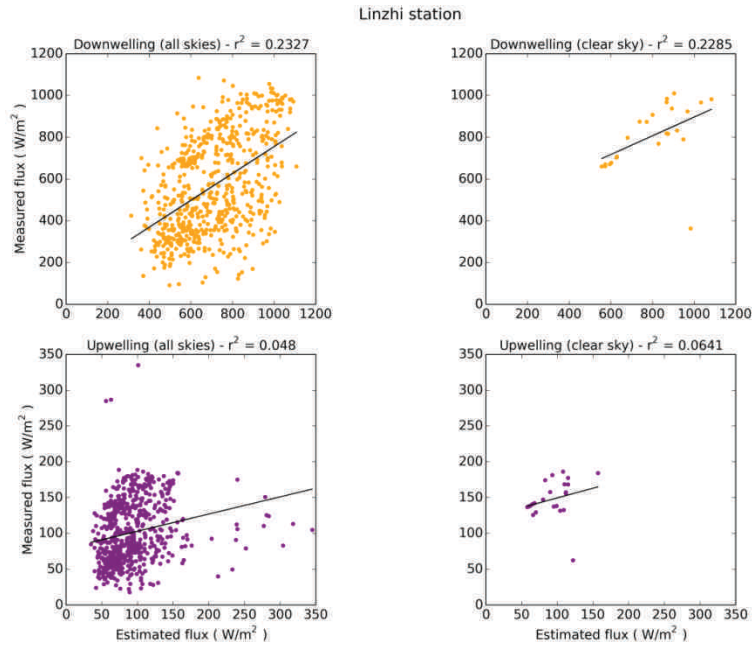


Figure 3.13: Solar radiation validation for downwelling (orange) and upwelling (purple) fluxes, for all skies (left) or clear sky (right) conditions, at Linzi station for the entire time series

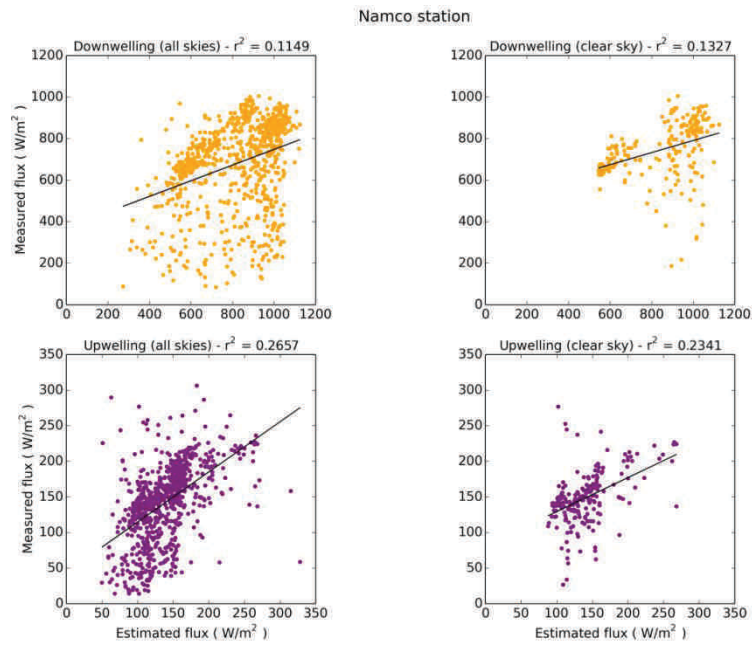


Figure 3.14: Solar radiation validation for downwelling (orange) and upwelling (purple) fluxes, for all skies (left) or clear sky (right) conditions, at NamCo station for the entire time series

The results presented in Figure 3.11 to 3.14 show that when estimating shortwave surface irradiance, better results are obtained for clear sky conditions, except for the Linzhi and NamCo stations (Figures 3.13 and 3.14) where the correlation remains low for both sky conditions. For the specific case of Linzhi, it is important to underline that only 14 clear sky days were available for validation which explains the small difference between clear sky and all skies results.

Even if better results are obtained for clear sky conditions, the correlation between estimated and measured surface irradiance is quite low. The inaccuracy observed in the estimation of the downwelling shortwave radiation can be partially explained by the fact that some of the data used in the computation of the atmospheric transmissivity are scarcely available over the Plateau (Table 3.1). Then, the missing data need to be replaced by less accurate estimates, like weekly or monthly averaged values, knowing that the quality of the output is directly linked to the quality of the input data. From Table 3.1, it appears clearly that the most problematic atmospheric variable is the AOD. However, due to the high altitude of the Tibetan Plateau, the atmosphere is thin and the AOD is very small over that area (Xin et al. 2007). This can also be the reason for the important rate of missing data, *i.e.* the particular conditions of the Plateau may go beyond the limits of the AOD retrieval algorithm. Furthermore, except after a sand storm in the Gobi area, a limited variation in aerosol load was observed (Xia et al. 2008). Then using monthly estimates should not be critical in this case.

Table 3.1: Percentage of missing data for some randomly chosen day of the year for each of the atmospheric products used in the atmospheric transmissivity factor calculation

	<b>2008</b>	<b>2009</b>	<b>2010</b>	<b>Comments</b>
<b>Surface pressure</b>	2.2% (+/- 0.6%)	2.4% (+/- 3.2%)	2.2% (+/- 0.6%)	Gaps between tiles
<b>Precipitable water</b>	3.7% (+/- 2.8%)	4.1% (+/- 4.4%)	4% (+/- 3.4%)	Gaps + missing data
<b>Total ozone</b>	50% (+/- 12.6%)	48.9% (+/- 12.3%)	50.3% (+/- 12%)	Missing data
<b>AOD</b>	84.5% (+/- 4.9%)	83.9% (+/- 4.6%)	84.7% (+/- 4.6%)	Missing data

Another reason for the low correlation between the estimated and the ground measured fluxes is linked to the validation method. Indeed, the temporal resolution and spatial footprint of the two compared datasets may cause large errors. First, the difference between the MODIS and the ground stations temporal frequency can generate part of the observed differences. The time used in the computation is the one provided by the land surface temperature MODIS product and corresponds to the exact satellite overpass time. The ground datasets used for the validation provides a measurement every 30 minutes corresponding to an integration of measured radiation over that period. As the cloud cover

at a specific location can evolve rapidly, its impact on data integrated over 30 minutes can be important (Chapter 4). This error adds up to the error due to the inaccuracy of the computation. Second, it is necessary to assess the impact of the spatial footprint when validating a variable estimated from remote sensing with ground measurement. As shown in Figure 3.15, the stations are located within pixels comprising several land cover types. Then the measurements collected at the stations are not representative of the pixel heterogeneity. Several studies stressed that a direct comparison is very challenging because of this scale issue and the heterogeneity of the land surface at the satellite spatial resolution that reduces the spatial representativeness of ground point measurements (Liu et al. 2010; Liang et al. 2010; Cescatti et al. 2012).

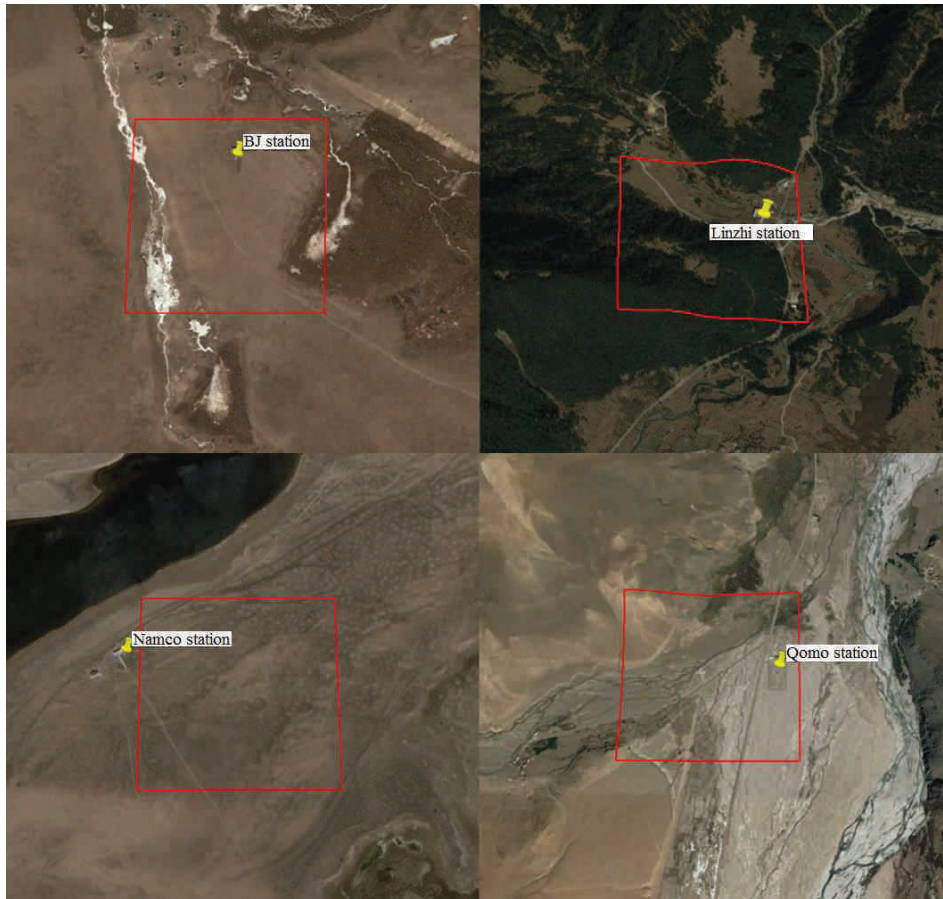


Figure 3.15: The four ground stations location on the Tibetan Plateau (yellow pin) and the footprint of the pixel used for the validation (red lines)

To deepen the validation of the solar radiation budget time series, a comparison with satellite data at the same spatial resolution is performed. This validation method allows to overcome the footprint issue mentioned above. The main objective here is to verify if the retrieval of the atmospheric transmissivity for the estimation of surface irradiance is accurate. To do so, the surface irradiance is estimated following the proposed method. Next, the surface reflectance provided by MODIS products is used to compute the surface (BOA) upwelling radiance. The latter is then converted to TOA upwelling radiance using atmospheric transmissivity values computed with the same approach but for the view zenith angle instead of the sun zenith angle. Finally, the estimated TOA upwelling radiance is compared to the TOA upwelling radiance measured by MODIS. The atmospheric transmissivity and the surface irradiance being estimated broadband, a prerequisite to this comparison is the conversion of the spectral reflectance and radiance data provided by MODIS to broadband estimates (section 2.5.2). The validation is performed over the study area subset (Figure 2.2) and over the whole year 2010, considering only clear sky days. The results of the comparison are presented in Figure 3.16.

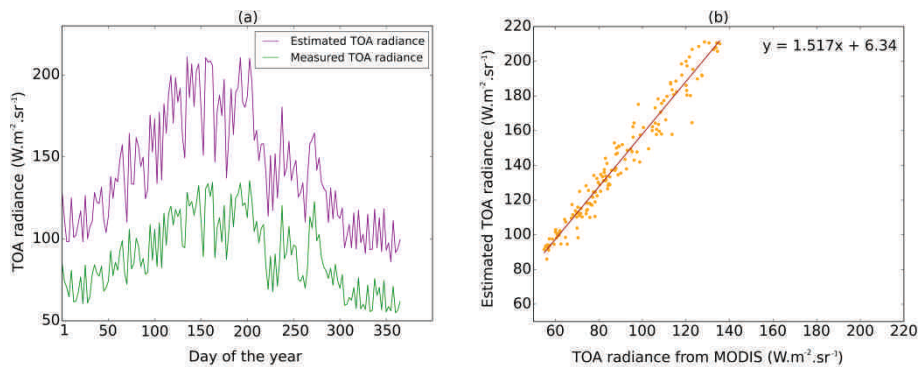


Figure 3.16: Comparison between TOA upwelling radiance estimated using MODIS surface reflectance and TOA upwelling radiance measured by MODIS sensor: (a) mean TOA upwelling radiance estimated (purple) and measured (green) for the entire study area; (b) the regression between the both mean TOA upwelling radiance

This comparison highlights a constant shift between the estimated and the measured TOA upwelling radiance. This is confirmed by the equation of the regression which shows a slope of 1.517 and an intercept very close to 0. There are two potential reasons for this shift. First, the assumptions made to convert the measured spectral radiance to broadband radiance could lead to an underestimation of the broadband radiance. As the land cover is

relatively stable over the test area, this underestimation could generate a constant bias. Second, the atmospheric transmissivity computed by MODIS to retrieve the surface reflectance is lower than the one estimated with the approach proposed in this chapter. In this thesis, the atmospheric transmissivity for clear days is around 0.9 which is confirmed by the data measured at the ground. It is also possible that those two potential errors add to each other. However, this comparison shows that the way the atmospheric transmissivity is modelled in the proposed method is providing suitable results for clear sky days and confirms that the problem mostly come from cloudy conditions. Thus, as the clear sky atmospheric transmissivity is correct, the surface irradiance retrieved for clear sky condition is also correct. Then, the low accuracy observed for the estimated upwelling radiance under clear sky conditions (Figure 3.14), is probably caused by the MODIS albedo product. This is supported by the fact that the ground validation shows that the overall estimates of upwelling radiance are worse than estimates of downwelling radiance with no correlation between the ground measurements and the estimates. The ground validation of the upwelling fluxes also shows that NamCo and BJ present a bit better estimates than Qomo and Linzhi, which are both located in rougher areas where albedo estimates from satellite are often less accurate. Furthermore, the albedo product from MODIS provides a value every 8 days, which may be a temporal resolution too coarse for the daily monitoring of radiative fluxes over the Tibetan Plateau which often undergoes fast changes.

When checking visually the time series outputs, it appeared that, for some days and in area where the slope is very steep, some pixels present extreme values. One of the reasons is that the algorithms used in this method have been developed and tested on more homogeneous areas than the Tibetan Plateau and then the specificities of the Plateau go beyond their range of operation. However, those extreme values represent a small amount of pixels (less than 2% of the entire image) and, in the developed tool, are filtered out and replaced by the average of the surrounding pixels values.

### 3.8 Conclusion

The method proposed in this chapter allows to model the solar radiation budget instantaneously and daily, at the square kilometer level over the entire Tibetan Plateau using MODIS data products. Even if the overall accuracy is not better than already existing products, this method provides solar radiation estimates at the square kilometer level on a daily basis - key input for further use in climatic models – whereas the other net radiation datasets covering that area provide the same estimates but at coarser spatial or temporal resolution. Furthermore it uses the local solar incident angle in the computation of irradiance while the terrain geometry is often neglected.

The method was tested and used to produce a 3-year time series, from 2008 to 2010. As for other large scale solar radiation budget products, the validation remains an

issue and shows some discrepancies with the ground data. To overcome this problem, a sensor comparison was also performed to evaluate the proposed method. It appears that a large part of the errors is due to the inaccuracy of the inputs and to the integration of the clouds. Thus, the estimation of the solar radiation budget should be improved considering two main aspects. First, the largest errors are observed for the upwelling radiations, especially over areas with important topography, which is directly related to the estimation of the albedo. Then, some effort should be put in the integration of the topographic effects when retrieving albedo from space, especially considering the sub-pixel variability as the estimation of albedo is performed at the kilometric resolution. In addition, the temporal resolution of the albedo data should also be refined, as pointed out with the missed snow event at the station of Qomolangma. Second, the estimation under cloudy conditions is not providing good results due to the inadequacy of the cloud cover parameterization. Further investigation on the impact of spatial and temporal variability of the clouds on solar radiative fluxes should be conducted. It is also of interest to mention the lack of AOD data pointed out by the validation. However, as the AOD is very low and quite constant over the Tibetan Plateau and that the clear sky atmospheric transmissivity is properly retrieved by the proposed method, no further investigations are performed on that aspect in this thesis. Furthermore, Hansen et al. (2002) showed that, in case of strong relief, the topography has a greater effect on the net solar radiation than a lack of atmospheric correction.

Considering the issues pointed out by the validation, improvements are proposed in the following chapters to deal with the sub-pixel variability aspect related to clouds and topography.

## **Chapter 4**

# **Impact of spatial and temporal variability of clouds on solar radiation: a case study**

### **4.1 Introduction**

The cloud cover is a fundamental parameter influencing the solar radiative fluxes at the ground as it can significantly impact the partitioning between direct and diffuse radiation (Cess et al. 1995). Additionally, the cloud cover evolution during the day directly impacts the sunshine duration estimation commonly used to convert instantaneous to daily solar radiation. Even if several parameterization schemes exist to model the impact of clouds on radiative fluxes (Holloway et al. 1971; Stephens 1978; Stephens et al. 1984; Slingo 1987; Randall 1989; Harshvardhan 1995), the clouds are still responsible for the largest errors in climate modeling (IPCC 2007; Randall et al. 2003). The properties as well as the amount and distribution of the clouds are important to consider when taking into

account their effects on radiative fluxes. As the approach to take into account the clouds in the method proposed in Chapter 3 does not provide satisfying results, this chapter investigates the impact of spatial distribution and temporal variability of cloud cover on solar radiation in order to provide some leads on how parameterization of cloudy conditions for solar radiation budget estimation could be improved.

Because of their high spatial and temporal variability, the definition and detection of clouds represent a hard task especially when using satellite data (Silva et al. 2013). The spatial distribution of the clouds is often summarized by pixel as estimated cloud fraction and the daily temporal variability of the clouds is roughly derived from few measurements over the day. Another issue when using satellite data is the difficulty to determine solar obstruction accurately for a specific site due to uncertainties in cloud height and depth retrievals (Ghonima et al. 2012). On the other hand, the cloud cover information provided by operational weather stations remains poorly documented. A common numerical representation of cloud cover is the octa, derived from visual observation from experimented operators. This index gives very little time granularity - usually one instantaneous observation, hourly - and no guarantee that such observations can be replicated from an operator or station to another (WWRP (World Weather Research programme) 2012).

A local experiment conducted at the ground was set up to collect quantitative information on both spatial distribution and temporal variability of the clouds. Those data were used to explore the impact of clouds spatial organization on solar radiative fluxes and to measure the sensitivity of sunshine duration estimation to the measurement temporal frequency. Dedicated commercial sensors have been designed to evaluate cloud cover from the ground, but remain expensive. In this work, an operational approach was developed to capture short term variation of the cloud cover with a simple and low-cost combination of hardware. Although this thesis focuses on solar radiation, longwave fluxes measured at the ground are used in this chapter for validation purposes.

First, the optical setup used for the data collection and the pre-processing steps are presented. Then, a short state of the art is provided followed by the description of the image classification and cloud indices extraction processes. Next, some results on the classification accuracy and the correlations with the radiative fluxes as well as the investigation on sunshine duration and radiative fluxes temporal aggregation are presented. Finally, some conclusions are provided.

## 4.2 Fieldwork set up and data calibration

### 4.2.1 Measurement set up

Hemispherical images taken from the ground provide suitable quantitative information on both spatial distribution and temporal variability of the clouds over a large field of view (FOV). Several types of instruments, from commercial to experimental, are currently used to collect hemispherical images of the sky. Two main instrumentation setups can be found: (1) a CCD (Charged Coupled Device) mounted with a fisheye lens looking toward the sky (*e.g.* Whole Sky Imager (Shields et al. 1993)) or (2) a CCD looking down at a convex mirror (*e.g.* the Total Sky Imager (Long et al. 2001)). In most cases, the CCD is recording in the red-green-blue (RGB) channels and sometimes also in the near infrared. A good overview of the ground-based automatic imagers that have been in operation around the world for the determination and assessment of cloud cover is provided in Tapakis et al. (2013).

The instrumental setup presented here is composed of a standard reflex CCD camera (Canon EOS 350D) recording in the Red-Green-Blue (RGB) spectral bands, with two optical lenses: a Canon EF-S 18-55 zoom lens and an Opteka HD<sup>2</sup> fisheye lens with a view angle of about 140°. The latter is mounted on the first using a standard 58 mm mounting ring. A remote control is used to automate image acquisition at a constant time step, a camera specific adapter ensures continuous power supply, and the whole system is conditioned in a weatherproof box with a glass hemisphere (Figure 4.1). The whole system is oriented in such a way that, once the camera is pointing to the sky, the bottom of the camera is heading south and the system remains perfectly horizontal. The aperture of the camera is set constant for a given day of acquisition to either  $f/18$  or  $f/22$ , while the time of exposure is automatically set by the camera depending on lighting conditions.



Figure 4.1: Instrument set up to record the hemispherical images (front) and net radiation instrument to record the radiative fluxes (back) at the NamCo station

Various tests performed in the design phase of this experiment showed this setting to give a higher flexibility since: (1) the time of exposure dynamic is much larger than the aperture one, ranging from 1/3000 to 5 seconds; (2) a long exposure time does not lead to significant blur effects during dawn and sunset except with very low clouds and strong wind; (3) the diffraction effect induced by small aperture does not visually affects the sharpness of the images.

#### **4.2.2 Raw images**

The implemented set up acquired raw images at a 10 seconds frequency. Although such a frequency is far higher than the usual frequency of acquisition of radiation data, it allowed to ensure a proper monitoring of the spatial and temporal variability of the clouds, and to resample the data collected adequately. For data processing reasons, only one image every 30 seconds has been used during the analyses presented in this chapter.

A raw image is shown on Figure 4.2. It consists of an array of size [1728;1152] where black pixels belong to the optical hardware and were disregarded in further analyses, while the round image shows a clear view of nearly the entire hemisphere. Assuming a tropopause at 5 km above ground (Tibet mean elevation being over 4000 m), the hemisphere is roughly 17 km wide, the FOV being 120°. Depending on the solar exposure, additional chromatic aberrations may appear beyond the edge of the field of view of the fisheye (in light grey on the lower right side of the circle on Figure 4.3), and do not affect the quality of the processed image. Each image is saved as JPEG with the lowest compressing ratio, together with standard EXIF metadata to ensure a proper recording of the time stamp.



Figure 4.2: An example of raw hemispherical image

### 4.2.3 FishEye calibration

Prior to process the images, a geometrical calibration of the whole system is performed to determine the polar coordinates of each pixel. The methodology used here follows the one presented in the CAN-EYE user manual (Weiss et al. 2010). For the specific combination of lenses used here, it was required to build a calibration bench, to take a series of pictures to accurately determine the optical center in terms of pixel coordinates on an image and to measure the optical distortions from the focal axis to the edge of the field of view of the fisheye lens. A polynomial fitting is then obtained to convert from pixel to polar coordinates (Equation 4.1). The convention applied here is: (1) azimuthal angles  $\phi$  are expressed as such that  $0^\circ$  is north, and (2) zenith angles  $\theta$  are expressed such that nadir is  $0^\circ$ , while elevation is expressed as 90 minus the zenith angle.

$$R_D = 7e^{-8} R_P^3 - 1.152e^{-5} R_P^2 + 1.0871751e^{-1} R_P \quad 4.1$$

with  $R_D$  and  $R_P$  being the distance to the optical center in degree and pixel respectively.

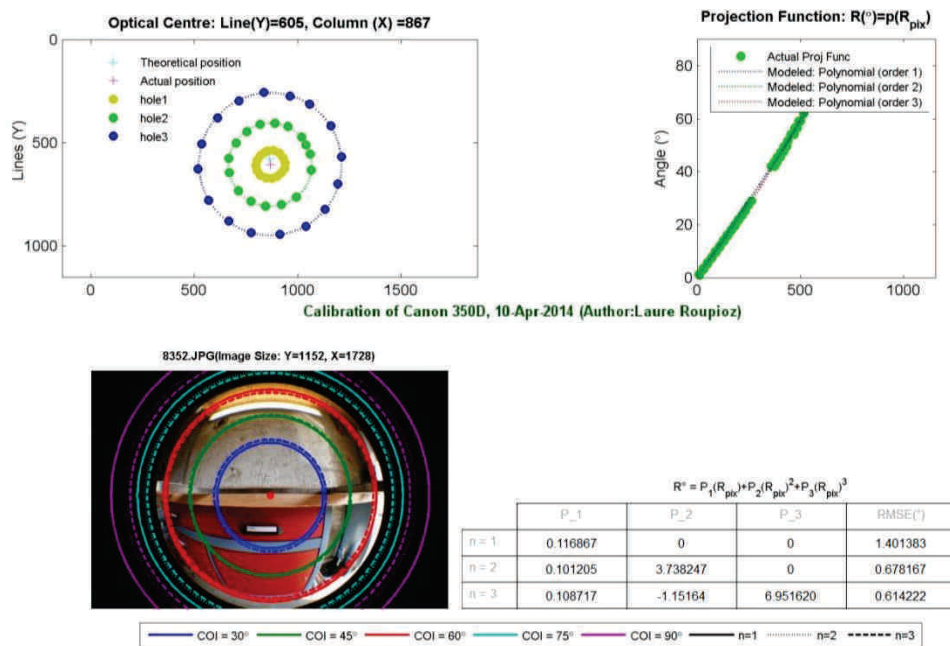


Figure 4.3: Can-Eye calibration module output with the optical center estimation (top left), the projection function (top right), the polar distances from the optical center (bottom left) and the regression RMSE (bottom right)

The regression performed for the polynomial fit leads to a root mean square error (RMSE) of  $0.614^\circ$  which correspond to about 6 pixels at nadir and 3.7 pixels on the edges, knowing that the size of the pixel increases with the distance from the nadir. To give an order of magnitude, an uncertainty of  $0.614^\circ$  would lead to an error in estimating the position of a cloud located 3,000 meters above the camera of about 32 meters at nadir. It is important to quote that this uncertainty will be added to the other experimental errors, *e.g.* errors in locating the optical focal center on the images or slight variations of the orientation of the camera in the field, which are both hard to evaluate. However, the calibration method applied here provides satisfying results for this study as the sum of potential errors does not significantly affect either the extracted clouds indices or the identification of the sunspot based on geometrical computation (section 4.3.1).

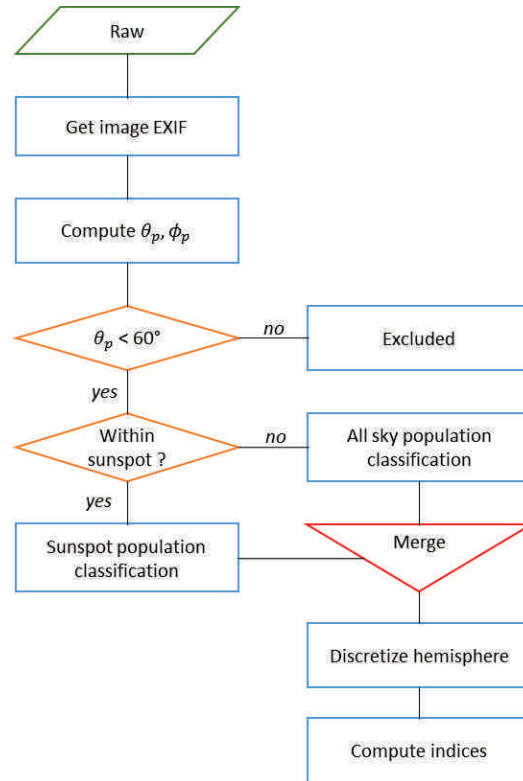
It should be noted that geometrical and chromatic aberrations become significant for pixels near the edge of the field of view of the fisheye, as quoted in Silva et al. (2013). Therefore, pixels corresponding to zenith angles larger than  $60^\circ$  are neglected in later analyses. Other chromatic aberrations may also occur depending on the quality of the hemispheric glass protecting the lens, leading to small prism effects under direct solar radiation.

To derive quantitative information on both spatial distribution and temporal variability of the clouds from the hemispherical images, the proposed methodology starts with the classification of the images pixels as clear sky or clouds. Then, integrating the calibration function, the indices characterizing the cloud cover are extracted (Figure 4.4). After evaluation of the accuracy of the classification, the indices can be used to explore the impact of clouds spatial organization on solar radiative fluxes and to measure the sensitivity of sunshine duration estimation to the measurement temporal frequency.

#### **4.2.4 Hemispherical images classification**

The classification phase is a fundamental task for further application because it is the precondition for deriving information, such as cloud fraction, cloud type and cloud brokenness (Long et al. 2006). Therefore, some efforts have been put in this thesis to establish a robust classification method to retrieve accurate quantitative information about cloud spatial distribution and temporal variability. The processing sequence for the image classification phase is as follows:

- (1) Separation of the image pixels in two populations: within or outside of the sunspot
- (2) Pre-processing of a band or combination of bands as an input for classification
- (3) Classification of each population in either clear sky (0) or clouds (1)

Figure 4.4: Hemispherical processing steps for a pixel  $p$ 

Hiding the sunspot from the view of the camera using a shadow band or shadow ball requires dedicated hardware and leads to lost pixels (Long et al. 2006). Here the sunspot is part of the image, as in Heinle et al. (2010), Kazantzidis et al. (2012) and Fu et al. (2013). Whether the sun is visible or not, the distribution of pixel values for a band or combination of bands will strongly vary. Despite direct exposure to the sun, the CCD only saturates in the sunspot, and the overall image dynamic is preserved. However, as suggested by Calbó et al. (2008), separating pixels in two populations according to the distance to sun center improves classification results. Hence the exact sun location is computed from the location of the camera and the timestamp of a given image extracted from the EXIF meta-data. The diameter of the sunspot is fixed and slightly larger than the actual one to compensate for errors due to: (1) uncertainties in the horizontality and orientation of the instrument; (2) uncertainty in the timestamp provided by the camera clock, while limited when synchronized with a GPS clock. The pixels included in the sunspot are classified separately.

#### 4.2.4.1 *State of the art*

The most commonly used camera's RGB bands combination to detect clouds from hemispherical images is the red-blue ratio ( $RB_R$ ) (Shields et al. 1993; Li et al. 2011; Long et al. 2006; Kreuter et al. 2009; Ghonima et al. 2012). Some studies also showed the relevance of using only the red band (Ferreira et al. 2010), the normalized sky index (Yoshimura et al. 2013; Tohsing et al. 2014), the brightness index (Yoshimura et al. 2013) or the red minus blue difference (Heinle et al. 2010). The conversion of the original image from the RGB to HSV (Hue Saturation Value) color space is also suggested by Martins et al. (2003) and Souza-Echer et al. (2006), since the saturation layer can help to discriminate between open sky and cloudy pixels.

Once the band pre-processing is performed, there are several techniques to separate clear sky from cloudy pixels. Some studies used a fixed threshold derived from statistics or defined manually (Souza-Echer et al. 2006; Long et al. 2006; Ferreira et al. 2010; Silva et al. 2013). Other studies utilize comparisons with pre-computed reference library (Shields et al. 1993; Kreuter et al. 2009; Ghonima et al. 2012). There are also more complex classification methods based on neural networks (Cazorla et al. 2008; Ferreira et al. 2010; Gonzales et al. 2012), binary decision tree (Buch et al. 1995), multi-criterion analysis (Kazantzidis et al. 2012) or multidimensional Euclidean geometric distance and Bayesian methods to classify image pixels based on cloud and sky patterns (Neto et al. 2010). Finally, Li et al. (2011) developed a hybrid thresholding technique (HYTA) that is based on both fixed and adaptive thresholding techniques for cloud detection. Some authors improved their results by using different thresholds according to the relative position between the pixel and the sun in order to take into account the angular dependence of the scattering processes and the effects of the increased path length with increasing solar zenith angle (Long et al. 1998; Pfister et al. 2003; Kazantzidis et al. 2012). Shields et al. (2010) also added an adaptive thresholding technique to take into account variations in haze amount in real time.

According to the instruments characteristics and the method applied for the cloud detection, different levels of classifications can be reached. The simplest classifications identify the pixels as cloud or clear sky. Some methods sub-classified the cloudy pixels as either thin or opaque (Pfister et al. 2003; Crispim et al. 2008; Ghonima et al. 2012). Some attempts have also been made to develop algorithms for cloud type classification (Long et al. 2006; Calbó et al. 2008; Heinle et al. 2010), estimation of cloud base height (Kassianov et al. 2005) or identification of high and low clouds (Cazorla et al. 2008). Calbó et al. (2008) showed that it is possible to recognize different cloud types from processing digital images taken by sky cameras using features based on statistics and Fourier transform. Heinle et al. (2010) presented a cloud classification algorithm based on a set of mainly statistical features describing the color as well as the texture of an image and using a k-

Nearest-Neighbor (kNN) classifier. They distinguished seven different types of sky conditions (cumulus, cirrus and cirrostratus, cirrocumulus and altocumulus, clear sky, stratocumulus, stratus and altostratus, cumulonimbus and nimbostratus).

#### 4.2.4.2 Classification method

Many studies highlighted the fact that the band - or bands combination - to be used and the determination of the threshold values depend on the digital camera (*e.g.* the color response of the CCD sensor) and of aerosol conditions (Kazantzidis et al. 2012; Long et al. 2006). Thus, prior to the classification, an analysis of the proper CCD band or bands combination to be used is performed to find the most suitable approach for the cloud detection. A preliminary analysis on a variety of cloud coverage situations shows that, with the CCD used for this study: (1) the red band usually provides most of the information as compared to red on blue indexes; (2) the saturation layer usually gives similar results as the red band, while requesting additional processing and being more sensitive to aerosols (Figure 4.5). In Figure 4.5, the red band clearly provided the highest contrast whatever the cloud conditions. The images provided by the saturation (sat) also show a good contrast but more noisy results over clear sky. In the analyses presented here, the red band is used after stretching the histogram and normalizing values. A gamma correction did not enhance the band contrast and is not used here.

The classification of images into clear sky and cloud pixels can be performed using either supervised or unsupervised classification approaches. However, a supervised approach can hardly be considered operational and most of the studies presented in the previous paragraph are using unsupervised classification approaches. An initial study with a large variety of images taken under different cloud cover and lighting conditions showed that: (1) a bi- or multi-modal distribution can usually be identified on a band or index; (2) a fixed threshold between open sky and cloud populations can give acceptable results for scattered sky conditions (though its value is camera specific); (3) a constant threshold does not give any good results for overcast sky or mixing of low and high clouds (*e.g.* cumulus and fuzzy cirrus). Neto et al. (2010) also concluded that fixed threshold methods are not capable of correctly detecting thin clouds.

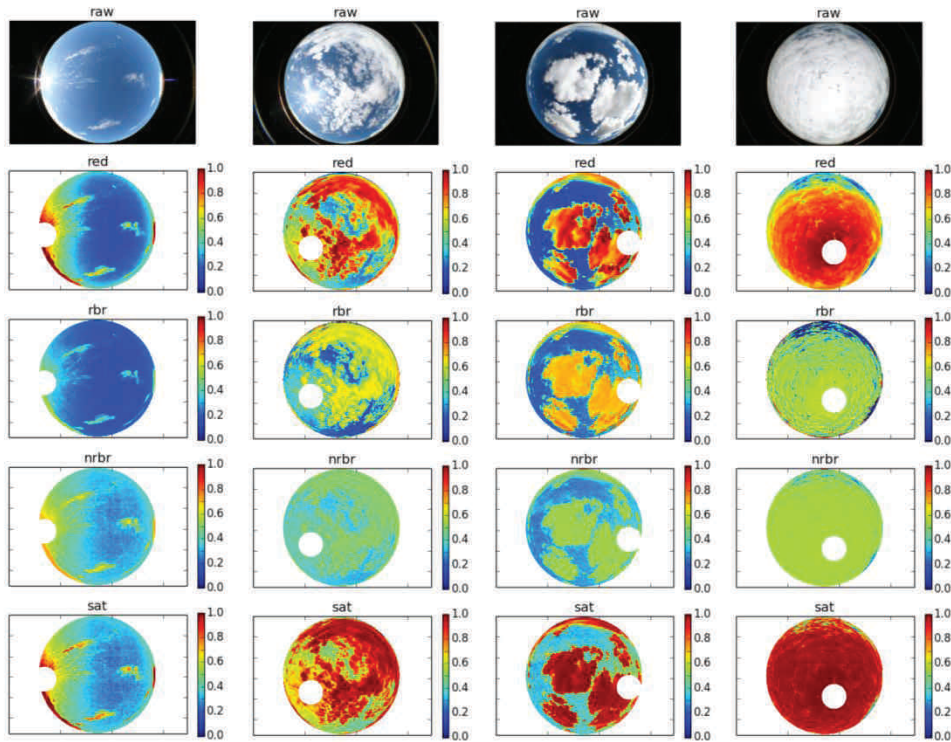


Figure 4.5: Comparison of different band pre-processing (normalized) for cloud classification. Examples are provided for low cloud cover, medium cloud cover with visible sun, medium cloud cover with hidden sun and high cloud cover (from left to right column). The red band, the red/blue ratio (rbr), the normalized red/blue ratio (nrbr), the saturation (sat) are displayed (from top to bottom) and the sunspot is masked

Considering our target acquisition frequency (one image every 10 to 30 seconds), the computation time has to be taken into account. Therefore, a simple histogram based classification is used and the threshold is determined for each image according to the pixel distribution in the red band. Several tests were performed to find the most efficient method to define automatically the threshold between clear sky and clouds, using the detection of the modes in the distribution. From those tests, it appears that setting the threshold as the local minimum between two modes was performing the best (Figure 4.6 and 4.7). Figure 4.6 and 4.7 show the comparison between classifications obtained using split values defined by the local mean and the local median identification. In all the cases, the classifications

based on the local mean provide satisfying results and outperform the ones based on the local median which tend to overestimate the cloud cover.

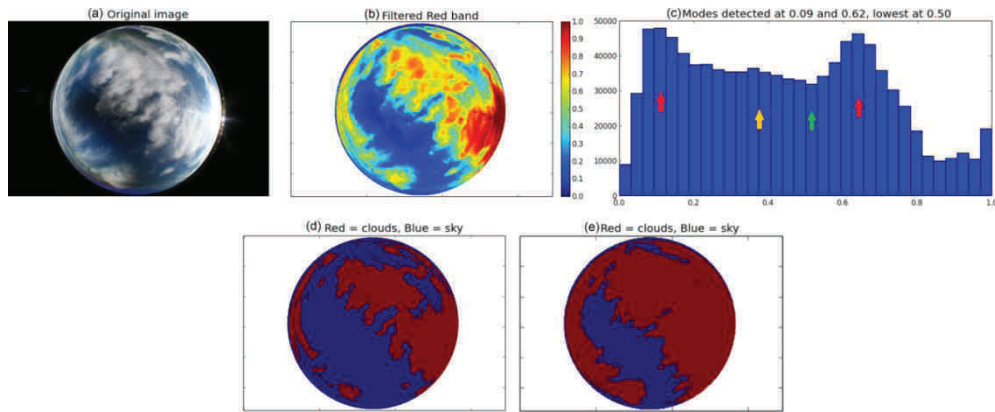


Figure 4.6: Comparison of classifications using split value based on local min or median. (a) Raw image, (b) Red band with histogram stretched, (c) Red band pixel distribution with two modes (red arrow), a local minimum (green arrow) and a local median (orange arrow), (d) and (e) Classified images (clear sky in blue and clouds in red) using local min and median respectively

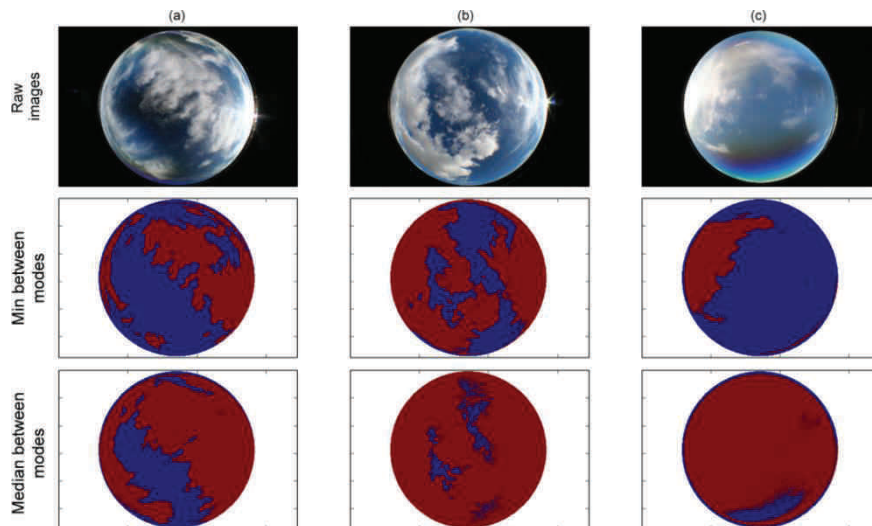


Figure 4.7: Comparison of classifications obtained using split value identified based on local min and median for three different cloud cover conditions (a, b and c)

However, the distribution observed is not always bi-modal, and then a more complex decision tree is developed based on the local minimum identification to cover a larger range of pixel distribution patterns. Finally, two decision trees were applied, one for the pixels located within the sunspot and one the remaining sky (Figure 4.8). Concerning the sunspot area, even if some of the pixels located within the sunspot are saturated, there are some variations. Then, the same classification method is applied but in that case the decision of the classification will classify all those pixels as clear or cloudy, providing information concerning the visibility of the sun.

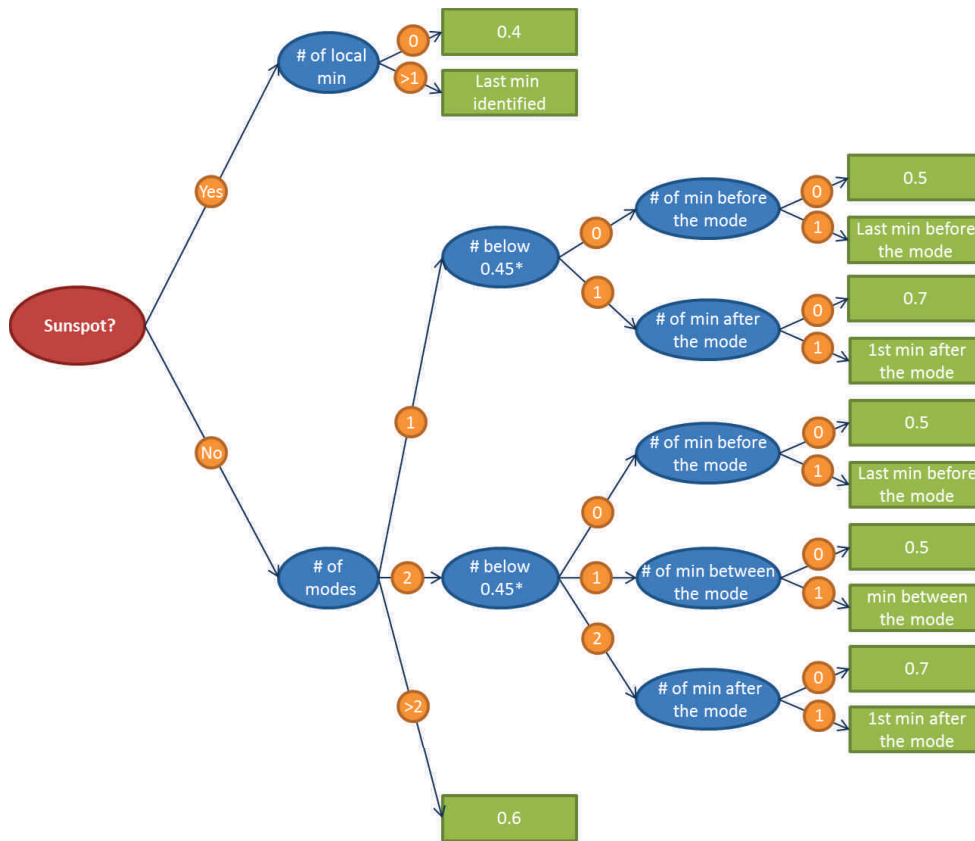


Figure 4.8: Decision tree to define the split value between clear sky and clouds based on the number and location of the modes identified as well as the location of the local minimums (\*Should correspond at least to the 13<sup>th</sup> bin of the histogram, otherwise the limit is set as the value of the 13<sup>th</sup> bin)

#### 4.2.5 Cloud cover indicators

Once the hemispherical images are classified, it is possible to derive several indices to describe the cloud cover variability. Two types of indices can be derived: the indices that are already usable products as such for other applications and the indices that would be potentially useful to correlate with ground measurements to analyze the impact of cloud cover on radiative fluxes. As output of the classification, two indices have been extracted:

- Cloud fraction
- Cloud distribution

In this study, several ways to calculate the cloud fraction have been experimented. The first one is the most used cloud fraction  $C_{fT}$  which corresponds to the total number of cloudy pixels divided by the total number of pixels, including the pixels within the sunspot. The same total cloud fraction has been calculated but excluding the pixel within the sunspot, and is noted  $C_{fS}$  hereafter. Those two cloud fractions quantify the amount of clouds over the hemisphere but do not account for their spatial distribution. Another cloud fraction, noted  $C_{fD}$  was calculated integrating a weight factor ( $W_S$ ) according to the distance of the clouds from the sunspot ( $D_S$ ). In that case, the spatial distribution of the clouds is taken into account as the closer the cloudy pixels are from the sunspot the higher weight value they have. A similar cloud fraction has been computed but weighted ( $W_N$ ) according to the distance to the nadir ( $D_N$ ), and is noted  $C_{fN}$  hereafter. The weighting factors are computed according to Equations 4.2 and 4.3 using distance in pixels. All these cloud fractions are taking into account the fisheye distortions.

$$W_S = 1 - (D_S / \max(D_S)) \quad 4.2$$

$$W_N = 1 - (D_N / \max(D_N)) \quad 4.3$$

The indices to be correlated with the ground measurements have been selected on the basis of existing literature (Pfister et al. 2003; Long et al. 2006; Fu et al. 2013) and according to their potential to relate the cloud cover characteristics to the variations in the radiative fluxes measured at the ground:

- Cloud fractions  $C_{fT}$ ,  $C_{fS}$ ,  $C_{fD}$  and  $C_{fN}$
- Sun visibility
- Cloud brokenness index  $Bi$  (total cloud edge length / total cloud area)
- Mean Red/Blue ratio over cloud or sunspot
- Number of saturated pixels and mean intensity level in sunspot
- Intensity mean and variance over the entire image and over cloudy pixels

## 4.3 Results and validation

### 4.3.1 Cloud classification validation

As mentioned earlier, a proper classification of the hemispherical images is crucial for the extraction of meaningful cloud indices and thus an accurate analysis of the impact of cloud spatial and temporal variability on radiative fluxes at the ground. It is then important to evaluate the accuracy of this classification. The first part of the validation is performed visually, comparing the raw images with the classified ones.

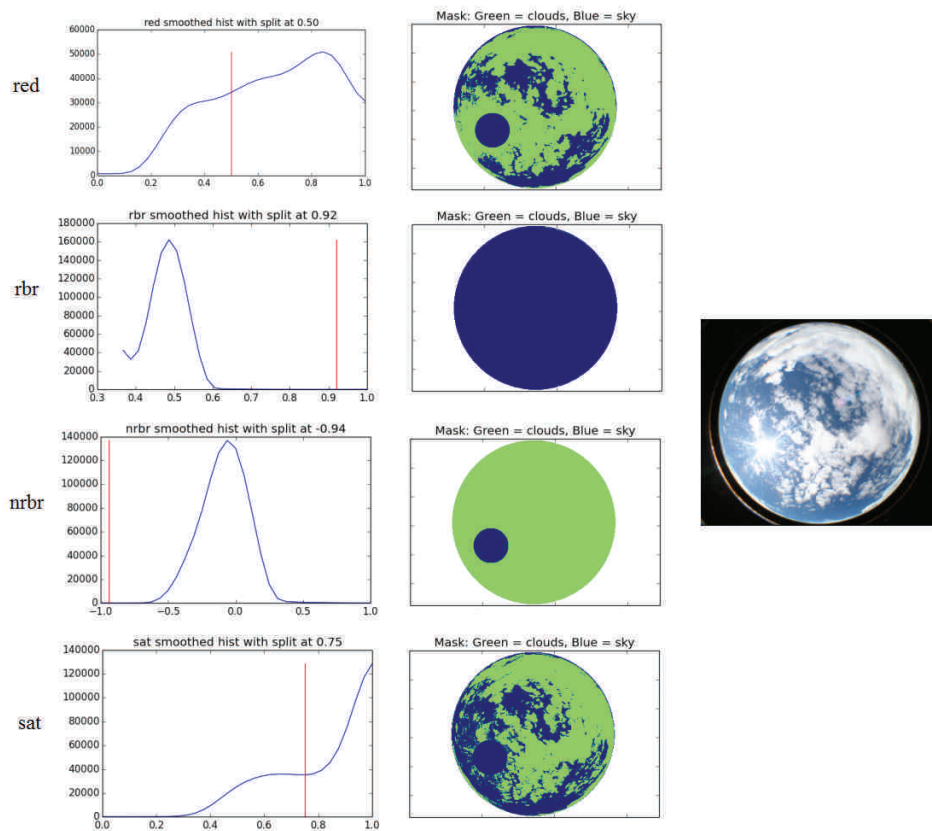


Figure 4.9: Left: pixel distribution plots with classification threshold to cluster pixels into open sky and clouds. Middle: classification mask with the sky in blue and the clouds in green obtained using the red band (red), the red/blue ratio (rbr), the normalized red/ blue index (nrbr) and the saturation band (sat). Right: the original image

Figure 4.9 shows the comparison between different cloud discrimination methods. On the left, the pixel distribution plots are displayed, with the red line showing the value obtained from the automated classification method to cluster pixels into open sky and clouds. In the middle, the classification mask, with the sky in blue and the clouds in green, confirm the comments in section 4.2.4. It highlights that the best results are provided by the red and the saturation methods. From the histogram, it appears that the red and saturation methods provide pixel distribution that allow for a satisfying discrimination between the open sky and cloud population, while the rbr and nrbr show a more unimodal distribution. The total cloud fraction  $C_{fT}$  ranges from 0.64 (red) to 0.6 (sat), the rbr and nrbr index leading to a  $C_{fT}$  of 0 and 1 respectively. The results between the red and sat methods are relatively similar but the red method tends to give larger errors around the sunspot. In some other tested cases, the red and sat methods also provided similar results but, on the contrary, the red method was performing better with thin clouds than the sat method. Then in mixed sky, the two methods both provided satisfying cloud discrimination even if, as Souza-Echer et al. (2006) pointed out, the HSV performs better if no sun is in the field of view. However, it appears that with completely overcast sky, the red method was performing better (Figure 4.10). Also note that the sun was always correctly detected as unobstructed in Figure 4.9 and as obstructed in Figure 4.10.

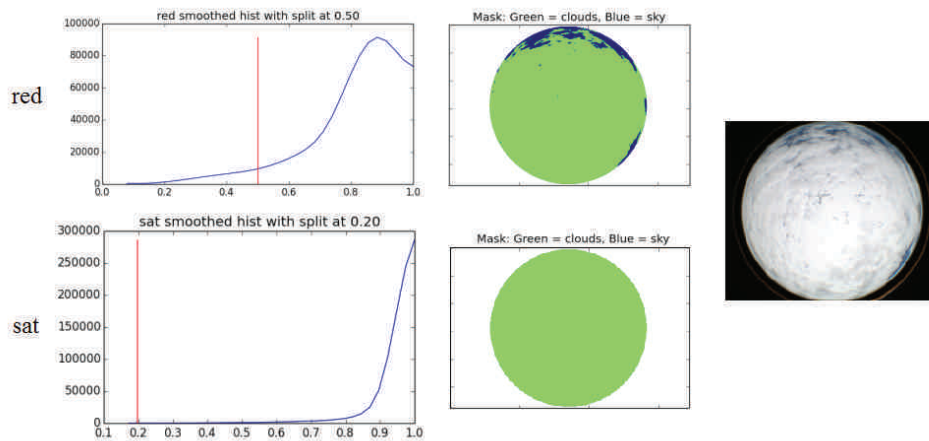


Figure 4.10: Left: pixel distribution plots with classification threshold to cluster pixels into open sky and clouds. Middle: classification mask with the sky in blue and the clouds in green obtained using the red band (red) and the saturation band (sat). Right: the original image

In order to validate quantitatively the classification outputs, a reference dataset is first generated from a set of 107 raw images chosen randomly. These images are classified and controlled manually, providing a validation dataset for a wide range of observed cloud conditions. To perform this validation, the metrics of cloud fraction described in the previous paragraphs are computed for both the raw and reference images. Additionally, the visibility of the sunspot is checked both manually and with the automated approach. The validation has been performed for 4 solar zenith angle ( $\theta_s$ ) settings: (1) Images taken at all solar zenith angles, (2) for solar zenith angle lower than  $75^\circ$ , (3) for solar zenith angle lower than  $70^\circ$  and (4) for solar zenith angle lower than  $65^\circ$ . The results are summarized in Table 4.1, providing the root mean squared error (RMSE) between the cloud fractions derived from the images classified manually and the images classified automatically. From the validation it appears clearly that the best results are obtained for hemispherical images collected when the solar zenith ranges from nadir up to  $75^\circ$ . Limiting the range from nadir to  $70^\circ$  or  $65^\circ$  does not significantly improve the results. Better results are obtained when the solar zenith angle is smaller, *i.e.* when the sun is higher in the sky, because of the minimum illumination conditions required by the camera. When the sun is too low, not enough light is available to get proper images allowing the correct distinction of clouds. Consequently, only images registered when the solar zenith angle is lower than  $75^\circ$  are considered for the rest of the study. The largest errors between the automatic and manual classifications are observed for the unweighted cloud fraction considering the pixels within the sunspot. The best results are observed for the cloud fraction weighted according to the distance to the nadir. This can be explained by the fact that most of the classification errors are usually located on the edge of the hemisphere due to chromatic aberrations or more difficult classification conditions (Pfister et al. 2003; Long et al. 2006; Heinle et al. 2010; Neto et al. 2010). Generally, the weighted cloud fractions  $C_{fD}$  and  $C_{fN}$  provide closer results than the unweighted ones. It is also important to mention that the observed differences are not only due to misclassification by the automatic method. Indeed, the cloud edges are sometimes very blurry in the visible domain and the boundary between clear sky and clouds can be very difficult to detect, even for human eyes (Silva et al. 2013). This is true at the vicinity of the sun as well. Then some errors can be done in the manually classified images concerning the exact limit of the clouds and also about what should be considered as thin clouds or not. In that regards, the automatic method is more consistent and objective and, with a RMSE of maximum 8.3%, provides good results. Especially considering that the cloud cover determination by a human observer, dividing the sky in tenths or octas, has at least 10 % uncertainty for the measurements of cloud cover, except for cloud-free and overcast scenarios (Sabburg et al. 2004; Jeong et al. 2010). However, the results concerning the classification of the sunspot to determine the sun visibility is about 64% of correctly classified cases and will require further improvement.

Table 4.1: RMSE between cloud fractions retrieved from images classified automatically and the same cloud fractions retrieved from images classified manually

	$\theta_s < 90^\circ$	$\theta_s < 75^\circ$	$\theta_s < 70^\circ$	$\theta_s < 65^\circ$
<b>Number of images</b>	107	93	89	84
<b>RMSE of <math>C_{fT}</math></b>	14.6%	8.3%	8.2%	8%
<b>RMSE of <math>C_{fS}</math></b>	14.3%	7.8%	7.8%	7.7%
<b>RMSE of <math>C_{fD}</math></b>	9.1%	5.7%	5.6%	5.5%
<b>RMSE of <math>C_{fN}</math></b>	9%	5.3%	5.3%	5.1%
<b>Direct sun detected (in % match)</b>	63%	62%	63%	64%

When checking the results visually, the main problems observed with the automatic classification are mostly located over and around the sunspot, on the cloud edges, and for the detection of very thin or very dark clouds (Figure 4.11).

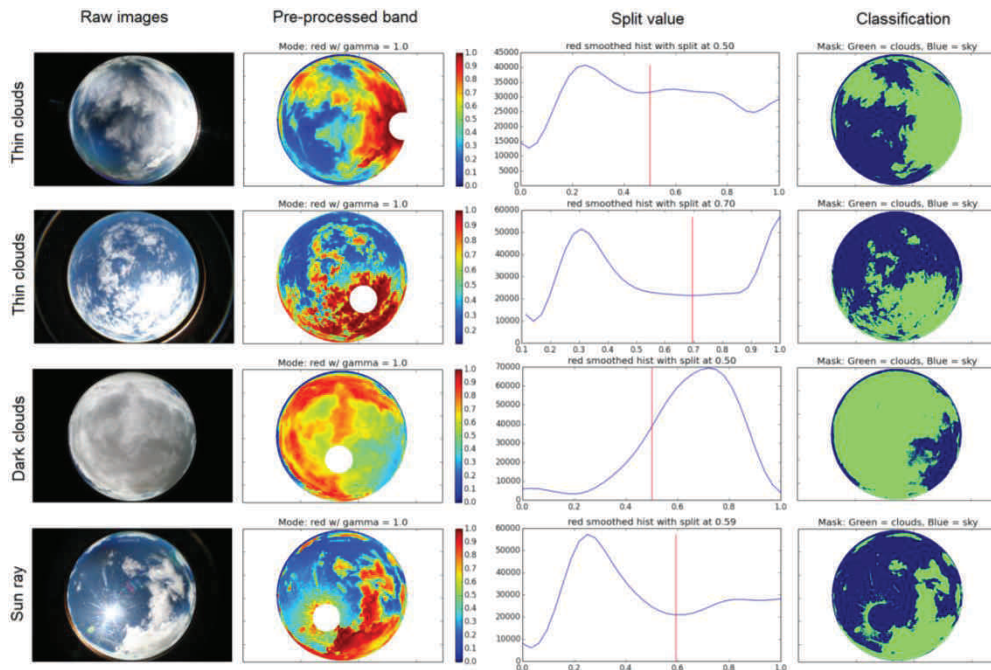


Figure 4.11: Example of the different classification difficulties encountered during the cloud detection. Each row illustrates an identified source of error, from top to bottom: thin clouds, dark clouds and sun ray. For each problem the different processing steps are provided, from left to right: raw images, pre-processed band, pixel distribution and split value and the classification

The problem with very thin or dark clouds is closely related to the sun position and illumination conditions, leading to the correct detection of clouds in some cases and their omission in some other cases. This is in line with the main problems raised in several studies dealing with cloud detection. According to Silva et al. (2013), a successful application of the classification depends hugely on the intensity of light in the atmosphere, which depends on the solar zenith angle ( $\theta_s$ ), the cloud cover, the cloud type, and the aerosol load in the atmosphere. Gonzales et al. (2012) also quotes the sunspot as a persistent problem, especially at large zenith angles and/or under considerable aerosol load (Long et al. 2010). Pfister et al. (2003) pointed out the confusion between clouds and whitish sky in hazy conditions, especially near the sun or the horizon. Similar problem occurs for high-altitude or far clouds, which are bluish due to Rayleigh scattering in the air layer between the clouds and the ground, and for dark clouds (Silva et al. 2013). Some studies even considered the regions near the sun and the horizon as too complicated to be automatically handled so they cropped them out of the analysis (Long et al. 2006; Heinle et al. 2010; Neto et al. 2010). Aerosols are, most of the time, not a problem over the Tibetan Plateau. Because of the high altitude, the AOD is usually very low. Then, the main problem is mainly due to the sky illumination, thus  $\theta_s$ , and data provided by the RGB channels are not enough to completely go over those problems.

#### **4.3.2 Cloud distribution**

One of the objectives of this experiment is to investigate the impact of the spatial distribution of the clouds on the surface radiative fluxes. In that respect, besides providing accurate and consistent estimation of the cloud fraction, the proposed approach also provide information about the spatial distribution of the clouds, as illustrated in Figure 4.12. Using the polar coordinates, the hemisphere is divided in segments, with zenith increment of  $10^\circ$  and azimuthal increment of  $22.5^\circ$  which creates a segmentation grid (Figure 4.12 - left). Then, the information contained by each pixel after the classification is used to compute a cloud fraction for each segment providing a cloud distribution map (Figure 4.12 – right). The latter being a very valuable output of the method as the distribution of the cloud fraction is of primary interest for accurate modelling of the radiative balance over a 3D structure, *e.g.* a group of building, a sharp relief or any other cases where some elements of a given surface structure has a limited sky view factor. In this thesis, the distribution information is considered through the distribution of the clouds with respect to the distance to the sunspot or to the image nadir ( $C_{fD}$  and  $C_{fN}$ ).

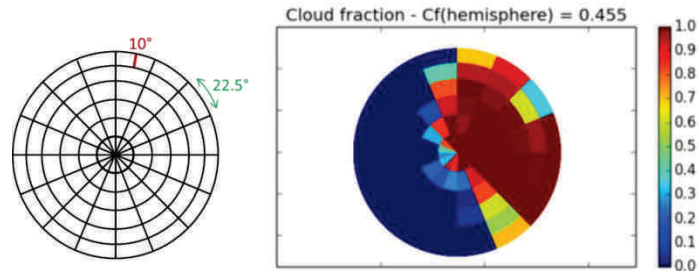


Figure 4.12: Segmentation grid (left) and example of cloud distribution maps (right), the color bar representing the fraction of cloud coverage per segment

### 4.3.3 Correlation with ground measurements

Once the classification outputs are validated, the different cloud fractions and indices extracted from the images have been correlated with the radiative fluxes measured at the ground to analyze the impact of the cloud distribution. In this thesis, only the cloud fractions provided interesting results. Figure 4.13 illustrates the various cloud fractions used in the correlation analysis along with a new cloud fraction, computed only in a buffer around the sunspot (noted  $C_{fC}$ ).

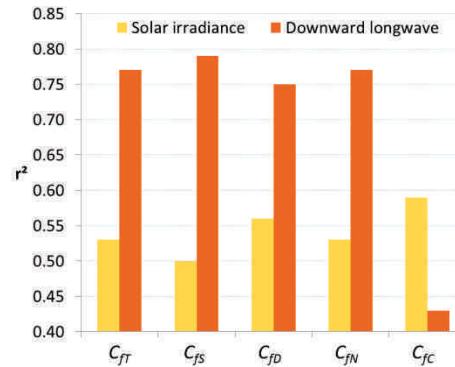


Figure 4.13: Correlation between downward ground fluxes measurement for shortwave (yellow) and longwave (orange) and the different cloud fractions

Concerning the downward longwave radiation, the correlation with the different cloud fractions is high except for the cloud fraction computed close to the sun. The

correlation is mostly lower for the solar irradiance, for which the highest correlations are obtained with  $C_{fD}$  and  $C_{fC}$ . This highlights the fact that regarding solar irradiance, more than the information about the amount of clouds, the localization of those clouds in relation to the sun is of influence. This observation is confirmed by the results showed in Figure 4.14 where a time series of irradiance measured at the ground over 2 days is compared with the retrieved  $C_{fS}$ . The theoretical TOA irradiance for completely clear sky is shown by the dashed line. As expected, when the cloud cover is low, the measured irradiance is closer to the clear sky modelled irradiance, while when the cloud cover is higher, the measured irradiance is lower than the modelled one. This is observed over the major part of the time series. However in two cases, highlighted in grey color in Figure 4.14, there is a high cloud cover but almost no difference between the measured and the modelled irradiance.

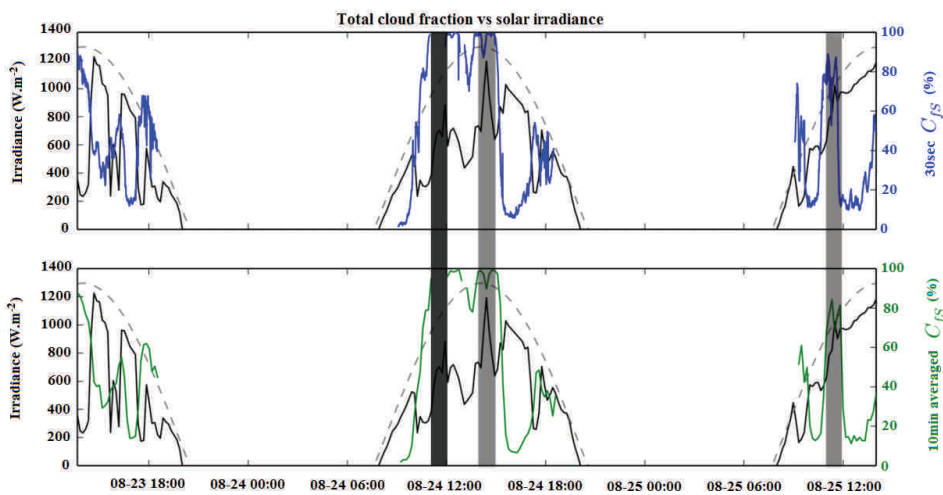


Figure 4.14: Time series of solar irradiance measured at the ground (black line) and cloud fraction estimates (blue at the top and green at the bottom) with missing data (dark grey) and interesting phenomena (light grey). The dashed line represents the clear sky modelled irradiance. The  $C_{fS}$  is provided at 30 second (top) and 10 min averaged (bottom) time steps

Those two cases were investigated and it comes out that, even if the cloud fraction was correctly estimated from the hemispherical images, the sun was visible so direct sunlight was received at the ground (Figure 4.15), which explains the measured irradiance behaving as if it was clear sky. Those observations reinforce the analysis of Figure 4.13 about the necessity of cloud distribution information when working in the solar domain, but

also the importance of keeping and processing the pixels located within and around the sunspot when performing cloud detection.

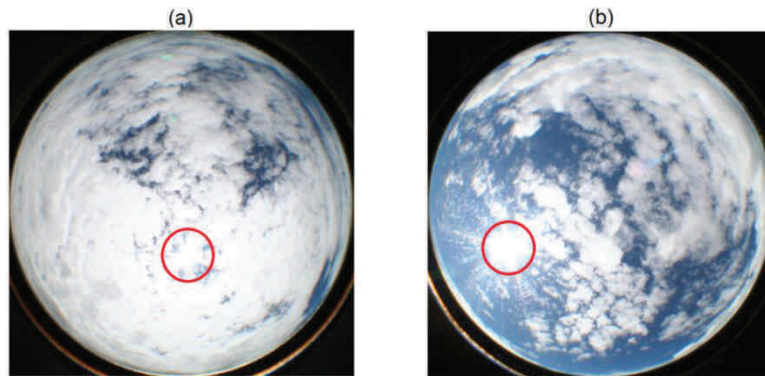


Figure 4.15: Illustration corresponding to the first (a) and second (b) anomalies identified in Figure 4.14. The visible sun is highlighted in red

Figure 4.16 shows the same  $C_{fS}$  time series but compared with the longwave downward radiative fluxes measured at the ground. A very good match is observed with high cloud cover leading to high measured downward fluxes. Unlike in Figure 4.14, no unexpected phenomena are observed. This supports the results from Figure 4.13 and confirms that the longwave radiative fluxes are not significantly impacted by the cloud distribution but by the total cloud cover. Moreover, regarding the temporal variability of the cloud cover, the very similar pattern of the two times series highlights the sensitivity and fast response of longwave downward radiative fluxes to change of the cloud fraction. However, when comparing the top and bottom graphs in Figure 4.14 and 4.16, the 10 minutes averaged  $C_{fS}$  gives a better fit with the ground measurements while the 30 second  $C_{fS}$  shows more fluctuations which do not appear in the ground data. There is a small shift as well between the measured fluxes and the retrieved cloud fraction. This highlights the fact that 10 minutes averages of radiative fluxes are not sufficient to capture correctly the fast changes of the cloud cover conditions even though Long et al. (2010) defined the typical decorrelation time of the sky as being about 10 to 15 min.

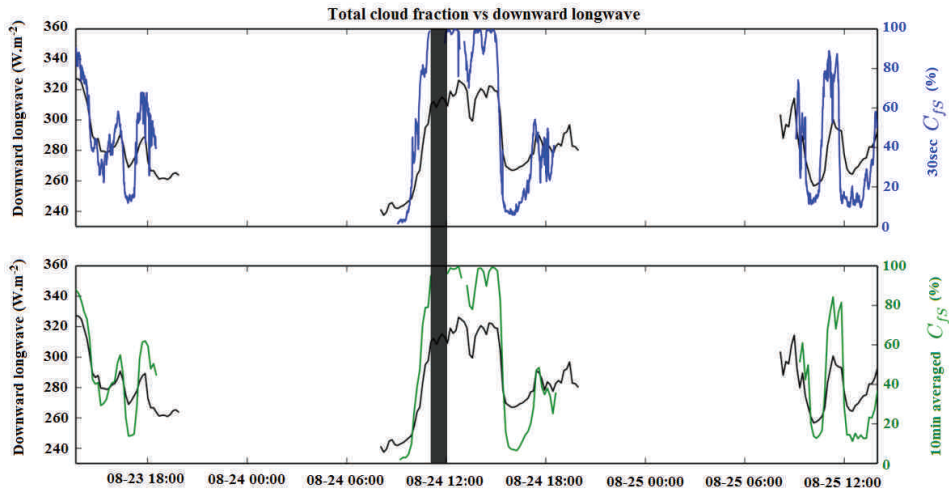


Figure 4.16: Time series of downward longwave measured at the ground (black line) and cloud fraction estimates (blue at the top and green at the bottom) with missing data (dark grey). The  $C_{fs}$  is provided at 30 second (top) and 10 min averaged (bottom) time steps

The possible relationship between cloud fraction estimated from hemispherical images and radiative fluxes measured at the ground is further investigated using a linear regression. Figure 4.17 shows the scatter diagrams of the short and longwave downward radiative fluxes against the  $C_{fs}$  estimates. In this figure, the shortwave irradiance is expressed as the difference between clear sky modelled irradiance and the irradiance measured at the ground. Graphs (a) and (b) show 10 minutes averages of measurements between 9.30 am and 6.30 pm while graphs (c) and (d) show similar averages but only the measurements between 11 am and 6 pm were considered. Graph (a) shows that, even if the time series of irradiance measured at the ground and the estimated  $C_{fs}$  present an opposite trend most of the time, there is no significant correlation between both variables. On the contrary, there is a high correlation ( $r^2 = 0.8$ ) between longwave radiative fluxes and  $C_{fs}$ , with the longwave downward radiative fluxes increasing with the increase of cloud fraction. The large solar zenith angles observed at the beginning and end of the day, leading to lower sky illumination, were quoted as one of the major sources of errors in the cloud detection thus in the cloud fraction estimation. Figure 4.17(c) and (d) show that when ignoring the data collected before 11 am and after 6 pm, the regression coefficient improves from 0.8 to 0.9 for the longwave while no changes is observed for the shortwave irradiance. In line with the previous remarks, the longwave radiative fluxes are highly correlated to the cloud fraction while the shortwave irradiance, even if the latter is strongly impacted by the

presence of cloud, is not correlated with a cloud fraction which does not account for the cloud distribution.

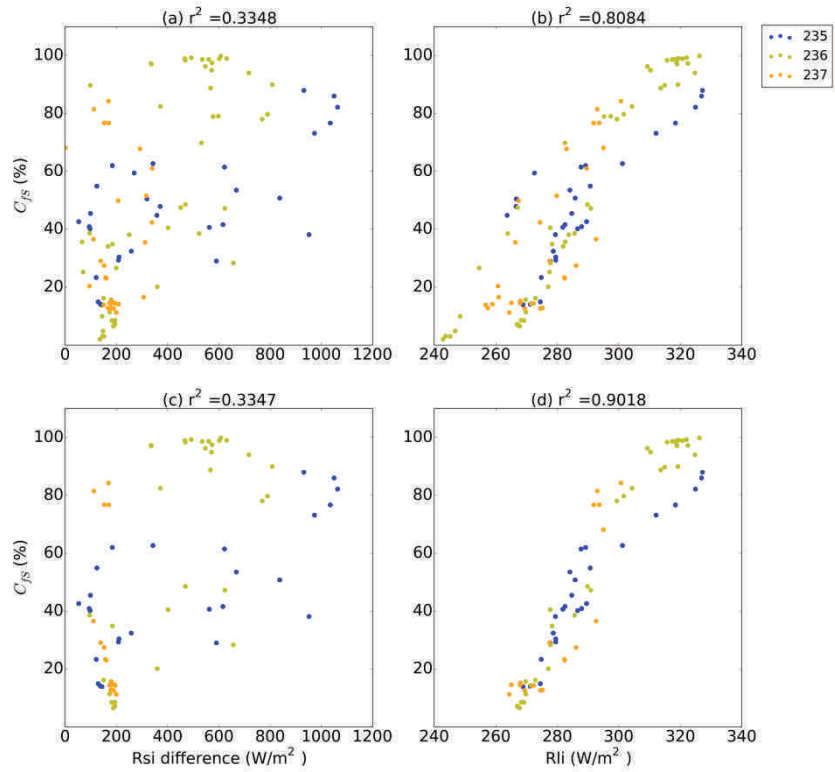


Figure 4.17: Regression analysis between estimated  $C_{fs}$  and (a) difference between clear sky modelled and measured shortwave irradiance between 9.30am and 6.30pm, (b) downward longwave fluxes measured between 9.30am and 6.30pm, (c) difference between clear sky modelled and measured shortwave irradiance between 11am and 6pm and (d) downward longwave fluxes measured between 11am and 6pm, for data collected over 3 days (doy 235 in blue, 236 in light green and 237 in orange). 10 min averaged  $C_{fs}$  and ground fluxes are used

#### 4.3.4 Daily solar radiation integration considering cloud effects

The second objective of this chapter is to investigate the sensitivity of sunshine duration estimation, used to average radiative fluxes over time, to the cloud temporal variability. As mentioned previously, Long et al. (2010) estimated the typical decorrelation

time of the sky to be about 10 to 15 min. The hemispherical images collected every 30 seconds allow for a detailed analysis of the impact of measurements frequency on estimated sunshine duration. Additionally, three methods to retrieve sunshine duration from the hemispherical images are compared. The different estimates are used to temporally aggregate radiative fluxes in order to identify the most accurate retrieval method.

To investigate the temporal variability of the cloud cover, several hourly  $C_{fS}$  are computed using hemispherical images recorded at different temporal resolutions and compared to a reference hourly  $C_{fS}$  derived from images collected every 30 seconds. The different hourly  $C_{fS}$  are computed using respectively one image every minute, every 5 minutes, every 15 minutes, every half-hour and finally a single hourly image. Each of the hourly  $C_{fS}$  is subtracted from the reference one and the differences are summarized as boxplots in Figure 4.18(a). Differences in cloud fraction estimates can be observed when the latter are retrieved using data with different temporal resolutions. While using data collected every minute is not very different from using data collected every 30 seconds, there are already significant differences with the data collected every 5 minutes. Difference in  $C_{fS}$  can go beyond 15% when using data collected every 30 minutes.

The same analysis is carried out for the sunshine duration, computed according to the sun visibility. If the sun is visible, the sun visibility is set to 1, else it is set to 0 for the obstructed sun. The sunshine visibility is accumulated over an hour and the hourly sunshine duration is expressed in minutes. As for the  $C_{fS}$ , the hourly sunshine duration computed from images collected every 30 seconds is used as reference. Then, the hourly sunshine duration is estimated using data collected at different time intervals: every minute, every 5 minutes, every 15 minutes, every half-hour and one value each hour. The difference between the reference and the other sunshine duration estimates is shown in Figure 4.18(b). Significant differences occur when using time steps larger than 1 minute. When dealing with sunshine duration, the impact of the data temporal resolution is stronger than for the cloud fraction estimation. In section 4.3.3, the results showed that the distribution of clouds over and around the sunspot -and thus the visibility of the sunspot- has a major impact on shortwave irradiance at the surface. Consequently, the important differences observed when using larger time step highlights the necessity to consider the cloud temporal variability as well. This conclusion underscores the need for cloud cover data at high temporal resolution when dealing with shortwave radiative fluxes. It is important to specify that this analysis is performed using data collected over 3 days, thus over a relatively short period. It does not change the significance of those results but a more extended study would allow for a more detailed investigation by sampling more diverse sky conditions.

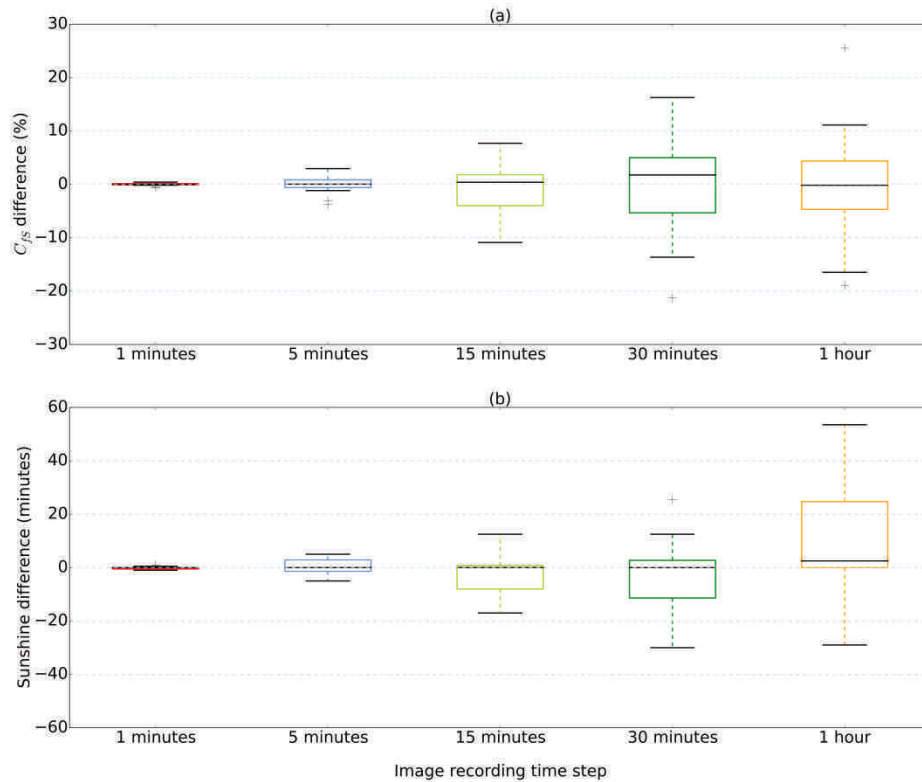


Figure 4.18: Comparisons between hourly  $C_{fS}$  (a) and sunshine duration (b) computed with different time steps. A reference dataset is computed from observations collected every 30". This reference is compared to daily estimations obtained for various observation frequencies by sampling data each 1', 5', 15', 30' and 60'.

A similar comparison is carried out for the computation of daily  $C_{fS}$  and sunshine duration from images collected at different time steps, for three consecutive days (Figure 4.19). As for the hourly computations, the sunshine duration estimates are more impacted by the variation of time step than the  $C_{fS}$ . For one day, this difference can reach up to 2 hours while for the  $C_{fS}$  the largest differences observed are around 6%. Figure 4.19 points out that the differences are not constant from one day to another. This mainly depends on the cloud cover fluctuations observed within each day. For the three days considered, there is not much difference between  $C_{fS}$  and sunshine duration retrieved from data collected with time steps below 5 minutes. However, more days and cloudy conditions should be analyzed to strengthen these conclusions.

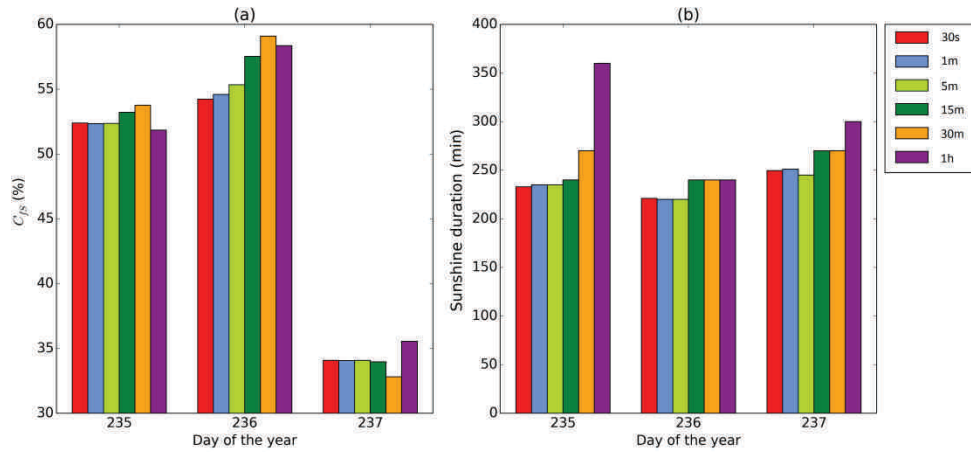


Figure 4.19: Comparisons between daily  $C_{fs}$  (a) and sunshine duration (b) computed with different time steps. A reference dataset is computed from observations collected every 30". This reference is compared to daily estimations obtained for various observation frequencies by sampling data each 1', 5', 15', 30' and 60'.

Sunshine duration estimates are essential to accurately convert instantaneous to daily solar radiation budget (section 3.4). From the previous analysis, it appears that the estimation of sunshine duration is very sensitive to the temporal variability of the cloud cover thus to the temporal frequency of the measurement. Additionally, to determine the best way to derive it from hemispherical images, three methods are compared. In this thesis, the sunshine duration is estimated over time periods of 2 hours. Then, the estimates are used to compute 2-hourly solar radiation budget averages. From the three methods used to estimate sunshine duration, the first method is the one based on the sunspot visibility used previously while the second and third methods derive the sunshine duration from the cloud fraction information,  $C_{fS}$  and  $C_{fD}$  respectively. To do so, the cloud fraction estimates were averaged over the considered time period, here 2 hours, and then used to weight the maximum sunshine duration possible that correspond to the total time period. The sunshine duration time series obtained with the three methods and the computed 2-hourly solar radiation budget averages are presented in Figure 4.20. On the right (Figure 4.20(b)), the solar radiation budget averages computed using the three different sunshine duration estimates are plotted against the solar radiation budget measured at the ground.

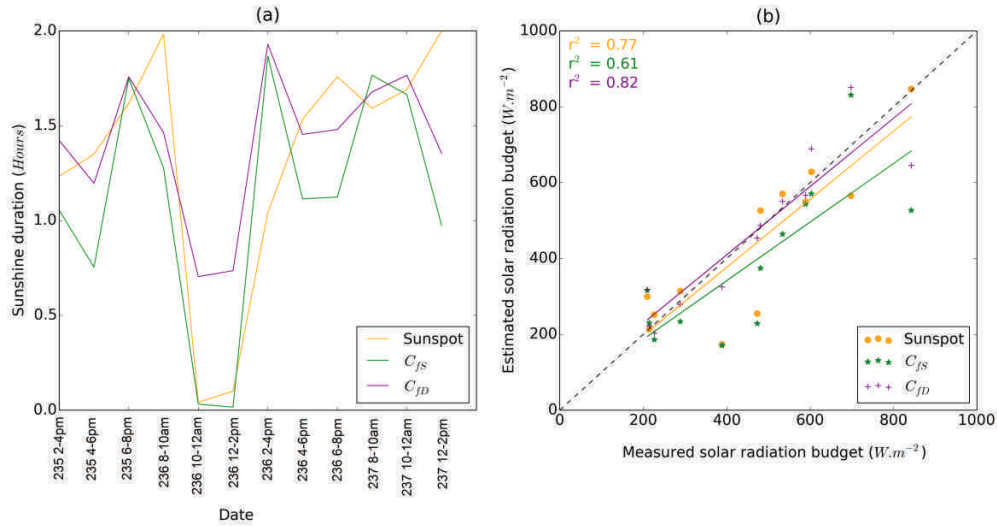


Figure 4.20: Comparison between (a) the three sunshine duration estimates (hours) over 2 hours periods and (b) the 2-hourly solar radiation budget averages computed using the three sunshine duration estimates and plotted against the solar radiation budget measured at the ground

Figure 4.20(a) shows that even if the three sunshine duration time series have similar patterns, very large differences are observed between the three estimates, up to 45 minutes difference. From Figure 4.20(b), it appears that the most accurate 2-hourly estimates of the solar radiation budget are obtained using the sunshine duration derived from the cloud fraction weighted by the distance to the sun ( $C_{fD}$ ), then accounting for the clouds distribution. Using the sunshine duration derived from the sun visibility only also provides good but less accurate results, while using sunshine duration derived from the cloud fraction only ( $C_{fS}$ ) provides the worst results with a significant under-estimation of the 2-hourly solar radiation budget. Those results point out that information about the sunspot visibility only is not the most suitable way to derive sunshine duration to temporally average the solar radiation budget.  $C_{fD}$  was more efficient, reinforcing the importance of cloud distribution.

## 4.4 Conclusion

This chapter investigated the impact of cloud spatial distribution on solar radiative fluxes and of cloud temporal variability on temporally averaged estimates of the solar radiation budget. A method was presented to accurately and consistently retrieve cloud fraction and cloud distribution from hemispherical images at very high temporal frequency.

The experiment performed at NamCo illustrates the flexibility and reliability of the proposed setup and image processing approach for operational or intensive retrieval of cloud cover and distribution. The validation shows very good results concerning the different cloud fractions estimates, which are more accurate and consistent than the observer estimations. The observed misclassification errors are mostly due to thin clouds or located over and around the sunspot area.

The hemispherical images were used to explore the impact of cloud cover on radiative fluxes measured at the ground and to estimate sunshine duration. Even if most of the extracted indices do not correlate with the radiative fluxes measured at the ground, the cloud fractions show interesting patterns. It appears that the longwave downward radiative fluxes correlate very closely with the cloud fraction while the solar irradiance depends strongly on the cloud distribution, enhancing the necessity to consider the spatial organization of clouds. The proposed approach is then very valuable as it is easy and low-cost to set up. Furthermore the image processing is very fast, completely automatic and provides a distribution map of the clouds, essential when dealing with irradiance. However, it provides measurements at local scale only.

Another important advantage of this approach is the high temporal resolution of the collected cloud data. The analysis shows that the estimation of the sunshine duration, commonly used to convert instantaneous to daily solar radiative fluxes, is very sensitive to the data collection time step, thus to the clouds temporal variability. It shows that, in case of heterogeneous sky conditions, significant errors can be made if the sampling interval is longer than 15 minutes. In this case, exploiting the high temporal frequency of geostationary satellites, such as MSG providing an image every 15 minutes, would be very beneficial for solar irradiance estimation and temporal aggregation. Furthermore, using the cloud fraction weighted by the distance to the sun ( $C_{fD}$ ) appears to be the best way to derive sunshine duration for the temporal aggregation of the solar radiation budget, providing better results than using sunspot visibility or basic cloud fraction only. It reinforces the need for cloud distribution information and showed that  $C_{fD}$  is a good proxy for this information. Unlike the sunspot visibility,  $C_{fD}$  can be retrieved from satellite observations combining the current cloud fraction with sun geometry computation to apply the sun distance weighting function. Then, the use of satellite data would overcome the spatialization problem inherent to all ground measurements and provide large area estimates.

In the light of those results, the operational method presented in Chapter 3 could greatly benefit from using new clouds parameters inputs, especially accounting for the cloud distribution, measured at higher temporal frequency. The latter could be derived from geostationary data such as provided every 30 minutes by FY-2 series or 15 minutes by MSG.

## **Chapter 5**

# **Sub-pixel topography effects on solar irradiance estimated using remote sensing**

### **5.1 Introduction**

The mandatory radiometric calibration of satellite data appears to be often ignored or underestimated (Baraldi 2009), especially in mountainous area. Topographic corrections are essential to improve the retrieved ground objects properties and also very beneficial for the detection of true anomalies for monitoring purposes (Song et al. 2003). In Chapter 3, the pixel-wise mean slope and azimuth were used to compute the local illumination angle required to estimate surface irradiance. However, considering terrain geometry only is not enough to accurately integrate the effects induced by topography as the impact of shadow and the radiation reflected by the surrounding slopes is not taken into account. Furthermore, the terrain parameters used in Chapter 3 were at the square kilometer, neglecting the

topographic spatial variability within the pixels. The objective of this chapter is to investigate the impact of topography on estimated surface irradiance considering all the effects of topography at sub-pixel level. To do so, a new sub-pixel topographic correction method is proposed.

Thanks to the increasing availability of terrain elevation data, several authors have estimated the effects induced by topography on satellite measured radiometric data (Rochon et al. 1979; Kawata et al. 1988; Proy et al. 1989; Meyer et al. 1993; Liu et al. 1996; Richter 1997; Wen et al. 2009a). They highlighted that terrain induces distortions in the observed radiance and thus also in the estimation of surface properties. Different methods have been developed to take into account the impact of topography at a pixel level and some were proven efficient to improve the accuracy of retrieval of surface radiance (Riano et al. 2003; Richter et al. 2009; Szantoi et al. 2013). In the past years, more accurate DEM became available at a global scale with a resolution of up to 30 m. On the other hand, most of the methods to derive solar radiation budget from remote sensing make use of satellite data at the kilometric level, which is also the case in this thesis with MODIS products (Chapter 3) or FY-2E data (Chapter 6) at the square kilometer. The availability of higher resolution DEM enables to consider terrain effects on the measured radiance at a finer resolution and to investigate the effects of topography at a sub-pixel level. The issue was tackled by Wen et al. (2009b) who described the sub-pixel topographic effects on the surface albedo estimation and developed a correction factor. This study illustrated already the necessity of sub-pixel topographic correction in rugged areas and showed promising results. However, it did not consider all the effects of topography, such as the pixel adjacency effect which was neglected although it has been proved as having a high influence on satellite measured radiance in rugged areas (Dozier et al. 1981; Sugawara et al. 2010). In this chapter, a method to correct sub-pixel topography induced effects on estimated surface irradiance using a fine resolution DEM and integrating the sub-pixel adjacency effect is presented. The sub-pixel topographically corrected irradiance can then be used to derive sub-pixel corrected reflectance and albedo from kilometric pixel size satellite data (Chapter 6).

The proposed sub-pixel topographic correction method assumes a separation between direct and diffuse irradiance. Then, an investigation was carried out to evaluate the impact of the fraction of diffuse skylight estimation on irradiance retrieved after sub-pixel topographic correction. Two methods to estimate the direct irradiance, diffuse irradiance and the fraction of diffuse skylight were compared: one using the US standard atmospheric profile in MODTRAN and the other one using actual atmospheric conditions derived from MODIS products. The results from both methods have been compared and used to estimate surface irradiance over different types of topography.

This chapter starts with a theoretical background on the pixel level topographic correction from Sandmeier (Sandmeier et al. 1997), which inspired the proposed sub-pixel

topography correction method. Then, the latter is presented and more detailed descriptions of the correction parameters are given, followed by the analysis of the impact of topography on the estimated irradiance. Next, the comparison of the two ways to estimate the direct-diffuse irradiance ratio and the impact of this ratio on corrected irradiance is presented. Finally some conclusions are provided.

## 5.2 Impact of topography: Sub-pixel topographic correction

### 5.2.1 Topographic correction at pixel level

The solar irradiance is strongly affected by the surface orientation, as an object lying in the shadow gets less solar irradiance than those exposed to the sun. Furthermore, the geometry between the sun position and the surface orientation affects the ratio of direct and diffuse irradiance and the amount of terrain reflected radiance reaching an adjacent surface (Richter 1998). The topographic correction presented in Sandmeier et al. (1997) was quoted and applied in several studies (Wen et al. 2009a; Richter 1998; Shepherd et al. 2003; Baraldi et al. 2010) to correct the relief induced distortions on satellite measured data at pixel level. This topographic correction method is based on the fact that the total solar irradiance ( $E$ ) received at the surface should be calculated by taking into account the effects induced by the relief. Thus, it allows to compute a surface irradiance topographically corrected and directly analyses the impact of topography on surface irradiance. The equation proposed by Sandmeier et al. (1997) partitioned the irradiance received by a pixel in rugged terrain into four components:

- (1) The direct solar irradiance ( $E_d$ ), affected by terrain slope and topographic azimuth of the target pixel itself.
- (2) The isotropic diffuse irradiance ( $E_{iso}$ ), affected by the same factors as the first component.
- (3) The circumsolar diffuse irradiance ( $E_{cir}$ ), affected by terrain shading.
- (4) The surrounding terrain irradiance ( $E_t$ ), affected by the reflectance of neighbor pixels.

The isotropic and circumsolar diffuse irradiances are the two components of the diffuse irradiance ( $E_f = E_{iso} + E_{cir}$ ). Each component is corrected individually to take into account the effects of topography allowing to compute corrected direct irradiance ( $E_{dc}$ ), corrected diffuse irradiance ( $E_{fc}$ ) and the contribution from terrain irradiance ( $E_t$ ). While the surface irradiance for a horizontal surface ( $E$ ) is the sum of  $E_d$  and  $E_f$  (Equation 3.6),

the surface irradiance for a tilted surface ( $E_c$ ) is made of corrected direct, corrected diffuse and terrain irradiance, and is expressed as:

$$E_c = E_{dc} + E_{fc} + E_t \quad 5.1$$

with the diffuse irradiance divided into isotropic and circumsolar:

$$E_c = E_{dc} + (E_{iso} + E_{cir}) + E_t \quad 5.2$$

The following equations are used to correct each component of the surface irradiance (Sandmeier et al. 1997):

$$E_{dc} = \theta * E_d * \frac{\cos \theta_i}{\cos \theta_s} \quad \text{Direct irradiance} \quad 5.3$$

$$E_{iso} = E_f * k * \frac{\cos \theta_i}{\cos \theta_s} \quad \text{Isotropic diffuse irradiance} \quad 5.4$$

$$E_{cir} = E_f * (1 - k) * V_d \quad \text{Circumsolar diffuse irradiance} \quad 5.5$$

$$E_t = (E_d + E_f) * V_t * \rho_{adj} \quad \text{Terrain irradiance} \quad 5.6$$

Equation 5.3 shows the cosine law (Meyer et al. 1993) applied to direct irradiance  $E_d$  on a horizontal surface and results in the amount of direct irradiance on a tilted target and  $\theta$  is the binary coefficient to control cast shadow. Equations 5.4 and 5.5 represent respectively the isotropic and circumsolar diffuse irradiance in a sloped terrain. They are derived using Hay's anisotropy index  $k$  which is calculated as the ratio of direct irradiance on a horizontal surface ( $E_d$ ) and the TOA irradiance ( $E_0$ ) (Hay 1979 quoted in Souza et al. 2013), as follows:

$$k = E_d/E_0 \quad 5.7$$

$E_{cir}$  can be modelled for topography in the same way as the direct irradiance, though it is part of the diffuse irradiance.  $E_{iso}$  is a function of the proportion of sky hemisphere not obstructed by topography defined by the sky-view factor  $V_d$ .

Equation 5.6 refers to terrain irradiance with  $V_t$  the terrain-view factor and  $\rho_{adj}$  the average reflectance of adjacent objects. Especially in the case of deep valleys, radiance received from neighboring slopes contributes to the irradiance on adjacent surfaces. The amount of the terrain irradiance depends upon the total irradiance ( $E_d + E_f$ ) reaching the adjacent slopes, the portion and distance of visible adjacent terrain ( $V_t$ ) and the reflectance of the adjacent objects  $\rho_{adj}$ . The impact of terrain irradiance is very important especially for shadowed pixels with a large  $V_t$ .

The irradiance parameters  $E_d$ ,  $E_f$  and  $k$  were estimated using MODTRAN (MODerate resolution atmospheric TRANsmittance and radiance). The aim of this chapter being the analysis of the impact induced by topography on the surface irradiance estimation, one of the MODTRAN standard profiles was used: the “1976 US Standard Atmosphere” profile. Then a large number of MODTRAN inputs, namely tape5 files, were generated according to the parameters and options summarized in Table 5.1. In total 3 212 000 tape5 files were created. To facilitate the topographic correction process in the following steps, look-up-tables have been generated to gather and pre-process the MODTRAN outputs. The parameters modified to create the different tape5 files have been selected to represent as much as possible the study area and cover the maximum of topographic configurations. With this in mind, 5 ground altitude values were selected as representative of the area according to the analysis of the DEM values distribution over the area. At first, a sixth altitude class set for 6250 m and above was also selected but then dropped out as for this height the model did not perform well. In order to reduce the amount of tape5 files and the computation time, the simulations were run every 5 days. This temporal resolution of the simulation was also a reason why a standard profile was selected, supposed to be representative of general conditions. The latitude and longitude values have been defined according to the minimum and maximum limit of the study area and then a simulation was computed ever 5 degrees. The time step was chosen to be during daytime and also to fit with the geostationary satellite data collection time. The selection of the parameters was based on the best compromise between the spatial and temporal resolution and the computation time. Finally two surface reflectance values were defined to allow the computation of spherical albedo required in the topographic correction method.

Table 5.1: MODTRAN parameters and options set for the estimation of  $E_d$ ,  $E_f$  and  $k$  used in the topographic correction method

	<i>Set in MODTRAN</i>	<i>Number of options</i>
<i>Atmospheric profile</i>	<i>1976 US Standard Atmosphere</i>	<i>1</i>
<i>Ground altitude</i>	<i>250 m, 1000 m, 2250 m, 3750 m</i>	<i>4</i>
<i>Day of the year</i>	<i>from 0 to 365 (5 days increment)</i>	<i>73</i>
<i>Latitude of observer</i>	<i>20 to 40 (5 degrees increment)</i>	<i>5</i>
<i>Longitude of observer</i>	<i>65 to 110 (5 degrees increment)</i>	<i>10</i>
<i>Greenwich decimal hour</i>	<i>1 to 11 (1 hour increment)</i>	<i>11</i>
<i>Surface reflectance</i>	<i>1 or 0.5</i>	<i>2</i>
	<i>Number of combinations :</i>	<i>3 212 000 tape5 files</i>

## 5.2.2 Topographic correction at sub-pixel level

### 5.2.2.1 Sub-pixel topography heterogeneity

The concept of sub-pixel was introduced in Chapter 1 (Figure 1.1). In this thesis, the 30 m spatial resolution DEM is considered as the sub-pixel level and the kilometeric pixel size satellite data as the pixel level. In order to characterize the topography of the plateau according to the sub-pixel concept, the distribution of slope and azimuth values at 30 m resolution within each square kilometer pixel was analyzed. To do so, two statistical parameters, skewness and kurtosis, which express the symmetry and shape of the distributions respectively, were used to describe the sub-pixel topography. Those parameters allow to classify the topography distribution within a kilometer resolution pixel as “normal” if the skewness equals zero and the kurtosis equals three (with a tolerance ranging from minus to plus twice the standard error of skewness and kurtosis respectively (Brown 2012)), as “maybe normal” if only one of the two parameters indicates a normal distribution and as “not normal” if none of the two parameters indicates a normal distribution.

The results are displayed in Figure 5.1, where the normality distribution within each 1 km pixel for the terrain azimuth is presented on the left and for the slope on the right. Those results illustrate that the sub-pixel distribution of slope and azimuth values within each kilometeric pixel is mostly not normal, which highlights the necessity to take into account this sub-pixel topography because the averaged slope and azimuth values at a pixel level would mask out the real effects of topography on the estimated irradiance.

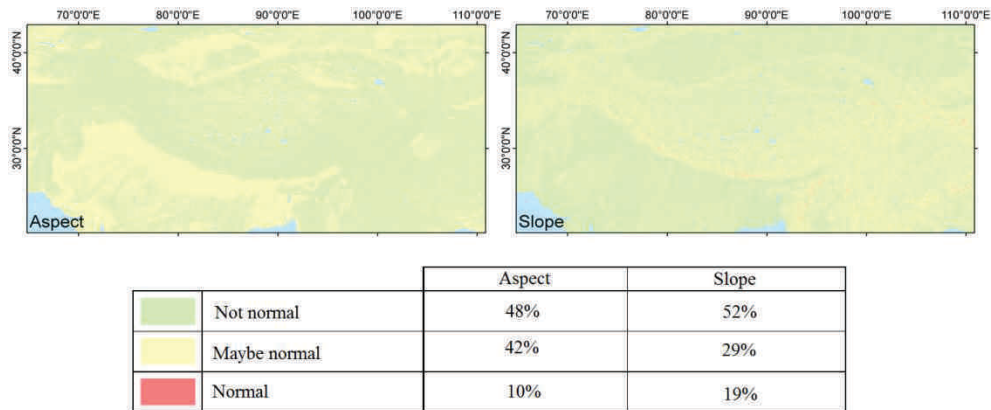


Figure 5.1: Slope and azimuth sub-pixel normality distribution maps and statistics within each square kilometer pixel over the Tibet Plateau and the surroundings

### 5.2.2.2 Sub-pixel topographic correction method

Until now, topographic correction methods were generally applied using a DEM and satellite data at the same spatial resolution. This is the case in Chapter 3 where the terrain impact on local illumination angle was taken into account using mean kilometeric terrain slope and azimuth. Considering an area as rugged as the Tibetan Plateau, the idea is to improve the retrieval of irradiance by making use of the higher resolution topographic data to take into account the pixel spatial topographic variability. Moreover, the terrain shadowing effect as well as the radiation reflected by the surrounding slopes neglecting in Chapter 3 are integrated. The sub-pixel topographic correction was developed in that objective. Referring to sub-pixel correction means to use high resolution data to perform a correction on lower resolution data, while keeping the original resolution of both datasets. In this case, to use a 30 m resolution DEM to topographically correct the surface irradiance which will be combined with kilometeric level geostationary satellite data later on instead of degrading the data from the DEM at the kilometeric level prior to applying the topographic correction.

The idea is to apply Equation 5.2 to each pixel of the 30 m DEM, considered as the sub-pixels of the geostationary radiometric optical data at 1 km spatial resolution. As compared to the initial topographic correction scheme of Sandmeier et al. (1997), the novelty of this method lies in the fact that the computation of the total surface irradiance accounting for topographic effects is performed at sub-pixel level preserving the original DEM information. Then the topographically corrected surface irradiance is averaged into a sub-pixel topographically corrected surface irradiance grid at 1 km ( $E_{csp}$ ) (Figure 5.2).

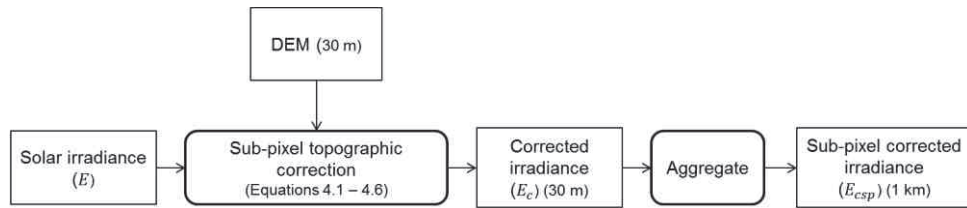


Figure 5.2: Irradiance sub-pixel topographic correction steps

### 5.2.2.3 Isotropy assumption

In the presented sub-pixel topographic correction, the sub-pixel surface anisotropy, also known as non-Lambertian property, is neglected, *i.e.* the surface reflectance is assumed as equal whatever the considered illumination or view angles. In reality surfaces are not Lambertian and their anisotropy is characterized by a bidirectional reflectance distribution function (BRDF) which is a four-dimensional function that defines how light is reflected by a surface. The function takes a negative incoming light direction and a positive outgoing direction, both defined with respect to the surface normal by an illumination and a view angle, and returns the ratio of reflected radiance. This is why the albedo products used and generated in this thesis are computed by bi-hemispherical integration of BRDF (Chapter 3 and 6). In this section, the neglected surface anisotropy is the sub-pixel anisotropy during the sub-pixel topographic correction used to estimate surface irradiance.

In order to quantify the impact of neglecting the sub-pixel surface anisotropic reflectance when applying the sub-pixel topographic correction on surface irradiance, a test was designed. For this test, a theoretical area of 30 by 30 pixels, and therefore 900 possible slope and azimuth combinations, is considered. The slope and azimuth values come from the ASTER-GDEM2 and are used to compute the sub-pixel corrected irradiance. For a given BRDF function taken from Engelsen (1996) and a given solar position, the sub-pixel reflectance is computed using the Rahman-Pinty-Verstraete (RPV) model (Rahman et al. 1993) (Chapter 6). Then two scenarios are run and compared. The first scenario assumes the sub-pixel surface isotropic, which means that, whatever the local solar and observations angles variations at sub-pixel level, a unique reflectance value is defined for all the sub-pixels as if the surface was Lambertian. In this scenario, the reflectance is retrieved from the BRDF function using the mean illumination and observation angles over the considered area. In the second scenario, the reflectance is retrieved accounting for its anisotropy, which means that a different reflectance value is obtained for each sub-pixel according to the illumination and observation angles applying to it. The reflectance values obtained from the

two scenarios are combined with the sub-pixel corrected irradiance to compute the sub-pixel radiance values. The latter are averaged over the entire area and compared. The first scenario provides an isotropic radiance while the second scenario provides an anisotropic radiance. This experiment is repeated for 10 sites selected over the mountainous part of the plateau, 6 different days and 3 different times for each day. The results are summarized in Figure 5.3 and Table 5.2 which presents the correlation and the normalized RMSE between the anisotropic and isotropic radiance values, respectively, produced by the two scenarios for 5 solar illumination angle classes and 5 different BRDF.

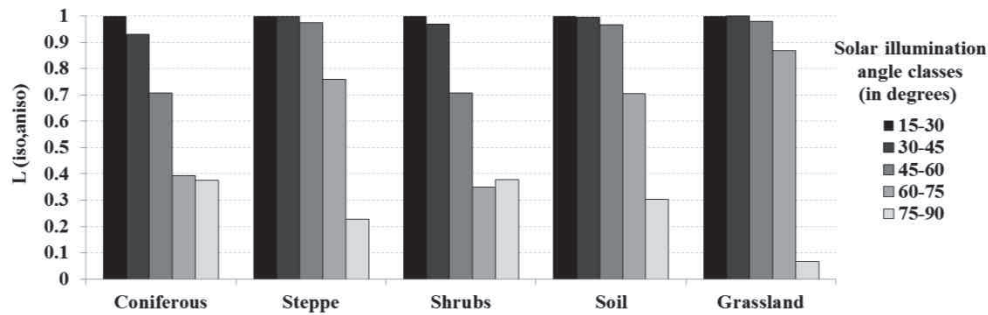


Figure 5.3: Correlation between anisotropic and isotropic radiance values for 5 solar illumination angle classes and 5 different BRDF

Figure 5.3 highlights that for illumination angles smaller than 60 degrees, the radiance computed considering the sub-pixel anisotropy are highly correlated with the ones computed assuming the sub-pixel level as being isotropic. The correlation is no longer significant for larger illumination angles. Focusing on coniferous and shrubs, weaker correlation results can be observed for solar illumination angles between 45 and 60 degrees. Furthermore, Table 5.2 shows low percentage of difference between anisotropic and isotropic radiance values for illumination angles smaller than 60 degrees and even up to 75 degrees for steppe and grassland, which is in line with the results showed in Figure 5.3. The important differences observed for large illumination angles can be due to the sub-pixel anisotropy of the surface but also to the RPV model limitations when modelling BRDF at extreme solar angles. Large solar illumination angles can be observed just after sunrise and before sunset but they can also be the consequence of the terrain orientation. Thus, based on those results and the fact that less than 5% of the study area is covered by slopes larger than 40°, the sub-pixel isotropic assumption should not be a major issue in this thesis.

Table 5.2: Normalized RMSE between anisotropic and isotropic radiance values for 5 solar illumination angle classes and 5 different BRDF

$\theta_i$ (degrees)	<i>Coniferous</i>	<i>Steppe</i>	<i>Shrubs</i>	<i>Soil</i>	<i>Grassland</i>
<i>15-30</i>	1%	0%	0%	1%	0%
<i>30-45</i>	6%	1%	4%	2%	1%
<i>45-60</i>	7%	4%	7%	5%	4%
<i>60-75</i>	15%	8%	15%	10%	6%
<i>75-60</i>	46%	45%	46%	46%	42%

#### 5.2.2.4 Shadow binary factor

An essential parameter when correcting direct solar irradiance is the binary coefficient ( $\Theta$ ) used to control cast shadow coming from self-shadowing and shadow from surrounding topography, known as the shadow binary factor (SBF). The value of the SBF depends on the sun's position at the date and time of data acquisition, which means that it needs to be estimated each time a correction is carried out. To do so, a small module was developed to compute automatically the SBF according to the topography, the day of the year and the local time for each sub-pixel inspired by the methodology presented in Kastendeuch (2013). The aim of this algorithm is to generate a raster at sub-pixel resolution filled with values of 0 or 1, characterizing a pixel in the shadow or a pixel receiving direct sunlight respectively. To compute the SBF, each pixel is tested individually following the decision steps showed in Figure 5.4.

The first test consists of checking if the pixel itself (1), without considering the surrounding topography, receives direct light from the sun or not. This is done by comparing the respective solar azimuth and elevation angles with the pixel azimuth and slope values. If the pixel is not self-shadowing, then it can be tested for the shadow from surrounding pixels (2). Using the sun azimuth angle, the pixels located on the path between the sun and the center of the tested pixel are identified. In Figure 5.5(a), the tested pixel is colored in dark grey and the pixels located on the path to the sun are colored in light grey. All the pixels located on the path to the sun could potentially bring shadow to the tested pixel if their elevation is higher than the sun elevation (Figure 5.5(b)). As soon as a pixel is identified as shadowing the tested pixel, the test stops, the value of the tested pixel set to 0 and the algorithm starts to test the next pixel. If none of the pixels located on the path to the sun have a larger elevation angle than the sun, then the tested pixel is in the sunlight, its value is set to 1, and the algorithm starts to test the next one.

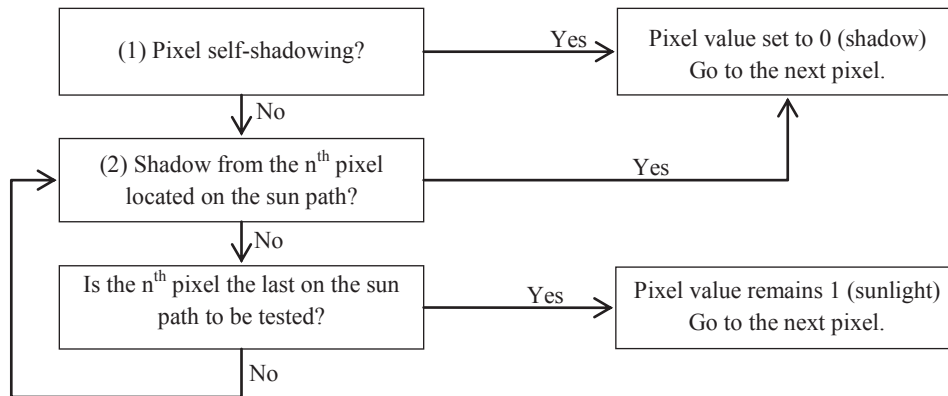


Figure 5.4: Shadow Binary Factor computation: decision tree

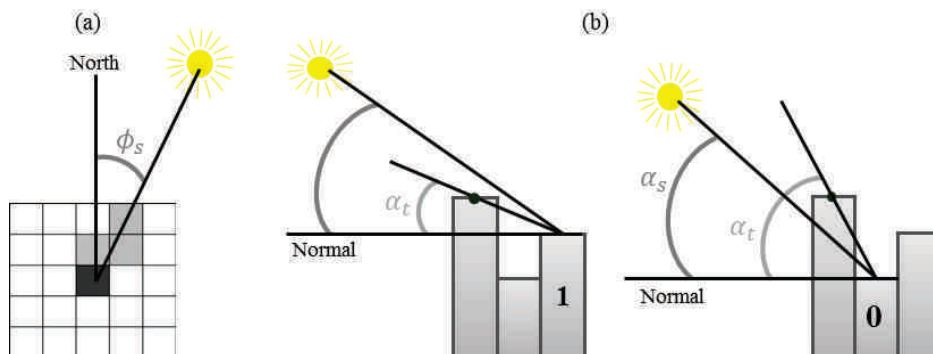


Figure 5.5: SBF computation steps ( $\phi_s$  = sun azimuth,  $\alpha_s$  = sun elevation,  $\alpha_t$  = Terrain elevation). (a) Identification of the pixels located on the path to the sun, (b) Test of shadowing effect of neighboring pixels according to the difference between terrain and sun elevation angles.

Figure 5.6 shows the outputs of the SBF algorithm run for the 300<sup>th</sup> day of the year between 9.00 am and 12.00 pm local time with an increment step of 1 hour over the subset study site. The computation is performed using the 30 m DEM (sub-pixel level) and the same DEM aggregated at 1 km (pixel level). The first row of this figure highlights the important variations in the amount of shaded areas in one hour time which can represent the time step between two subsequent geostationary satellite data acquisitions. Moreover, the

strong relief located in the southern part of the study site shows that a significant amount of pixels remained in the shadow even when around mid-day. When comparing between using a 30 m or a kilometric DEM to compute the SBF, the difference is very large and it is clear that the shaded areas are underestimated when working at lower resolution. It highlights the necessity to take into account the impact of shadow in area characterized with strong relief and that a higher accuracy DEM allow for a more accurate integration of those shaded areas.

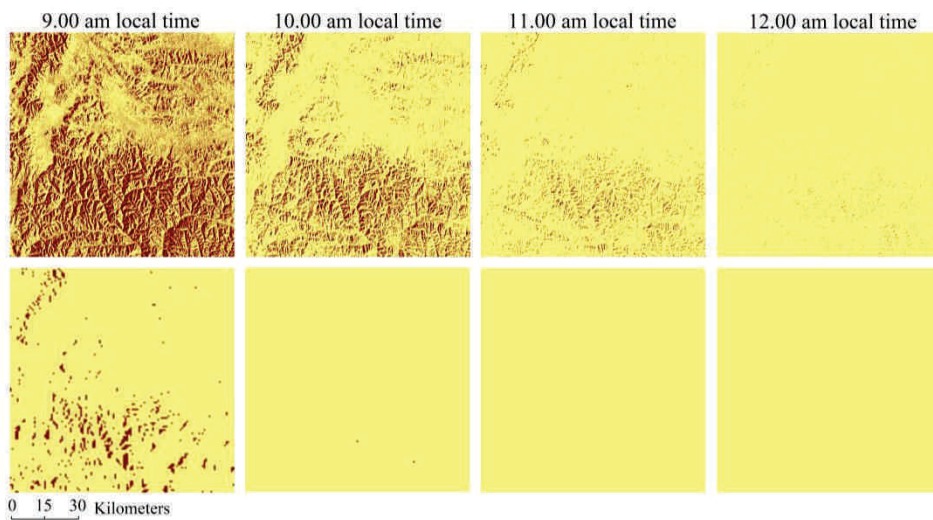


Figure 5.6: Shadow Binary Factor evolution over day time (shaded pixels in brown and illuminated pixels in yellow) computed at sub-pixel level (first row) and pixel level (second row)

#### 5.2.2.5 Sky and terrain view factors

A view factor is a geometric ratio expressing the fraction of the radiation output from one surface that is intercepted by another (Oke 1987). The sky view factor ( $V_d$ ) takes into account the portion of the overlying hemisphere visible to a grid point while the terrain view factor ( $V_t$ ) takes into account the portion of overlying hemisphere obstructed by the surrounding terrain. Both are dimensionless and ranging from 0 to 1. There are several approaches to obtain  $V_t$  and  $V_d$  (Kondratyev 1969; Dozier et al. 1981; Dozier et al. 1990; Corripio 2003; Helbig et al. 2014). They can be estimated using a simple trigonometric approach, which only integrates the local slope angle ( $\alpha_t$ ) to estimate the amount of sky and terrain seen from a point according to the following:

$$V_d = \frac{1 + \cos(\alpha_t)}{2} \quad 5.8$$

$$V_t = \frac{1 - \cos(\alpha_t)}{2} \quad 5.9$$

With this approach, the impact of adjacent terrain reducing the amount of visible sky is neglected. In that regards, an analytical approach such as the one presented in Dozier (1981; 1990), considering the terrain surrounding each pixel, provides more accurate results. This method requires the slope and azimuth values of the point, along with the horizon angles (H) over the entire azimuth circle in a discrete set of directions. A horizon angle represents the largest slope angle between the DEM-point and any other DEM-point in a given direction  $\phi$ .  $V_d$  and  $V_t$  are then obtained by the integration of those horizon angles over the azimuth circle. From this, Dozier (1981) expressed the portion of overlying hemisphere which is obstructed by terrain as:

$$V_t = \frac{1}{2\pi} \int_0^{2\pi} \sin(H[\phi]) d\phi \quad 5.10$$

In this thesis, the sky view factor is computed according to this analytical approach, using the algorithm developed by Zakšek (Zakšek et al. 2011). For a set of  $n$  search directions,  $V_d$  and  $V_t$  are computed as:

$$V_d = 1 - \frac{\sum_{i=1}^n \sin H_i}{n} \quad 5.11$$

$$V_t = 1 - V_d \quad 5.12$$

The algorithm computes vertical elevation angle of the horizon in a user defined number of directions and radius range expressed in pixels. For the purpose of this study, several tests have been carried out to know what would be the best compromise between accuracy and computation time when choosing the number of search directions and radius range to compute the sky-view factor. The two first graphs presented in Figure 5.7 shows the improvement, expressed as mean difference, achieved: (a) by increasing the radius range for different set of directions and (b) by increasing the number of search directions for different radius ranges. The third graphs (c), shows the computation time required depending on the number of search directions and radius range.

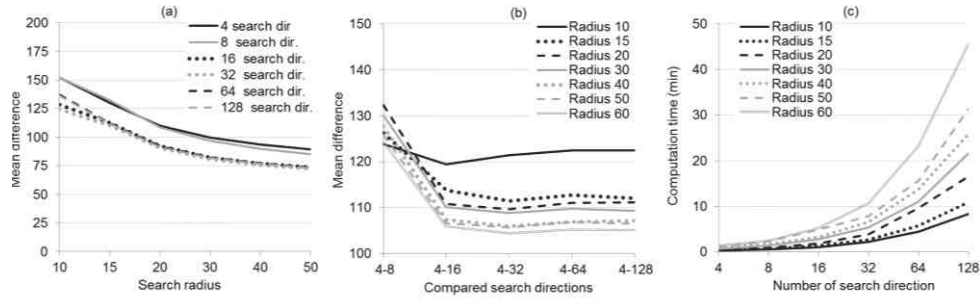


Figure 5.7: Sky-view factor parameter tests: (a) mean difference according to search radius value for difference search direction, (b) mean difference according to the number of search direction for difference search radius values, (c) computation time required depending on the number of search directions and search radius values

In the Figure 5.7, graph (a) shows that, whatever the number of search directions, the difference in  $V_d$  values obtained with different radius range reduces significantly between 10 and 30 pixel radius range. Over 30 pixels, the difference due to the increase of radius range is varying less. If one relates this results to graph (c), showing that when the number of search directions or the radius range increases the computation time increases as well, a radius range of 30 pixels appears as the best setting in this case. The same reasoning is followed to define the optimum number of search directions. Graph (b) shows that when using a radius range over 10 pixels, the major difference is between using 8 or 16 search directions. Increasing the number of search directions over 16 would only increase the computation time. From the results of these tests, directions and radius have been set to 16 directions and 30 pixels respectively, which is in line with the thresholds given in Dozier et al. (1990) and Zaksek et al. (2011).

### 5.2.3 Slope and azimuth impact on estimated irradiance

To quantify the impact of sub-pixel topography on the surface irradiance, the latter has been computed according to Equation 5.2 for different slope and azimuth combinations and subtracted to the irradiance value obtained assuming a flat terrain. The slope ranges from 0 to 45° and the relative azimuth, *i.e.* the difference between the solar azimuth angle and the terrain azimuth, ranges from 0 to 180°. The computation is performed hourly from 9 am to 6 pm (UTC+8), and the SBF and the sky view factor have been set to 1. Figure 5.8(a) shows hourly maps presenting the irradiance difference ( $\text{W}\cdot\text{m}^{-2}$ ) between

computation without and with sub-pixel topographic correction. As a summary, Figure 5.8(b) provides the percentage of sub-pixel topographically corrected pixels that are overestimated, underestimated or equal as compared to the irradiance values estimated without topographic correction for each hour during day time. The objective of this analysis is to highlight the impact of slope and azimuth on estimated surface irradiance and to identify if there could be some compensation effects between slope and azimuth variations.

The graph presented in Figure 5.8(b) shows that, whatever the time of the day, assuming a flat terrain would not lead to an error in surface irradiance estimation in only 2.17 % (green line) of the cases. Thus, in 2.17 % of the tested combinations there is a compensation effect between the slope and azimuth values that leads to the same results as if the surface was flat. Moreover, Figure 5.8 shows that the observed differences are not equally spread between under and over-estimation. Indeed, for the whole range of slope and azimuth combinations tested, neglecting the sub-pixel topography mostly leads to an over-estimation of the surface irradiance. The over-estimation is even more important around the solar noon where it represents more than 70% of the cases. The observed errors can reach up to  $\pm 600 \text{ W.m}^{-2}$  in some extreme topographic configurations with strong slope or azimuth values, almost leading to a self-shadowing of the pixel. In those cases, there is far less direct illumination as compared to the corresponding flat surface and the irradiance that would be received by a flat surface at solar noon (about  $1100 \text{ W.m}^{-2}$ ) is almost divided by 2. Those results support the observation made at the beginning of this chapter (section 5.2.2.1), concerning the necessity to take into account the sub-pixel topography effects because the averaged slope and azimuth values at a pixel level would mask out the real effects of topography on the measured radiance. More than the fact that the distribution within kilometric pixel in this area is mostly not normal, the compensation effect that could be expected from a normal distribution of slope and azimuth is not confirmed.

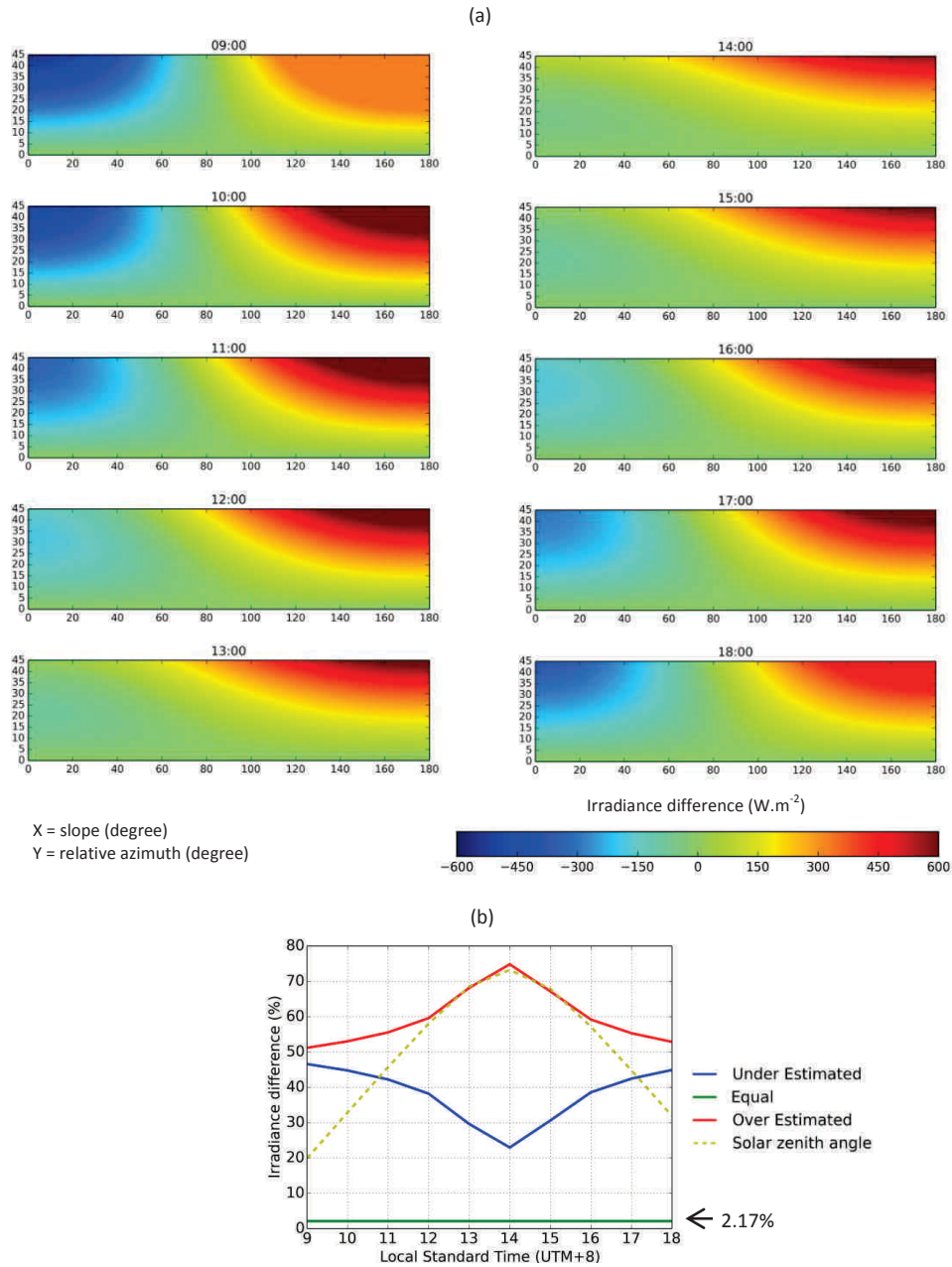


Figure 5.8: Difference between irradiance ( $W.m^{-2}$ ) computed without and with sub-pixel topographic correction over the day (DOY=115): (a) Difference maps ranging from -600 (blue) to 600 (red) with the X axis representing the slope gradient and the Y axis the relative azimuth, both in degree. (b) Irradiance difference summary according to local standard time in %.

To further explore the effect of applying a topographic correction at the sub-pixel level when computing surface irradiance, a second test is performed applying Equation 5.2 over the study site and assuming the reflectance of the adjacent terrain to be equal to 0.2 (arbitrary value representative of the subset study area). Thus, only the slope and azimuth parameters derived from the DEM and available at a sub-pixel level are changing over the scene along with the different view and sun angles used in the computation which vary according to the day and time of the day. The irradiance maps are computed each five days of the year and each hour of the day, from 9am to 6pm (UTC+8). This time range was chosen because it represents a constant period over the year during which the study site is always illuminated. The maps obtained with the pixel level method are subtracted to the corresponding maps obtained with the sub-pixel level method. Then the difference maps are summarized according to the five-number summary method that provides the sample minimum, first quartile, median, third quartile and maximum. From this, the spread of the difference between irradiance computed at pixel and sub-pixel level is derived hourly over the whole year, as presented in Figure 5.9. The spread of the difference is expressed as the interquartile range, which is the range between the first and the third quartile computed in the five-number summary. The graphs (a) and (b) show this daily interquartile variation over the year for the SBF and for the ratio between solar incidence and solar zenith angle ( $\cos \theta_i / \cos \theta_s$ ), respectively. Concerning the SBF, the difference is expressed as the difference in lighted area ( $\text{km}^2$ ). Those two variables have the highest impact in the difference between computing the total irradiance at pixel or at sub-pixel level (Equation 5.2). The level of computation of the sky and terrain view factors is also impacting the topographic correction but, as it depends only on the topography, the difference is constant over the day and the year. The graphs (c) and (d) show the daily interquartile difference spread over the year for the total irradiance, with real and normalized data respectively. The normalized difference ( $Diff_n$ ) between the irradiance corrected at sub-pixel level ( $E_{csp}$ ) and the irradiance corrected at pixel level ( $E_c$ ) is computed as:

$$Diff_n = \frac{E_{csp} - E_c}{E_{csp}} \quad 5.13$$

The direct, diffuse and terrain irradiance values used in Equation 5.2 vary over the day and the year and are identical for both correction levels. Their values can then influence the shape of the graph but not the difference between the two methods.

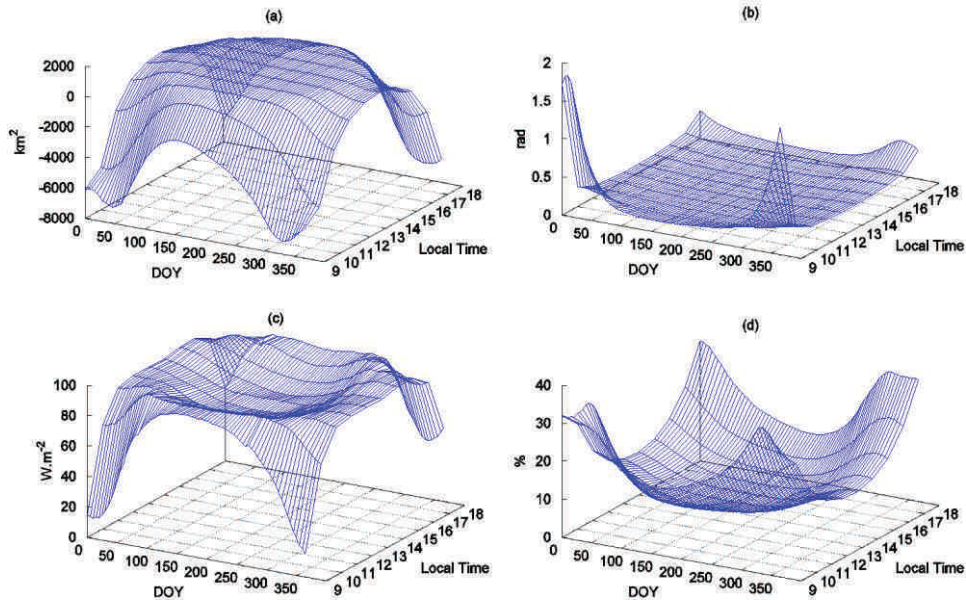


Figure 5.9: Hourly and daily variation of differences between sub-pixel and pixel level corrections for: (a) Shadow binary factor, in  $\text{km}^2$  of lightened area; (b) ratio between incidence and zenith solar angle in radian; (c) Total irradiance values in  $\text{W.m}^{-2}$ ; (d) Total irradiance normalized (Equation 5.13) values in %

Figure 5.9 shows that the differences between the two methods depend on the period of the year as well as on the time of the day. Concerning the total irradiance, it is important to make the distinction between the expression of the difference between pixel and sub-pixel level method expressed in  $\text{W.m}^{-2}$  (Figure 5.9(c)) and the normalized value (Figure 5.9(d)) giving the difference in percentage. The latter shows that the largest differences between pixel and sub-pixel level topographic correction can reach 40% difference and occur just after sunrise or just before sunset, especially in winter time when the sun elevation is low. This is explained by the fact that the total irradiance is mainly driven by the direct irradiance which is itself strongly impacted by the SBF. The latter, set to 0 or 1, controls the cast shadow of a pixel which means that it defines if a certain pixel receives direct irradiance or not. From the graph (a) in Figure 5.9, it appears that the largest differences in lightened area occur during the first and last hours of sunlight. The same observation is made for the ratio between sun incident and zenith angles. The dissymmetry of graph (b) is due to the fact that the computations are run between 9 am and 6 pm, so they are not always centered on the local solar noon. However, when looking at the difference between the two methods with respect to the total amount of irradiance expressed in  $\text{W.m}^{-2}$ , the largest discrepancies can be observed in the middle of the day and especially in winter

time with differences of about  $100 \text{ W.m}^{-2}$ . This is linked to the fact that the largest values of direct and diffuse irradiance value occurs at this time of the day.

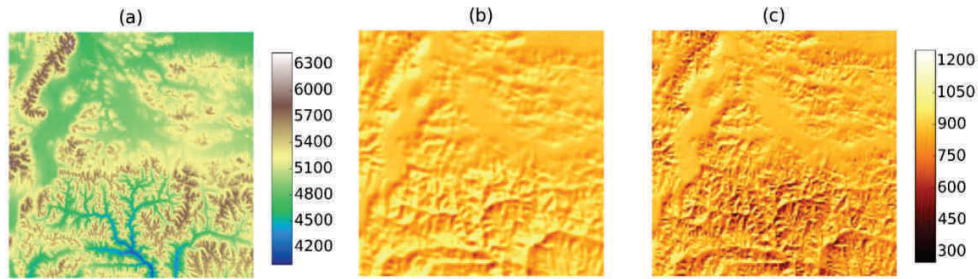


Figure 5.10: Comparison of topographic correction at pixel and sub-pixel levels: (a) DEM (m), (b) corrected irradiance at pixel level ( $\text{W.m}^{-2}$ ) and (c) corrected irradiance at sub-pixel level ( $\text{W.m}^{-2}$ )

Figure 5.10 evidences the improvement achieved by integrating the sub-pixel topographic effects in the irradiance estimation at 1 km compared to pixel level correction. Three maps are shown in this figure: (a) the DEM of the area; (b) a surface irradiance map topographically corrected at pixel level ( $E_c$ ), performed using the slope and azimuth values degraded from 30 m to 1 km pixel size and (c) a surface irradiance map topographically corrected at sub-pixel level ( $E_{csp}$ ). It appears that in area where there is a significant topography, a higher level of terrain effects details is obtained when performing a sub-pixel topographic correction. The main difference between the two levels of correction is due to a better resolution of the SBF and sky view factor.

## 5.3 Impact of the atmosphere: Fraction of diffuse skylight estimation

### 5.3.1 Estimation of the actual fraction of diffuse skylight from MODIS atmospheric products

The TOA solar irradiance penetrates the atmosphere and undergoes several absorption and dispersion processes before to reach the Earth surface (Chapter 3). Those processes determine the atmosphere transmittance and divide the solar irradiance between direct and diffuse irradiance, the fraction diffuse skylight depending on the composition of the atmosphere. Thus, to derive the fraction diffuse skylight, the atmospheric shortwave transmittance ( $\tau$ ) needs to be estimated. In this section, the objective is to analyze the

impact of the fraction of diffuse skylight estimation on the retrieved surface irradiance, thus only clear sky conditions are considered here. As described in section 3.6.1, the transmittance function of the atmosphere can be defined by two elements, the beam transmittance ( $T_B$ ) and the diffuse transmittance ( $T_D$ ) (Yang et al. 2007) (Equations 3.29-3.33). Once  $T_B$  and  $T_D$  are calculated, the direct and diffuse surface irradiance can be derived, assuming flat terrain, as follow:

$$E_d = E_0 * T_B * \cos \theta_s \quad 5.14$$

$$E_f = E_0 * T_D * \cos \theta_s \quad 5.15$$

### ***5.3.2 Impact of the fraction of diffuse skylight estimation on irradiance retrieved over different type of topography***

For the analysis of the impact of the topography on the surface irradiance presented in the previous section, the fraction of diffuse skylight was estimated using MODTRAN. In Chapter 3, the atmospheric transmittance controlling the partitioning of the irradiance between direct and diffuse was derived from real atmospheric content provided by the MODIS products. Then, the idea is to investigate the impact of using a standard atmosphere profile in a complex radiative transfer model or a modelled atmospheric transmittance estimated from space when correcting irradiance for sub-pixel topographic effects. As the MODTRAN simulations were performed once every 5 days, only those days are considered in the analyses, covering the whole year 2010. Moreover the irradiance values presented correspond to irradiance estimated at the time of MODIS Terra overpass over the study area (10.15 am local time). For sake of clarity when looking at the results, the same local time was used over the entire scene.

Firstly, the direct and diffuse irradiance as well as the fraction of diffuse skylight derived with both methods have been compared over the entire Tibet Plateau study area for the complete year 2010. Figure 5.11 shows the direct irradiance, diffuse irradiance and the fraction of diffuse skylight mean and standard deviation values both when estimated from MODTRAN or from the MODIS products over the Plateau as described in Chapter 3 (Equations 5.14-15). From this figure, it appears that both methods provided comparable direct irradiance values even if the direct irradiance estimated with MODTRAN is generally lower than the one estimated from MODIS. Concerning the diffuse irradiance, there are larger differences and higher values are obtained with MODTRAN. Consequently, the ratio between direct and diffuse irradiance is different between the two methods. Graph (c) shows that MODTRAN provides higher proportion of diffuse irradiance as compared to the MODIS-based method. It also highlights that the differences between the two methods

are more important at the beginning and end of the year and that, in both cases, the MODIS-based method provides more spread values.

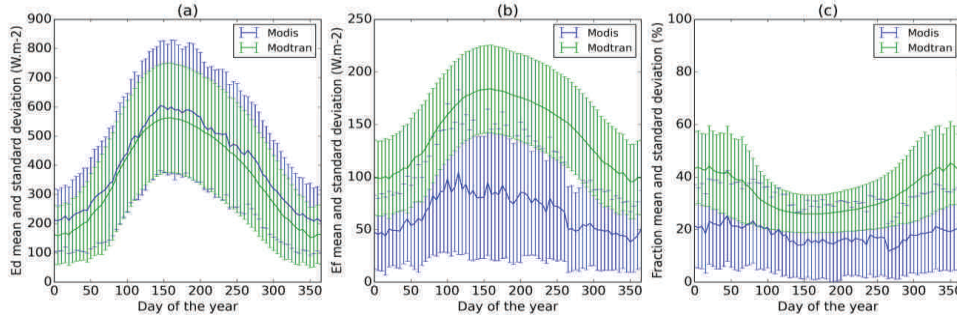


Figure 5.11: Comparison between MODTRAN and MODIS-based: (a) Direct irradiance, (b) Diffuse irradiance and (c) Fraction of diffuse skylight every 5 days over the whole year 2010

Additionally, Figure 5.12 provides a detailed comparison between total irradiance estimated from MODTRAN and from MODIS. The graph (a) represents  $E$  estimated by the two methods over 2010. Graphs (b) and (c) present a quantitative comparison between the two computed by subtracting the  $E$  obtained with MODTRAN from the one obtained with the MODIS-based method. In graph (b), the values are expressed in  $\text{W.m}^{-2}$  and in graph (c) the difference is normalized as follow:

$$Diff_E = \frac{E_{MODIS} - E_{MODTRAN}}{[(E_{MODIS} + E_{MODTRAN})/2]} \quad 5.16$$

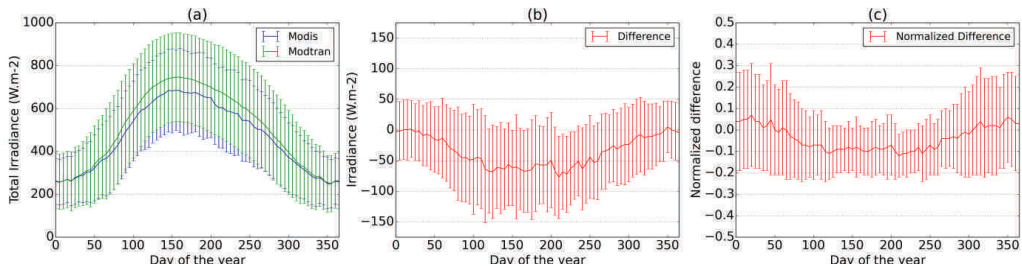


Figure 5.12: Daily  $E$  mean and standard deviation from MODTRAN and MODIS over the entire Plateau every 5 days for the year 2010: (a) daily values ( $\text{W.m}^{-2}$ ) (b) difference ( $\text{W.m}^{-2}$ ) and (c) normalized difference

Figure 5.12(a), shows relatively similar estimated  $E$  from MODTRAN and MODIS, especially in winter time. The largest differences are observed in summer time where MODTRAN provides higher values than MODIS. Graphs (b) and (c) confirm this observation. In graph (b), the mean difference between the irradiance computed from MODTRAN and MODIS is close to zero at the beginning of the year and can decrease to  $-50 \text{ W.m}^{-2}$  in summer time. The stronger variations observed in summer could be explained by the fact that for a constant local time over the year the solar irradiance is higher in summer than in winter. However, the same pattern is observed with the normalized data showed in graph (c). The relative mean difference between the two methods ranges from  $-12 \%$  to  $+7 \%$ , with the largest difference still observed in summer time. With regards to Figure 5.11(c), it shows that, when no correction is performed and when observed at the scale of the Tibetan Plateau, large variations in the fraction of skylights between MODTRAN and MODIS-based estimations can lead in some cases to similar retrieved total irradiance, like in winter time.

As shown, the estimation of the ratio between direct and diffuse irradiance is different. However, depending on the time of the year, the two methods can provide comparable total solar irradiance estimates. As the sub-pixel topographic correction method presented in the previous section is considering direct and diffuse irradiance separately, it is of interest to measure the impact of the ratio difference on the produced corrected irradiance. To do so,  $E_d$  and  $E_f$  estimated with both methods have been used to feed the sub-pixel topographic correction model (Equation 5.2), then the corrected irradiance values are compared. This experiment is run over the subset study area, for the entire year 2010. Figure 5.13 shows the difference mean and standard deviation between MODTRAN and MODIS-based uncorrected ( $E$ ) and corrected ( $E_{csp}$ ) irradiance. Graphs (a) and (d) represent  $E$  and  $E_{csp}$  respectively, estimated by the two methods. Graphs (b) and (e) show the quantitative difference between the two methods for  $E$  and  $E_{csp}$  in  $\text{W.m}^{-2}$  respectively, while the graphs (c) and (f) show the same difference but normalized according to Equation 5.16.

Over the subset study area, the  $E$  means (Figure 5.13(a)) differ significantly between the two methods. The one retrieved using MODTRAN is relatively stable while the one based on MODIS product is fluctuating over time and is spatially more heterogeneous. These fluctuations have an impact on the observed differences (Figure 5.13(b) and (c)). The  $E$  mean difference spreads from  $+55 \text{ W.m}^{-2}$  at the beginning and end of the year to  $-150 \text{ W.m}^{-2}$  in summer time. As quoted previously, the use of a constant local time over the year can explain those larger differences. When looking at the  $E$  normalized differences, the latter range from  $+25 \%$  to  $-30 \%$  and occur all over the year. On the other hand,  $E_{csp}$  means (Figure 5.13(d)) are relatively similar between the two methods, even if the MODTRAN one tends to provides higher values. The comparison of graph (a) and (d) also

highlights the smoothing effect generated by the sub-pixel topographic correction. The fluctuations observed for the MODIS-based retrieved irradiance without topographic correction (Figure 5.13(a)) is mainly due to the use of products providing the actual composition of the atmospheric products then including the spatial variations. Those products have missing data, due to clouds or algorithm limitations, and the gap filling procedure used (Chapter 2) could introduce heterogeneity in the filled scenes which could explain the large standard deviation values. Furthermore, because of the high roughness of the Tibetan Plateau leading to extreme illumination angles and shaded areas, the retrieval algorithms may reach their limitations over this area and generate inconsistent values. The sub-pixel topographic correction is computed at 30 m and then aggregated at 1 km which tends to smooth those fluctuations. The  $E_{csp}$  mean differences (Figure 5.13(e)) are relatively constant over the year and are oscillating between -5 and -46  $W.m^{-2}$  which highlights that the MODIS-based method provides slightly lower corrected irradiance estimates than MODTRAN. However, the normalized differences ranges from -1% to -21% (Figure 5.13(f)), the largest differences occurring at the beginning and the end of the year. Thus, the differences observed between the MODTRAN and MODIS-based fraction of diffuse skylight estimations (Figure 5.11) all over the year affects significantly the sub-pixel topographic correction outputs in winter time only. The largest differences are observed at the beginning and the end of the year when the fraction difference is the highest. Furthermore, the sun is low during this period, so there are more shaded areas. In the shadow, the received irradiance is only made of diffuse illumination then, when there are more shadowed pixels the impact of the difference in diffuse irradiance is accentuated. However it is important to keep in mind that the topography in this area is very strong and that these results could be different in flatter areas.

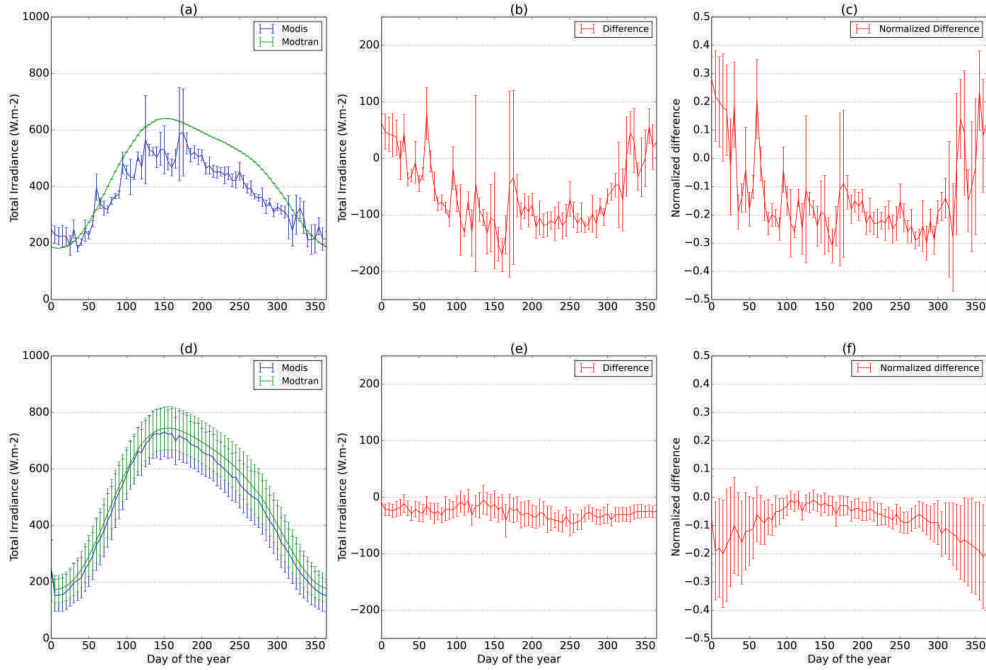


Figure 5.13: Daily irradiance mean and standard deviation from MODTRAN and MODIS over the study site every 5 days for 2010: (a)  $E$  daily values in  $W.m^{-2}$ ; (b) difference of  $E$  in  $W.m^{-2}$ ; (c) normalized difference of  $E$ ; (d)  $E_{csp}$  daily values in  $W.m^{-2}$ ; (e) difference of  $E_{csp}$  in  $W.m^{-2}$ ; (f) normalized difference of  $E_{csp}$

In order to investigate the sensitivity of the sub-pixel topographic correction method to the direct-diffuse irradiance ratio over different types of topography, a test is performed using synthetic data simulating a gradual change for this ratio. To do so, a fixed value for the total irradiance on a horizontal surface is defined, called initial irradiance ( $E_{ini}$ ). Then, the  $E_{csp}$  is computed for a direct-diffuse ratio ( $F_{DD}$ ) varying from 0 to 100% of  $E_d$ , with an increment of 10%. In each case,  $E_d$ ,  $E_f$  and  $k$  are computed according to this ratio. The test is run for different sun zenith angles which represent the variation of illumination over the day and the year. The sun zenith angle values spread from 10 to 70°, with an increment of 10°.  $E_{ini}$  is defined as representative of the computation location and sun zenith angle. Finally, the test is run over 3 test areas presenting different degree of topography, from relatively flat to rough area. The results of the sensitivity analysis are presented as two ratios: (1) the ratio between  $E_{csp}$  mean and  $E_{ini}$  ( $r_{Em}$ ) and (2) the ratio between  $E_{csp}$  standard deviation and  $E_{ini}$  ( $r_{Esd}$ ) (Equations 5.17 and 5.18). Those ratios are summarized

in Figure 5.14 where the results of computations with the different sun zenith angles are presented in individual graphs grouping the 3 types of topography.

$$r_{Em} = \frac{\overline{E_{csp}}}{E_{ini}} \quad 5.17$$

$$r_{Esd} = \frac{\sigma_{E_{csp}}}{E_{ini}} \quad 5.18$$

Performing the sub-pixel topographic correction for different  $F_{DD}$ , various sun zenith angles and over different topography types, highlights the sensitivity of the method to those parameters. First, the behavior of the  $r_{Em}$  is relatively similar for the 3 types of topography and remains the same whatever the solar zenith angles considered. Furthermore, there are no strong  $r_{Em}$  variations between the different  $F_{DD}$ . For this analysis, the initial irradiance is set according to the considered sun zenith angle which explains why the  $r_{Em}$  remains relatively the same in each graph of Figure 5.14. In contrast, larger differences are observed for the  $r_{Esd}$  between the different topography types and sun zenith angles. An increase of the sun zenith angle, corresponding to a decrease of the sun elevation, leads to an increase of the  $r_{Esd}$ , especially over a strong relief. The  $F_{DD}$  also influences the  $r_{Esd}$  which increases with the fraction of direct irradiance. Thus, the largest variations of corrected irradiance values are observed for the area presenting a strong topography, when the sun zenith angle is the largest and when the surface irradiance is mostly made of direct illumination. Large sun zenith angles correspond to early morning or late afternoon daytime periods but also occur at the beginning and end of the year. Those results confirm the observations made for Figure 5.13.

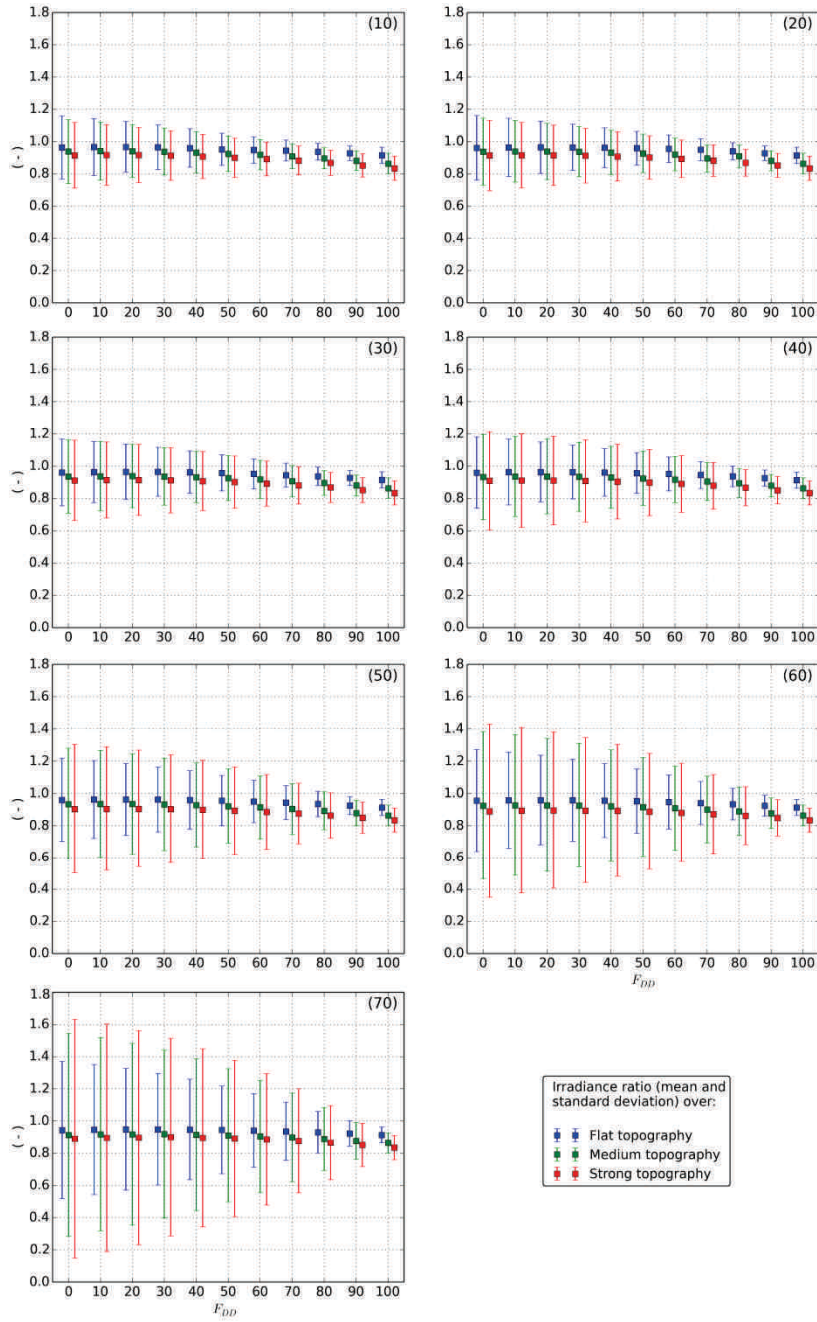


Figure 5.14: Ratio between  $E_{csp}$  mean and standard deviation and  $E_{mi}$  by topography types (blue for flat, green for medium and red for strong topography) and sun zenith angle (indicated on the top right of the graph between brackets) for different direct-diffuse ratios ( $F_{DD}$ )

The strong impact of the  $F_{DD}$  on sub-pixel topographic correction for high fraction of direct irradiance in rough areas and for large sun zenith angles is explained by the fact that, in the correction method, the direct irradiance is strongly controlled by the SBF (Equation 5.3). With an initial irradiance mainly made of direct illumination, the shaded pixels present very low values while lighted pixels have high corrected irradiance values. Only the diffuse and terrain irradiance are reaching the shaded pixels, then the differences are less important when most of the  $F_{DD}$  is diffuse illumination. As in rough areas or when the sun zenith angles are large the proportion of shadow increases, the variation in retrieved sub-pixel corrected irradiance increases as well. The  $F_{DD}$  incremented every 10 % shows that, between each step there is a significant difference, especially when  $F_{DD}$  is above 20 %. It highlights the fact that, even for a similar total irradiance, it is important to retrieve accurately the  $F_{DD}$  in order to estimate correctly the sub-pixel corrected irradiance, especially in atmospheric conditions leading to a higher diffuse illumination ratio, in rough areas and when the period of low sun elevation. This support the previous results showing that the differences between the MODTRAN and MODIS-based method ranging from -25 to 30 % lead to differences in corrected irradiance up to 21 % (Figure 5.13).

## 5.4 Conclusion

In this chapter, the impact of sub-pixel topography on estimated surface irradiance over the Tibetan Plateau was investigated, taking into account the orientation of the terrain, the impact of shadow and the radiation reflected by the surrounding slopes. Additionally the influence of the estimation of the fraction of diffuse skylight on the computation of sub-pixel corrected irradiance was explored. Concerning the topography, the necessity to take into account its effect when estimating surface irradiance from space was quantified and a method to correct for those effects was presented. This method considers the sub-pixel topography by using a high spatial resolution DEM, which allows to compute parameters such as the sky view factor and SBF very accurately. In the literature, the sky view factor is presented as being an important parameter for the calculation of incoming diffuse radiation (Dubayah et al. 1995; Duguay 1995; Varley et al. 1996). The SBF is also described as essential because of its dominant influence on the solar radiation budget in complex terrain (Corripio 2003). The results show that neglecting topography when estimating surface irradiance could lead to error up to  $600 \text{ W.m}^{-2}$  under certain extreme conditions. Those results are in line with the one presented in Borel et al. (1998) who found that the inclusion of shading may decrease the incident radiation by 20 to 60 %, and the ones of Chow et al. (2006) who confirmed the significant influence of shading solar irradiance, especially during sunrise and sunset.

Regarding the analysis of the influence of the fraction of diffuse skylight, two retrieval methods have been tested. Despite the different ratios between direct and diffuse

irradiance provided by the two methods, it appears that after applying the sub-pixel topographic correction the obtained total irradiance are very similar when tested over a rough area in summer time. In winter time, some significant differences are observed. To deepen this investigation, a sensitivity analysis has been run to simulate the impact of different direct and diffuse irradiance ratios on sub-pixel corrected irradiance retrieved over several topography types and for different sun elevations. It shows that, even when using a similar total irradiance as input, the corrected total irradiance estimated presents some large variations over rough areas, for large illumination angles and when the portion of direct skylight is high. Thus, when estimating solar irradiance in area with strong relief, the impact of topography and especially the shading effect, is affected by the ratio between direct and diffuse irradiance estimation. It is then important to retrieve the actual atmospheric conditions as accurately as possible to estimate more accurately the sub-pixel corrected surface irradiance.

This chapter shows that accurately integrating all the effect of topography, and especially considering the sub-pixel terrain variability when working with large pixels, can greatly improve the estimation of solar radiation budget from space. Furthermore, some effort should also be put in the modeling of the atmosphere as the fraction of diffuse skylight has an influence on the accuracy of the results as well. In the following chapter, the sub-pixel corrected irradiance is used to derive sub-pixel corrected surface reflectance from satellite measured radiance and then compute the sub-pixel corrected albedo.

## Chapter 6

# Land surface albedo in rugged terrain

### 6.1 Introduction

Chapter 5 demonstrated the benefit of taking into account topographic effects at sub-pixel level when estimating surface irradiance over rugged areas. The objective of this chapter is then to investigate if correcting for the sub-pixel terrain variability can improve the reflectance and albedo retrieval as well. Moreover, the low temporal resolution of the MODIS albedo product was pointed out in Chapter 3 as one of the shortcomings of the solar radiation budget estimation method. Thus, the possibility to increase the temporal resolution of the albedo estimates by using geostationary satellite data is also investigated.

To take into account sub-pixel topography effects on the albedo estimation, the first step is to correct the surface reflectance for those effects using the sub-pixel corrected irradiance (Chapter 5). In the second step, an accumulation of those sub-pixel corrected reflectance recorded at different illumination/view angles can be used to reconstruct the surface BRDF and then to derive the corrected albedo. The latter is a narrowband albedo corresponding to the satellite band width and needs to be converted to broadband albedo.

Different types of satellite observations can be used to build up the multiple angular data sampling required to estimate the albedo. Some instruments such as MISR (Diner et al. 2005) record almost simultaneously multiple angular views whereas other sensors such as MODIS (Chapter 2), METEOSAT (Pinty et al. 2000) or FY-2E (Chapter 2) accumulate angular observations over a period of several days or hours. Whatever the instrument, these directional observations can be coupled with parametric models to characterize the BRDF and derive albedo (Lucht et al. 2000a). Based on the high temporal resolution and the variation in illumination angle of the geostationary satellite data, it is possible to reconstruct the BRDF from the measured surface reflectance and derive by angular integration the surface albedo (Pinty et al. 2000; Govaerts et al. 2006). As compared to polar orbiting sensors, geostationary satellites allow to accumulate the required observations over a relatively short period always focused on the same area. This makes it feasible to retrieve albedo over shorter periods of time. In this chapter, a method is proposed to derive sub-pixel corrected albedo from geostationary satellite data using the RPV model.

This chapter starts with a presentation of the method to correct surface reflectance and albedo for the sub-pixel topographic effects (as opposed to the mean slope and azimuth applied in Chapter 3), as well as an approach to convert narrowband into broadband albedo. Then, the sub-pixel corrected reflectance is evaluated. The albedo retrieval method is applied on synthetic data for a sensitivity analysis and on real geostationary satellite FY-2E data allowing validation against ground measurements and comparison with other existing albedo products. Finally some conclusions are drawn.

## 6.2 Albedo estimation using sub-pixel topography correction

### 6.2.1 Surface reflectance

Radiometers carried on-board Earth observation satellites measure the spectral radiance reflected back by the surface and the atmosphere towards the sensor. Prior to further analysis, the surface radiance is often converted to surface reflectance, which is the ratio between reflected and incident radiation depending on both the viewing and the illumination direction. The reflected radiance measured by the satellites consists of the path radiance, which does not interact with the surface but is scattered back to the sensor by the atmosphere, and the radiance reflected by the Earth surface to the sensor ( $L_s$ ), which has a complex interaction at the Earth surface and atmosphere boundary. After correcting the TOA radiance measured by the satellite for atmosphere effects,  $L_s$  is obtained but still needs to be corrected for topographic effects.  $L_s$  is converted in surface reflectance ( $\rho$ ) according to Equation 6.1, which assumes that the surface target is a Lambertian reflector.

$$\rho = \frac{\pi L_s}{E} \quad 6.1$$

Topographic correction methods are generally applied using a DEM and satellite data at the same spatial resolution (see Chapter 3). However, as the irradiance retrieved after applying the sub-pixel topographic correction provides a higher level of detail (Figure 5.10) and different results than a pixel level correction (Figure 5.9), it was of interest to investigate the improvement that could be achieved by making use of this sub-pixel topographically corrected irradiance ( $E_{csp}$ ) for the conversion of measured radiance into corrected surface reflectance ( $\rho_{csp}$ ) as follows:

$$\rho_{csp} = \frac{\pi L_s}{E_{csp}} \quad 6.2$$

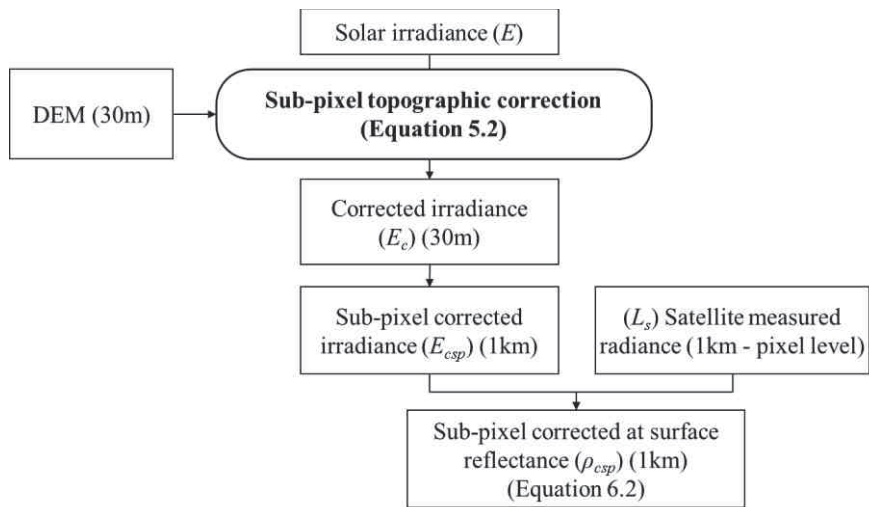


Figure 6.1: Sub-pixel topographically corrected surface reflectance computation steps

### 6.2.2 BRDF reconstruction using RPV

For many years, BRDF models have been developed to directly retrieve surface properties from the physical quantities measured by satellite instruments (Walthall et al. 1985; Roujean et al. 1992; Lucht et al. 2000b; Schaaf et al. 2002; Jacquemoud et al. 2009). During the last decade, those models increasingly considered and exploited the dependence of the surface reflectance on variations in the sun-sensor geometry (Geiger et al. 2008), *i.e.* the variation in illumination and view angles. Among them, the BRDF model developed by Rahman–Pinty–Verstraete, so-called RPV model (Rahman et al. 1993) is an efficient and simple parametric model aiming at representing the surface anisotropy. To do so, RPV approximates the surface reflectance of an arbitrary surface as a function of the physical and structural properties of this surface as well as the geometry of illumination and observation (Lavergne et al. 2007) using four parameters. Those parameters represent the BRDF shape by separating it into overall brightness ( $\rho_0$ ), bowl-bell shaped anisotropy ( $k'$ ), degree of forward or backward scattering ( $\Xi$ ), and hotspot ( $\rho_h$ ) components. While  $\rho_0$  and  $k'$  are two empirical surface parameters,  $\rho_h$  controls the width of the hotspot and is usually neglected, the reflectance at the hot spot being assumed equal to  $\rho_0$ . This reduces the model to a three parameters model (Rahman et al. 1993). The RPV model expresses the surface reflectance ( $\rho$ ) as below:

$$\rho(\theta_i, \theta_v, \phi_r; \rho_0, \Xi, k') = \rho_0 \rho_{afs}(\theta_i, \theta_v, \phi_r; \Xi, k') \quad 6.3$$

where  $\rho_{afs}$  is the angular shape of the surface reflectance expressed by (Pinty et al. 2000):

$$\rho_{afs}(\theta_i, \theta_v, \phi_r; \rho_0, \Xi, k') = M(\theta_i, \theta_v, k') F_{HG}(\Xi_{HG}, g) H(\rho_0, G) \quad 6.4$$

The relative azimuth angle,  $\phi_r$ , is zero when the source of illumination is behind the observer (Engelsen et al. 1996). From Equation 6.4, the RPV model can be described as a non-linear model including a modified Minneart function ( $M$ ), a Henyey–Greenstein phase function ( $F_{HG}$ ) to modulate the overall contributions in the forward and backward scattering and a function accounting for the hotspot ( $H$ ), where:

$$M(\theta_0, \theta_v, k') = \frac{\cos^{k'-1} \theta_0 \cos^{k'-1} \theta_v}{(\cos \theta_0 + \cos \theta_v)^{1-k'}} = \frac{(\cos \theta_0 \cos \theta_v)^{k'-1}}{(\cos \theta_0 + \cos \theta_v)^{1-k'}} \quad 6.5$$

$$F_{HG}(\Xi_{HG}, g) = \frac{1 - \Xi_{HG}^2}{[1 + 2\Xi_{HG} \cos g + \Xi_{HG}^2]^{3/2}} \quad 6.6$$

$$H(\rho_0, G) = 1 + \frac{1 - \rho_0}{1 + G} \quad 6.7$$

with :

$$\cos g = \cos \theta_v \cos \theta_i + \sin \theta_v \sin \theta_i \sin \phi_r \quad 6.8$$

$$G = [\tan^2 \theta_i + \tan^2 \theta_v - 2 \tan \theta_i \tan \theta_v \cos \phi_r]^{1/2} \quad 6.9$$

When the three (or four) parameters listed above are provided as input to the model along with illumination, zenith and view angles, the model produces for each angles combination the corresponding reflectance value. An inverted version of this model (Gobron et al. 2002; Lavergne et al. 2007) is also available requiring a set of bi-directional reflectance values measured from satellite at different view and illumination angles along with some initial surface parameters values to retrieve the real surface parameters values. The retrieval algorithm then delivers the optimized set of the RPV parameters characterizing the anisotropic surface reflectance.

### 6.2.3 Albedo retrieved from geostationary satellite data

Geostationary satellites allow to accumulate observations acquired under constant viewing conditions but changing illumination angles due to the course of the sun during the day (Figure 6.2). Assuming that the observed target does not undergo important changes during the period of data accumulation, the temporal sampling of the radiance field for a given location can be interpreted as an instantaneous angular sampling of the same TOA radiance field (Govaerts et al. 2008), and then used for surface parameters retrieval. The MODIS albedo retrieval algorithm providing the products used in Chapter 3 also relies on an accumulation of multiangular surface observations built up over time to characterize the surface BRDF (Schaaf et al. 2002). However, because of the revisit frequency of the Terra satellite, the data are accumulated over 16 days but by combining observations from both Terra and Aqua platforms, the 8-day product can be generated. Thanks to their high temporal resolution, geostationary satellites allow for a relatively shorter period for data accumulation, which allows to retrieve albedo over a shorter period and then reduces the possibility of significant changes in surface conditions and surface reflectance. The acquired angular sampling can be fitted or inverted against a parametric BRDF model like RPV to perform an angular integration of the reflectance distribution, thus to characterize surface properties (Govaerts et al. 2006).

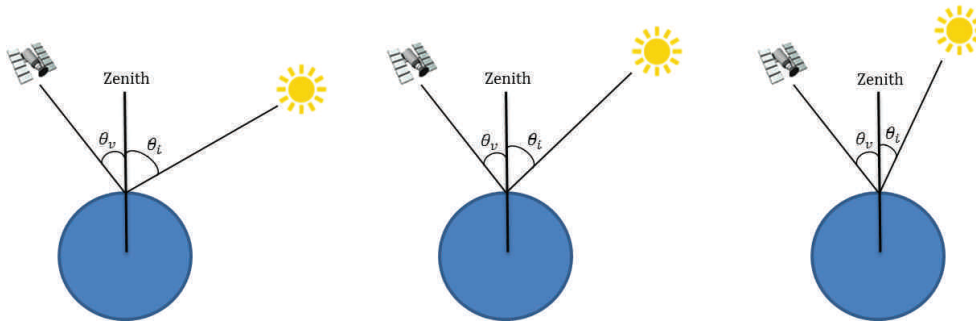


Figure 6.2: Principle of angular sampling data accumulation from geostationary satellite with  $\theta_v$  and  $\theta_i$  as view and illumination angles respectively

The approach proposed to retrieve sub-pixel corrected albedo relies on the principle of the accumulation of sub-pixel corrected reflectance values acquired under different illumination conditions which can be provided as input to the inverted RPV model. The RPV model has already proved its efficiency in several studies (Engelsen et al. 1996; Vogt et al. 2000; Koetz et al. 2005), especially for the extrapolation of reflectance values corresponding to arbitrary illumination and viewing directions (Lattanzio et al. 2007) and also for BRDF reconstruction and albedo retrieval from space as it is used operationally for the METEOSAT albedo product (EUMETSAT 2010).

The procedure to retrieve the sub-pixel corrected albedo from a set of corrected reflectance observed at different illumination angles is performed in several steps (Figure 6.3). First, it is important to insure that a minimum of six clear-sky observations with a suitable angular configuration is available for a satisfactory estimation of albedo (Govaerts et al. 2008). After atmospheric correction and cloud filtering, the set of sub-pixel topographically corrected reflectance, along with some initial surface parameters values, can be inverted against the RPV model in order to retrieve the optimized set of BRDF parameters. From the latter, the surface albedo is computed. To do so, the forward version of RPV is used. The retrieved BRDF parameters are provided to the model along with the angular range and increment steps for the different sun angles. Then the model delivers the reflectance value for the required angular sampling. The integration of those reflectance values leads to the estimation of the different albedos (section 3.3.1). To compute  $a_{BS}$ , a fixed illumination angle of  $30^\circ$  is provided, while the observation angle spreads from  $0^\circ$  to  $80^\circ$  and the relative azimuth from  $0$  to  $180^\circ$  with an increment of  $1^\circ$ . For  $a_{WS}$ , both illumination and observation angles range from  $0^\circ$  to  $80^\circ$ . The integration of  $a_{BS}$  and  $a_{WS}$  is performed according to Equations 3.12 and 3.13. Finally, the blue-sky albedo is

interpolated from  $a_{BS}$  and  $a_{WS}$  according to the method given in Román et al. (2009) using the AOD derived from MODIS to estimate the fraction of diffuse skylight  $F(\lambda, \theta_i, \phi_i)$  (Equation 3.14). Lattanzio et al. (2007) proved in their study the possibility and relevance of using consecutively the inverted and the forward version of the RPV model.

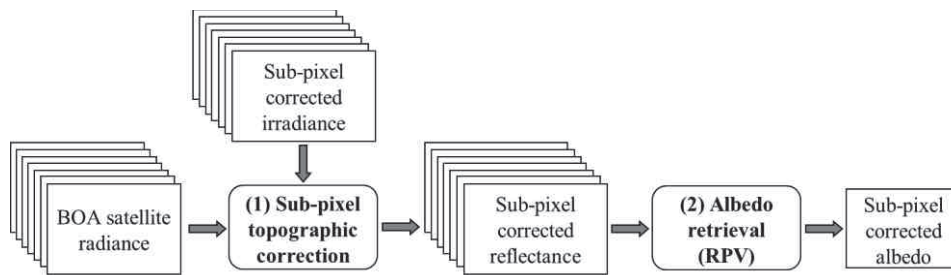


Figure 6.3: Main steps of land surface albedo retrieval using sub-pixel topographic correction

#### 6.2.4 Narrowband to broadband albedo conversion

Using geostationary satellite data recorded in one “narrow” visible band allows to derive a spectral, or “narrowband,” albedo while the actual albedo must represent the total broadband region of solar radiation, *i.e.* approximately 0.4-2.5  $\mu\text{m}$ . A conversion is then necessary to extrapolate the narrowband albedo values retrieved from geostationary sensors to the full, or “broadband,” albedo. This conversion is performed using narrowband-to-broadband conversion coefficients. There are several methods used to derive those conversion coefficients, ranging from field methods to modeling approaches. However, as it is not realistic to attempt to produce large scale applicable conversion through ground sampling, this option was not considered. A modeling approach was used to simulate many different surface, atmosphere, and viewing conditions. This approach is used in Liang et al. (2001; 2003) to produce conversion equations for a series of eight different satellite sensors and obtained accuracies of less than 0.02 when compared to ground measurements for several surface types. Many of the existing method for narrowband-to-broadband conversion are made for sensors providing measurements in several spectral bands over the visible domain. Considering the FY-2E satellite, only one band spreading between 0.4-1, is available. Thus, the method used to derive the conversion coefficient is based on the one developed for the METEOSAT first generation satellites, presenting similar sensor characteristics (Govaerts et al. 2006; Loew et al. 2010).

To derive the conversion coefficient for FY-2E, 116 spectral signatures available in the ASTER library (Baldrige et al. 2009) and 3 different atmospheric conditions were

used. The spectral signatures from different vegetation types, bare soils, water and snow were selected to cover as much as possible the type of surfaces observed in the study area. Each spectral signature was used to calculate the narrowband albedo (Equation 6.10) in the wavelength interval of the FY-2E visible band and the corresponding broadband albedo (Equation 6.11). Concerning the FY-2E albedo, the spectral reflectance was weighted by the satellite response function. Linear regressions between both values were then used to derive coefficients to convert from narrowband to broadband albedo. The FY-2E albedo ( $a_{nb}$ ) and the broadband albedo ( $a_{bb}$ ) were computed as:

$$a_{nb} = \frac{\int_{0.4}^1 f(\lambda) \rho(\lambda) E_0(\lambda) \tau(\lambda) d\lambda}{\int_{0.4}^1 f(\lambda) E_0(\lambda) \tau(\lambda) d\lambda} \quad 6.10$$

$$a_{bb} = \frac{\int_{0.4}^{2.5} \rho(\lambda) E_0(\lambda) \tau(\lambda) d\lambda}{\int_{0.4}^{2.5} E_0(\lambda) \tau(\lambda) d\lambda} \quad 6.11$$

In Equations 6.10 and 6.11,  $\rho(\lambda)$  represents the reflectance,  $f(\lambda)$  the satellite response function,  $E_0(\lambda)$  the TOA irradiance and  $\tau(\lambda)$  the atmospheric transmittance, all at a given wavelength  $\lambda$ .

Figure 6.4 shows the linear regression performed between broadband and narrowband albedo to derive the conversion coefficients. At first, some spectral signatures characterizing snow elements were included in the analysis (graph a), but as they were the ones introducing the most errors, they have been excluded (graph b). The regression between the computed broadband and narrowband albedo provides a regression slope close to 1 with an intercept close to 0, *i.e.* the estimated conversion coefficients (1.016, -0.021) can be used to retrieve the broadband albedo from FY-2E data.

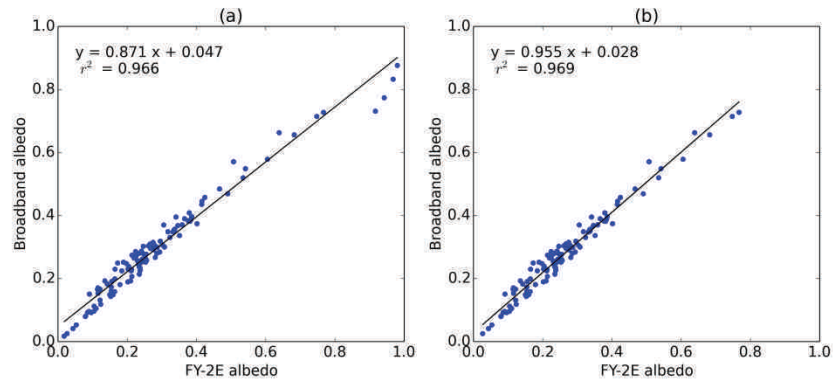


Figure 6.4: Regression between broadband and narrowband albedo to derive the conversion coefficient: (a) including and (b) without spectral signatures from snow elements

### 6.3 Sub-pixel topographically corrected reflectance

The sub-pixel topographically corrected reflectance values were derived from the satellite measured radiance using the sub-pixel corrected irradiance (Chapter 5). The relevance of applying a topographic correction at the sub-pixel level as compared to pixel level correction when retrieving surface reflectance from satellite data is evaluated quantitatively using a cloud free Landsat-7 scene. Theoretically, the correction method could be applied on different spatial resolution combinations but is tested and validated here using Landsat-7 data aggregated at 1 km resolution to simulate coarser satellite data along with the 30 m DEM over the subset study area. The Landsat data, available at 30 m resolution, can be used as ground truth and the same Landsat data aggregated at 1 km resolution are considered as radiance values measured by a geostationary satellite. For the validation, three datasets are produced and compared: (1) Landsat data at 30 m corrected using the DEM at the same resolution, which is then aggregated at 1 km. This dataset will be considered as the reference data (reference map); (2) Landsat radiometric data averaged over 1 km pixels and corrected for topography at pixel level (DEM at 1 km); (3) Landsat radiometric data averaged over 1 km but corrected for topography at sub-pixel level (DEM at 30 m).

To highlight the improvement achieved by integrating the sub-pixel topography effects in the reflectance retrieved at 1 km, the results of pixel level (2) and sub-pixel level (3) topographic correction are respectively compared to the reference map (1). The methodology is meant to be applied in the solar domain of the spectrum, thus the comparison is performed for the four first bands of the Landsat image as well as the

panchromatic band (band 8), spectrally close to the visible band of FY-2E. The differences obtained for the panchromatic band are presented in Figure 6.5 and the differences for all the processed bands are provided in Figure 6.6. Additionally, the mean and standard deviation of the difference for all the bands are summarized in Table 6.1.

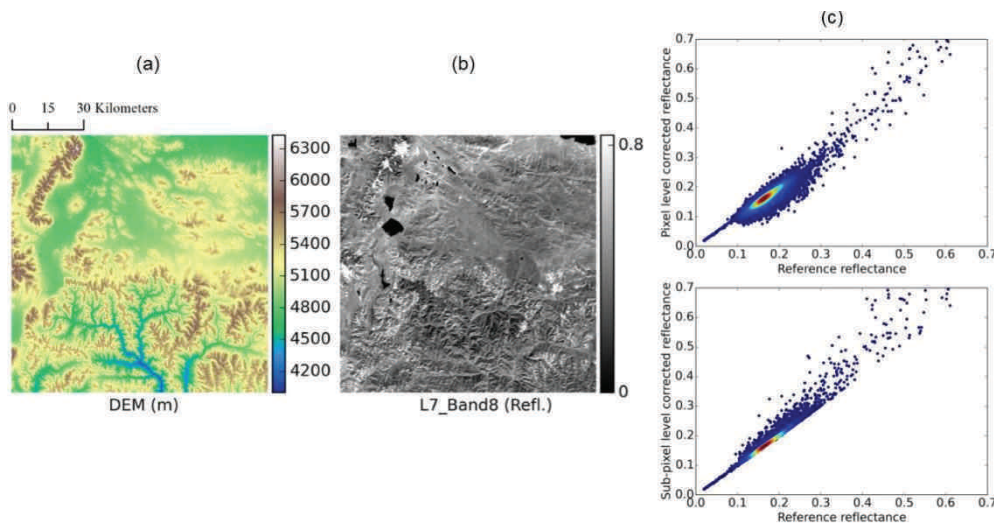


Figure 6.5: (a) Subset study area DEM, (b) Corresponding Landsat-7 scene and (c) Difference between reference reflectance and pixel (top) or sub-pixel (bottom) topographically corrected reflectance for the band 8 of Landsat-7

Figure 6.5c (top) shows a larger dispersion of the values for the difference between the reference and the pixel level correction while the difference between the reference and the sub-pixel level is more compact and located around zero. Then, the sub-pixel correction is providing better results than the pixel level one. However, when looking at the scatter plot presenting the difference between the reference reflectance and the sub-pixel topographically corrected reflectance (Figure 6.5c bottom), it seems that there is no value below the 1:1 line. Furthermore, the portion above the 1:1 line looks pretty similar for the two scatter plots. The histogram presented in Figure 6.6 (Band 8) gives more insight into this comparison showing a more compact histogram with a higher density of pixels located around zero and most of the error located above 0 for the data corrected at sub-pixel level. The proportion of positive errors still remains lower than the ones measured after the pixel level correction. This supports the conclusions drawn from Figure 6.5c showing the improvement brought by applying a topographic correction at sub-pixel level.

This result is the same for the five bands as shown by the statistics in Table 6.1 and Figure 6.6. Thus, whatever the considered band, the sub-pixel topographic correction method provides more accurate results than the pixel level correction method in all the considered bands even if this method tends to slightly overestimate the retrieved reflectance. This overestimation is the consequence of an underestimation of the surface irradiance. This may be explained by the fact that the correction method applied in this study is using the cosine law to take into account topographic effects on direct irradiance estimation (Equation 5.3) and several studies showed that this function tends to overestimate the corrected reflectance values (Kustas 2000; Richter et al. 2009; Szantoi et al. 2013). Even if the proposed correction method also takes into account diffuse and terrain irradiance, the corrected values are still overestimated. However this overestimation remains low and concerns less than 30% of the pixels and is mostly under 0.03. In contrast, the pixel level correction tends to overestimate the surface reflectance for more than 60% of the pixels and this error can reach 0.05.

Table 6.1: Difference mean and standard deviation (std) between the reference reflectance and pixel (left) or sub-pixel (right) topographically corrected reflectance for Landat-7 band 1, 2, 3, 4 and 8

	<i>Pixel Level Mean</i>	<i>Pixel Level std</i>	<i>Sub-Pixel Level Mean</i>	<i>Sub-Pixel Level std</i>
<b><i>Band 1</i></b>	0.007	0.012	-0.001	0.008
<b><i>Band 2</i></b>	0.007	0.013	-0.002	0.010
<b><i>Band 3</i></b>	0.007	0.015	-0.003	0.010
<b><i>Band 4</i></b>	0.007	0.017	-0.004	0.011
<b><i>Band 8</i></b>	0.007	0.016	-0.003	0.012

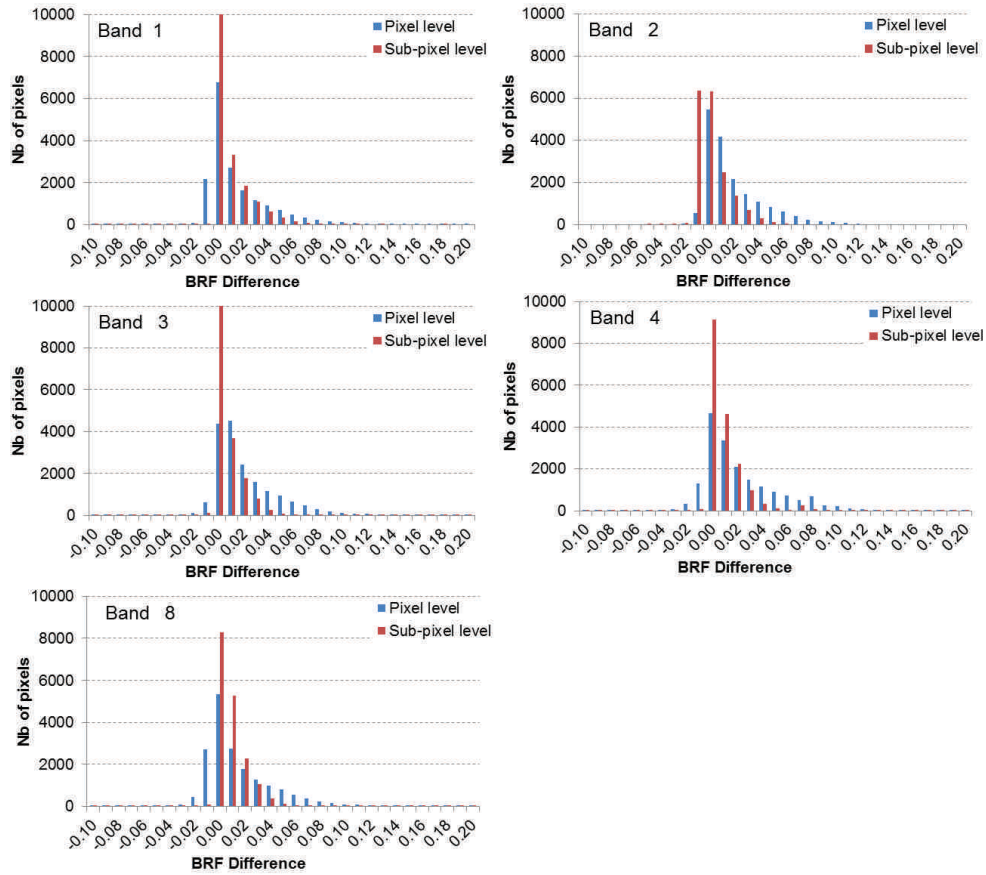


Figure 6.6: Comparison of pixel and sub-pixel topographically corrected reflectance for bands number 1, 2, 3, 4 and 8 of Landsat 7

Furthermore, to quantify the impact of sub-pixel topography on reflectance retrieved from the Landsat-7 image aggregated at 1 km resolution, the standard reflectance product (Landsat Surface Reflectance High Level Data Products<sup>16</sup>) computed without taking into account topography is compared to the sub-pixel topographically corrected reflectance. Figure 6.7a shows the reflectance difference obtained when subtracting the sub-pixel corrected reflectance map from the uncorrected reflectance map. Along with the histogram (Figure 6.7b), it shows that the sub-pixel corrected reflectance values are mostly higher than the uncorrected ones. This means that the surface reflectance is underestimated, then that the total irradiance is overestimated, when the sub-pixel topography effects are not

<sup>16</sup> [http://landsat.usgs.gov/CDR\\_LSR.php](http://landsat.usgs.gov/CDR_LSR.php)

considered. This result is logical and in line with the results presented in Chapter 5 as no shadow effect is taken into account when neglecting sub-pixel topography effects. The Landsat-7 image used was recorded on October 27<sup>th</sup> at 10.40 am (local solar time) with a sun elevation angle of  $42.5^\circ$ , *i.e.* the scene was then illuminated from the lower right corner. The only pixels without sub-pixel topographic correction where the reflectance values are higher are the pixels with a slope facing the sun (red pixels on Figure 6.7a). In this case, assuming a flat terrain led to an underestimation of the received irradiance and thus an overestimation of the reflectance.

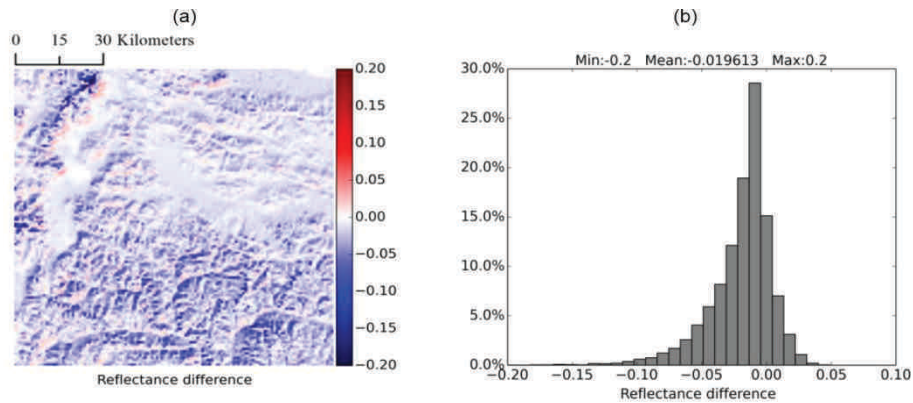


Figure 6.7: (a) Maps of the differences between reflectance values estimated from Landsat-7 band 8 with sub-pixel topographic reflectance as compared to the uncorrected reflectance value, (b) graph summarizing the distribution of those differences

The correction method is run over the FY-2E subset study area. In that case, there are also clear improvements achieved by integrating the sub-pixel topography effects in the reflectance retrieved at 1 km, as depicted in the Figure 6.8. The top line of this figure shows three irradiance maps: (a) an uncorrected irradiance map; (b) an irradiance map corrected at pixel level, using the slope and azimuth values degraded from 30 m to 1 km; and (c) an irradiance map corrected at sub-pixel level. The corresponding surface reflectance maps retrieved using those irradiance maps (Equations 6.1 and 6.2) are provided in the bottom line of the figure: (d) a surface reflectance map without any topographic correction; (e) a surface reflectance map topographically corrected at pixel level; (f) a surface reflectance map topographically corrected at sub-pixel level. From this figure and further visual checks, it appears that in areas where there is a significant topography, a higher level of radiometric detail is obtained when performing a sub-pixel topographic correction.

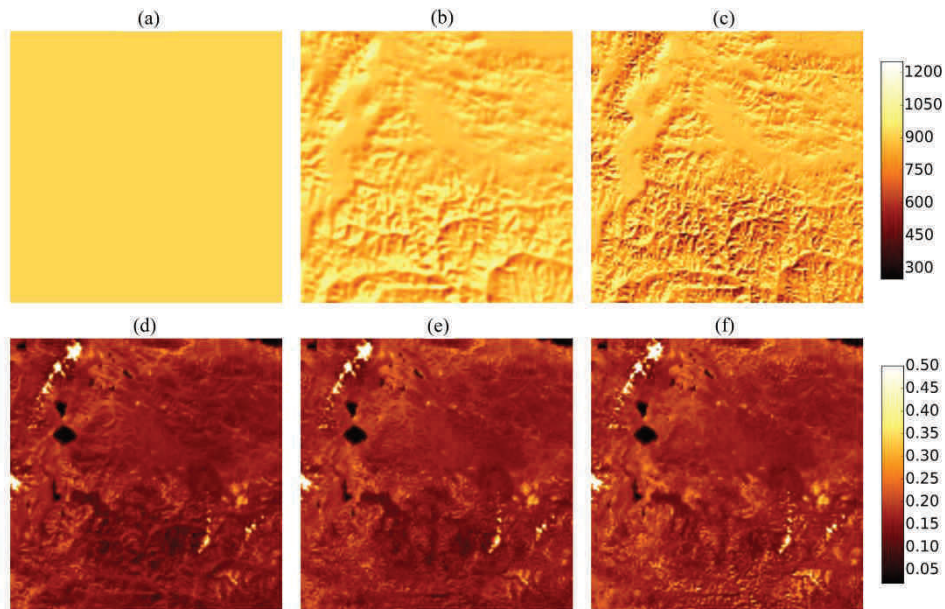


Figure 6.8: Comparison of the topographic correction at different levels. (a) Irradiance with no topographic correction ( $\text{W.m}^{-2}$ ), (b) Corrected irradiance at pixel level ( $\text{W.m}^{-2}$ ), (c) Corrected irradiance at sub-pixel level ( $\text{W.m}^{-2}$ ), (d) Surface reflectance with no topographic correction, (e) Corrected surface reflectance at pixel level, (f) Corrected surface reflectance at sub-pixel level

## 6.4 Sub-pixel topographically corrected albedo

Until now, the integration of topographic induced effects at sub-pixel level has been proved beneficial for the retrieval of reflectance from satellite data recorded over rugged areas, as over the South part of the Tibetan Plateau. Theoretically, using more accurate surface reflectance to reconstruct the surface BRDF would lead to more accurate albedo estimates. The following section verifies this hypothesis, starting with a sensitivity analysis of the albedo retrieval method to sub-pixel topography as well as to sub-pixel land cover heterogeneity. Then, the sub-pixel topography correction method was applied on real satellite data to produce albedo data for the entire year 2010 which have been used for validation and comparison with other albedo data products available.

### 6.4.1 Albedo retrieval sensitivity

Prior to validate the albedo retrieved on real FY-2E data, an analysis was performed to investigate the sensitivity of the method to sub-pixel topography but also to the sub-pixel

land cover heterogeneity. To do so, three synthetic land cover (LC) maps with different degrees of heterogeneity have been simulated: one with low (L), one with medium (M) and one with high (H) heterogeneity. Each of the maps included 5 different land cover classes in different proportions, which justify their degree of heterogeneity. The 5 classes represent land covers that can be found on the Tibetan Plateau and are characterized by their BRDF parameters values which are taken from Engelsen et al. (1996) (Table 6.2). Figure 6.9 shows the land cover classes distribution for each of the synthetic land cover map. For the relief, three topographic configurations have been selected from the DEM: one relatively flat (F), one hilly (M) and one rough area (S), as presented in Figure 6.10.

Table 6.2: Land cover classes BRDF parameters for RPV

<i>Land cover BRDF parameters</i>	$\rho_0$	$\theta_{HG}$	$k$
<i>Coniferous (1)</i>	0.013	-1.192	0.359
<i>Steppe (2)</i>	0.114	-0.394	0.882
<i>Shrubs (3)</i>	0.031	-0.270	1.061
<i>Soil (4)</i>	0.059	-1.024	0.700
<i>Grassland (5)</i>	0.179	-0.263	0.811

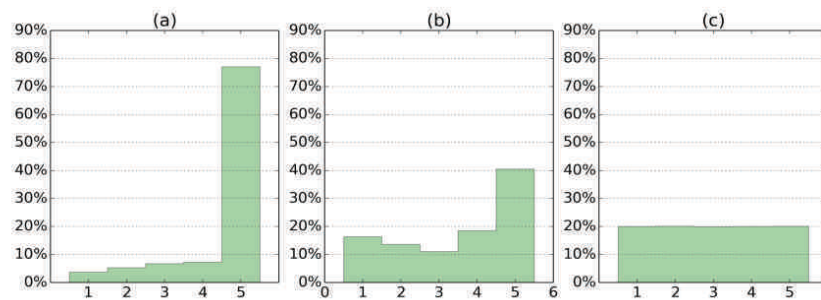


Figure 6.9: Land cover classes distribution for the three synthetic land cover maps used as input with an increasing degree of heterogeneity: (a) low, (b) medium and (c) high

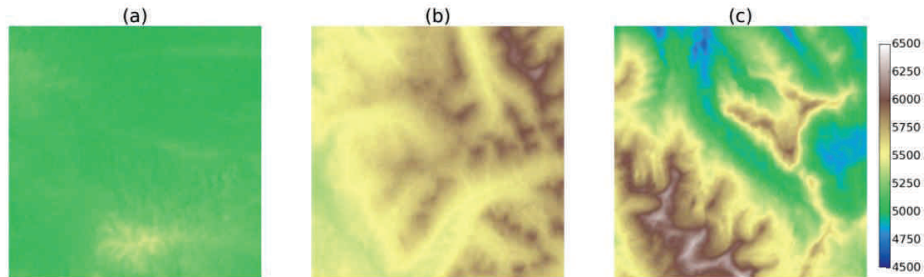


Figure 6.10: Topographic maps used as input with an increasing degree of roughness (a) relatively flat, (b) medium and (c) rough topography (Elevation in m)

In total, 9 land cover/topography combinations were tested. From the land cover BRDF parameters in combination with the view and illumination geometry derived from the DEM, 30 m resolution radiance maps could be simulated to represent actual radiance data that would be measured from a satellite, without atmospheric effects (Figure 6.11). The data are simulated hourly for the day 80 (21<sup>st</sup> of March) between 10.00 am and 6.00 pm.

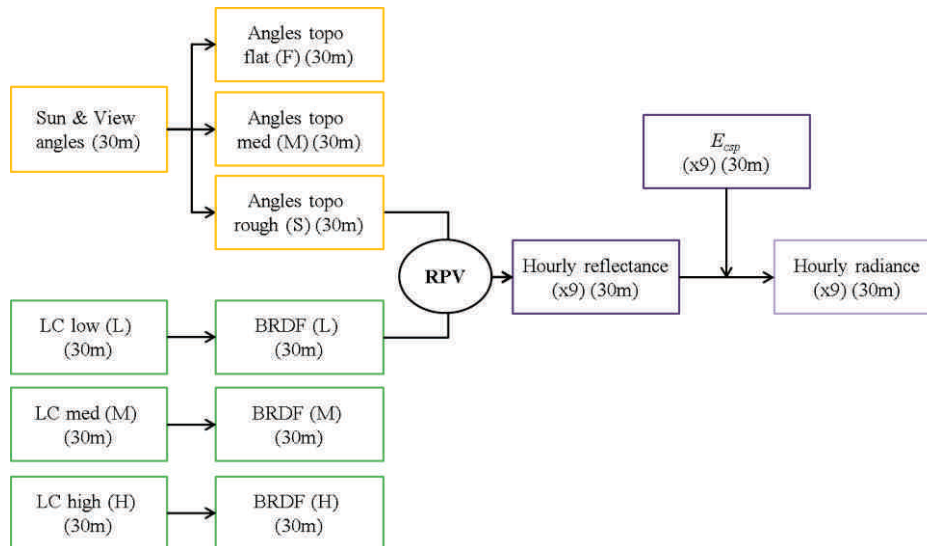
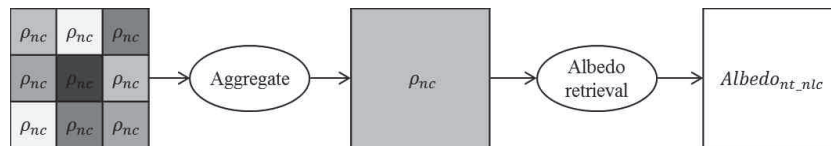


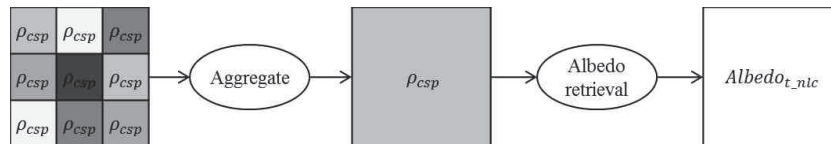
Figure 6.11: Processing steps for the simulated datasets representing the radiance data measured from a satellite, without atmospheric effects

The land cover BRDF being predefined, the actual albedo to be retrieved is known and can be used as reference for comparison. Then, four black-sky albedos are computed, based on uncorrected and sub-pixel corrected reflectance,  $\rho_{nc}$  and  $\rho_{csp}$  respectively:

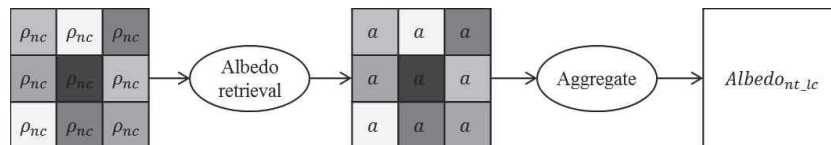
- (1) Without taking into account neither sub-pixel topography nor sub-pixel LC heterogeneity ( $Albedo_{nt\_nlc}$ )



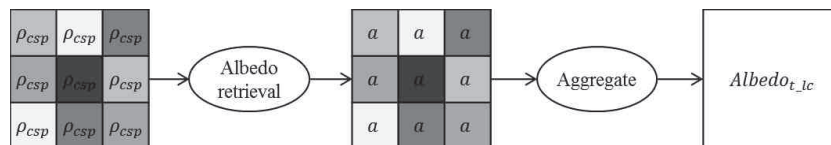
- (2) Taking into account sub-pixel topography but neglecting sub-pixel LC heterogeneity ( $Albedo_{t\_nlc}$ )



- (3) Neglecting sub-pixel topography but taking into account sub-pixel LC heterogeneity ( $Albedo_{nt\_lc}$ )



- (4) Taking into account both sub-pixel topography and sub-pixel land cover heterogeneity ( $Albedo_{t\_lc}$ )



The processing steps are detailed in Figure 6.12. The cases (3) and (4) require the albedo values at 30 m to be aggregated at 1 km. Following the energy conservation principle and knowing that the radiances can be averaged, the mean albedo is calculated using Equation 6.14.

For a given pixel  $i$ , the radiance can be expressed as:

$$L_{si} = a_{BSi} E_i \quad 6.12$$

The radiance being an energy flux density, it can be averaged:

$$\begin{aligned} \bar{L}_s &= \overline{a_{BS}} \bar{E} = \overline{a_{BS}} \times \frac{1}{n} \sum_{i=1}^n E_i \\ &= \frac{1}{n} \sum_{i=1}^n a_i E_i \end{aligned} \quad 6.13$$

Thus, the mean black-sky albedo is calculated as:

$$\overline{a_{BS}} = \frac{\sum_{i=1}^n a_i E_i}{\sum_{i=1}^n E_i} \quad 6.14$$

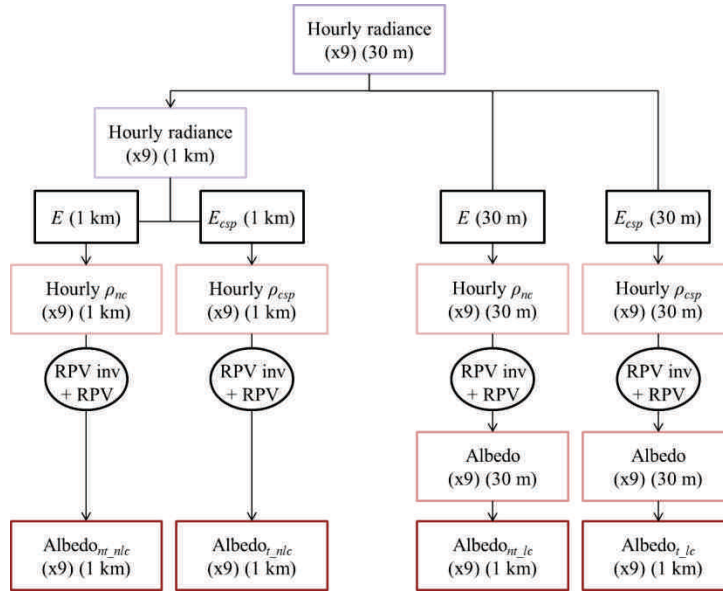


Figure 6.12: Processing steps for the computation of the uncorrected albedo, the sub-pixel topographically corrected albedo, the sub-pixel LC heterogeneity corrected albedo and sub-pixel topographically and LC corrected albedo (from left to right)

In order to evaluate the impact of the different sub-pixel corrections on the albedo estimates, each output was compared with its corresponding reference albedo, for the 9 possible combinations. The metrics used for the comparison were: the root mean square error (RMSE), the difference in inter-quartile (IQ) range and the median difference between the computed and the reference albedo. When talking about difference, in all cases, the variables derived from the computed albedos are subtracted from the reference albedo. Figure 6.13 shows in spider diagrams, the RMSE, the IQ range and median difference obtained for the 9 combinations for each of the computations. The median difference is presented in two different diagrams as this difference can be positive or negative.

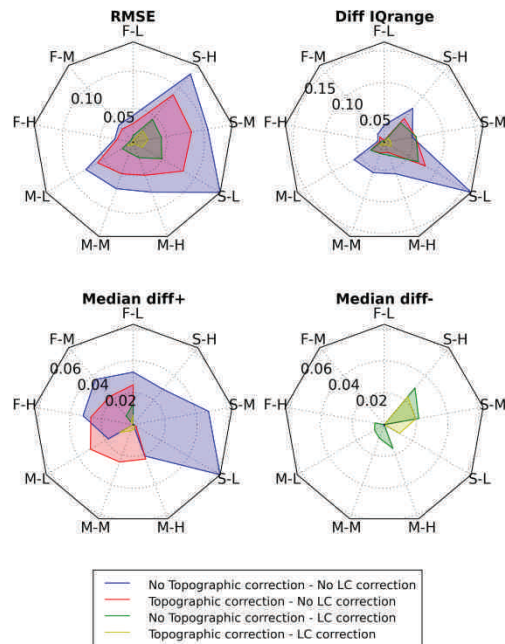


Figure 6.13: Comparison of the RMSE, the IQ range difference, the positive and negative median difference between the four computed albedos and the reference albedo

As expected, the lowest RMSE is obtained when correcting for sub-pixel topography as well as for sub-pixel LC heterogeneity and the largest RMSE occurs when no correction at all is performed. Correcting for the sub-pixel topography can reduce the RMSE by up to 0.07 as compared to no correction at all, and taking into account sub-pixel land cover heterogeneity can reduce the RMSE by up to 0.095. The largest differences are observed when the relief is rough and the LC heterogeneity is low. Over a flat terrain the difference

between the four computation methods are smaller, and only the land cover heterogeneity correction bring a significant improvement. The IQ range difference provides an indication about the dispersion of the data as compared to the reference one. As for the RMSE, the largest difference is observed over the rough relief and low LC heterogeneity when no correction is applied and the lowest when both sub-pixel corrections are carried out. However, the gain brought by either of the two corrections is similar. The median difference gives an indication about the under or overestimation of the albedo estimated by the 4 computations. When no correction is applied, the estimated albedo is generally over estimated, especially over rough relief and low LC heterogeneity. After sub-pixel topographic correction only, the values are less but still over estimated over flat and medium topography but almost completely corrected over rough topography. Applying sub-pixel LC heterogeneity correction only or both corrections lead in most of the cases to a small underestimation of the albedo.

#### **6.4.2 FY-2E albedo**

The retrieval of albedo after sub-pixel topographic correction using synthetic data showed encouraging results. The method was then tested on real case using one year of FY-2E data (2010). To accurately retrieve albedo from reflectance values measured at different illumination angles, RPV needs a minimum sample of measurements. When the set of measurements covers a good range of illumination angles, 6 valid observations are already enough to retrieve satisfying surface BRDF characteristics (Govaerts et al. 2008). So, theoretically, as the FY-2E dataset used in this study contains hourly images, there should be enough data over a day to retrieve the daily albedo. However, because of meteorological conditions and also because of the topography, the angular sampling of reflectance over a day is often not sufficient to accurately estimate the albedo. Then, in order to have accurate estimates and to meet the objective of improving the temporal resolution of albedo, a 3-day albedo time series was produced for the whole year 2010, assuming that the surface doesn't significantly change in three days. During the validation, only broadband albedos are used. The albedo retrieved from FY-2E is converted from narrowband to broadband using the coefficient provided in section 6.2.4.

The first step to validate the sub-pixel topographically corrected FY-2E albedo is to compare it to two well-known albedo products over the Gobi desert area, where the surface conditions are very stable over time and the terrain is relatively flat. Figure 6.14 presents the comparison between the MSA (METEOSAT Albedo), MODIS and FY-2E corrected and uncorrected black-sky and white-sky albedo. In this case, special narrowband to broadband albedo conversion coefficients have been computed, considering only spectral signatures characteristics from a desert area (*e.g.*: Silicate (SiO<sub>2</sub>), Quartz, Gypsum, Orthoclase). In Figure 6.14, no difference is observed between sub-pixel corrected and uncorrected FY-2E albedo. The correction method is not introducing a bias in the retrieved

albedo. It also appears that the FY-2E albedo is fluctuating more than the MODIS product. The reason could be that the albedo from MODIS comes from an operational algorithm including several filtering options, smoothing the extreme values that can be generated by mathematical functions. Furthermore, a simple cloud screening, as compared to the more advanced ones applied for the other products, is used in this research and unfiltered clouds can lead to incorrect results. The MSA fluctuates as well but as it is a 10-day product, it looks a bit more stable. However, even if the white-sky albedo is underestimated, the black sky and total albedo are, in average, coherent with the other albedo products. The FY-2E albedo shows a bell-shape trend over the year, which is not the case of the other products. When looking at the minimum, maximum and mean illumination zenith angles used as input for RPV according to the day of the year, it appears that larger illumination zenith angle values are provided at the beginning and end of the year, due to low sun position in the sky (Figure 6.15).

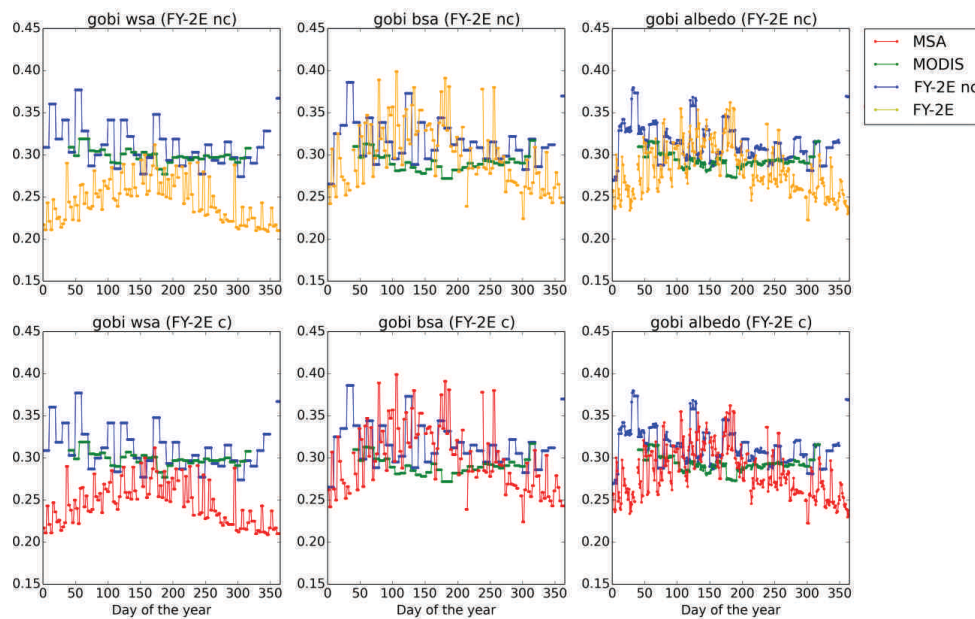


Figure 6.14: Comparison between MSA, MODIS and FY-2E uncorrected (top) black-sky and white-sky albedos and corrected (bottom) black-sky and white-sky albedos over the Gobi desert area

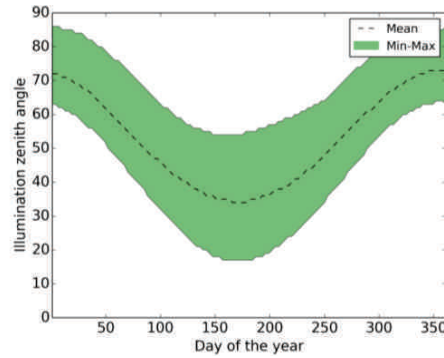


Figure 6.15: Minimum, maximum and mean illumination zenith angles used for the BRDF reconstruction over the Gobi

The mean illumination zenith angles values presents the same bell-shape pattern but inverted as compared to the FY-2E albedo. Furthermore, Figure 6.16, plotting the mean illumination zenith angle against the difference between the FY-2E albedo and the corresponding ground measurements, highlights the sensitivity of the retrieved albedo to the angular sampling provided as input to RPV. It shows that when measurements taken at large zenith angles only are available, the accuracy of the retrieved albedo as compared to the ground station is decreasing. Thus, the bell-shape trend observed for the FY-2E albedo is due to the RPV sensitivity to the angular sampling used for the BRDF reconstruction.

To validate the 3-day broadband albedo time series retrieved from the FY-2E data, the albedo values measured at the ground stations of NamCo and Qomolangma are used, along with three well known global albedo products, namely MODIS, MSA and Globalbedo. The FY-2E albedo and the three albedo products are compared to their corresponding ground values. Concerning the FY-2E albedo, the sub-pixel topographically corrected (FY-2E) and uncorrected (FY-2E nc) albedo values are used for the validation.

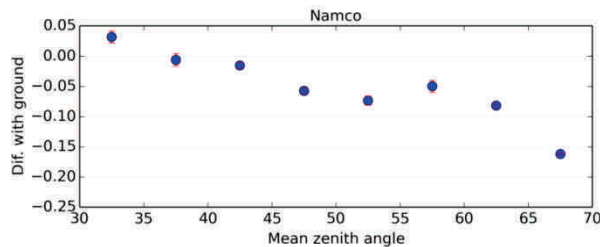


Figure 6.16: Difference between ground measured and estimated albedo according to the RPV input dataset mean zenith angle

Figure 6.17 shows the difference between ground measurements and the albedo provided by each of the products. Looking at FY-2E and FY-2E nc, it appears that for the NamCo station, which is located in a relatively flat area, the mean difference between corrected and uncorrected albedo is not very large. Only the spread of the difference is lower for corrected data. This confirms that the sub-pixel correction method does not introduce any bias in the albedo retrieval and even, is able to smooth extreme events. For the Qomolangma station, there is a clearer improvement in the corrected data as compared to the uncorrected ones. Even if surrounded by a rough terrain, the ground station is located over a relatively flat area. Then the major difference between corrected and uncorrected probably comes from the fact that the correction method takes into account adjacent terrain contribution. However the comparison with the three other albedo products shows that the FY-2E corrected albedo provides more accurate results over NamCo but less accurate results over Qomolangma. In NamCo, the mean difference with ground data is lower than the MODIS and Globalbedo and similar to MSA. In Qomolangma, the mean difference with ground data is higher than the three other products. The differences observed for the FY-2E albedo are also more spread than for the other products. As explained above, the lack of filters in the algorithm and the simple cloud screening can explain some of those largest differences observed. The sensitivity of RPV to angular sampling (Figure 6.16) is also affecting the albedo retrieved in winter time in those cases, increasing the measured error.

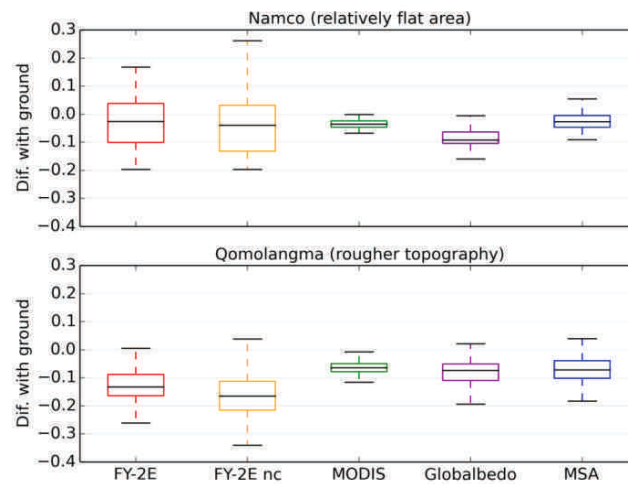


Figure 6.17: Comparison of the different albedo products with measurements at two ground stations NamCo (top) and Qomolangma (bottom). FY-2E = sub-pixel topographically corrected albedo, FY-2E nc = uncorrected albedo

The albedo estimation method provides good results over Gobi and NamCo, but not over Qomolangma even if some improvement is observed between corrected and uncorrected albedo. Further analyses were performed to explain the lower accuracy observed for the albedo retrieved over Qomolangma. The correlation with ground data is always very complex when validating albedo retrieved from space (Liang et al. 2010), especially in such heterogeneous area as the surrounding of the Qomolangma station. The ground measurement footprint of only a few square meters may be not representative of the kilometer satellite pixel value. Thus, the validation of FY-2E will be essentially performed by taking the MODIS albedo product as a reference. The first hypothesis explored to explain the differences between the FY-2E and the MODIS products is the possibility that the two sensors measured different reflectance values. Figure 6.18, comparing the TOA reflectance measured by MODIS and FY-2E, does not show any strong differences between the two sensors, keeping in mind that the spectral bands between the two sensors are not the same.

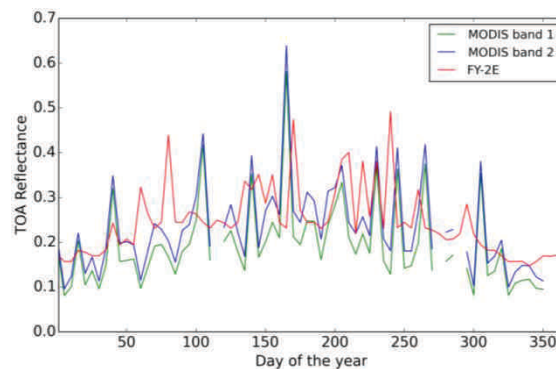


Figure 6.18: Unfiltered TOA reflectance comparison between MODIS (Band1: 0.6450 and Band2: 0.8585) and FY-2E over Qomolangma for the year 2010

As Figure 6.18 shows, the accuracy of the retrieved albedo depends on the angular sampling provided to RPV. In rough terrain, the illumination zenith angles corrected for the topography can be larger than over a flat terrain, leading to an increase of the illumination zenith sample mean. Then, the second hypothesis is that the important relief in the Qomolangma area generates angular sample with large mean illumination zenith angle values decreasing the accuracy of the retrieved albedo. To investigate this hypothesis, the different illumination zenith angles used for each 3-day products are plotted and compared with the one used for NamCo and Gobi (Figure 6.19).

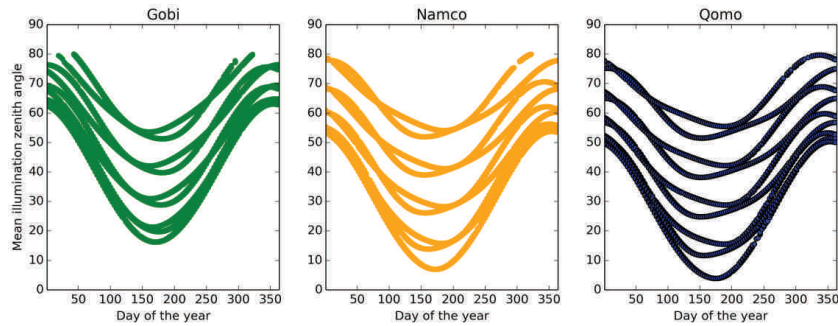


Figure 6.19: Illumination zenith angular sampling used for the BRDF reconstruction over Gobi, NamCo and Qomolangma

Figure 6.19 shows that the illumination zenith angles distribution over the year for Qomolangma is very similar to the one observed over NamCo, as well as for the number of reflectance values used (Figure 6.20). This observation and the reflectance comparison show that the problem does not come from the data provided to RPV.

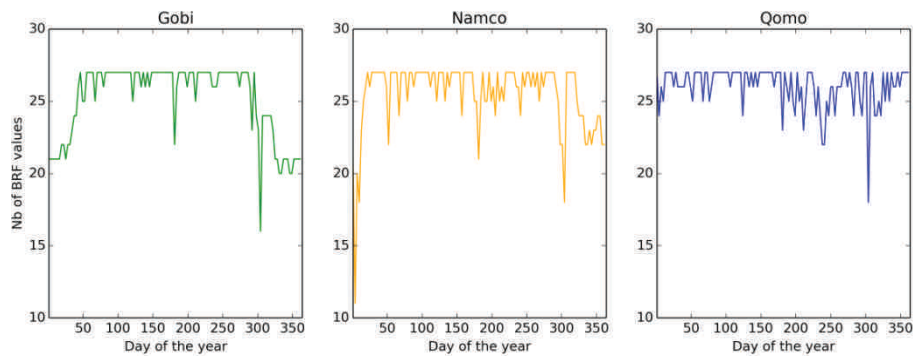


Figure 6.20: Number of reflectance measurements used to reconstruct the BRDF every 3 days over Gobi, NamCo and Qomolangma

Knowing that the RPV retrieval provides good results over Gobi and NamCo when angular sampling is satisfactory, a last hypothesis to explore in order to explain the FY-2E albedo inaccuracy over Qomolangma is the influence of the narrowband to broadband

albedo conversion. Indeed, the conversion coefficients were derived from a regression using several rocks, bare soil and vegetation spectral signatures that may compose a pixel recorded over the Tibetan Plateau (section 6.2.4), which is suitable for the NamCo area. However, the site description of the Qomolangma station provided in section 2.5.1 indicates that the land cover of the area is dominated by gravel and when looking at the albedo measured at the station, the values are mostly located around 0.3 which corresponds to bare soil or a soil with very sparse vegetation. Then, the conversion coefficients established earlier may not be suitable. Figure 6.21 provides the same inter-products comparison as the one presented in Figure 6.17, but for FY-2E broadband albedos computed with difference conversion coefficients. The initial conversion coefficients have been computed using all the spectral signatures (section 6.2.4) and the new conversion coefficients have been computed using spectral signatures from rocks only, bare soils only, vegetation only and finally the ones developed for the Gobi desert area.

Figure 6.21 highlights the strong impact of the conversion coefficients on the broadband albedo estimates. This is a common issue when retrieving albedo from space. A high resolution land cover map would be necessary to derive the land cover composition of each FY-2E pixel and then an accurate knowledge of the land cover spectral signatures would be required to characterize the pixel composition and derive the correct conversion coefficients. Unfortunately this information was not available for this research. However, according to the description of the Qomolangma site provided by Babel et al. (2011) and the visual checks performed on several satellite images, the conversion coefficients to use for this station would be the one derived for bare soils or desert areas, which provide the best estimates (Figure 6.21).

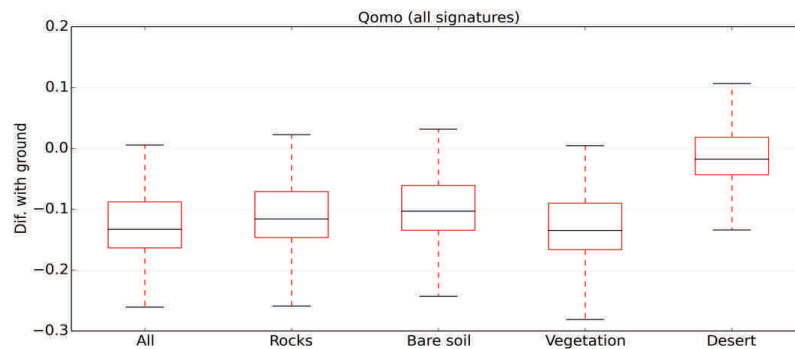


Figure 6.21: Difference between broadband albedo measured at the ground and derived from corrected FY-2E data estimated using difference conversion coefficients computed with, from left to right: all spectral signatures, rocks signatures only, bare soils signatures only, vegetation signatures only and desert elements signatures only

Another important source of error to consider is that the FY-2E data present some georeferencing inaccuracies up to 17 pixels (Zhao et al. 2014). Those errors are not constant over the entire scene and vary over time because of satellite drifting and georeferencing software instability. Then, even if they have been corrected prior to this study, some error can still remain and the fit between the DEM (or land cover map if used) and the satellite data was not always very accurate in that very heterogeneous area. The NamCo area being more homogeneous, the impact is less important there.

## 6.5 Conclusion

This chapter provided a method to correct the surface reflectance and albedo retrieved from satellite data for the sub-pixel topographic effects using the sub-pixel corrected irradiance produced in Chapter 5. Beyond the improvement of the retrieved estimates, the temporal resolution was also increased to 3-day estimates by using geostationary satellite data.

Compared with pixel level topographic correction, the sub-pixel correction method shows better results in retrieving the surface reflectance from satellite, especially over rugged area. Those results are in line with the findings of Wen et al. (2009b). The largest differences observed between the two levels of correction are linked to the more detailed integration of the effects of the underlying topography when estimating the direct solar irradiance received by the surface. Either at pixel or sub-pixel level, the corrected irradiance is mainly controlled by the shadow binary factor (section 5.2.2.4). The estimation of the latter at sub-pixel level is crucial because it allows taking into account partial shadowing at pixel level. Indeed, as it is a binary parameter, it does not consider the possibility of partial shadowing of the pixel, while a significant fraction of the area covered by a kilometeric pixel tagged as shadowed might actually see the sun. This can significantly affect the retrieved surface reflectance whereas 30 m resolution computations are much less affected by this discrepancy. In addition to the previous studies carried out on sub-pixel topographic heterogeneity, the integration of the adjacent terrain irradiance in the correction is a significant improvement as it represents an important contribution (in some cases more than 150 W.m<sup>2</sup>) to the total irradiance when a pixel does not received direct sunlight (Dozier et al. 1981).

Regarding the albedo estimation, the sensitivity analysis performed using synthetic data highlights the benefits of using sub-pixel level correction, especially in rugged areas. It also points out the necessity to consider the sub-pixel LC heterogeneity as in Liu et al. (2008). The corrected FY-2E albedo retrieved over NamCo appears more than or as accurate as other existing products. However, the conclusion concerning the albedo values retrieved over Qomolangma is less clear due to their strong dependency on the spectral conversion of the albedo from narrow to broadband. It is still interesting to notice that, in

relatively flat areas, the method does not bring any bias and in rugged areas, the albedo retrieved after sub-pixel topographic correction provides better results than with no correction. Moreover, as an improvement is observed for the sub-pixel corrected reflectance values and when using synthetic data, one can reasonably conclude that, in case of rough topography, the sub-pixel topography correction method gives the best results and that it is essential to take into account topography induced effects at sub-pixel level to accurately estimate albedo from satellite observations.

This chapter confirms the conclusions from Chapter 5 and supports the need to accurately integrate sub-pixel terrain variability within kilometeric pixel to improve the estimation of albedo and thus the estimation of solar radiation budget from space. Furthermore, the use of hourly geostationary satellite data allows the production of 3-day albedo products while the MODIS albedo products used in Chapter 3 is an 8-day product. This improvement is also very valuable as surface properties can change very quickly over the Plateau. The use of higher temporal resolution data such as from MSG or the coming FY-2 satellites would certainly lead to even finer temporal resolution. Finally, the albedo spectral conversion remains a difficult issue and the use of better information about the underlying land cover would help improving this aspect.

## Chapter 7

# Conclusions and perspectives

The solar radiation budget is one of the essential climate variables, requiring consistent monitoring to better understand the climatic evolution (GCOS-128 2009). For climate studies, global coverage data on solar radiative fluxes at the surface are necessary. Thus, this thesis focuses on improving solar radiation budget monitoring over large and heterogeneous areas. The estimation of the solar radiation budget from satellite radiometric data already showed promising results to overcome the inherent limitations in spatial sampling of ground measurements. . However, current methods showed limitations over heterogeneous areas mainly due to the rough topography and cloud cover. Moreover, existing large area datasets are available at spatial and/or temporal resolutions which do not capture local variations. The main objective of this thesis was to propose an operational method which could provide daily solar radiative fluxes estimates at the square kilometer spatial resolution for climate modelling and other applications, along with some investigations to further improve the retrieval method by taking into account the sub-pixel variability of topography and spatial and temporal variability of clouds. Because of its extreme topography and interesting cloud coverage pattern and its major role in the

hydrology and climatology of the entire South East Asia, the Tibetan Plateau was selected as study area. This thesis, following three research questions, explored: (1) the possibility to derive the solar radiative fluxes from existing satellite data products, (2) the impact of cloud cover spatial and temporal characteristics retrieved from hemispherical images on radiative fluxes both measured at the ground and (3) the possibility to integrate terrain induced effects in the estimated surface irradiance and albedo at the sub-pixel level. After summarizing the key findings of this thesis in section 7.1, the research perspectives to improve solar radiation budget monitoring from space are provided in section 7.2.

## 7.1 Achievements

An operational method was developed to estimate the solar radiation budget instantaneously and daily, at the square kilometer level, and applied over the Tibetan Plateau using existing MODIS data products (Chapter 3). This method takes into account the terrain mean slope and azimuth in the computation of the local illumination angle to estimate surface irradiance and uses actual atmospheric and land surface properties characteristics derived from MODIS data products. The algorithm was used to produce a 3-year time series of instantaneous and daily solar radiative fluxes between 2008 and 2010 over the entire Tibetan Plateau. Even if the estimates are not more accurate than the ones from the other existing solar radiation datasets covering that area, this method offers a better spatial and temporal resolution. However, one of its main shortcomings is that the sub-pixel variability is neglected while working at the square kilometer resolution over a highly heterogeneous area. Thus, investigations to improve the estimation of large area solar radiation budget by taking into account the spatial and temporal distribution of the clouds (Chapter 4) and the spatial variability of the topography (Chapter 5 and 6) have been conducted.

To investigate the impact of cloud spatial distribution on solar radiative fluxes and temporal variability on sunshine duration and daily solar radiation budget estimates, a fieldwork experiment was set up to collect hemispherical images from the sky at very high temporal resolution simultaneously to solar radiative fluxes measured at the ground. The images were used to retrieve indices characterizing the cloud cover and to estimate sunshine duration. Next, the indices were correlated to the fluxes measured at the ground and the sunshine duration used to temporally aggregate instantaneous solar radiative fluxes. The validation shows that the proposed method can retrieve operationally cloud fraction and spatial distribution from the hemispherical images, providing estimates more accurate and consistent than estimations by human observers. From the correlation analysis, it appears that, even if the longwave downward radiative fluxes are directly influenced by the cloud fraction, the solar irradiance is mostly impacted by the cloud distribution. Information on cloud spatial distribution is then essential for surface irradiance modelling.

Furthermore, the use of high temporal resolution observations to estimate sunshine duration points out the sensitivity of this parameter to the data collection frequency. In line with the correlation analysis, it also shows that taking into account the cloud distribution, using the cloud fraction weighted by the angular distance to the sun when estimating sunshine duration, provides the most accurate temporal average of the solar radiation budget. The proposed approach is easy to set up and the retrieved information could greatly improve the solar radiation modelling but is only feasible at local scale. Nevertheless, the results are very valuable as they give indications on the kind of information that needs to be retrieved from satellite images, for instance the cloud fraction weighted by the distance to the sun, in order to estimate the solar radiation budget over large areas.

To take into account the influence of the sub-pixel terrain spatial variability on surface irradiance and albedo retrieved from space, a new topographic correction method was developed and evaluated: the topographic correction at sub-pixel level. The idea is to take advantage of the finer spatial resolution of available global DEM to correct for the effects of topography on the surface radiative fluxes estimated at the kilometric level. The application of the sub-pixel topographic correction on synthetic and real data highlights the necessity to take into account topography effects when estimating surface irradiance and evaluates the errors as reaching up to  $600 \text{ W.m}^{-2}$  if these effects are neglected. As the sub-pixel correction method considers separately the direct and diffuse components of the irradiance, the impact of atmosphere -expressed by the fraction of diffuse skylight- on the corrected irradiance is also analyzed and proven important. Even for a comparable total irradiance value, different partitioning between direct and diffuse irradiance can lead to different irradiance estimates after sub-pixel topographic correction. It is then required to retrieve the actual atmospheric conditions as accurately as possible to estimate properly the sub-pixel corrected surface irradiance. Next, the latter is used to retrieve the surface reflectance from geostationary satellite data which in turn is used to reconstruct the surface BRDF and derive the sub-pixel topographically corrected albedo. Compared to pixel level topographic correction, the reflectance and albedo estimated after sub-pixel correction provide better results. However, because of the problem encountered to estimate the coefficients for narrow-to-broadband conversion, the validation and the comparison with other data products were difficult. Even so, the results show that, in a relatively flat area, the method does not bring any bias and in rugged areas, the albedo retrieved after sub-pixel topographic correction provides better results than with no or pixel level correction. Additionally the retrieved albedo is more than or as accurate as other existing products and, for the Namco station, within the climate and weather forecast requirements with an absolute accuracy of 0.02 (Liang et al. 2010). Thus, the sub-pixel correction method proposed in this thesis allows taking into account the sub-pixel terrain variability when working with large pixels which can greatly improve the estimation of irradiance and albedo, and therefore the solar radiation budget estimated from space.

Finally, the albedo retrieval method based on geostationary satellite data, providing hourly observations, allows to increase the temporal resolution of the produced albedo to 3 days against 8 days for MODIS and 10 days for METEOSAT. This improvement is also very beneficial to solar radiation budget estimation as in Chapter 3 the low temporal resolution of the albedo was quoted as a weakness of the retrieval method. The use of higher temporal resolution data such as from MSG or the coming FY-2 satellites could lead to even finer temporal resolution.

## 7.2 Perspectives

The operational method developed in this thesis to derive solar radiative fluxes daily and at the square kilometer using satellite data products, led to the production of a solar radiation budget time series. Even though it is a significant improvement in comparison to existing large area datasets available over the Tibetan Plateau as regard the spatial and temporal resolution, the retrieval of solar radiation over heterogeneous areas could still be improved. To do so, two approaches have been proposed to address the sub-pixel heterogeneity issue in terms of spatial variability of the topography and distribution of the clouds along with the temporal variability of the cloud cover and its relation to temporal aggregation of radiative flux estimates.

The investigation of the impact of cloud cover spatial and temporal variability on solar radiative fluxes at the ground was a first attempt to automatically retrieve cloud fraction and distribution at very high temporal frequency and to relate them with ground measured radiative fluxes. Despite the very good results achieved, further work could be performed to enhance the proposed approach. Regarding the classification of the hemispherical images, the cloud detection within and around the sunspot should be improved as this area was proven as being an essential part of the image when dealing with solar irradiance. In that regard, the experiment could be completed by combining the current system with additional sensors, such as a sun tracking system and an infrared camera. This would probably help for the validation of the sunspot and direct radiation detection and allow to overcome the limitations due to using only RGB information. Additionally, some research could be conducted to extract further cloud information such as cloud thickness and height for example. When looking into the correlation with the radiative fluxes, the analysis could benefit from using higher ground measurements frequency than 10-minutes average, as significant variations in the cloud cover are observed in less than 10 minutes. It is also essential to run this test over a longer period of time in order to strengthen the correlation between cloud cover characteristics and surface radiative fluxes. The main objective is to find the best way to take into account cloud coverage in solar radiative budget estimations and see how this could be retrieved from satellite data to enable large area applications. For the time being, the cloud fraction weighted by the

angular distance to the sun appears to be a good proxy for cloud spatial distribution when dealing with solar radiation budget. In that context, the way forward would be to work on its retrieval from satellite data instead of the commonly used cloud fraction. This would help overcoming the inherent limitation in the spatial sampling provided by all ground measurements and to estimate sunshine duration over large areas. The use of geostationary satellite data, such as provided by MSG or FY-2 series, should be favored as it provides high temporal resolution observations very beneficial to retrieve the sunshine duration and for the temporal aggregation of estimated fluxes. Beyond the scope of this thesis, the information retrieved on cloud distribution by the proposed approach could benefit other applications, *e.g.* to take into account the actual distribution of the radiative forcing in 3D radiative and energy balance models, especially for case studies where orientation effects may be strong (*e.g.* rough relief or urban areas). Moreover, this experiment, performed locally, could be easily transferable to other locations where such measurements could be very beneficial to the currently collected weather station data.

The second approach, dealing with the sub-pixel topographic correction method, allows to improve the estimation of surface irradiance, reflectance and albedo derived using satellite data. The results clearly show a more accurate retrieval of the reflectance, even if it tends to slightly overestimate it. This overestimation could probably be corrected by replacing the cosine law function used in the first term of Equation 5.3 by a more efficient correction method, *e.g.* the Minneart function. As the overestimation remains quite small, it could also be due to the Lambertian surface assumption when computing the irradiance received from the adjacent terrain or to neglecting multiple reflection. Even if the anisotropy property of the surface was not proven as being a primary influencing factor, its integration in the sub-pixel topographic correction should be further investigated. Regarding the albedo retrieval, the sensitivity analysis shows an improvement due to the sub-pixel correction but also points out that, depending on its heterogeneity, the land cover affects the albedo estimation. Thus, a way to further improve the albedo estimates would be to integrate the sub-pixel land cover heterogeneity as well. However, when applied on real geostationary satellite data, the benefits of the correction method are less obvious, mainly because of the georeferencing issue with FY-2E data and the difficulties to define the narrow-to-broadband conversion coefficients. To reinforce those conclusions, it would be interesting to perform again this analysis but after georeferencing accurately the FY-2E data or using other geostationary satellite data, and the narrow-to-broadband conversion coefficients should be estimated using real land cover information. Additionally, a more efficient cloud screening would improve the entire process by helping to discriminate more efficiently the pixels contaminated by clouds and avoiding distortions in the BRDF reconstruction. Moreover, even if reliable, the RPV model used for the BRDF reconstruction appears to be sensitive to the input angular sampling. This should be investigated to define more accurately how to build up a suitable multi-angle observations

dataset and thus ensure correct albedo retrieval. A last point to explore in order to improve the albedo retrieval accuracy and temporal frequency would be to use more recent data from the enhanced FY-2 geostationary satellites: the FY-2F/G, launched in 2012 and 2014 respectively, and the forthcoming FY-2H, providing image data every 30 minutes. In other respects, the sub-pixel correction method used with pixel level data at 1km and sub-pixel level DEM at 30m in this thesis could be applied with other spatial resolution combinations. Then, the improvements due to this method could be very beneficial for the retrieval of reflectance with other sensors, *e.g.* on geostationary satellites such as MSG, FY-2 or GOES (Geostationary Operational Environmental Satellites), prior to be used for further products extraction. It is important to underline that the gain in accuracy as compared to the pixel level correction increases with the complexity of the underlying topography. Since sub-pixel level correction requires more computation time, the areas where it should be applied should be targeted when working at global scale.

Finally, the two approaches proposed to deal with the sub-pixel variability of the terrain and the clouds respectively should be applied over large areas in order to produce new surface irradiance and albedo satellite data. The latter could then be used as input to the solar radiation budget estimation method to quantify the improvement that can be achieved. In the near future, new or improved satellite data products will be made available and it will be interesting to use them as a replacement of the actual inputs of the method and to measure the actual benefit on the solar radiation budget estimation.

---

## References

- Allen, R.G., Trezza, R. & Tasumi, M., 2006. Analytical integrated functions for daily solar radiation on slopes. *Agricultural and Forest Meteorology*, 139(1-2), pp.55–73.
- Augustine, J.A., Hodges, G.B., et al., 2005. An Update on SURFRAD—The GCOS Surface Radiation Budget Network for the Continental United States. *Journal of Atmospheric and Oceanic Technology*, 22(10), pp.1460–1472.
- Babel, W., Eigenmann, R., et al., 2011a. *Analysis of turbulent fluxes and their representativeness for the interaction between the atmospheric boundary layer and the underlying surface on Tibetan Plateau, CEOP-AEGIS Deliverable Report De1.2*, University of Strasbourg, France.
- Babel, W., Li, M., et al., 2011b. *Aerodynamic and thermodynamic variables for four stations on Tibetan Plateau – Introduction on the CEOP-AEGIS database in NetCDF, CEOP-AEGIS Deliverable Report De1.3*, University of Strasbourg, France.
- Badescu, V., 2008. *Modeling Solar Radiation at the Earth's Surface*, V. Badescu, ed., Berlin, Heidelberg: Springer Berlin Heidelberg.
- Baede, A.P.M., Ahlonsou, E., et al., 2001. The Climate System:an Overview. In *Climate Change 2001: The Scientific Basis. Contribution of Working Group I to the Third Assessment Report of the Intergovernmental Panel on Climate Change*. Cambridge, United Kingdom and New York, NY, USA, p. 881.
- Baldridge, A.M., Hook, S.J., et al., 2009. The ASTER spectral library version 2.0. *Remote Sensing of Environment*, 113(4), pp.711–715.
- Baraldi, A., 2009. Impact of Radiometric Calibration and Specifications of Spaceborne Optical Imaging Sensors on the Development of Operational Automatic Remote Sensing Image Understanding Systems. *IEEE Journal of Selected Topics in Applied Earth Observations and Remote Sensing*, 2(2), pp.104–134.
- Baraldi, A., Girona, M. & Simonetti, D., 2010. Operational Two-Stage Stratified Topographic Correction of Spaceborne Multispectral Imagery Employing an Automatic Spectral-Rule-Based Decision-Tree Preliminary Classifier. *IEEE Transactions on Geoscience and Remote Sensing*, 48(1), pp.112–146.
- Barkstrom, B.R., 1984. The Earth Radiation Budget Experiment (ERBE). *Bulletin of the American Meteorological Society*, 65(11), pp.1170–1185.

- Bisht, G. & Bras, R.L., 2010. Estimation of net radiation from the MODIS data under all sky conditions: Southern Great Plains case study. *Remote Sensing of Environment*, 114(7), pp.1522–1534.
- Bisht, G., Venturini, V., et al., 2005. Estimation of the net radiation using MODIS (Moderate Resolution Imaging Spectroradiometer) data for clear sky days. *Remote Sensing of Environment*, 97(1), pp.52–67.
- Bisht, R.C., 2008. *International Encyclopaedia Of Himalayas (Vol.1)*, New Delhi, India: Mittal publications.
- Blanc, P., Gschwind, B., et al., 2011. The HelioClim project: Surface solar irradiance data for climate applications. *Remote Sensing*, 3(2), pp.343–361.
- Borel, J.L., Durand, Y., et al., 1998. Computing the radiative balance in mountainous areas: Modelling, Simulation and Visualization. *ERCIM News*, 34, pp.24–28.
- Bothe, O., Fraedrich, K. & Zhu, X., 2011. Large-scale circulations and Tibetan Plateau summer drought and wetness in a high-resolution climate model. *International Journal of Climatology*, 31(6), pp.832–846.
- Brisson, A., LeBorgne, P. & Marsouin, A., 1999. *Development of Algorithms for Surface Solar Irradiance retrieval at O&SI SAF low and Mid Latitude*, Météo-France/SCEM/CMS, Lannion, France.
- Brown, S., 2012. Measures of Shape: Skewness and Kurtosis. *Oak Road Systems*. Available at: [http://www.tc3.edu/instruct/sbrown/stat/shape.htm#Skew\\_CI](http://www.tc3.edu/instruct/sbrown/stat/shape.htm#Skew_CI).
- Buch, K.A., Sun, C.H. & Thorne, L.R., 1995. Cloud Classification Using Whole-Sky Imager Data. In *5th Atmospheric Radiation Measurement Science Team Meeting*. San Diego, CA, USA, pp. 19–23.
- Calbó, J. & Sabburg, J., 2008. Feature Extraction from Whole-Sky Ground-Based Images for Cloud-Type Recognition. *Journal of Atmospheric and Oceanic Technology*, 25(1), pp.3–14.
- Carrer, D., Geiger, B., et al., 2009. Land surface albedo from MSG/SEVIRI: Retrieval method, validation, and application for weather forecast. In *2009 IEEE International Geoscience and Remote Sensing Symposium*. IEEE, pp. IV–288–IV–291.
- Carroll, J.J., 1985. Global transmissivity and diffuse fraction of solar radiation for clear and cloudy skies as measured and as predicted by bulk transmissivity models. *Solar Energy*, 35(2), pp.105–118.
- Cazorla, A., Olmo, F.J. & Alados-Arboledas, L., 2008. Development of a sky imager for cloud cover assessment. *Journal of the Optical Society of America A*, 25(1), pp.29–39.

- Cescatti, A., Marcolla, B., et al., 2012. Intercomparison of MODIS albedo retrievals and in situ measurements across the global FLUXNET network. *Remote Sensing of Environment*, 121, pp.323–334.
- Cess, R.D., Zhang, M.H., et al., 1995. Absorption of solar radiation by clouds: Observations versus models. *Science*, 267(5197), pp.496–499.
- Chen, R., Kang, E., et al., 2007. An hourly solar radiation model under actual weather and terrain conditions: A case study in Heihe river basin. *Energy*, 32(7), pp.1148–1157.
- Chow, F.K., Weigel, A.P., et al., 2006. High-Resolution Large-Eddy Simulations of Flow in a Steep Alpine Valley. Part I: Methodology, Verification, and Sensitivity Experiments. *Journal of Applied Meteorology and Climatology*, 45(1), pp.63–86.
- Corripio, J.G., 2003. Vectorial algebra algorithms for calculating terrain parameters from DEMs and solar radiation modelling in mountainous terrain. *International Journal of Geographical Information Science*, 17(1), pp.1–23.
- Crispim, E.M., Ferreira, P.M. & Ruano, A.E., 2008. Prediction of the solar radiation evolution using computational intelligence technique and cloudiness indices. *International Journal of Innovative Computing, Information and Control*, 4(5), pp.1121–1133.
- Dedieu, G., Deschamps, P.Y. & Kerr, Y.H., 1987. Satellite estimation of solar irradiance at the surface of the earth and of surface albedo using a physical model applied to Meteosat data. *Journal of Climate & Applied Meteorology*, 26(1), pp.79–87.
- Deneke, H.M., Feijt, A.J. & Roebeling, R.A., 2008. Estimating surface solar irradiance from METEOSAT SEVIRI-derived cloud properties. *Remote Sensing of Environment*, 112(6), pp.3131–3141.
- Diner, D.J., Braswell, B.H., et al., 2005. The value of multiangle measurements for retrieving structurally and radiatively consistent properties of clouds, aerosols, and surfaces. *Remote Sensing of Environment*, 97(4), pp.495–518.
- Dozier, J., Bruno, J. & Downey, P., 1981. A faster solution to the horizon problem. *Computers & Geosciences*, 7(2), pp.145–151.
- Dozier, J. & Frew, J., 1990. Rapid calculation of terrain parameters for radiation modeling from digital elevation data. *IEEE Transactions on Geoscience and Remote Sensing*, 28(5), pp.963–969.
- Dubayah, R. & Rich, P.M., 1995. Topographic solar radiation models for GIS. *International Journal of Geographical Information Systems*, 9(4), pp.405–419.
- Duguay, C.R., 1995. An approach to the estimation of surface net radiation in mountain areas using remote sensing and digital terrain data. *Theoretical and Applied Climatology*, 52(1-2), pp.55–68.

- Engelsen, O., Pinty, B., et al., 1996. *Parametric Bidirectional Reflectance Factor Models: Evaluation, Improvements and Applications*, Report EUR16426EN, European Commission, Joint Research Centre, Space Application Institute, Ispra, Italy.
- EUMETSAT, 2010. *Meteosat Surface Albedo (MSA) Product User 's Manual and Format Guide*, EUM/FG/13, MSA version 2.1, May 2010.
- Ferreira, P.M., Martins, I.A.C. & Ruano, A.E., 2010. Cloud and clear sky pixel classification in ground-based all-sky hemispherical digital images. In *IFAC Proceedings Volumes (IFAC-PapersOnline)*. pp. 273–278.
- Fu, C.L. & Cheng, H.Y., 2013. Predicting solar irradiance with all-sky image features via regression. *Solar Energy*, 97, pp.537–550.
- Gautier, C., Diak, G. & Masse, S., 1980. A Simple Physical Model to Estimate Incident Solar Radiation at the Surface from GOES Satellite Data. *Journal of Applied Meteorology*, 19(8), pp.1005–1012.
- GCOS, 2007. *Global Climate Observing System, ensuring the availability of global observations for climate*, World Meteorological Organization (WMO), Geneva, Switzerland.
- GCOS-128, 2009. *Guideline for the Generation of Satellite-based Datasets and Products meeting GCOS Requirements*, World Meteorological Organization (WMO)/TD No. 1488, Geneva, Switzerland.
- Geiger, B., Carrer, D., et al., 2008. Land Surface Albedo Derived on a Daily Basis From Meteosat Second Generation Observations. *IEEE Transactions on Geoscience and Remote Sensing*, 46(11), pp.3841–3856.
- Geraldi, E., Romano, F. & Ricciardelli, E., 2012. An advanced model for the estimation of the surface solar irradiance under all atmospheric conditions using MSG/SEVIRI data. *IEEE Transactions on Geoscience and Remote Sensing*, 50(8), pp.2934–2953.
- Ghonima, M.S., Urquhart, B., et al., 2012. A method for cloud detection and opacity classification based on ground based sky imagery. *Atmospheric Measurement Techniques*, 5(11), pp.2881–2892.
- Gilgen, H. & Ohmura, A., 1999. The Global Energy Balance Archive. *Bulletin of the American Meteorological Society*, 80(5), pp.831–850.
- Gobron, N. & Lajas, D., 2002. A new inversion scheme for the RPV model. *Canadian Journal of Remote Sensing*, 28(2), pp.156–167.
- Gonzales, Y., Lopez, C. & Cuevas, E., 2012. Automatic observation of cloudiness: Analysis of all-sky images. In *TECO-2012, WMO Technical Conference on Meteorological and Environmental Instruments and Methods of Observation*. Brussels, Belgium.

- Govaerts, Y.M., Lattanzio, A., et al., 2008. Generating global surface albedo products from multiple geostationary satellites. *Remote Sensing of Environment*, 112(6), pp.2804–2816.
- Govaerts, Y.M., Pinty, B., et al., 2006. Spectral Conversion of Surface Albedo Derived From Meteosat First Generation Observations. *IEEE Geoscience and Remote Sensing Letters*, 3(1), pp.23–27.
- Gueymard, C.A., 2003a. Direct solar transmittance and irradiance predictions with broadband models. Part I: detailed theoretical performance assessment. *Solar Energy*, 74(5), pp.355–379.
- Gueymard, C.A., 2003b. Direct solar transmittance and irradiance predictions with broadband models. Part II: validation with high-quality measurements. *Solar Energy*, 74(5), pp.381–395.
- Hammer, A., Heinemann, D., et al., 2003. Solar energy assessment using remote sensing technologies. *Remote Sensing of Environment*, 86(3), pp.423–432.
- Hansen, L.B., Kamstrup, N. & Hansen, B.U., 2002. Estimation of net short-wave radiation by the use of remote sensing and a digital elevation model—a case study of a high arctic mountainous area. *International Journal of Remote Sensing*, 23(21), pp.4699–4718.
- Harshvardhan, R.C.E., 1995. Simple parameterizations of the radiative properties of cloud layers: a review. *Atmospheric Research*, 35(2-4), pp.113–125.
- Hay, J.E., 1979. Calculation of monthly mean solar radiation for horizontal and inclined surfaces. *Solar Energy*, 23(4), pp.301–307.
- Heinle, A., Macke, A. & Srivastav, A., 2010. Automatic cloud classification of whole sky images. *Atmospheric Measurement Techniques*, 3(3), pp.557–567.
- Helbig, N. & Löwe, H., 2014. Parameterization of the spatially averaged sky view factor in complex topography. *Journal of Geophysical Research: Atmospheres*, 119(8), pp.4616–4625.
- Hollmann, R., Mueller, R.W. & Gratzki, A., 2006. CM-SAF surface radiation budget: First results with AVHRR data. *Advances in Space Research*, 37(12), pp.2166–2171.
- Holloway, J.L. & Manabe, S., 1971. Simulation of Climate by a Global General Circulation Model. *Monthly Weather Review*, 99(5), pp.335–370.
- IPCC, 2007. *Climate Change 2007: The Physical Science Basis. Contribution of Working Group I to the Fourth Assessment Report of the Intergovernmental Panel on Climate Change* S. Solomon, D. Qin, et al., eds., Cambridge, United Kingdom and New York, NY, USA: Cambridge University Press.
- Iqbal, M., 1983. *An Introduction to Solar Radiation*, Academic Press.

- Jacobowitz, H., Soule, H.V., et al., 1984. The earth radiation budget (ERB) experiment: an overview. *Journal of Geophysical Research: Atmospheres*, 89(D4), pp.5021–5038.
- Jacquemoud, S., Verhoef, W., et al., 2009. PROSPECT+SAIL models: A review of use for vegetation characterization. *Remote Sensing of Environment*, 113(SUPPL. 1), pp.S56–S66.
- Jeong, M.J. & Li, Z., 2010. Separating real and apparent effects of cloud, humidity, and dynamics on aerosol optical thickness near cloud edges. *Journal of Geophysical Research: Atmospheres*, 115(D7).
- Jia, L. & Menenti, M., 2006a. Response of vegetation photosynthetic activity to net radiation and rainfall: a case study on the Tibetan Plateau by means of Fourier analysis of MODIS fAPAR time series. *Advances in Earth Sciences*, 21, pp.1254 – 1259.
- Jia, L., Roupioz, L., et al., 2011b. *Anomalies maps of net radiation, LST and FPAR, CEOP-AEGIS Deliverable Report De9.7*, University of Strasbourg, France.
- Jia, L., Zhou, J., et al., 2011. *Tools for time series analysis of vegetation response to drought & Tools for drought prediction by analyzing vegetation response, CEOP-AEGIS Deliverable Report De9.3 & 9.4*, University of Strasbourg, France.
- Jiménez-Muñoz, J.C., Sobrino, J.A., et al., 2010. Atmospheric correction of optical imagery from MODIS and Reanalysis atmospheric products. *Remote Sensing of Environment*, 114(10), pp.2195–2210.
- Kalnay, E., Kanamitsu, M., et al., 1996. The NCEP/NCAR 40-year reanalysis project. *Bulletin of the American Meteorological Society*, 77(3), pp.437–471.
- Kassianov, E., Long, C.N. & Ovtchinnikov, M., 2005. Cloud Sky Cover versus Cloud Fraction: Whole-Sky Simulations and Observations. *Journal of Applied Meteorology*, 44(1), pp.86–98.
- Kastendeuch, P.P., 2013. A method to estimate sky view factors from digital elevation models. *International Journal of Climatology*, 33(6), pp.1574–1578.
- Kaufman, Y.J., 1984. Atmospheric effect on spatial resolution of surface imagery. *Applied Optics*, 23(19), pp.3400–3408.
- Kawata, Y., Ueno, S. & Kusaka, T., 1988. Radiometric correction for atmospheric and topographic effects on Landsat MSS images. *International Journal of Remote Sensing*, 9(4), pp.729–748.
- Kazantzidis, A., Tzoumanikas, P., et al., 2012. Cloud detection and classification with the use of whole-sky ground-based images. *Atmospheric Research*, 113, pp.80–88.
- Koetz, B., Baret, F., et al., 2005. Use of coupled canopy structure dynamic and radiative transfer models to estimate biophysical canopy characteristics. *Remote Sensing of Environment*, 95(1), pp.115–124.

- Kondratyev, K.Y., 1969. *Radiation in the atmosphere* Academic Press Inc., ed., London, United Kingdom: World Meteorological Organization.
- Kreuter, A., Zangerl, M., et al., 2009. All-sky imaging: a simple, versatile system for atmospheric research. *Applied Optics*, 48(6), p.1091.
- Kustas, W., 2000. Evaluating the Effects of Subpixel Heterogeneity on Pixel Average Fluxes. *Remote Sensing of Environment*, 74(3), pp.327–342.
- Kyle, H.L., 1990. A comparison of two major Earth Radiation Budget data sets. *Journal of Geophysical Research*, 95(D7), pp.9951–9970.
- Van Laake, P.E. & Sanchez-Azofeifa, G.A., 2004. Simplified atmospheric radiative transfer modelling for estimating incident PAR using MODIS atmosphere products. *Remote Sensing of Environment*, 91(1), pp.98–113.
- Latifovic, R. & Cihlar, J., 2003. A comparison of BRDF models for the normalization of satellite optical data to a standard sun-target-sensor geometry. *IEEE Transactions on Geoscience and Remote Sensing*, 41(8), pp.1889–1898.
- Lattanzio, A., Govaerts, Y.M. & Pinty, B., 2007. Consistency of surface anisotropy characterization with meteosat observations. *Advances in Space Research*, 39(1), pp.131–135.
- Lavergne, T., Kaminski, T., et al., 2007. Application to MISR land products of an RPV model inversion package using adjoint and Hessian codes. *Remote Sensing of Environment*, 107(1-2), pp.362–375.
- Leckner, B., 1978. The spectral distribution of solar radiation at the earth's surface - elements of a model. *Solar Energy*, 20(2), pp.143–150.
- Li, P., Shi, C., et al., 2013. Evaluation of ASTER GDEM using GPS benchmarks and SRTM in China. *International Journal of Remote Sensing*, 34(5), pp.1744–1771.
- Li, Q., Lu, W. & Yang, J., 2011. A Hybrid Thresholding Algorithm for Cloud Detection on Ground-Based Color Images. *Journal of Atmospheric and Oceanic Technology*, 28(10), pp.1286–1296.
- Liang, S., 2001. Narrowband to broadband conversions of land surface albedo: I. Algorithms. *Remote Sensing of Environment*, 76(2), pp.213–238.
- Liang, S., Shuey, C.J., et al., 2003. Narrowband to broadband conversions of land surface albedo: II. Validation. *Remote Sensing of Environment*, 84(1), pp.25–41.
- Liang, S., Wang, K., et al., 2010. Review on Estimation of Land Surface Radiation and Energy Budgets From Ground Measurement, Remote Sensing and Model Simulations. *IEEE Journal of Selected Topics in Applied Earth Observations and Remote Sensing*, 3(3), pp.225–240.

- Liang, S. & Zhang, X., 2012. *Global Land Surface Products: Shortwave Radiation Product Data Collection(2008-2010)*, Beijing Normal University, Beijing, China.
- Liu, C.H., Chen, A.J. & Liu, G.R., 1996. A robust algorithm for correcting the topographic effect of satellite image over mountainous terrain. In K. Kraus & P. Waldhäusl, eds. *XVIIIth ISPRS Congress, Technical Commission VII: Resource and Environmental Monitoring*. Vienna, Austria, pp. 105–111.
- Liu, S., Liu, Q., et al., 2010. The Angular and Spectral Kernel Model for BRDF and Albedo Retrieval. *IEEE Journal of Selected Topics in Applied Earth Observations and Remote Sensing*, 3(3), pp.241–256.
- Liu, W., Hu, B. & Wang, S., 2008. Improving Land Surface Pixel Level Albedo Characterization Using Sub-Pixel Information Retrieved from Remote Sensing. In *Geoscience and Remote Sensing Symposium, 2008. IGARSS 2008. IEEE International*. pp. II-801–II-804.
- Liu, X. & Dong, B., 2013. Influence of the Tibetan Plateau uplift on the Asian monsoon-arid environment evolution. *Chinese Science Bulletin*, 58(34), pp.4277–4291.
- Loew, A. & Govaerts, Y., 2010. Towards Multidecadal Consistent Meteosat Surface Albedo Time Series. *Remote Sensing*, 2(4), pp.957–967.
- Long, C.N. & DeLuisi, J.J., 1998. Development of an Automated Hemispheric Sky Imager for Cloud Fraction Retrievals. In *10th Symposium on Meteorological Observations and Instrumentation*. Phoenix, Arizona, USA.
- Long, C.N., Sabburg, J.M., et al., 2006. Retrieving Cloud Characteristics from Ground-Based Daytime Color All-Sky Images. *Journal of Atmospheric and Oceanic Technology*, 23(5), pp.633–652.
- Long, C.N., Slater, D.W. & Tooman, T., 2001. *Total Sky Imager Model 880 Status and Testing Results*, U.S. Department of Energy, Office of Energy Research, Office of Health and Environmental Research.
- Long, D., Gao, Y. & Singh, V.P., 2010. Estimation of daily average net radiation from MODIS data and DEM over the Baiyangdian watershed in North China for clear sky days. *Journal of Hydrology*, 388(3-4), pp.217–233.
- Lucht, W. & Roujean, J.L., 2000a. Considerations in the parametric modeling of BRDF and Albedo from multiangular satellite sensor observations. *Remote Sensing Review*, 18(2-4), pp.343–379.
- Lucht, W., Schaaf, C.B. & Strahler, A.H., 2000b. An algorithm for the retrieval of albedo from space using semiempirical BRDF models. *IEEE Transactions on Geoscience and Remote Sensing*, 38(2), pp.977–998.
- Ma, Y., Kang, S., et al., 2008. ROOF OF THE WORLD: Tibetan Observation and Research Platform. *Bulletin of the American Meteorological Society*, 89(10), pp.1487–1492.

- Madkour, M.A., El-Metwally, M. & Hamed, A.B., 2006. Comparative study on different models for estimation of direct normal irradiance (DNI) over Egypt atmosphere. *Renewable Energy*, 31(3), pp.361–382.
- Martin, G.M., Ringer, M.A., et al., 2006. The Physical Properties of the Atmosphere in the New Hadley Centre Global Environmental Model (HadGEM1). Part I: Model Description and Global Climatology. *Journal of Climate*, 19(7), pp.1274–1301.
- Martins, F.R., Souza, M.P. & Pereira, E.B., 2003. Comparative study of satellite and ground techniques for cloud cover determination. *Advances in Space Research*, 32(11), pp.2275–2280.
- Masuda, K., Leighton, H.G. & Zhanqing L., 1995. A new parameterization for the determination of solar flux absorbed at the surface from satellite measurements. *Journal of Climate*, 8(6), pp.1615–1629.
- Meyer, P., Itten, K.I., et al., 1993. Radiometric corrections of topographically induced effects on Landsat TM data in an alpine environment. *ISPRS Journal of Photogrammetry and Remote Sensing*, 48(4), pp.17–28.
- Molteni, F., Buizza, R., et al., 1996. The ECMWF ensemble prediction system: Methodology and validation. *Quarterly Journal of the Royal Meteorological Society*, 122(529), pp.73–119.
- Monteith, J.L. & Unsworth, M.H., 1990. *Principles of Environmental Physics* Second edi. E. Arnold, ed., London, United Kingdom: Elsevier Science.
- Muneer, T. & Gul, M.S., 2000. Evaluation of sunshine and cloud cover based models for generating solar radiation data. *Energy Conversion and Management*, 41(5), pp.461–482.
- Neto, S.L.M., Wangenheim, A. von, et al., 2010. The use of Euclidean geometric distance on RGB color space for the Classification of Sky and Cloud Patterns. *Journal of Atmospheric and Oceanic Technology*, 27, pp.1504–1517.
- Niemelä, S., Räisänen, P. & Savijärvi, H., 2001. Comparison of surface radiative flux parameterizations Part II. Shortwave radiation. *Atmospheric Research*, 58(2), pp.141–154.
- Noia, M., Ratto, C.F. & Festa, R., 1993a. Solar irradiance estimation from geostationary satellite data: I. Statistical models. *Solar Energy*, 51(6), pp.449–456.
- Noia, M., Ratto, C.F. & Festa, R., 1993b. Solar irradiance estimation from geostationary satellite data: II. Physical models. *Solar Energy*, 51(6), pp.457–465.
- Ohmura, A. & Raschke, E., 2005. Energy budget at the earth's surface. In M. Hantel, ed. *Observed Global Climate*. Springer Berlin Heidelberg, pp. 1–30.
- Oke, T.R., 1987. *Boundary Layer Climates*, Routledge, ed., London, United Kingdom.

- Paulescu, M., Paulescu, E., et al., 2013. *Weather Modeling and Forecasting of PV Systems Operation*, Springer London.
- Paulescu, M. & Schlett, Z., 2003. A simplified but accurate spectral solar irradiance model. *Theoretical and Applied Climatology*, 75(3-4), pp.203–212.
- Pekarek, A.H., 2001. Solar Forcing of Earth's climate. In C.G. Lee, E.H. William, & M.H. Bernold, eds. *Geological Perspectives of Global Climate Change*. AAPG, in collaboration with the Kansas Geological Survey and the AAPG Div./Environmental Geosciences, pp. 19–34.
- Perez, R., Cebecauer, T. & Šúri, M., 2013. Semi-Empirical Satellite Models. In *Solar Energy Forecasting and Resource Assessment*. pp. 21–48.
- Perez, R., Ineichen, P., et al., 2002. A new operational model for satellite-derived irradiances: Description and validation. *Solar Energy*, 73(5), pp.307–317.
- Pfister, G., McKenzie, R.L., et al., 2003. Cloud Coverage Based on All-Sky Imaging and Its Impact on Surface Solar Irradiance. *Journal of Applied Meteorology*, 42(10), pp.1421–1434.
- Pinker, R.T. & Ewing, J.A., 1985. Modeling surface solar radiation: model formulation and validation. *Journal of Climate & Applied Meteorology*, 24(5), pp.389–401.
- Pinker, R.T., Frouin, R. & Li, Z., 1995. A review of satellite methods to derive surface shortwave irradiance. *Remote Sensing of Environment*, 51(1), pp.108–124.
- Pinty, B., Roveda, F., et al., 2000. Surface albedo retrieval from Meteosat 1. Theory. *Journal of Geophysical Research: Atmospheres*, 105(D14), pp.18099–18112.
- Polo, J., Zarzalejo, L.F. & Ramírez, L., 2008. Solar radiation derived from satellite images. In *Modeling Solar Radiation at the Earth's Surface: Recent Advances*. pp. 449–461.
- Proy, C., Tanré, D. & Deschamps, P.Y., 1989. Evaluation of topographic effects in remotely sensed data. *Remote Sensing of Environment*, 30(1), pp.21–32.
- Rahman, H. & Dedieu, G., 1994. SMAC: a simplified method for the atmospheric correction of satellite measurements in the solar spectrum. *International Journal of Remote Sensing*, 15(1), pp.123–143.
- Rahman, H., Verstraete, M.M. & Pinty, B., 1993. Coupled surface-atmosphere reflectance (CSAR) model 1. Model description and inversion on synthetic data. *Journal of Geophysical Research*, 98(D11), pp.20,720–779,789.
- Randall, D.A., 1989. Cloud parameterization for climate modeling: Status and prospects. *Atmospheric Research*, 23(3-4), pp.345–361.
- Randall, D.A., Khairoutdinov, M., et al., 2003. Breaking the Cloud Parameterization Deadlock. *Bulletin of the American Meteorological Society*, 84(11), pp.1547–1564.

- Randall, D.A., Wood, R.A., et al., 2007. Climate Models and Their Evaluation. In S. Solomon, D. Qin, et al., eds. *Climate Change 2007: The Physical Science Basis. Contribution of Working Group I to the Fourth Assessment Report of the Intergovernmental Panel on Climate Change*. Cambridge, United Kingdom and New York, NY, USA, p. 74.
- Raphael, C. & Hay, J.E., 1984. An assessment of models which use satellite data to estimate solar irradiance at the Earth's surface. *Journal of Climate & Applied Meteorology*, 23(5), pp.832–844.
- Riano, D., Chuvieco, E., et al., 2003. Assessment of different topographic corrections in Landsat-TM data for mapping vegetation types. *IEEE Transactions on Geoscience and Remote Sensing*, 41(5), pp.1056–1061.
- Richter, R., 1997. Correction of atmospheric and topographic effects for high-spatial-resolution satellite imagery. In *Proceedings of SPIE - The International Society for Optical Engineering*. DLR, Wessling, Ger, pp. 216–224.
- Richter, R., 1998. Correction of satellite imagery over mountainous terrain. *Applied optics*, 37(18), pp.4004–4015.
- Richter, R., Kellenberger, T. & Kaufmann, H., 2009. Comparison of Topographic Correction Methods. *Remote Sensing*, 1(3), pp.184–196.
- Riihelä, A., Manninen, T. & Andersson, K., 2011. *Algorithm Theoretical Basis Document - Surface Broadband Albedo AVHRR / SEVIRI*, EUMETSAT Satellite Application Facility on Climate Monitoring.
- Ringer, M.A., Martin, G.M., et al., 2006. The Physical Properties of the Atmosphere in the New Hadley Centre Global Environmental Model (HadGEM1). Part II: Aspects of Variability and Regional Climate. *Journal of Climate*, 19(7), pp.1302–1326.
- Rochon, G., Audirac, H., et al., 1979. Radiometric correction for topographic effects on Landsat images of forests. *Teledetection et gestion des ressources*, I et II: c(congres de l'Association Quebecoise de Teledetection), pp.151–163.
- Román, M.O., Gatebe, C.K., et al., 2011. Variability in surface BRDF at different spatial scales (30m–500m) over a mixed agricultural landscape as retrieved from airborne and satellite spectral measurements. *Remote Sensing of Environment*, 115(9), pp.2184–2203.
- Román, M.O., Schaaf, C.B., et al., 2010. Assessing the coupling between surface albedo derived from MODIS and the fraction of diffuse skylight over spatially-characterized landscapes. *Remote Sensing of Environment*, 114(4), pp.738–760.
- Román, M.O., Schaaf, C.B., et al., 2009. The MODIS (Collection V005) BRDF/albedo product: Assessment of spatial representativeness over forested landscapes. *Remote Sensing of Environment*, 113(11), pp.2476–2498.

- Roujean, J.L., Leroy, M. & Deschamps, P.Y., 1992. A bidirectional reflectance model of the Earth's surface for the correction of remote sensing data. *Journal of Geophysical Research*, 97(D18).
- Ryu, Y., Kang, S., et al., 2008. Evaluation of land surface radiation balance derived from moderate resolution imaging spectroradiometer (MODIS) over complex terrain and heterogeneous landscape on clear sky days. *Agricultural and Forest Meteorology*, 148(10), pp.1538–1552.
- Sabburg, J.M. & Long, C.N., 2004. Improved sky imaging for studies of enhanced UV irradiance. *Atmospheric Chemistry and Physics*, 4, pp.2543–2552.
- Saha, K., 2008. The Incoming Solar Radiation – Interaction with the Earth's Atmosphere and Surface. In Springer, ed. *The Earth's Atmosphere: Its Physics and Dynamics*. Springer-Verlag Berlin Heidelberg, p. 367.
- Sandmeier, S. & Itten, K.I., 1997. A physically-based model to correct atmospheric and illumination effects in optical satellite data of rugged terrain. *IEEE Transactions on Geoscience and Remote Sensing*, 35(3), pp.708–717.
- Schaaf, C.B., Gao, F., et al., 2002. First operational BRDF, albedo nadir reflectance products from MODIS. *Remote Sensing of Environment*, 83(1-2), pp.135–148.
- Schaepman-Strub, G., Schaepman, M.E., et al., 2006. Reflectance quantities in optical remote sensing—definitions and case studies. *Remote Sensing of Environment*, 103(1), pp.27–42.
- Shepherd, J.D. & Dymond, J.R., 2003. Correcting satellite imagery for the variance of reflectance and illumination with topography. *International Journal of Remote Sensing*, 24(17), pp.3503–3514.
- Shields, J., Johnson, E., R.W. & Koehler, L.T., 1993. Automated whole sky imaging systems for cloud field assessment. In American Meteorological Society, ed. *Fourth Symposium on Global Change Studies*. Boston, Massachusetts, USA.
- Shields, J.E., Karr, M.E., et al., 2010. *Whole Sky Imager Characterization of Sky Obscuration by Clouds for the Starfire Optical Range, Scientific Report for AFRL Contract FA9451-008-C-0226*, Marine Physical Laboratory, Technical Note 275, Scripps Institution of Oceanography, University of California San Diego, USA.
- Silva, A.A. & de Souza Echer, M.P., 2013. Ground-based measurements of local cloud cover. *Meteorology and Atmospheric Physics*, 120(3-4), pp.201–212.
- Slingo, J.M., 1987. The Development and Verification of A Cloud Prediction Scheme For the Ecmwf Model. *Quarterly Journal of the Royal Meteorological Society*, 113(477), pp.899–927.
- Song, C. & Woodcock, C.E., 2003. Monitoring forest succession with multitemporal landsat images: factors of uncertainty. *IEEE Transactions on Geoscience and Remote Sensing*, 41(11), pp.2557–2567.

- Souza, A.P. & Escobedo, J.F., 2013. Estimates of hourly diffuse radiation on tilted surfaces in southeast of Brazil. *International Journal of Renewable Energy Research*, 3(1), pp.207–221.
- Souza-Echer, M.P., Pereira, E.B., et al., 2006. A Simple Method for the Assessment of the Cloud Cover State in High-Latitude Regions by a Ground-Based Digital Camera. *Journal of Atmospheric and Oceanic Technology*, 23(3), pp.437–447.
- Spencer, J.W., 1972. Computer estimation of direct solar radiation on clear days. *Solar Energy*, 13(4), pp.437–438.
- Stephens, G.L., 1978. Radiation Profiles in Extended Water Clouds. II: Parameterization Schemes. *Journal of the Atmospheric Sciences*, 35(11), pp.2123–2132.
- Stephens, G.L., Ackerman, S. & Smith, E.A., 1984. A shortwave parameterization revised to improve cloud absorption. *Journal of the Atmospheric Sciences*, 41(4), pp.687–690.
- Strugnell, N.C. & Lucht, W., 2001. An algorithm to infer continental-scale Albedo from AVHRR data, land over class, and field observation of typical BRDFs. *Journal of Climate*, 14(7), pp.1360–1376.
- Sugawara, M., Tanba, S. & Iikura, Y., 2010. Physically based evaluation of reflected terrain irradiance in satellite imagery for illumination correction. In *International Conference on Applied Computer Science - Proceedings*. pp. 226–233.
- Szantoi, Z. & Simonetti, D., 2013. Fast and Robust Topographic Correction Method for Medium Resolution Satellite Imagery Using a Stratified Approach. *IEEE Journal of Selected Topics in Applied Earth Observations and Remote Sensing*, 6(4), pp.1921–1933.
- Tang, B., Li, Z.L. & Zhang, R., 2006. A direct method for estimating net surface shortwave radiation from MODIS data. *Remote Sensing of Environment*, 103(1), pp.115–126.
- Tapakis, R. & Charalambides, A.G., 2013. Equipment and methodologies for cloud detection and classification: A review. *Solar Energy*, 95, pp.392–430.
- Tarpley, J.D., 1979. Estimating incident solar radiation at the surface from geostationary satellite data. *Journal of Applied Meteorology*, 18(9), pp.1172–1181.
- Tohsing, K., Schrempf, M., et al., 2014. Validation of spectral sky radiance derived from all-sky camera images – a case study. *Atmospheric Measurement Techniques*, 7(7), pp.2137–2146.
- Turner, R. & Spencer, M., 1972. Atmospheric model for the correction of spacecraft data. In *Proceeding of the 8th International Symposium on Remote Sensing of Environment*. Ann Arbor, USA (Ann Arbor: Environmental Research Institute of Michigan), pp. 895–934.

- Varley, M.J., Beven, K.J. & Oliver, H.R., 1996. Modelling solar radiation in steeply sloping terrain. *International Journal of Climatology*, 16(1), pp.93–104.
- Vogt, P., Verstraete, M.M., et al., 2000. The impact of multi-angular measurements on the accuracy of land-surface Albedo retrieval: Preliminary results for the proposed ESA LSPIM mission. *Remote Sensing Reviews*, 19(1-4), pp.191–204.
- Walthall, C.L., Norman, J.M., et al., 1985. Simple equation to approximate the bidirectional reflectance from vegetative canopies and bare soil surfaces. *Applied Optics*, 24(3), pp.383–387.
- Wang, H. & Pinker, R.T., 2009a. Shortwave radiative fluxes from MODIS: Model development and implementation. *Journal of Geophysical Research: Atmospheres*, 114(D20).
- Wang, K. & Liang, S., 2009b. Estimation of daytime net radiation from shortwave radiation measurements and meteorological observations. *Journal of Applied Meteorology and Climatology*, 48(3), pp.634–643.
- Wang, T., Yan, G., et al., 2014. Topographic correction of retrieved surface shortwave radiative fluxes from space under clear-sky conditions. In *Geoscience and Remote Sensing Symposium (IGARSS), 2014 IEEE International*. Quebec City, QC, pp. 1813–1816.
- Weiss, M. & Baret, F., 2010. *Can-Eye v6.1 User Manual*, French National Institute of Agronomical Research (INRA), Avignon, France.
- Wen, J., Liu, Q., et al., 2009a. Parametrized BRDF for atmospheric and topographic correction and albedo estimation in Jiangxi rugged terrain, China. *International Journal of Remote Sensing*, 30(11), pp.2875–2896.
- Wen, J., Liu, Q., et al., 2009b. Scale effect and scale correction of land-surface albedo in rugged terrain. *International Journal of Remote Sensing*, 30(20), pp.5397–5420.
- Wen, J., Zhao, X., et al., 2014. An Improved Land-Surface Albedo Algorithm With DEM in Rugged Terrain. *IEEE Geoscience and Remote Sensing Letters*, 11(4), pp.883–887.
- Wu, G., Liu, Y., et al., 2007. The Influence of Mechanical and Thermal Forcing by the Tibetan Plateau on Asian Climate. *Journal of Hydrometeorology*, 8(4), pp.770–789.
- Wu, G., Mao, J., et al., 2006. Current progresses in study of impacts of the Tibetan Plateau on Asian summer climate. *Acta Meteorologica Sinica*, 20(2), pp.144–158.
- WWRP (World Weather Research programme), 2012. *Recommended Methods for Evaluating Cloud and Related Parameters*, World Meteorological Organization (WMO), Geneva, Switzerland.
- Xia, X., Wang, P., et al., 2008. Aerosol optical depth over the Tibetan Plateau and its relation to aerosols over the Taklimakan Desert. *Geophysical Research Letters*, 35(16).

- Xin, J., Wang, Y., et al., 2007. Aerosol optical depth (AOD) and Ångström exponent of aerosols observed by the Chinese Sun Hazemeter Network from August 2004 to September 2005. *Journal of Geophysical Research: Atmospheres*, 112(D5).
- Yang, K., Huang, G.W. & Tamai, N., 2001. A hybrid model for estimating global solar radiation. *Solar Energy*, 70(1), pp.13–22.
- Yang, K., Koike, T., Stackhouse, P., et al., 2006a. An assessment of satellite surface radiation products for highlands with Tibet instrumental data. *Geophysical Research Letters*, 33(22).
- Yang, K., Koike, T. & Ye, B., 2006b. Improving estimation of hourly, daily, and monthly solar radiation by importing global data sets. *Agricultural and Forest Meteorology*, 137(1-2), pp.43–55.
- Yang, K., Koike, T., et al., 2007. Development and validation of an advanced model estimating solar radiation from surface meteorological data. In T. P. Hough, ed. *Recent Developments in Solar Ebergy*. Nove Science, p. 369.
- Yang, K., Pinker, R.T., et al., 2008. Evaluation of satellite estimates of downward shortwave radiation over the Tibetan Plateau. *Journal of Geophysical Research*, 113(D17).
- Yoshimura, M. & Yamashita, M., 2013. Contribution of Ground-Based Cloud Observation to Satellite-Based Cloud Discrimination. *Journal of Environmental Science and Engineering A*, 2, pp.487–493.
- Zakšek, K., Oštir, K. & Kokalj, Ž., 2011. Sky-View Factor as a Relief Visualization Technique. *Remote Sensing*, 3(12), pp.398–415.
- Zhang, Q., Chen, J. & Becker, S., 2007. Flood/drought change of last millennium in the Yangtze Delta and its possible connections with Tibetan climatic changes. *Global and Planetary Change*, 57(3-4), pp.213–221.
- Zhang, T., Stackhouse, P.W., et al., 2013. The validation of the GEWEX SRB surface shortwave flux data products using BSRN measurements: A systematic quality control, production and application approach. *Journal of Quantitative Spectroscopy and Radiative Transfer*, 122, pp.127–140.
- Zhang, Y., 2004. Calculation of radiative fluxes from the surface to top of atmosphere based on ISCCP and other global data sets: Refinements of the radiative transfer model and the input data. *Journal of Geophysical Research*, 109(D19).
- Zhanqing, L., Leighton, H.G. & Cess, R.D., 1993. Surface net solar radiation estimated from satellite measurements: comparisons with tower observations. *Journal of Climate*, 6(9), pp.1764–1772.
- Zhao, Y., Shan, X. & Tang, P., 2014. Spatial Consistency Analysis and Relative Geometric Correction of Low Spatial Resolution Multi-source Remote Sensing Data. *Remote Sensing Technology and Application*, 29(1), pp.155–163.



## Summary

*INTRODUCTION.* Monitoring the spatial distribution and temporal variation of solar radiation budget at global scale is essential to understand the climate and its evolution. Remote sensing, with its ability to cover large areas and overcome the inherent limitation in the spatial sampling provided by ground measurements, has become one of the main data sources to model solar radiative fluxes. Even if some of the methods provide promising results, most of the existing global datasets have too coarse spatial or temporal resolution to accurately capture the local variations, especially over heterogeneous areas. The temporal frequency required by solar radiation budget monitoring imposes the use of high temporal resolution satellites, whose spatial resolution is of a square kilometer at best. At this spatial resolution, the problem of the pixel spatial heterogeneity is raised, especially concerning clouds and topography which strongly impact the solar radiation budget. However, most of the current retrieval algorithms do not consider the terrain and clouds heterogeneity within kilometeric pixels, which leads to large estimation errors. In this thesis, this intra-pixel variability is taken into account by a sub-pixel correction. The sub-pixel spatial distribution of clouds directly influences the partitioning between direct and diffuse irradiance. Likewise, the sub-pixel topography, mostly through shadowing effects has an impact on irradiance and albedo estimates. The main objective of this thesis is to develop an operational method based on remote sensing for all-sky solar radiation budget daily monitoring over large heterogeneous areas and to propose improvement for the estimation of irradiance and albedo considering sub-pixel spatial variability of topography and clouds. To operationally monitor the radiative fluxes on a daily basis using satellite data constraints the estimation to a square kilometer pixel resolution. Some satellite data products characterizing atmospheric and land surface properties are available at these spatial and temporal resolution. Thus, this thesis explores first the possibility to combine those products to estimate the solar radiation budget. However, as it does not take into account sub-pixel variability, further research is carried out to improve the solar radiation budget estimates addressing the sub-pixel heterogeneity in terms of spatial variability of the topography and distribution of the clouds. The temporal variability of the cloud cover and its relation to temporal aggregation of radiative flux estimates is also investigated.

*MONITORING SOLAR RADIATION BUDGET USING CURRENT SATELLITE DATA PRODUCTS.*

At first, an algorithm combining satellite data products characterizing atmospheric and land surface properties available daily and at the square kilometer resolution to estimate the solar

radiation budget is proposed and applied to retrieve instantaneous and daily solar radiative fluxes over the Tibetan Plateau. This method integrates the terrain mean slope and azimuth using a Digital Elevation Model (DEM) in the computation of the local illumination angle required for irradiance estimation and takes into account actual atmospheric and land surface properties characteristics derived from MODIS data products. The algorithm is used to produce a 3-year time series of solar radiative fluxes between 2008 and 2010, validated by comparison against ground measurements and satellite data at the same resolution. Even if the accuracy of the produced dataset is not better than the existing ones, this method enables to monitor solar radiation at a finer spatial and temporal resolution. Then, two approaches are proposed to improve the solar radiation budget estimates retrieval from remote sensing by integrating sub-pixel terrain and clouds heterogeneity.

*IMPACT OF SPATIAL AND TEMPORAL VARIABILITY OF CLOUDS ON THE SOLAR RADIATION.* To investigate the impact of cloud spatial distribution on solar radiative fluxes and temporal variability on sunshine duration and daily solar radiation budget estimates, a fieldwork experiment was carried out to collect hemispherical images of the sky at very high temporal resolution simultaneously to solar radiative fluxes measured at the ground. The hemispherical images are used to characterize the cloud cover spatial distribution and to estimate sunshine duration using several indices retrieved with a fully automatized method developed for that purpose. The retrieved indices are correlated with the ground solar radiative fluxes to identify potential relationships, while the estimated sunshine duration is used to temporally aggregate instantaneous solar radiative fluxes. The proposed approach, easy to set up and to apply, allows to accurately and consistently retrieve cloud fraction and distribution from the hemispherical images. Although the thin clouds and the sunspot area remain difficult to classify, the results appear to be more accurate and consistent than estimations by a human observer. Among all the parameters extracted from the images, only the different cloud fraction and spatial distribution estimates show a correlation with the radiation fluxes. The latter points out that, even though the longwave downward radiative fluxes correlates very well with the cloud fraction, the solar irradiance is mostly determined by the cloud distribution. Then, information about cloud distribution is essential to improve surface irradiance modelling. Furthermore, the high temporal resolution of the data collected is very valuable when dealing with shortwave radiative fluxes as the sunshine duration estimates, commonly used for the instantaneous to daily conversion, appears to be very sensitive to the sampling interval of measurements. The correlation analysis shows that taking into account the cloud distribution, using the cloud fraction weighted by the angular distance to the sun to estimate sunshine duration, provides the most accurate temporal average of solar radiation budget. The proposed approach is easy to set up and the retrieved information on cloud spatial and temporal distribution could greatly benefit the solar radiation modelling but these measurements are only feasible at the local scale.

Nevertheless, the results give indications on the kind of information that needs to be retrieved from satellite images, for instance the cloud fraction weighted by the distance to the sun, in order to improve solar radiation budget estimation at large scale.

*INTEGRATION OF TOPOGRAPHIC VARIABILITY AT SUB-PIXEL LEVEL TO IMPROVE SURFACE IRRADIANCE AND ALBEDO RETRIEVED USING REMOTE SENSING.* A second approach is proposed to improve the irradiance and albedo estimates retrieved from space by taking into account the sub-pixel spatial variability of the terrain. First, the impact of sub-pixel topography on the surface irradiance is quantified and then corrected. Second, the sub-pixel corrected irradiance is used to retrieve the surface reflectance and albedo. To do so, a new topographic correction method is developed and evaluated: the sub-pixel topographic correction. This method is based on the assumption that, instead of using a DEM at the same spatial resolution as the radiometric satellite data, it could be beneficial to take advantage of the finer spatial resolution of available global DEM to characterize and correct for the effects of topography at a finer spatial resolution. As this correction method considers separately the direct and diffuse components of the irradiance, the impact of atmosphere -expressed by the fraction of diffuse skylight- on the corrected irradiance was also analyzed. The application of the sub-pixel topographic correction method to synthetic and real data highlighted the necessity to take into account sub-pixel topography effects when estimating irradiance. Furthermore, the influence of the fraction of diffuse skylight when applying this topographic correction method was also pointed out. Even for a comparable total irradiance value, different partitioning between direct and diffuse irradiance can lead to different irradiance estimates after topographic correction. It is then important to retrieve the actual atmospheric conditions as accurately as possible to estimate properly the sub-pixel corrected surface irradiance.

Once corrected for the sub-pixel topographic effects, the surface irradiance is used to retrieve surface reflectance from geostationary satellite data which in turn is used to reconstruct the surface bidirectional reflectance distribution function (BRDF) and derive the sub-pixel topographically corrected albedo. The corrected reflectance and albedo datasets are produced and validated using ground data and existing satellite data products. As compared to pixel level topographic correction, the reflectance and albedo retrieved from satellite data after sub-pixel topographic correction provide better results. The validation clearly shows a more accurate retrieval of the reflectance, even if the correction tends to slightly overestimate it. For the albedo, the sensitivity analysis using synthetic data also provided the same outcomes. However, because of the difficulty to estimate the narrow-to-broadband conversion coefficients, the validation and comparison of albedo derived from real satellite data against ground measurements is more complex. Even so we may conclude that in a relatively flat area the method does not bring any bias, while in

rugged areas the albedo retrieved after sub-pixel topographic correction provides better results than with none or pixel level correction. Additionally the retrieved albedo is more than or as accurate as other existing products and, for the Namco station, it meets the climate and weather forecast requirements. The proposed approach also leads to an improvement of the temporal resolution of the albedo. The retrieval method based on hourly geostationary satellite data allows to produce a 3-days albedo against 8 days for MODIS and 10 days for METEOSAT. This improvement appears as very valuable as it pointed out some fluctuations in the measured albedo that were missed by other albedo products with lower temporal resolution.

*CONCLUSIONS AND PERSPECTIVES.* The main conclusions drawn from this thesis are that current satellite data products allow to model solar radiation budget daily and at the square kilometer spatial resolution. However, when working over heterogeneous areas such as the Tibetan Plateau, the estimates need to be improved by considering the sub-pixel spatial and temporal variability of terrain and cloud cover. The surface irradiance estimation would benefit from using cloud distribution instead of cloud fraction to take into account the cloud cover. Furthermore, information about the cloud cover at high temporal resolution leads to a better temporal average of the radiative fluxes. Then, as the cloud fraction weighted by the angular distance to the sun appears to be a good proxy for cloud spatial distribution, it could be derived at suitable temporal resolution from current and upcoming geostationary satellite data. The integration of the sub-pixel topographic effects using high resolution DEM would also improve the estimates of irradiance as well as of albedo. The temporal resolution of the latter is also to consider and, as for cloud cover characterization, the use of geostationary satellite would allow to increase the retrieval frequency. The improvements of all those aspects would directly improve the solar radiation budget estimates. Then, based on multi-source and multi-resolution remote sensing data, the developed method provides a usable solar radiation budget dataset and the two proposed approaches to improve the estimates pave the way for a new operational methodology which adequately takes into account sub-pixel heterogeneity when producing large area time series of solar radiation budget at the surface.

## Samenvatting

*INLEIDING.* Monitoren van de ruimtelijke verdeling en de temporele variatie van het solaire stralingsbudget op globale schaal is essentieel voor het begrip van het klimaat en de evolutie ervan. Remote sensing, waarmee men grote gebieden kan bestrijken zonder de inherente beperkingen van bemonstering met terreinwaarnemingen, is een van de belangrijkste gegevensbronnen voor het modelleren van zonnestralingsfluxen geworden. Hoewel sommige methoden veelbelovende resultaten geven, hebben de meeste globale datasets een te grove ruimtelijke of temporele resolutie om de lokale variaties, vooral in sterk heterogene gebieden, voldoende nauwkeurig weer te geven. De tijdfrequentie die nodig is voor het monitoren van het zonnestralingsbudget vereist het gebruik van satellieten met een hoge temporele resolutie, die in het beste geval een ruimtelijke resolutie van een vierkante kilometer hebben. Bij deze resolutie wordt de heterogeniteit binnen de pixels een probleem, vooral bij wolken en bij topografie met een grote invloed op het zonnestralingsbudget. De meeste retrieval-algoritmes houden echter geen rekening met de heterogeniteit van het terrein of met de wolken binnen kilometerpixels, hetgeen tot grote fouten in de schattingen leidt. In dit proefschrift wordt inter-pixel variabiliteit wel meegenomen in de vorm van sub-pixel correctie. De sub-pixel ruimtelijke verdeling van wolken heeft rechtstreeks invloed op de verhouding tussen directe en diffuse straling. Ook heeft sub-pixel topografie, vooral door schaduw-effecten, invloed op instralings- en albedoschattingen. Het hoofddoel van dit proefschrift is een operationele methode te ontwikkelen, gebaseerd op remote sensing, voor het dagelijks monitoren van het zonnestralingsbudget over grote, heterogene, gebieden, en om instraling en albedo beter te schatten, gelet op sub-pixel ruimtelijke variabiliteit van topografie en wolken. Bij operationeel dagelijks monitoren van stralingsfluxen met satellietgegevens zijn de schattingen beperkt tot een ruimtelijke resolutie van een vierkante kilometer. Satellietgegevens voor het karakteriseren van kenmerken van de atmosfeer en het aardoppervlak, met deze resolutie, zijn beschikbaar. Daarom wordt in dit proefschrift allereerst onderzocht of deze producten gecombineerd kunnen worden om het zonnestralingsbudget te schatten. Maar omdat daarmee de sub-pixel variatie niet wordt meegenomen, wordt verder gezocht naar verbetering van schattingen van het stralingsbudget door te kijken naar sub-pixel heterogeniteit veroorzaakt door de ruimtelijke verdeling van topografie en wolken. De verandering in wolkenbedekking over de tijd en de relatie met stralingsfluxschattingen worden ook onderzocht.

*MONITOREN VAN HET ZONNESTRALINGSBUDGET MET DE HUIDIGE SATELLIETGEGEVENS.*

Eerst beschrijft dit proefschrift een algoritme voor het combineren van satellietgegevens van de atmosfeer en het landoppervlak, zoals deze dagelijks op kilometerresolutie beschikbaar zijn, voor het schatten van dagelijkse zonnestraling, en past dit toe om de momentane en de dagelijkse zonnestralingsfluxen op de Tibetaanse hoogvlakte af te leiden. Deze methode combineert de gemiddelde hellingshoek en -richting van een Digitaal Hoogtemodel (DEM) bij het berekenen van de plaatselijke instralingshoek, die nodig is om de instraling te schatten, en houdt rekening met de momentane eigenschappen van de atmosfeer en het landoppervlak, afgeleid uit MODIS dataproducten. Het algoritme is gebruikt om een driejarige tijdreeks van de zonnestralingsflux te vervaardigen tussen 2008 en 2010, die gevalideerd wordt met terreinmetingen en satellietgegevens op dezelfde resolutie. Deze datasets zijn niet nauwkeuriger dan de bestaande, maar toch kan met deze methode de zonnestraling met een meer gedetailleerde ruimtelijke en temporele resolutie worden gemonitord. Daarna worden twee werkwijzen beschreven om met remote sensing het zonnestralingsbudget beter te schatten, door de sub-pixel heterogeniteit van het terrein en de wolken te integreren.

*INVLOED VAN RUIMTELIJKE EN TEMPORELE RESOLUTIE VAN WOLKEN OP ZONNESTRALING.* Om de invloed te onderzoeken van de ruimtelijke verdeling van wolken op de zonnestralingsfluxen, alsmede van de temporele variabiliteit van de zonneduur en de dagelijkse zonnestralingsschattingen, is een veldexperiment uitgevoerd om hemisferische beelden met hoge temporele resolutie op te nemen, tegelijk met solaire stralingsfluxmetingen in het terrein. De hemisferische beelden zijn gebruikt om de ruimtelijke verdeling van wolkenbedekking te beschrijven en om de zonneduur te schatten met behulp van diverse indices van een volautomatische methode, die speciaal hiervoor ontwikkeld werd. Deze indices worden gecorreleerd met zonnestralingsfluxen op de grond, om mogelijke verbanden aan te wijzen, terwijl de geschatte zonneduur gebruikt wordt om momentane zonnestralingsfluxen te aggregeren. Deze benadering kan gemakkelijk worden voorbereid en uitgevoerd, en maakt het mogelijk de wolkenfractie en -verdeling nauwkeurig uit de hemisferische beelden af te leiden. Hoewel dunne bewolking, evenals de *sun spot area*, nog steeds moeilijk te classificeren zijn, blijken de resultaten nauwkeuriger en consistentere te zijn dan handmatige waarnemingen. Van alle uit de beelden afgeleide parameters laten alleen de verschillende wolkenfracties en de schattingen van de ruimtelijke verdelingen een correlatie met stralingsfluxen zien. Daaruit blijkt dat, ondanks de correlatie tussen langegolfstraling en bewolgingsfractie, de instraling van de zon vooral bepaald wordt door de wolkenverdeling. Daarom is informatie over de wolkenverdeling noodzakelijk voor betere instralingsmodellen van het oppervlak. Verder is een hoge temporele resolutie van de gegevens zeer waardevol bij het werken met kortegolfstralingsfluxen, omdat de schattingen van zonneduur, die doorgaans gebruikt

worden voor de momentaan-naar-dagelijkse omzetting, zeer gevoelig blijken voor de tijdsduur tussen de metingen. Analyse van de correlatie laat zien dat rekening houden met de wolkenverdeling, op grond van de bewolkingsfractie en de temporele verdeling gewogen met de zonnehoek, het nauwkeurigste gemiddelde over de tijd van het zonnestralingsbudget oplevert. De voorgestelde aanpak is gemakkelijk uitvoerbaar en kan zeer nuttig zijn bij het afleiden van informatie over de ruimtelijke en temporele verdeling van bewolking, maar de metingen zijn alleen toepasbaar op lokale schaal. Niettemin geven de resultaten aanwijzingen voor het type informatie dat uit satellietwaarnemingen afgeleid moet worden, zoals de fractie van bewolking gewogen met de hoekafstand tot de zon, om de schatting van het grootschalige zonnestralingsbudget te verbeteren.

*INTEGRATIE VAN TOPOGRAFISCHE VARIABILITEIT OP SUB-PIXEL NIVEAU VOOR BETERE AFLEIDING VAN OPPERVLAKTE-INSTRALING EN ALBEDO MET REMOTE SENSING.* Om de instraling en de albedo vanuit de ruimte te schatten wordt een tweede benadering beschreven, die rekening houdt met de sub-pixel variabiliteit in het terrein. Ten eerste wordt de sub-pixelinvloed van de topografie gekwantificeerd en gecorrigeerd, ten tweede wordt de subpixel-gecorrigeerde instraling gebruikt om de oppervlaktereflectiviteit en -albedo af te leiden. Daartoe werd een nieuwe sub-pixel topografische correctiemethode ontwikkeld en geëvalueerd. In plaats van een DEM met dezelfde resolutie als het radiometrische beeld, is de betere resolutie van een beschikbaar wereldwijd DEM wellicht beter om de effecten van de topografie te beschrijven en ervoor te corrigeren. Omdat zo'n correctiemethode de directe en diffuse instralingscomponenten apart bekijkt, hebben we de invloed van de atmosfeer – uitgedrukt als het aandeel van diffuus *skylight* – op de gecorrigeerde instraling ook geanalyseerd. Toepassing van de sub-pixel topografische correctiemethode op synthetische en echte gegevens bracht de noodzaak aan het licht om sub-pixel topografische effecten mee te nemen bij instralingsschattingen. Bovendien kwam de invloed van de fractie van de diffuse belichting bij het toepassen van deze topografische correctiemethode duidelijk naar voren. Zelfs bij vergelijkbare totaalwaarden voor de belichting kunnen verschillende onderverdelingen van directe en diffuse instraling leiden tot instralingsverschillen na topografische correctie. Vervolgens moet men de actuele atmosferische omstandigheden zo nauwkeurig mogelijk afleiden om de sub-pixelgecorrigeerde oppervlakte-instraling juist te schatten.

Na correctie voor sub-pixel topografische correctie wordt de oppervlakte-instraling gebruikt om de oppervlaktereflectiviteit uit geostationaire satellietgegevens af te leiden, die op zijn beurt gebruikt wordt om de bi-directionele reflectiviteitsverdelingsfunctie (BRDF) te reconstrueren, en de sub-pixel topografisch gecorrigeerde albedo af te leiden. De gecorrigeerde reflectiviteit- en albedodatasets worden vervaardigd en gevalideerd onder gebruikmaking van terreingegevens en bestaande satellietgegevensproducten. Vergeleken

met topografische correcties op pixelniveau, laten de reflectiviteit en albedo, afgeleid van satellietgegevens na topografische correctie, betere resultaten zien. Validatie laat een beduidend betere reflectiviteit zien, ondanks een enigszins te hoge schatting. Voor albedo geeft gevoeligheidsanalyse met synthetische gegevens dezelfde uitkomst. Echter, doordat de coëfficiënten voor de smal-naar-breedbandconversie moeilijk te schatten zijn, is validatie en vergelijking van albedo uit satellietwaarnemingen met terreinmetingen ingewikkeld. Toch kunnen we concluderen dat in betrekkelijk vlak terrein de methode geen systematische fout introduceert, terwijl in geaccidenteerde gebieden de albedo, die na sub-pixel topografische correctie ontstaat, een beter resultaat laat zien dan zonder (of met alleen pixel-niveau) correctie. Bovendien is de albedo minstens zo nauwkeurig als die van andere bestaande producten en voldoet deze tevens, voor het Namco-station, aan de vereisten voor klimaat- en weersverwachting. De beschreven aanpak leidt ook tot verbetering van de temporele albedo-resolutie. De *retrieval*-methode gebaseerd op uurgegevens van geostationaire satellieten, maakt 3-daagse albedo mogelijk, tegenover 8 dagen voor MODIS en 10 dagen voor METEOSAT. Deze verbetering bleek erg waardevol toen deze enkele fluctuaties in de gemeten albedo liet zien die niet opgemerkt werden door andere albedoproducten met een lagere temporele resolutie.

*CONCLUSIE EN PERSPECTIEF.* De belangrijkste conclusie van dit proefschrift is dat met de huidige satellietgegevensproducten modellering van het zonnestralingsbudget dagelijks op kilometerniveau mogelijk is. Echter, in heterogene gebieden, zoals de Tibetaanse hoogvlakte, moeten de schattingen verbeterd worden door sub-pixel ruimtelijke en temporele variabiliteit van terrein- en wolkenbedekking mee te nemen. De oppervlakte-instralingsschatting zou kunnen verbeteren door de wolkenverdeling (in plaats van de wolkenfractie) te bekijken. Bovendien leidt informatie over wolkenbedekking bij hoge temporele resolutie tot een beter temporeel gemiddelde van stralingsfluxen. Tevens, omdat de wolkenfractie, gewogen met de hoek-afstand tot de zon, een goede *proxy* voor de ruimtelijke verdeling van het wolkendek blijkt, zou deze afgeleid kunnen worden uit een geschikte temporele resolutie met huidige en toekomstige satellietgegevens. Integratie van de sub-pixel topografische effecten uit een hogeresolutie DEM kan schatting van instraling en albedo verbeteren. De temporele resolutie daarvan is ook van belang en, voor de kenmerken van het wolkendek, zouden geostationaire satellieten aan de afleidingsfrequentie kunnen bijdragen. Dit alles zou de schattingen van het zonnestralingsbudget direct verbeteren. Dan biedt de beschreven methodiek, op basis van *multi-source* en *multi-resolution* remote sensing een bruikbare zonnestralingsbudget dataset. De twee benaderingen om de schattingen te verbeteren effenen het pad voor een nieuwe operationele methodiek, die adequaat omgaat met sub-pixel heterogeniteit bij het vervaardigen van lange tijdreeksen van zonnestralingsbudget op het aardoppervlak.

## Résumé

*INTRODUCTION.* Le suivi des variations spatiale et temporelle du bilan radiatif solaire à l'échelle globale est essentiel pour comprendre le climat et son évolution. La télédétection, de par sa capacité à couvrir de larges zones, est devenue l'une des principales sources de données pour la modélisation des flux radiatifs solaires à la surface. Bien que les méthodes présentées dans la littérature permettent d'obtenir des résultats satisfaisants, la résolution spatiale et/ou temporelle de la plupart des jeux de données à l'échelle globale qui en découlent est trop rudimentaire pour appréhender avec précision la variabilité locale, en particulier dans les zones fortement hétérogènes. Cette thèse, initiée dans le cadre d'un projet international d'étude de l'hydrologie du Plateau Tibétain, a pour objectif de développer une méthode d'estimation du bilan radiatif solaire journalier de cette région à la topographie particulièrement marquée. La fréquence temporelle requise pour le suivi du bilan radiatif solaire impose l'utilisation de satellites à courte revisite, et donc à une résolution spatiale ne descendant pas en dessous du kilomètre carré. À cette résolution, le problème de l'hétérogénéité sous-pixel est posé, en particulier en ce qui concerne les effets de la nébulosité et de la topographie. Cependant, la plupart des algorithmes actuels travaillant à la résolution kilométrique ne tiennent pas compte de l'hétérogénéité sous-pixel du terrain et des nuages, conduisant à des erreurs significatives. La distribution spatiale de la nébulosité influence directement le partitionnement entre l'éclairement direct et diffus. De même, la topographie sous-pixel a un impact sur les estimations de l'éclairement et de l'albédo, principalement par effet d'ombrage. L'objectif de cette thèse est donc, plus spécifiquement, de développer une méthode opérationnelle basée sur des données issues de la télédétection permettant le suivi du bilan radiatif journalier par tous les temps pour de grandes zones hétérogènes, et de proposer des améliorations pour l'estimation de l'éclairement et de l'albédo en prenant en compte la variabilité spatiale sous-pixel de la topographie et de la nébulosité. Le fait d'utiliser des données satellitaires pour effectuer un suivi journalier des flux radiatifs de manière opérationnelle limite la résolution spatiale des estimations au kilomètre carré. Des produits satellitaires caractérisant les propriétés de la surface et de l'atmosphère sont disponibles à ces résolutions spatiale et temporelle. Ainsi, cette thèse explore d'abord la possibilité de combiner ces produits afin d'estimer le bilan radiatif solaire. Cependant, la variabilité sous-pixel n'étant pas considérée dans ces produits, des investigations supplémentaires sont effectuées dans le but d'améliorer les estimations du bilan radiatif solaire en intégrant l'hétérogénéité sous-pixel en termes de variabilité spatiale de la topographie et de distribution spatiale et temporelle de la nébulosité.

*SUIVI DU BILAN RADIATIF SOLAIRE A L'AIDE DE PRODUITS SATELLITAIRES EXISTANTS.*

Dans un premier temps, un algorithme combinant les produits satellitaires MODIS caractérisant les propriétés de la surface et de l'atmosphère, disponibles de façon journalière et à une résolution de 1 km, est proposé pour estimer le bilan radiatif solaire. Cette méthode prend en compte la pente et l'orientation moyenne du terrain, extraites d'un modèle numérique de terrain (MNT), dans le calcul de l'angle d'illumination nécessaire pour estimer l'éclairement et considère les propriétés réelles de l'atmosphère et de la surface dérivées des produits MODIS. L'algorithme est utilisé pour produire une série temporelle de flux radiatifs solaires instantanés et journaliers entre 2008 et 2010 sur l'ensemble du Plateau Tibétain. Cette série temporelle est validée par comparaison avec des mesures au sol et des données satellitaires à la même résolution. Même si la précision du jeu de données produit n'est pas meilleure que celle des jeux de données existants, cette méthode permet le suivi du bilan radiatif solaire à une résolution spatiale et temporelle plus fine. Afin d'améliorer l'estimation du bilan radiatif solaire à partir de données issues de la télédétection, deux approches intégrant respectivement l'hétérogénéité sous-pixel de la nébulosité et de la topographie sont proposées.

*IMPACT DE LA VARIABILITE SPATIALE ET TEMPORELLE DE LA NEBULOSITE SUR LE RAYONNEMENT SOLAIRE.*

Afin d'étudier l'impact de la distribution spatiale de la couverture nuageuse sur les flux radiatifs solaires ainsi que celui de la variabilité temporelle des nuages sur l'estimation de la durée d'ensoleillement et du bilan radiatif solaire journalier, une campagne de terrain a été menée pour collecter des images hémisphériques du ciel à très haute résolution temporelle. En parallèle, des mesures de flux radiatifs au sol ont été effectuées. Dans le but de caractériser la distribution spatiale de la couverture nuageuse et d'estimer la durée d'ensoleillement, plusieurs indices ont été extraits des images hémisphériques à l'aide d'une méthode entièrement automatisée développée à cet effet. Les indices ont ensuite été corrélés avec les flux radiatifs mesurés au sol afin d'identifier des relations potentielles, tandis que la durée d'ensoleillement a été utilisée pour l'agrégation temporelle des flux radiatifs solaires instantanés. L'approche proposée est facile à mettre en œuvre et permet d'estimer avec précision la fraction et la distribution de la nébulosité à partir d'images hémisphériques. Bien que les nuages fins et la zone autour de la tache solaire restent difficiles à classifier, les résultats obtenus sont plus précis et constants que les estimations faites par un observateur humain. Parmi tous les indices extraits des images, seules les différentes fractions nuageuses et les estimations de la distribution spatiale des nuages présentent une corrélation avec les flux radiatifs. Cette corrélation met en évidence que, même si le rayonnement infrarouge thermique descendant est très corrélé avec la fraction nuageuse, le rayonnement solaire est principalement influencé par la répartition des nuages dans l'hémisphère. Il est donc essentiel de caractériser la distribution des nuages afin d'améliorer la modélisation de rayonnement solaire à la surface. De plus, il a été

démonstré qu'il est indispensable d'utiliser des données à haute résolution temporelle (maximum 15 minutes) car l'estimation de la durée d'ensoleillement, couramment utilisée pour la conversion du bilan radiatif solaire instantané à journalier, s'est révélée très sensible à l'échantillonnage des mesures. Les analyses de corrélation montrent également que l'intégration de la distribution des nuages en utilisant la fraction nuageuse pondérée par la distance à la tache solaire pour estimer la durée d'ensoleillement fournit la valeur de bilan radiatif solaire moyennée la plus précise. Les recherches menées sur la nébulosité ont donc montré que la modélisation du rayonnement solaire pourrait grandement bénéficier de l'intégration de données sur la distribution spatiale et temporelle de la couverture nuageuse. Même si l'approche présentée n'est réalisable qu'à l'échelle locale, les résultats fournissent des indications sur les informations qui devraient être extraites des images satellites, comme par exemple la fraction nuageuse pondérée par la distance à la tache solaire, afin d'améliorer l'estimation de bilan radiatif solaire à grande échelle.

*INTEGRATION DE LA VARIABILITE TOPOGRAPHIQUE AU NIVEAU SOUS-PIXEL POUR AMELIORER L'ESTIMATION DE L'ECLAIREMENT ET L'ALBEDO A LA SURFACE A PARTIR D'IMAGES SATELLITES.* Une deuxième approche est proposée afin d'améliorer l'estimation de l'éclairement et de l'albédo basée sur des données issues de la télédétection en prenant en compte la variabilité spatiale du terrain au niveau sous-pixel. Tout d'abord, l'impact de la topographie sous-pixel sur l'éclairement est quantifié puis corrigé. Ensuite, l'éclairement corrigé au niveau sous-pixel est utilisé pour estimer la réflectance de la surface puis l'albédo. Pour réaliser cela, une nouvelle méthode de correction topographique est développée et évaluée : la correction topographique sous-pixel. Cette méthode est fondée sur l'hypothèse que, au lieu d'utiliser un MNT à la même résolution spatiale que les données radiométriques, il serait profitable de tirer avantage de la résolution spatiale plus fine des MNT disponibles à l'échelle globale pour caractériser et corriger les effets de la topographie au niveau sous-pixel. Cette correction topographique considère les composantes directe et diffuse de l'éclairement séparément. Donc, en plus de la correction en tant que telle, l'impact de l'atmosphère -exprimé par la fraction du diffus- sur l'estimation de l'éclairement corrigé a été analysé. La correction topographique sous-pixel a été testée sur des données synthétiques et réelles. Les résultats ont mis en évidence la nécessité d'intégrer les effets de la topographie sous-pixel lors de l'estimation de l'éclairement. Par ailleurs, l'influence de l'estimation de la fraction du diffus a également été démontrée. En effet, pour une valeur d'éclairement total comparable, différents partitionnements entre éclairement direct et diffus peuvent conduire à des estimations d'éclairement corrigé différentes. Il est donc également important d'intégrer les conditions atmosphériques réelles aussi précisément que possible afin d'estimer correctement l'éclairement corrigé au niveau sous-pixel.

Une fois corrigé pour les effets de la topographie au niveau sous-pixel, l'éclairement est utilisé pour calculer la réflectance de la surface à partir de données de satellites géostationnaires (Feng-Yun 2E). A leur tour, les valeurs de réflectance corrigées sont utilisées pour reconstruire la fonction de distribution de la réflectance bidirectionnelle de surface (BRDF) et dériver l'albédo topographiquement corrigé au niveau sous-pixel. Les valeurs de réflectance et l'albédo corrigés au niveau sous-pixel sont validés à l'aide de données terrain et de produits satellitaires existants. Comparés à une correction topographique au niveau du pixel, la réflectance et l'albédo estimés à partir de données satellitaires après une correction topographique sous-pixel présentent de meilleurs résultats. La validation montre clairement une estimation plus précise de la réflectance, même si la correction tend à légèrement surestimer les valeurs. Concernant l'albédo, l'analyse de sensibilité effectuée en utilisant des données synthétiques montre les mêmes résultats. Toutefois, en raison de la difficulté à estimer les coefficients nécessaires à la conversion bande étroite / bande large, la validation et la comparaison de l'albédo dérivé à partir de données satellitaires réelles est plus complexe. Cependant, il est possible de conclure que dans une zone relativement plane, la méthode n'apporte aucun biais et que dans les zones accidentées l'albédo estimé après une correction topographique sous-pixel fournit de meilleurs résultats que sans correction ou avec une correction au niveau du pixel. De plus, l'albédo estimé est aussi plus précis que celui fourni par d'autres produits existants. L'approche proposée permet également une amélioration de la résolution temporelle de l'albédo. La méthode d'estimation à partir de données géostationnaires horaires permet de produire une valeur d'albédo tous les 3 jours contre 8 jours pour MODIS et 10 jours pour METEOSAT. Cette amélioration a permis de mettre en évidence des fluctuations d'albédo qui n'apparaissent pas dans les produits d'albédo avec une résolution temporelle inférieure.

*CONCLUSIONS ET PERSPECTIVES.* Lorsque l'on considère des régions relativement planes, les produits satellitaires actuels permettent de modéliser le bilan radiatif solaire journalier à une résolution spatiale d'un kilomètre de manière satisfaisante. Cependant, comme cela est démontré dans cette thèse, dès lors que l'on travaille sur des zones hétérogènes telles que le Plateau Tibétain, les estimations doivent être améliorées en intégrant tant la variabilité spatiale et temporelle du terrain que la couverture nuageuse au niveau sous-pixel. Par ailleurs, la prise en compte de l'état de la couverture nuageuse en termes de distribution plutôt que de fraction bénéficie à l'estimation de l'éclairement à la surface. Comme la fraction nuageuse pondérée par la distance à la tache solaire semble être un bon indicateur pour la distribution spatiale des nuages, cet indice pourrait être estimé à une résolution temporelle convenable à partir des données fournies par les satellites géostationnaires actuels et à venir. De plus, des informations sur la couverture nuageuse à haute résolution temporelle conduisent à une meilleure agrégation temporelle des flux radiatifs. L'intégration des effets topographiques sous-pixel dérivés de MNT à haute

---

résolution spatiale permettent également d'améliorer les estimations de l'éclairement ainsi que l'albédo. La variabilité temporelle de ce dernier est également à considérer et, comme pour la caractérisation de la nébulosité, l'utilisation de données issues de satellite géostationnaire permettrait d'augmenter la fréquence des estimations. Les approches et propositions citées précédemment doivent permettre l'amélioration des estimations du bilan radiatif solaire. Fondée sur l'utilisation de données multi-sources et multi-résolution issue de la télédétection, la méthode développée dans cette thèse fournit une série temporelle d'estimations du bilan radiatif solaire, et les deux approches proposées pour améliorer ces estimations ouvrent la voie à une nouvelle méthode opérationnelle qui intègre de manière adéquate l'hétérogénéité sous-pixel lors de la production de séries temporelles d'estimation du bilan radiatif solaire à la surface.



# Résumé étendu

## 1. Introduction

### 1.1 Contexte

Le soleil est la principale source d'énergie du système climatique terrestre (Pekarek 2001). Les échanges d'énergie radiative entre la surface de la Terre et l'atmosphère sont l'un des mécanismes principal de ce système. La plupart des échanges ont lieu à la surface (Ohmura et al. 2005) où une partie du rayonnement solaire incident est absorbé tandis que le reste est renvoyé dans l'espace. Le bilan radiatif solaire ( $R_{ns}$ ) est défini par la différence entre les flux radiatifs solaires incidents ( $R_{S\downarrow}$ ) et réfléchis ( $R_{S\uparrow}$ ) à la surface de la Terre à un certain moment (Equation 1.1):

$$R_{ns} = R_{S\downarrow} - R_{S\uparrow} \quad 1.1$$

Un flux radiatif est généralement exprimé comme une densité de flux en  $\text{W}\cdot\text{m}^{-2}$ , soit la quantité d'énergie par unité de temps par unité de surface. Bien que le bilan d'énergie à la surface terrestre intègre également les radiations dans le domaine des grandes longueurs d'onde, cette thèse traite uniquement du rayonnement solaire. Une exception est faite dans le paragraphe 3, où les radiations thermiques sont mentionnées lors de l'analyse de la nébulosité. Le rayonnement net à la surface, intégrant solaire et thermique, est redistribué entre le flux de chaleur dans le sol et les flux turbulents, à savoir flux de chaleur sensible et latente (Monteith et al. 1990). Les flux turbulents affectent à leur tour la couche limite de l'atmosphère, et donc le climat de la Terre dans son ensemble. Dans ce contexte, le bilan radiatif solaire est le principal moteur de processus tel que l'évaporation et le réchauffement du sol et de l'air (Bisht et al. 2010). De plus, son suivi est essentiel pour de nombreuses applications telles que l'étude du changement climatique ou de la dynamique de la végétation, la gestion des ressources en eau et des productions agricoles ainsi que l'anticipation de périodes de sécheresse (Jia et al. 2006; Jia et al. 2011). L'organisation mondiale de la Météorologie (WMO) l'a déclaré comme étant une composante fondamentale du bilan d'énergie global de surface (GCOS 2007), lui-même crucial pour presque tous les aspects du climat, et devant être suivi de manière systématique à l'échelle régionale ou mondiale.

L'estimation du bilan radiatif solaire nécessite une quantification précise du flux radiatif solaire incident atteignant la surface, communément appelé éclairage solaire ( $E$ ), ainsi que la détermination de la fraction du rayonnement réfléchi par la surface. La quantité de rayonnement réfléchi est directement liée aux propriétés de la surface, généralement décrite par le facteur de réflexion ( $\rho$ ), appelé réflectance, et l'albédo ( $a$ ). La réflectance de surface est définie comme étant la fraction du rayonnement réfléchi par la surface pour des angles d'illumination et d'observation donnés, tandis que l'albédo de surface est une intégration de la réflectance directionnelle pour toutes les combinaisons d'angles d'illumination et d'observation (Schaepman-Strub et al. 2006). Cette intégration directionnelle est communément obtenue par l'intégration de la fonction de distribution de la réflectance bidirectionnelle (BRDF), qui décrit la dépendance de la réflectance aux angles d'illumination et d'observation.  $R_{ns}$  peut donc être exprimé en fonction de l'albédo de la surface ( $a$ ) et l'éclairage ( $E$ ,  $W.m^{-2}$ ) comme suit:

$$R_{ns} = (1 - a) E \quad 1.2$$

Le rayonnement solaire couvre l'ensemble du domaine spectral des ondes courtes, de 0,4 à 2,5  $\mu m$  environ, aussi appelé rayonnement solaire bande large. Contrairement à la bande large, le rayonnement solaire à bande étroite ne couvre qu'une partie du spectre solaire. Dans cette étude, le terme rayonnement désigne un rayonnement bande large, sauf mention contraire.

En climatologie, l'estimation des flux radiatifs solaires à la surface est un sujet d'intérêt depuis plusieurs années et qui est toujours d'actualité. Ces estimations peuvent être dérivées à partir de mesures au sol, d'observations satellitaires ou à l'aide de modèles, avec une certaine incertitude associée à chaque méthode. Les flux mesurés au sol sont considérées comme des données précises ( $< 20 W.m^{-2}$  (Liang et al. 2010)), avec une résolution temporelle pouvant être très élevée (jusqu'à quelques minutes). Cependant ces données ne sont représentatives que très localement, pour les environs proches de la station de mesure, les rendant donc peu adaptées aux études à grande échelle. Avec l'avènement des radiomètres spatiaux, un certain nombre d'algorithmes ont été développés pour estimer le bilan radiatif solaire à la surface à partir de données satellites à l'échelle locale, régionale et mondiale. Les images satellites, offrant une large couverture spatiale, ont conduit à des recherches plus approfondies sur le bilan radiatif terrestre. Cependant, même si les résultats sont prometteurs, l'estimation des flux radiatifs de surface à partir d'images satellites reste un défi, surtout en conditions nuageuses (Wang et al. 2009). De plus, bien que la résolution temporelle puisse-t-être jusqu'à horaire, la résolution spatiale des produits existants est souvent grossière (plusieurs kilomètres), la résolution spatiale diminuant généralement lorsque la résolution temporelle augmente. Les estimations de flux radiatifs fournies par les

modèles numériques ont généralement des résolutions spatiales plus grossières que les produits de télédétection mais des résolutions temporelles plus fines. Le degré de complexité de la physique utilisée pour caractériser la dynamique de la surface diffère d'un modèle à l'autre, bien que tous aient tendance à surestimer l'éclairement solaire (Liang et al. 2010). De nombreuses études ont également révélé de fortes divergences lorsque ces modèles ont été comparés à des produits satellites.

Le bilan radiatif solaire dépend de nombreux facteurs tels que la composition de l'atmosphère, la couverture nuageuse, les propriétés de la surface comme la couverture du sol et son albédo, ainsi que la pente et l'orientation du terrain (Baede et al. 2001). L'éclairement lui-même varie selon la géométrie Terre-Soleil en fonction de l'heure de la journée, le moment de l'année et l'emplacement géographique considéré (Boes 1981). Par conséquent, le bilan radiatif solaire varie considérablement dans l'espace et le temps et des estimations précises sont essentielles pour tenir compte de cette hétérogénéité spatiale ainsi que de la variabilité temporelle. Pour un suivi à l'échelle régionale ou mondiale de ce bilan, les observations au sol sont trop éparpillées alors que la télédétection répond parfaitement au besoin d'une couverture spatiale étendue et d'observations régulières au fil du temps. Comme indiqué dans l'équation 1.2, les deux principaux composants requis pour estimer le bilan radiatif solaire sont l'éclairement et l'albédo de surface. Des estimations précises de ces deux variables peuvent être dérivées d'images satellites, à condition que les effets combinés de l'atmosphère et de la topographie soient bien pris en compte. Plusieurs algorithmes permettent une description précise des effets atmosphériques (Turner et al. 1972; Kaufman 1984; Rahman et al. 1994; Song et al. 2003; Van Laake et al. 2004; Jiménez-Muñoz et al. 2010). Cependant, les effets des nuages restent difficiles à paramétrer (Wang et al. 2009) alors qu'ils impactent fortement l'éclairement, pouvant réfléchir 70-80% du rayonnement solaire incident (Saha 2008). En ce qui concerne l'impact de la topographie, même si de nombreux algorithmes ont été développés pour corriger les effets induits par le terrain (Rochon et al. 1979; Kawata et al. 1988; Proy et al. 1989; Meyer et al. 1993; Richter 1998; Richter et al. 2009; Szantoi et al. 2013), cet aspect est souvent négligé, ce qui entraîne des erreurs importantes dans les estimations, en particulier dans les zones montagneuses (Yang et al. 2008; Wang et al. 2014).

Comme cité précédemment, un des principaux avantages de la télédétection est sa large couverture spatiale. Cependant, l'estimation des flux radiatifs est déterminée par l'heure de passage du satellite et la fréquence d'estimation est donc directement liée à la résolution temporelle de ce dernier. Actuellement, les satellites géostationnaires collectent des données toutes les 15,30 ou 60 minutes avec une résolution spatiale moyenne à faible tandis que les satellites à défilement fournissent une résolution spatiale plus élevée mais avec au mieux une revisite quotidienne. Le meilleur compromis pour le suivi du bilan radiatif solaire offrant une résolution temporelle satisfaisante contraint donc les estimations à l'échelle du kilomètre carré. A cette échelle, le problème de l'hétérogénéité spatiale intra-

pixel se pose, en particulier concernant les nuages et la topographie qui impactent fortement le bilan radiatif solaire. Des études ont exploré les effets de l'hétérogénéité spatiale intra-pixel sur l'estimation des propriétés de surface (Kustas 2000; Liu et al. 2008; Wen, Qiang Liu, et al. 2009; Román et al. 2011). Jusqu'ici, la plupart de ces études ont porté sur l'hétérogénéité de la couverture de sol à et quelques-unes ont commencé à se pencher sur la variabilité de la topographie. Ces dernières ont montré que si la variabilité de la topographie à l'intérieur du pixel est négligée en terrain accidenté, les propriétés de surface estimées à différentes résolutions spatiales peuvent être considérablement différentes même en utilisant le même modèle (Liu et al. 2008), soulignant la nécessité de prendre en compte cette hétérogénéité. Cependant, la plupart des algorithmes actuels considèrent que l'agrégation de l'hétérogénéité de la topographie et des nuages au sein de pixels kilométriques est suffisante pour tenir compte de la variabilité spatiale locale, ce qui conduit à des erreurs d'estimation. Dans cette thèse, cette variabilité intra-pixel est considérée et exprimée à travers le concept de sous-pixel. La topographie sous-pixel, principalement par les effets d'ombre, a un impact sur les estimations de l'éclairement et de l'albédo de surface. De même, la distribution spatiale sous-pixel des nuages influe directement sur la répartition entre l'éclairement direct et diffus.

Les observations satellite fournissent des valeurs instantanées de rayonnement, qui sont d'un intérêt limité pour les applications climatiques ou hydrologiques, ces dernières ayant principalement besoin de valeurs journalières à mensuelles. De plus, compte tenu des variations dans l'heure de passage du satellite et des changements saisonniers de la géométrie Terre-Soleil, l'utilisation de flux radiatifs solaires journaliers est plus appropriée au suivi temporel. Il existe plusieurs méthodes pour convertir le rayonnement solaire instantané en moyenne journalière, principalement basées sur la durée d'ensoleillement. La durée d'ensoleillement exprime la longueur cumulée des périodes d'exposition directe au soleil entre le lever et le coucher du soleil pour un endroit donné du globe. Si les considérations astronomiques permettent une estimation empirique de ce paramètre pour un ciel dégagé, très peu d'études tentent de rendre compte de la variabilité réelle de la couverture nuageuse, ce qui conduit à des erreurs importantes dans de nombreuses régions (Bisht et al. 2010).

Il est également important de considérer le fait que les données satellitaires sont collectées dans une ou plusieurs bandes étroites sur l'ensemble du spectre solaire. Divers procédés permettant de convertir les estimations à bandes étroites en bande large ont été développés. Ils utilisent généralement des coefficients de conversion dérivés d'interpolations ou de simulations et reposent sur des hypothèses physiques. La définition de ces coefficients est complexe car ils sont très dépendants des conditions atmosphériques et des propriétés de surface pour lesquelles ils ont été estimés. Cette conversion est un problème connu lors de l'estimation des flux radiatifs à partir de la télédétection et est souvent une source d'erreur pour l'estimation de l'albédo.

## 1.2 Objectifs

Comme souligné précédemment, le suivi du bilan radiatif solaire au niveau continental et global est crucial. Actuellement, très peu de jeux de données sont disponibles à cette échelle. En outre, leurs résolutions spatiales et/ou temporelles ne permettent généralement pas d'appréhender correctement les variations spatiales et temporelles des flux radiatifs solaires (Ryu et al. 2008) et, malgré les efforts visant à intégrer les effets de la topographie et de la couverture nuageuse, des améliorations sont encore nécessaires pour répondre aux exigences des études climatiques. Par conséquent, l'objectif de cette thèse est exprimé comme suit:

*Développer une méthode opérationnelle basée sur des données issues de la télédétection permettant le suivi du bilan radiatif journalier par tous les temps pour de grandes zones hétérogènes, et proposer des améliorations pour l'estimation de l'éclairement et de l'albédo de surface en prenant en compte la variabilité sous-pixel de la topographie et de la nébulosité.*

Le suivi des flux radiatifs solaires journaliers de manière opérationnelle à partir d'observations satellites contraint les estimations à une résolution de l'ordre du kilomètre carré. Certains produits satellites caractérisant les propriétés de l'atmosphère et de la surface terrestres sont disponibles à ces échelles spatiale et temporelle. Dans un premier temps, un algorithme combinant ces produits est proposé pour estimer le bilan radiatif solaire. Toutefois, ce dernier ne tient pas compte de la variabilité sous-pixel. Par conséquent, des analyses plus approfondies sont menées pour améliorer les estimations du bilan radiatif solaire se concentrant sur la prise en compte de l'hétérogénéité sous-pixel en termes de variabilité spatiale de la topographie et de la distribution de la nébulosité. La variabilité temporelle de la couverture nuageuse et son impact sur l'agrégation temporelle des estimations des flux radiatifs est également étudiée. Ce travail de recherche peut être développé suivant trois questions :

*1: Les produits satellites actuels permettent-ils un suivi précis du bilan radiatif solaire à grande échelle pour des zones hétérogènes, de façon journalière et à une résolution d'un kilomètre carré?*

Plusieurs produits satellites fournissent actuellement des estimations journalières des paramètres atmosphériques nécessaires pour estimer l'éclairement de surface ainsi que des estimations hebdomadaires de l'albédo, tous au kilomètre carré. L'idée est donc de proposer une méthode opérationnelle pour produire des séries temporelles de flux radiatifs solaires journaliers au kilomètre carré, en se basant sur des algorithmes existants et les derniers développements dans le domaine. La série temporelle produite peut alors être

évaluée pour vérifier si les estimations dérivées des produits satellites permettent un suivi précis du bilan radiatif solaire pour de larges surfaces hétérogènes.

*2: La caractérisation spatiale et temporelle de la couverture nuageuse améliore-t-elle l'estimation de l'éclairement de surface et du bilan radiatif solaire journalier?*

Actuellement, l'intégration de la nébulosité dans le bilan radiatif solaire a deux limitations principales. Premièrement, dans la plupart des cas, la répartition spatiale des nuages au sein de chaque pixel est exprimée par la fraction nuageuse qui ne contient aucune information concernant la distribution spatiale. Deuxièmement, la caractérisation de la couverture nuageuse au cours de la journée, utilisée pour calculer la moyenne journalière du bilan radiatif solaire, est faite à partir de très peu de mesures. L'objectif est donc d'étudier en détail la relation entre la nébulosité et le rayonnement de surface ainsi que l'impact de la variabilité temporelle de la couverture nuageuse sur l'agrégation journalière du bilan radiatif solaire. Dans ce but, une campagne de terrain a été mise en place pour collecter des images hémisphériques du ciel à résolution temporelle très élevée en parallèle de mesures de flux radiatifs au niveau du sol.

*3: L'éclairement et l'albédo de surface estimés à partir d'images satellites peuvent-ils être améliorés par l'intégration de la variabilité topographique sous-pixel?*

Afin de suivre le bilan radiatif solaire, une résolution temporelle fine est nécessaire avec comme contrepartie une résolution spatiale kilométrique conduisant à une variabilité topographique à l'intérieur des pixels. Par conséquent, l'hypothèse est faite qu'au lieu d'utiliser un modèle numérique de terrain (MNT) à la même résolution spatiale que les données radiométriques, il pourrait être bénéfique de tirer avantage de la résolution plus fine des MNT actuels afin d'intégrer les effets de la topographie sous-pixel. Tout d'abord, quelques tests sont effectués pour quantifier l'impact de la topographie sur l'éclairement solaire dérivé à partir de données satellites. Ensuite, l'éclairement corrigé au niveau sous-pixel est utilisé pour estimer la réflectance de surface, qui permet à son tour de dériver l'albédo, pour vérifier si elle conduit à l'amélioration de l'estimation de ces deux paramètres.

### **1.3 Etude de cas: le plateau du Tibet**

Le plateau du Tibet, avec ses altitudes élevées, ses caractéristiques géographiques uniques, sa faune très diversifiée, ses ressources en eau et en minéraux a été baptisé le «Toit du Monde» ou le «Troisième pôle de la Terre» (Bisht 2008). Le plateau du Tibet influence fortement l'hydrologie et le système climatique de l'ensemble de l'Asie du Sud-Est. Des études récentes ont démontré le rôle du plateau dans les processus atmosphériques à l'échelle continentale et en particulier dans la détermination de la dynamique de la mousson en Asie et des événements de précipitations extrêmes en Chine et en Inde (Liu et al. 2013;

Bothe et al. 2011; Wu et al. 2007; Zhang et al. 2007; Wu et al. 2006). Plus de 40% de la population terrestre et l'ensemble de l'écosystème de l'Asie du Sud-Est, souffrant régulièrement de sécheresses extrêmes et d'inondations, dépendent de la mousson et de sa prévisibilité. Dans ce contexte, le suivi des flux radiatifs sur le plateau est un préalable essentiel pour mieux comprendre et modéliser ce système hydrologique particulier. Le plateau du Tibet est une zone d'intérêt pour les études météorologiques et hydrologiques depuis maintenant plusieurs décennies. Cela a commencé en 1996 avec le projet GAME<sup>17</sup>-Tibet mené dans le cadre du Programme mondial de recherche sur le climat (WCRP) visant à une meilleure compréhension des interactions terre-atmosphère sur le plateau. Après 10 années de recherche expérimentale et de modélisation, le projet CEOP-AEGIS<sup>18</sup> a été lancé dans le but d'améliorer les connaissances sur l'hydrologie et de la météorologie du plateau du Tibet et son rôle sur le climat, la mousson et les événements météorologiques extrêmes, afin de d'aider à la gestion des ressources en eau en Asie du Sud-Est. De par ce fait et en raison de ses caractéristiques géomorphologiques particulières ainsi que sa nébulosité saisonnière intéressante, le plateau du Tibet est une excellente zone d'étude pour les recherches effectuées dans le cadre de cette thèse.

Comme énoncé précédemment, l'une des principales questions lors du suivi des flux radiatifs solaires de surface à grande échelle est le manque de connaissances fondamentales sur la variabilité spatiale et temporelle des flux et cela est particulièrement vrai pour le plateau du Tibet. En raison de son élévation, la surface de plateau absorbe une grande quantité du rayonnement solaire et subit des changements saisonniers importants de flux de chaleur et d'eau à la surface. La spatialisation des estimations des flux radiatifs solaires de surface à des résolutions spatiales et temporelles fines est donc essentielle non seulement comme données de base pour la modélisation hydrologique, mais aussi comme proxy pour les systèmes de première alerte contre les inondations et la sécheresse. De plus, les stations météorologiques étant concentrées dans la partie Sud-Est du Plateau à des altitudes allant de 1500m à 4700m, tandis que le plateau atteint jusqu'à 8844 m (Mont Everest), les flux radiatifs ne peuvent pas être estimés avec précision à partir de mesures collectées au sol (Yang et al. 2006), soulignant la nécessité d'utiliser la télédétection. Parmi les produits de bilan radiatif existants pour cette zone, la plupart ont une résolution spatiale trop grossière (de 30 à 280 km de résolution) et ne sont pas adaptés pour caractériser les spécificités du plateau du Tibet. Yang et al. (2008) ont évalué certains de ces produits et ont constaté de grandes différences entre eux surtout pour les zones très hétérogènes (comme dans la région de l'Himalaya). De ce fait, des estimations du bilan radiatif solaire journalier au kilomètre carré, prenant mieux en compte les effets de la topographie et de la nébulosité,

---

<sup>17</sup> Global Energy and Water Cycle Experiment (GEWEX) Asian Monsoon Experiment (GAME)

<sup>18</sup> Coordinated Asia-European long-term Observing system of Qinghai-Tibet Plateau hydro-meteorological processes and the Asian-monsoon system with Ground satellite Image data and numerical Simulations

seraient très bénéfiques au suivi du bilan radiatif dans une région comme le plateau du Tibet, affectant le climat de l'Asie du Sud-Est dans son ensemble.

#### **1.4 Sources de données**

Les travaux menés au cours de cette thèse ont conduit à l'élaboration d'une méthode permettant le suivi des flux radiatifs solaires sur le plateau du Tibet et à des investigations plus approfondies sur l'influence de la topographie et de la nébulosité. Pour cela, plusieurs sources de données satellites ainsi qu'un MNT et des données collectées au sol ont été utilisés. La plupart des données proviennent de capteurs satellites, la télédétection étant la façon la plus cohérente et efficace pour collecter des données pour le suivi des flux radiatifs à grande échelle pour des zones à forte variabilité spatiale et temporelle. Le MNT à haute résolution spatiale est un jeu de données clé dans cette étude, il est essentiel pour caractériser et intégrer les effets de la topographie sur les flux radiatifs de surface au niveau sous-pixel.

## **2. Bilan radiative solaire à partir de produits satellitaires existants**

Certains produits satellites ont été développés et régulièrement améliorés pour caractériser les propriétés de l'atmosphère et de la surface avec une résolution spatiale d'un kilomètre carré et de manière journalière. L'objectif est donc de proposer une méthode opérationnelle qui s'appuie sur ces produits existants permettant le suivi des flux radiatifs solaires journaliers au kilomètre carré pour des zones hétérogènes et d'évaluer la précision qui peut être atteinte grâce à l'utilisation de ces produits. La méthode d'estimation des flux radiatifs solaires a été développée à partir d'algorithmes existants et des derniers développements dans le domaine. Les produits MODIS ont été sélectionnés comme données d'entrée car elles sont librement, largement et -pour la plupart des produits- disponibles de façon journalière. Une des principales caractéristiques influençant la modélisation des flux radiatifs solaires sur le plateau du Tibet est la topographie, essentiellement au Sud du plateau. La méthode proposée utilise donc la pente et l'azimut moyen du terrain de chaque pixel pour calculer l'éclairement selon l'angle d'illumination solaire réel et intègre la variabilité atmosphérique au niveau kilométrique. Les flux instantanés calculés pour toutes les conditions du ciel sont ensuite convertis en moyennes journalières. La méthode a été testée et utilisée pour produire une série temporelle de 3 ans, de 2008 à 2010 ce qui a permis d'effectuer une validation approfondie des résultats.

La validation à l'aide de données mesurées au sol a montré que la méthode développée permet de modéliser le bilan radiatif solaire instantané et journalier, au kilomètre carré sur l'ensemble du plateau du Tibet en utilisant des produits de données MODIS. Même si la précision globale des estimations ne semble pas meilleure que celle

des produits existants, cette méthode fournit des estimations à l'échelle du km<sup>2</sup> sur une base journalière – données clé pour une utilisation ultérieure dans les modèles climatiques - alors que les autres jeux de données de rayonnement net couvrant cette même zone fournissent des estimations à des résolutions spatiale ou temporelle plus grossières. Cependant, comme pour les autres produits fournissant des estimations du bilan radiatif solaire à grande échelle, la validation reste difficile et montre quelques divergences avec les données de terrain. Pour contourner ce problème, une comparaison radiométrique a également été réalisée pour évaluer la méthode proposée. Il semble qu'une grande partie des erreurs observées dans les estimations soient dues à l'imprécision des données initiales et à la manière d'intégrer la nébulosité. Tout d'abord, les erreurs les plus importantes sont observées pour le rayonnement montant, en particulier pour les zones avec une topographie marquée, ce qui est directement liée à l'estimation de l'albédo. Des efforts doivent donc être fournis pour intégrer les effets de la topographie lors de l'estimation de l'albédo à partir de données satellites, en particulier en ce qui concerne la variabilité sous-pixel de la topographie quand l'estimation de l'albédo est effectuée à une résolution kilométrique. De plus, la résolution temporelle des estimations de l'albédo doit également être affinée, comme l'a mis en avant la présence d'épisodes neigeux passagers non détectés lors des analyses. D'autre part, les estimations faites en présence de couvert nuageux ne fournissent pas de bons résultats en raison d'une prise en compte non adaptée de la nébulosité. Une investigation plus approfondie de l'impact de la variabilité spatiale et temporelle des nuages sur les flux radiatifs solaires est donc nécessaire. Il est également intéressant de mentionner l'absence de données sur le contenu de l'atmosphère en aérosols dans les produits MODIS mise en évidence par la validation. Cependant, considérant que la quantité d'aérosol dans l'atmosphère au-dessus du plateau du Tibet est très faible et constante et que la transmissivité de l'atmosphère par ciel clair est correctement estimée par la méthode proposée, aucune autre analyse ne sera réalisée sur cet aspect dans cette thèse. De plus, Hansen et al. (2002) a montré que, en cas de fort relief, la topographie a un effet plus important sur le rayonnement solaire net qu'une erreur dans la correction atmosphérique. Considérant les problèmes mis en évidence par la validation, des améliorations sont proposées dans les paragraphes suivants pour intégrer la variabilité sous-pixel liés aux nuages et à la topographie.

### **3. Impact de la variabilité spatiale et temporelle de la nébulosité sur le rayonnement solaire: une étude de cas**

La nébulosité est un paramètre fondamental qui influence les flux radiatifs solaires de surface de par le fait qu'elle a un impact significatif sur le partitionnement entre rayonnement direct et diffus (Cess et al. 1995). De plus, l'évolution de la couverture nuageuse au cours de la journée influence directement la durée d'ensoleillement,

couramment utilisée pour convertir les estimations instantanées de rayonnement solaire en estimation journalière. Même si différents schémas de paramétrisation existent pour intégrer l'impact de la nébulosité sur les flux radiatifs (Holloway et al. 1971; Stephens 1978; Stephens et al. 1984; Slingo 1987; Randall 1989; Harshvardhan 1995), les nuages sont encore la cause des erreurs les plus importantes en modélisation climatique (IPCC 2007; Randall et al. 2003). Les propriétés ainsi que la quantité et la distribution des nuages sont à prendre en compte quand on intègre leurs effets sur les flux radiatifs. L'impact de la distribution spatiale et de la variabilité temporelle de la couverture nuageuse sur le rayonnement solaire a donc été analysé afin de fournir des pistes pour améliorer l'intégration des conditions nuageuses lors de l'estimation du bilan radiatif solaire.

De par leur importante variabilité spatiale et temporelle, la définition et la détection des nuages est une tâche difficile, tout particulièrement à partir d'observation satellites (Silva et al. 2013). La distribution spatiale des nuages est souvent réduite à une valeur par pixel et exprimée en tant que fraction nuageuse, masquant ainsi toute information sur la distribution spatiale de la couverture nuageuse, et leur variabilité temporelle journalière est grossièrement dérivée d'un petit nombre de mesures au cours de la journée. Un autre problème lié à l'utilisation de données satellitaires est la difficulté à déterminer précisément si le soleil est obstrué pour un endroit donné à cause des incertitudes concernant l'estimation de la hauteur et de l'épaisseur des nuages (Ghonima et al. 2012). D'autre part, les informations sur la couverture nuageuse fournies par les stations météorologiques sont peu documentées. Une représentation numérique courante de la couverture nuageuse est l'octa, dérivé à partir d'observations visuelles faite par des opérateurs expérimentés. Cet indice a une faible résolution temporelle et spatiale, généralement une observation toutes les heures, et n'offre aucune garantie concernant la répétabilité de la mesure d'une station ou d'un opérateur à l'autre (WWRP (World Weather Research programme) 2012).

Une expérience sur le terrain, conduite à la station de NamCo, a été mise en place pour collecter des informations quantitatives sur la distribution spatiale et la variabilité temporelle des nuages. Ils existent des instruments commerciaux dédiés pour mesurer la nébulosité à partir du sol, mais ces derniers sont chers. Pour cette étude, une approche opérationnelle a été développée pour capturer les variations à court terme de la couverture nuageuse à l'aide d'une combinaison d'éléments hardware simple et peu coûteux. Le dispositif instrumental composé d'un objectif fish-eye monté sur un appareil photo numérique reflex a permis de collecter des images hémisphérique du ciel à très haute fréquence simultanément à des mesures de flux radiatifs mesurés sur la station. Après calibration, les images hémisphériques ont été divisées en deux classes - nuage et ciel clair - permettant de dériver plusieurs indices utilisés ensuite pour investiguer l'impact de la distribution spatiale de la couverture nuageuse sur les fluxes radiatifs solaires et pour mesurer la sensibilité de l'estimation de la durée d'ensoleillement à la fréquence temporelle des acquisitions. Pour la classification, une méthode complètement automatique a été

développée, basée sur la segmentation de l'histogramme de distribution de la bande rouge de l'image hémisphérique. Les indices dérivés des images classifiées se répartissent en deux catégories : les indices utilisables directement par d'autres applications, tel que la fraction et la distribution du couvert nuageux, et ceux potentiellement intéressants pour la corrélation avec les flux radiatifs mesurés afin de comprendre l'impact de la nébulosité. Concernant la fraction nuageuse, différentes façon de la calculer ont été utilisées intégrant ou non l'information fournie par la distribution.

Une fois les indices extraits des images hémisphériques, ils peuvent être corrélés aux flux radiatifs mesurés simultanément afin d'explorer l'impact de la nébulosité sur ces flux. Bien que cette thèse ne traite que du rayonnement solaire, le rayonnement thermique mesuré à la surface est aussi utilisé au cours de cette analyse dans le cadre de la corrélation. Tout d'abord la validation de la classification des images hémisphériques a été réalisée afin de s'assurer de l'exactitude des indices utilisés par la suite. L'expérience réalisée à la station de Namco illustre la flexibilité et la fiabilité de l'installation et de la méthode de traitement d'images proposées pour la collecte opérationnelle et intensive de la couverture nuageuse et de sa distribution. La validation montre de très bons résultats concernant les différentes estimations des fractions de nuages, qui sont plus précises et cohérentes que les estimations faites par les observateurs. Les erreurs de classification observées sont principalement dues à des nuages fins ou situés sur et autour de la tache solaire.

Les résultats de l'analyse des indices montrent que, même si la plupart des indices ne présentent pas de corrélation avec les flux radiatifs mesurés au sol, les fractions de nuages montrent des tendances intéressantes. Il apparaît que dans le domaine du thermique les flux radiatifs sont très corrélés avec la fraction de nuages alors que l'éclairement solaire dépend fortement de la répartition des nuages, ce qui met en évidence la nécessité de considérer l'organisation spatiale des nuages. L'approche proposée est alors très utile, car elle est peu coûteuse et facile à mettre en place. En outre, le traitement des images est très rapide, entièrement automatique et fournit une carte de la distribution des nuages, essentielle lors d'estimation de l'éclairement. Toutefois, les données sont fournies à petite échelle. L'analyse montre également que l'estimation de la durée d'ensoleillement, couramment utilisée pour convertir le rayonnement instantané en journalier, est très sensible au pas de temps auquel les données sont collectées, donc à la variabilité temporelle des nuages. Un autre avantage de cette approche est, par conséquent, la haute résolution temporelle des données recueillies. Les résultats montrent que, pour un ciel hétérogène, des erreurs significatives peuvent être faites si l'intervalle d'échantillonnage est de plus de 15 minutes. Dans ce cas, l'exploitation de la haute fréquence temporelle des satellites géostationnaires, comme MSG<sup>19</sup> fournissant une image toutes les 15 minutes, serait très bénéfique pour l'estimation de l'éclairement et l'agrégation temporelle des flux

---

<sup>19</sup> Meteosat Second Generation

radiatifs solaire. De plus, l'utilisation de la fraction nuageuse pondérée par la distance angulaire au soleil s'est avérée être la meilleure façon de dériver la durée d'ensoleillement pour l'agrégation temporelle du bilan radiatif, en fournissant de meilleurs résultats que l'utilisation de la visibilité de la tache solaire ou la fraction nuageuse classique. Ces observations renforcent la nécessité de dériver des informations sur la distribution des nuages et montre que la fraction nuageuse pondérée par la distance au soleil est un bon indicateur de cette information. Contrairement à la visibilité de la tache solaire, la fraction nuageuse pondérée par la distance au soleil pourrait être estimée à partir d'observations satellites combinant la fraction nuageuse actuelle avec le calcul de la géométrie solaire. De plus, l'utilisation des données satellites permettrait de surmonter le problème de la spatialisation inhérente à toutes les mesures au sol et de fournir des estimations à grande échelle.

À la lumière de ces résultats, l'estimation des flux radiatifs solaires de manière opérationnelle pourrait grandement bénéficier de l'utilisation de nouvelles données concernant la nébulosité, en particulier prenant en compte la distribution des nuages, mesurées à une fréquence temporelle plus élevée. Ces données pourraient être extraites d'observation de satellites géostationnaires fournies toutes les 30 minutes par la série des FY-2<sup>20</sup> ou toutes les 15 minutes par MSG.

#### **4. Effets de la topographie sous-pixel sur l'estimation de l'éclairement solaire à partir de données satellites**

Les corrections radiométriques nécessaires pour une utilisation correcte des données satellites semblent être souvent négligées ou sous-estimées (Baraldi 2009), en particulier dans les régions montagneuses. Les corrections topographiques sont essentielles pour améliorer l'estimation des propriétés de la surface et sont aussi essentielles pour la détection d'anomalies lors de suivi temporel (Song et al. 2003). Dans la méthode développée initialement (§ 2), la pente et l'azimut moyen de chaque pixel sont utilisés pour calculer l'angle d'illumination local nécessaire pour estimer l'éclairement de surface. Cependant, ne considérer que la géométrie du terrain n'est pas suffisant pour intégrer avec précision les effets induits par la topographie, l'impact des effets d'ombre et du rayonnement réfléchi par les pentes environnantes n'étant pas pris en compte. De plus, les paramètres utilisés sont à l'échelle kilométrique, négligeant la variabilité spatiale de la topographie à l'intérieur des pixels. L'objectif est donc d'étudier l'impact de la topographie sur l'estimation de l'éclairement solaire à la surface en intégrant tous les effets de la topographie au niveau sous-pixel. Pour cela, une méthode novatrice de correction topographique sous-pixel est proposée.

---

<sup>20</sup> FengYun 2

La disponibilité croissante des MNT a permis d'estimer les effets induits par la topographie sur les données radiométriques collectées par les satellites. Des études ont montré que la topographie induit des distorsions de la radiance observée et donc aussi de l'estimation des propriétés de surface (Rochon et al. 1979; Kawata et al. 1988; Proy et al. 1989; Meyer et al. 1993; Liu et al. 1996; Richter 1997; Wen, Qinhua Liu, et al. 2009). Différentes méthodes ont été mises au point pour corriger l'effet de la topographie au niveau du pixel, permettant d'améliorer la précision de la radiance de surface mesurée (Riano et al. 2003; Richter et al. 2009; Szantoi et al. 2013). Au cours des dernières années, des MNT à résolution plus fine ont été produits à l'échelle mondiale avec une résolution spatiale pouvant atteindre jusqu'à 30m. D'autre part, la plupart des méthodes pour estimer le bilan radiatif solaire à partir de données de télédétection utilisent des données satellites à l'échelle kilométrique, ce qui est aussi le cas dans cette thèse avec les produits MODIS ou les données FY-2E. La disponibilité de MNT à plus haute résolution offre donc la possibilité d'explorer les effets du terrain sur la radiance mesurée à une résolution plus fine et ainsi d'analyser les effets de la topographie au niveau sous-pixel. Cette problématique a été abordée par Wen et al. (2009), mettant en évidence la nécessité d'une correction topographique sous-pixel dans les zones accidentées. Cette étude présente des résultats prometteurs, cependant, tous les effets liés à la topographie ne sont pas considérés. L'impact des pixels environnants a été négligé bien qu'il ait été prouvé comme ayant une grande influence sur la radiance mesurée par les satellites dans les zones accidentées (Dozier et al. 1981; Sugawara et al. 2010). Une méthode permettant de corriger les effets induits par la topographie sous-pixel sur l'estimation de l'éclairement solaire de surface à l'aide d'un MNT à résolution fine et intégrant l'effet des pentes environnantes est donc proposée.

Dans cette thèse, l'éclairement de surface n'est pas directement dérivé des données satellites, mais ces dernières sont utilisées pour estimer la transmissivité atmosphérique nécessaire pour convertir l'éclairement au sommet de l'atmosphère en éclairement de surface. La correction topographique sous-pixel présentée et appliquée ensuite est inspirée de la correction topographique proposée par Sandmeier & Itten (1997). Cette méthode traite séparément l'éclairement direct et diffus. Une analyse a donc été conduite pour évaluer l'impact de l'estimation de la fraction de rayonnement diffus sur l'estimation de l'éclairement après correction topographique sous-pixel. Deux méthodes pour estimer l'éclairement direct, le diffus et la fraction de rayonnement diffus ont été comparées: l'une utilisant le profil atmosphérique américain standard de MODTRAN et l'autre utilisant des conditions atmosphériques réelles dérivées des produits MODIS. Les résultats des deux méthodes ont été comparés et utilisés pour estimer l'éclairement pour différents types de topographie.

Grace à la méthode développée, l'effet de la topographie sous-pixel sur l'estimation de l'éclairement de surface pour le plateau du Tibet a été étudié, prenant en compte l'orientation du terrain, l'impact de l'ombre et du rayonnement réfléchi par les pentes

environnantes. De plus, l'influence de l'estimation de la fraction de rayonnement diffus sur le calcul de l'éclairement corrigé au niveau sous-pixel a été explorée. Cette méthode intègre la topographie au niveau sous-pixel en utilisant un MNT avec une résolution spatiale élevée, ce qui permet de calculer des paramètres tels que le « sky view factor » (SVF) et le « shadow binary factor » (SBF), deux paramètres utilisés pour l'intégration des effets de la topographie, de manière très précise. Dans la littérature, le SVF est présenté comme étant un paramètre important pour le calcul du rayonnement diffus descendant (Dubayah et al. 1995; Duguay 1995; Varley et al. 1996). Le SBF est aussi décrit comme essentiel en raison de son influence dominante sur le bilan radiatif solaire en terrain complexe (Corripio 2003). Les résultats montrent que négliger la topographie lors de l'estimation de l'éclairement de surface peut conduire à des erreurs allant jusqu'à  $600 \text{ W.m}^{-2}$  dans certaines conditions extrêmes. Ces résultats sont cohérents avec ceux présentés dans Borel et al. (1998), ces derniers montrant que l'intégration des ombres pouvait diminuer l'estimation de l'éclairement de 20 à 60%, et ceux de Chow et al. (2006), qui ont confirmé l'influence notable de l'ombre sur l'éclairement solaire, en particulier pendant le lever et le coucher du soleil.

L'analyse de l'influence de la fraction de rayonnement diffus montre que malgré des partitionnements différents entre le direct et le diffus fournis par les deux méthodes testées, la correction topographique sous-pixel conduit à des valeurs d'éclairement total très similaires. Ces résultats ont été obtenus pour un essai sur une zone accidentée en période estivale. Cependant, des différences significatives sont observées en hiver. Pour approfondir ces résultats, une analyse de sensibilité a été menée afin de simuler l'impact de différents partitionnements entre éclairage direct et diffus sur l'éclairement corrigé au niveau sous-pixel, pour plusieurs types de topographie et différentes élévations solaires. Cette analyse montre que, même en fournissant un éclairage total identique, l'éclairement total corrigé présente d'importantes variations pour les zones accidentées lorsque les angles d'illumination sont importants et que la proportion de rayonnement direct est élevée. L'estimation du partitionnement entre éclairage direct et diffus affecte donc le résultat de la correction topographique sous-pixel et plus spécifiquement l'impact des ombres sur l'estimation de l'éclairement solaire dans des zones au relief accidenté. Il est alors important d'estimer les conditions atmosphériques réelles aussi précisément que possible afin d'estimer l'éclairement solaire de surface corrigé au niveau sous-pixel le plus correctement possible.

Ces résultats montrent que l'intégration précise de tous les effets liés à la topographie, et surtout l'intégration de la variabilité intra-pixel, lorsque l'on travaille avec de grands pixels, peuvent grandement améliorer l'estimation du bilan radiatif solaire dérivé d'images satellites. De plus, des efforts devraient également être fournis en ce qui concerne la modélisation de l'atmosphère, la fraction de rayonnement diffus ayant aussi une influence sur l'exactitude des résultats. L'éclairement solaire topographiquement corrigé au niveau

sous-pixel peut ensuite être utilisé pour dériver la réflectance et l'albédo corrigés au niveau sous-pixel à partir de données satellites à l'échelle kilométrique.

## 5. Albédo de surface en terrain accidenté

Les bénéfices apportés par l'intégration des effets de la topographie au niveau sous-pixel lors de l'estimation de l'éclairement de surface pour des zones accidentées ayant été démontré, l'objectif est donc maintenant d'étudier si la correction des effets liés à la variabilité du terrain au niveau sous-pixel permet également d'améliorer l'estimation de la réflectance et de l'albédo de surface. De plus, la résolution temporelle du produit d'albédo MODIS ayant été citée comme un des points faibles de la méthode d'estimation du bilan radiatif solaire proposée, la possibilité d'augmenter cette résolution temporelle en estimant l'albédo à partir de données de satellite géostationnaire est également étudiée.

Afin d'intégrer les effets de la topographie sous-pixel lors de l'estimation de l'albédo, la première étape est de corriger la réflectance de surface en utilisant l'éclairement solaire corrigé au niveau sous-pixel produit précédemment. Ensuite, la seconde étape consiste à accumuler ces valeurs de réflectance corrigées au niveau sous-pixel pour des combinaisons d'angles d'observations et d'illuminations différentes permettant de reconstruire la BRDF de surface et ainsi de dériver l'albédo corrigé au niveau sous-pixel. L'albédo produit à partir d'images satellites est un albédo à bande étroite correspondant à la largeur de la bande spectrale du satellite utilisé. Une conversion pour passer en albédo à bande large est donc nécessaire. Différent types d'observations satellites peuvent être utilisés pour construire l'échantillonnage angulaire nécessaire à l'estimation de l'albédo : les satellites à défilement ou les géostationnaires. Quel que soit l'instrument, les observations directionnelles peuvent être couplées avec un modèle paramétrique pour caractériser la BRDF et dériver l'albédo (Lucht et al. 2000). En se basant sur la haute résolution temporelle et les variations de l'angle d'illumination des données fournies par les satellites géostationnaires, il est possible de reconstruire la BRDF à partir des mesures de réflectance de surface et de dériver par intégration angulaire l'albédo de surface (Pinty et al. 2000; Govaerts et al. 2006). Contrairement aux satellites à défilement, les satellites géostationnaires permettent l'accumulation des observations nécessaires sur une période de temps relativement courte et donc d'estimer l'albédo plus fréquemment. Dans cette thèse, une méthode pour estimer l'albédo corrigé au niveau sous-pixel à partir d'images du satellite géostationnaire FY-2E et utilisant le modèle RPV (Rahman-Pinty-Verstraete) (Rahman et al. 1993) est proposée. Contrairement à la méthode basée sur les produits satellitaires existants (§ 2), cette méthode vise à corriger la réflectance et l'albédo de surface pour les effets de la topographie sous-pixel et non pour la pente et l'orientation moyenne du terrain uniquement. Une approche pour convertir l'albédo bande étroite en bande large est également présentée.

Les analyses réalisées mettent en avant de meilleurs résultats pour l'estimation de la réflectance de surface après la correction topographique au niveau sous-pixel qu'après la correction au niveau du pixel, surtout dans les zones fortement accidentées. Ces résultats sont cohérents avec ceux présentés dans Wen et al. (2009). Les différences les plus importantes observées entre les deux niveaux de correction sont principalement liées à l'intégration plus détaillée des effets de la topographie sous-jacente lors de l'estimation de l'éclairement solaire direct reçu par la surface. Que ce soit au niveau pixel ou sous-pixel, l'éclairement corrigé est principalement influencé par le SBF. L'estimation de ce dernier au niveau sous-pixel est cruciale car il permet de prendre en compte les cas d'ombrage partiel des pixels kilométriques. En effet, comme il s'agit d'une variable binaire, le SBF ne prend pas en compte la possibilité d'un ombrage partiel du pixel alors qu'une proportion significative de la zone couverte par un pixel d'un kilomètre carré marqué comme ombragé peut en réalité voir le soleil si le calcul est réalisé au niveau pixel. Ceci peut affecter de façon significative l'estimation de la réflectance de surface alors que les calculs effectués à une résolution plus fine sont bien moins affectés par ce problème. De plus, en comparaison des études déjà réalisées sur l'hétérogénéité de la topographie sous-pixel, l'intégration de l'éclairement réfléchi par les pentes environnantes dans la correction est une amélioration significative, ce dernier pouvant représenter une contribution importante à l'éclairement total reçu par un pixel (dans certains cas plus de  $150 \text{ W.m}^2$ ), surtout quand ce dernier ne reçoit aucun rayonnement solaire direct (Dozier et al. 1981).

Concernant l'estimation de l'albédo, l'analyse de sensibilité réalisée à l'aide de données synthétiques a mis en évidence les avantages liés à l'utilisation de la correction sous-pixel, tout particulièrement dans les zones montagneuses. La nécessité de considérer également l'hétérogénéité de la couverture de sol au niveau sous-pixel a aussi été mise en évidence comme dans Liu et al. (2008). La validation a montré que l'albédo corrigé estimé à partir des données FY-2E pour NamCo est autant plus précis que celui fourni par d'autres produits satellites existants. Cependant, les résultats pour l'albédo de Qomolangma sont moins évidents, principalement à cause de la conversion de bande étroite à bande large. Il est cependant intéressant de souligner que, pour des zones relativement planes, la méthode proposée n'apporte aucun biais et que pour les zones accidentées, l'albédo estimé après correction topographique au niveau sous-pixel fournit de meilleurs résultats que sans correction. De plus, de par l'amélioration observée pour les estimations de la réflectance de surface et également de par les résultats obtenus lors de l'utilisation des données synthétiques, il est raisonnable de conclure que, en cas de forte topographie, la méthode de correction topographique sous-pixel fournit les meilleurs résultats et qu'il est essentiel d'intégrer les effets induits par la topographie au niveau sous-pixel pour estimer précisément l'albédo à partir de données satellites.

Ces conclusions sont cohérentes avec celles présentées dans le paragraphe précédent et renforcent la nécessité d'intégrer de façon précise la variabilité intra-pixel de la topographie

pour les pixels à l'échelle kilométrique afin d'améliorer l'estimation de l'albédo et donc l'estimation du bilan radiatif solaire à partir de données satellites. De plus, l'utilisation de données satellites géostationnaires fournies à pas horaire permet la production d'une valeur d'albédo tous les 3 jours contre une valeur tous les 8 jours pour les produits MODIS utilisés précédemment. Cette amélioration est très bénéfique, les propriétés de surface pouvant varier très rapidement sur le plateau. L'utilisation de données à plus haute résolution temporelle comme celle fournies par MSG ou les satellites FY-2 à venir permettront certainement de produire des valeurs d'albédo à une résolution temporelle encore plus fine. Cependant, la conversion spectrale de l'albédo reste un problème et l'utilisation de données plus précises sur la couverture de sol sous-jacente permettrait sûrement d'améliorer cet aspect.

## 6. Conclusions and perspectives

Le bilan radiatif solaire est une variable climatique essentielle nécessitant un suivi régulier à l'échelle régionale ou mondiale afin de mieux comprendre l'évolution du climat (GCOS-128 2009). Dans ce contexte, cette thèse explore les possibilités d'amélioration du suivi du bilan radiatif solaire pour des zones étendues et hétérogènes. L'objectif principal est de proposer une méthode opérationnelle fournissant des estimations de flux radiatifs solaires journaliers à l'échelle du kilomètre carré et d'explorer des pistes d'amélioration de cette méthode en prenant en compte la variabilité sous-pixel de la topographie et la variabilité spatiale et temporelle de la nébulosité. L'étude a été conduite sur le plateau du Tibet en raison de sa topographie marquée, de sa nébulosité intéressante et son rôle majeur dans l'hydrologie et la climatologie de l'ensemble de l'Asie du Sud-Est.

La méthode opérationnelle développée dans cette thèse pour dériver flux radiatifs solaires journaliers et au kilomètre carré en utilisant des produits satellites, a conduit à la production d'une série temporelle de bilan radiatif solaire. Même si ce jeu de données est une amélioration significative par rapport à ceux disponibles pour le plateau du Tibet en ce qui concerne la résolution spatiale et temporelle, les estimations du rayonnement solaire sur les zones hétérogènes pourraient encore être améliorées. Pour cela, deux approches ont été proposées afin de résoudre les problèmes liés à l'hétérogénéité sous-pixel en termes de distribution spatiale et temporelle des nuages et de variabilité spatiale de la topographie. L'analyse menée sur l'impact de la distribution spatiale de la couverture nuageuse et de sa variabilité temporelle sur les flux radiatifs solaires à la surface était un premier essai visant à estimer automatiquement la fraction nuageuse et la distribution des nuages à une fréquence temporelle très élevée et de les corrélérer avec les flux radiatifs mesurés à la surface. Malgré les très bons résultats obtenus, d'autres travaux pourraient être effectués afin d'améliorer l'approche proposée. En ce qui concerne la classification des images hémisphériques, la détection des nuages à l'intérieur et autour de la tache solaire devrait être

améliorée, cette portion de l'hémisphère ayant été identifiée comme étant un élément essentiel de l'image lors de l'estimation de l'éclairement solaire. À cet égard, l'expérience pourrait être réitérée en combinant le système actuel avec des capteurs supplémentaires, un «sun tracker» et une caméra infrarouge par exemple. Cela aiderait probablement pour la détection de la tache solaire ainsi que pour l'estimation du rayonnement direct et permettrait de s'affranchir des limitations liées à l'utilisation de données RGB uniquement. De plus, des recherches pourraient être menées dans le but d'extraire plus d'informations caractérisant la nébulosité telles que l'épaisseur et la hauteur des nuages par exemple. Au vu des résultats de la corrélation avec les flux radiatifs, l'analyse pourrait bénéficier de l'utilisation de mesures au sol à un pas plus fin que des valeurs agrégées sur 10 minutes, des variations importantes dans la couverture nuageuse ayant été observées en deçà de ce pas de temps. Il est également essentiel de refaire cette expérience sur une plus longue période afin de renforcer les conclusions sur la corrélation entre les caractéristiques de la couverture nuageuse et les flux radiatifs de la surface, l'objectif principal étant de trouver la meilleure façon de prendre en compte la nébulosité lors des estimations du bilan radiatif solaire et de voir comment cela pourrait être dérivé des données satellites pour permettre la mise en application sur de larges zones. Pour le moment, la fraction nuageuse pondérée par la distance angulaire au soleil semble être un bon indicateur pour la distribution spatiale des nuages lors de l'estimation du bilan radiatif solaire. Dans ce contexte, la prochaine étape serait de travailler sur l'estimation de cet indicateur à partir des données satellites au lieu de la fraction nuageuse classique couramment utilisée. Cela permettrait de s'affranchir de la limitation inhérente à l'échantillonnage spatial des mesures terrestres et donc de travailler sur des zones plus étendues. L'utilisation des données provenant de satellites géostationnaires devrait être privilégiée car les observations sont fournies à haute résolution temporelle ce qui est très profitable à l'estimation de la durée d'ensoleillement et à l'agrégation temporelle des flux. Au-delà des applications évoquées dans cette thèse, les cartes de distribution des nuages produites par l'approche proposée pourraient être bénéfiques pour d'autres applications, par exemple pour intégrer la distribution réelle du forçage radiatif dans les modèles de bilan radiatif et de bilan d'énergie 3D, en particulier pour les études où les effets d'orientation peuvent être forts (zones accidentées ou zones urbaines). De plus, cette approche pourrait être facilement transférable aux stations météorologiques où ces mesures seraient un complément intéressant aux autres mesures effectuées.

La deuxième approche proposée, la méthode de correction topographique sous-pixel, permet d'améliorer l'estimation de l'éclairement de surface, de la réflectance et de l'albédo dérivés à partir des données satellites. Les résultats montrent clairement une estimation plus précise de la réflectance, même si elle tend à être légèrement surestimée. Cette surestimation pourrait probablement être corrigée en remplaçant la loi du cosinus utilisée pour la correction de l'éclairement direct par une méthode de correction plus efficace, telle

que la fonction Minneart. Comme la surestimation reste assez faible, elle pourrait aussi être causée par l'hypothèse définissant la surface comme lambertienne lors du calcul de l'éclairement réfléchi par le terrain adjacent ou par le fait de négliger la réflectivité multiple. Même si la propriété anisotrope de la surface n'a pas été prouvée comme étant un facteur ayant une forte influence, son intégration dans la correction topographique sous-pixel devrait être étudiée davantage. En ce qui concerne l'estimation de l'albédo, l'analyse de sensibilité montre une amélioration résultant de la correction sous-pixel, mais met également en évidence l'impact de la couverture de sol au niveau sous-pixel en fonction de son hétérogénéité. Les estimations de l'albédo pourraient donc être encore améliorées par l'intégration de l'hétérogénéité sous-pixel de la couverture de sol. Lorsqu'elle est appliquée sur des données réelles provenant de satellites géostationnaires, les avantages apportés par la méthode de correction sont moins évidents, principalement en raison des problèmes de géoréférencement des données FY-2E et des difficultés à définir les coefficients de conversion spectrale. Pour renforcer les conclusions avancées dans cette thèse, il serait intéressant d'effectuer à nouveau cette analyse mais après un géoréférencement précis des données FY-2E ou en utilisant d'autres données de satellites géostationnaires, et en estimant les coefficients de conversion spectrale à l'aide de données réelles sur la couverture de sol. De plus, une discrimination des nuages plus adaptée permettrait d'améliorer l'ensemble du processus en aidant à distinguer plus efficacement les pixels contaminés par les nuages et donc à éviter les distorsions dans la reconstruction de la BRDF. Il est important de signaler également que, même si fiable, le modèle RPV utilisé pour la reconstruction de la BRDF semble être sensible à l'échantillonnage angulaire fourni en entrée. Ce point devrait être approfondi afin de définir avec plus de précision comment construire un échantillon d'observations multi-angulaires adapté et d'assurer ainsi une estimation correcte de l'albédo. Un dernier aspect à explorer afin d'améliorer l'estimation de l'albédo ainsi que sa résolution temporelle serait d'utiliser des données FY-2 plus récentes et de meilleure qualité: les données fournies par FY-2F/G, lancés respectivement en 2012 et 2014, et le futur FY-2H, collectant des images toutes les 30 minutes. Il est également important de préciser que la méthode de correction sous-pixel proposée a été appliquée dans cette thèse sur des données à l'échelle kilométrique avec un MNT à 30m mais pourrait également être appliquée à d'autres combinaisons de résolutions spatiales. Ainsi, les améliorations apportées par cette méthode pourraient être profitables à l'estimation des propriétés de surface à partir d'images provenant d'autres satellites. Il est important de souligner que le gain en précision par rapport à la correction pixel classique croît avec la complexité de la topographie sous-jacente. La correction sous-pixel nécessitant plus de temps de calcul, les zones où l'appliquer devraient donc être ciblées dans le cas d'études à l'échelle mondiale.

Pour finir, les deux approches proposées devraient être appliquées sur des zones plus étendues afin de produire de nouveaux produits d'éclairement et d'albédo de surface. Ceux-ci pourraient alors être utilisés comme données d'entrée pour la méthode d'estimation du

bilan radiatif solaire et permettraient de quantifier l'amélioration ainsi obtenue. De nouveaux produits satellitaires plus précis seront disponibles à l'avenir et il sera alors intéressant de les utiliser en remplacement des produits utilisés actuellement par la méthode et d'évaluer l'avantage réel pour l'estimation du bilan radiatif solaire.

## Curriculum Vitae



Laure Roupioz was born the 14<sup>th</sup> of June 1984 in Lyon (France). Graduated from the Engineering School of Agriculture and Environmental Sciences (ISARA, Lyon) in 2008, she obtained her master degree in Geo-Information Science at the Wageningen University (The Netherlands) with distinctions the same year. From August 2008 to early 2015, she worked as a researcher in remote sensing and GIS at ALTERRA Wageningen University and Research, where she contributed to numerous international research programs and gained good skills in collaborative work and project management, as well as a high level of expertise in GIS, LIDAR data processing and remote sensing for environmental studies. In October 2010, she started her PhD entitled “Observing at-surface irradiance and albedo from space: the Tibet experiment” under the co-supervision of the University of Strasbourg, France, and of the Delft University of Technology, The Netherlands. Involved in the European FP7 program CEOP-AEGIS focusing on the hydrology of the Tibetan Plateau, she was in charge of improving the estimates of the radiative balance of the entire plateau from remote sensing, and proposed innovative approaches to account for strong topography and clouds effects. In the frame of the Dragon 3 Young Scientist program -a cooperation between the European Space agency and the Ministry of Science and Technology of the P.R. China- she designed and conducted an experiment on the monitoring of clouds on the Tibetan plateau in August 2013. Her research work lead to the publication of 20 papers and scientific reports, and was presented in 6 international conferences. Besides, she also taught remote sensing at the French National Institute for Applied Sciences, Strasbourg, as part of the first and second grade of the land-surveying master program of this engineering school. At the time of writing, Laure Roupioz continues her research as a post-doc in the ICube Laboratory, Strasbourg, France, where she focuses on the use of ground based infrared imaging radiometers for vegetation evaporation monitoring, as part of a major study on the urban climate of Strasbourg supported by the french National Center for Space Studies.



## List of Publications

### Articles

- Mücher, C.A., Roupioz, L., Kramer, H., Bogers, M.M.B., Jongman, R.H.G. et al., 2015. Synergy of airborne LiDAR and Worldview-2 satellite imagery for land cover and habitat mapping: A BIO\_SOS-EODHaM case study for the Netherlands. *International Journal of Applied Earth Observation and Geoinformation*, 37, p.48-55.
- Roupioz, L., Colin, J., Jia, L., Nerry, F., Menenti, M., 2015. Quantifying the impact of cloud cover on ground radiation flux measurements using hemispherical images. *International Journal of Remote Sensing*, (Accepted).
- Roupioz, L., Nerry, F., Jia, L., Menenti, M., 2014. Improved Surface Reflectance from Remote Sensing Data with Sub-Pixel Topographic Information. *Remote Sensing*, 6(11), pp.10356–10374.
- Roupioz, L., Jia, L., Nerry, F., Menenti, M., 2014. Correction of sub-pixel topographical effects on land surface albedo retrieved from geostationary satellite (FengYun-2D) observations. *IOP Conference Series: Earth and Environmental Science*, 17(1), p.012270.

### Conferences with proceedings

- Roupioz, L., Colin, J., Jia, L., Nerry, F., Menenti, M. Quantify the impact of cloud cover on radiation fluxes ground measurements from hemispherical images (oral presentation), *Recent Advances in Quantitative Remote Sensing (RAQRS IV)*, Valencia, Spain, September 2014.
- Roupioz, L., Nerry, F., Jia, L., Brigatti, M., Menenti, M. Estimate of daily surface albedo over highly heterogeneous area on the Tibetan Plateau using geostationary data (poster presentation), *Recent Advances in Quantitative Remote Sensing (RAQRS IV)*, Valencia, Spain, September 2014.
- Roupioz, L., Jia, L., Nerry, F., Menenti, M., 2014. Correction of the sub-pixel effects of topography on albedo retrieved from FengYun-2D data over the Tibetan Plateau (poster presentation). In *Dragon 3 Mid term results Symposium proceedings (ESA SP-724)*, Chengdu, P.R. of China, May 2014.
- Menenti, M., Liu, Q., Jia, L., Xin, X., Roupioz, L., Li, Z. et al., 2014. Terrestrial water cycle in south and east Asia: hydrospheric and cryospheric data products. In *Dragon 3 Mid-term results Symposium proceedings (ESA SP-724)*, Chengdu, P.R. of China, May 2014.

- Faivre, R., Ghafarian, H., Tang, B., Colin, J., Jia, L., Roupioz, L., 2012. Multi-annual data products on turbulent heat fluxes at the local and continental scale using AATSR and FY-2 data. In *Dragon 2 Final results Symposium proceedings (ESA SP-704)*, Beijing, P.R. of China, June 2012.
- Mücher, C.A., Roupioz, L.F.S., Kramer, H., Bunce, R.G.H., 2010. Use of LiDAR to map and monitor habitats. In *Proceedings of European LiDAR Mapping Forum (ELMF)*, The Hague, The Netherlands, November-December 2010.

### Conferences

- Roupioz, L., Jia, L., Nerry, F., Menenti, M. Correction of sub-pixel topographic effects on land surface albedo retrieved from geostationary satellite (FY-2D) observations (poster presentation), *Dragon 3 Symposium*, Palermo, Sicily, June 2013.
- Roupioz, L., Jia, L., Nerry, F., Menenti, M. Estimating net radiation flux over highly heterogeneous terrain on the Qinghai – Tibet Plateau by integrating multiple remote sensing and meteorological observables (oral presentation), *Watglobs*, April 2013, Beijing, China.
- Roupioz, L., Jia, L., Nerry, F., Menenti, M. Correcting sub-pixel topographical effects on land surface albedo retrieved from geostationary satellite (FengYun-2D) observations (oral presentation), *International Symposium on Remote Sensing of Environment ISRSE35*, April 2013, Beijing, China.
- Roupioz, L., Schmidt, A., Kramer, H. Object based classification of mussel banks in the Wadden Sea (oral presentation), *GEOgraphic Object-Based Image Analysis (GEOBIA)*, June-July 2010, Gent, Belgium.

### Reports

- Faivre, R., Colin, J., Roupioz, L., Ghafarian, H., Li, Z., Jia, L., Nerry, F., Menenti, M., 2013. Validated time-series maps of fluxes over 3 years, with a frequency of one day, *CEOP-AEGIS Deliverable Report De3.5*, University of Strasbourg, France, ISSN 2118-7843, 22p.
- Jia, L., Roupioz, L., Guangcheng, H., Zhou, J., 2013. Anomalies maps of net radiation, LST and FPAR, *CEOP-AEGIS Deliverable Report De9.7*, University of Strasbourg, France, ISSN 2118-7843, 25p.
- Faivre, R., Colin, J., Roupioz, L., Ghafarian, H., Jia, L., Menenti, M., 2012. Multi-scale parameterization of turbulent heat fluxes for heterogeneous land surfaces, *Dragon 2 Final report*, European Space Agency.
- Faivre, R., Colin, J., Roupioz, L., Ghafarian, H., Li, Z., Jia, L., Nerry, F., Menenti, M., 2012. Preliminary time-series maps of fluxes over 3 years, with a target frequency of one week, *CEOP-AEGIS Deliverable Report De3.4*, University of Strasbourg, France, ISSN 2118-7843, 27p.

- Colin, J., Roupioz, L., Ghafarian, H., Bai, J., Jia, L., Liu, S.M., Faivre, R. et al., 2011, Surface radiative and energy balance time-series processing and validation procedure document, *CEOP-AEGIS Deliverable Report De3.3*, University of Strasbourg, France, ISSN 2118-7843, 34p.
- Hazeu, G.W., Roupioz, L.F.S., Perez-Soba, M., 2010. Europe's ecological backbone: recognising the true value of our mountains, *EEA Report No 6/2010*, ISSN 1725-9177, 225p.
- Kramer, H., Oldengarm, J., Roupioz, L., 2010. Nederland is groener dan kaarten laten zien : mogelijkheden om 'groen' beter te inventariseren en monitoren met de automatische classificatie van digitale luchtfoto's, *WOt-werkdocument 216*, Wettelijke Onderzoekstaken Natuur & Milieu, 50p.
- Menenti, M., Colin, J., Faivre, R., Roupioz, L., Jia, L., 2010, Generalization of the surface energy balance calculation over the Tibetan Plateau, *CEOP-AEGIS Deliverable Report De3.2*, University of Strasbourg, France, ISSN 2118-7843, 32p.
- Perez-Soba, M., Hazeu, G.W., Verburg, P.H., Eupen, M. van, Danes, M.H.G.I., Roupioz, L., 2010. Analysis of land cover trends and projections of land use for the next 25 years. Reflecting environmental land use needs into EU policy: Preserving and enhancing the environmental benefits of "Land services": Soil sealing, biodiversity corridors, intensification / marginalisation of land use and permanent grassland, *Final report to the European Commission, DG Environment on Contract ENV.B.1/ETU/2008/0030*, Institute for European Environmental Policy / Alterra Wageningen UR., p. 47-86.
- Fey-Hofstede, F.E., Cremer, J.S.M., Dijkman, E.M., Jansen, J.M., Roupioz, L., Schmidt, A.M., 2009. Development of analysis techniques for the use of aerial photography in the monitoring of intertidal mussel beds and oyster beds, *Texel : IMARES (Report C004/09)*, p. 27.

## Modélisation et suivi de l'éclairement et de l'albédo de surface à partir de données satellitaires: le cas du Tibet

### Résumé

Le suivi journalier du bilan radiatif solaire est indispensable à l'étude des processus à l'interface sol-atmosphère, en particulier en climatologie et en hydrologie. Dans le cadre du projet CEOP-Aegis visant à étudier l'hydrologie du plateau du Tibet, cette thèse se concentre sur le développement d'une méthode permettant d'en estimer le bilan radiatif solaire de surface de façon quotidienne. Une série temporelle de flux radiatifs produite à partir de produits satellitaires existants met en évidence la nécessité d'intégrer la variabilité sous-pixel du terrain et des nuages pour les zones aussi hétérogènes que le Tibet. L'analyse de l'impact de la variabilité spatiale et temporelle des nuages sur le rayonnement solaire illustre le bénéfice lié à l'utilisation de la répartition des nuages plutôt que la fraction de nébulosité et l'importance d'une résolution temporelle élevée. Une méthode novatrice proposée pour la correction topographique sous-pixel montre que l'utilisation d'un modèle numérique de terrain à haute résolution spatiale améliore significativement l'estimation de l'éclairement ainsi que de l'albédo. Deux approches sont proposées pour améliorer l'estimation du bilan radiatif intégrant de manière adéquate l'hétérogénéité sous-pixel.

**Mots clés :** Bilan radiatif, Eclairement, Albédo, Topographie, Nébulosité

### Abstract

Monitoring the solar radiation budget on a daily basis is a prerequisite to study land surface processes, especially in climatology and hydrology. As part of the CEOP-Aegis project studying the hydrology of the Tibetan Plateau, this thesis focuses on developing a method to adequately estimate at-surface daily solar radiation budget over this particular area. A radiation budget time series produced based on existing satellite data products highlights the necessity to consider terrain and clouds sub-pixel variability when working over heterogeneous areas such as the Tibetan Plateau. The analysis of the impact of spatial and temporal variability of clouds on solar radiation demonstrates that the surface irradiance estimation would benefit from using cloud distribution instead of cloud fraction and the significance of high temporal resolution. A new sub-pixel topographic correction method is proposed and shows that using high resolution digital elevation model improves the irradiance as well as the albedo retrieval. Two approaches are proposed to improve solar radiation budget estimates taking into account adequately the sub-pixel heterogeneity.

**Keywords :** Radiation budget, Irradiance, Albedo, Topography, Clouds